The University of Nottingham
UNITED KINGDOM · CHINA · MALAYSIA

Abebe, Robert (2018) End Winding Mount Integrated Motor Drive. PhD thesis, University of Nottingham.

Access from the University of Nottingham repository:
http://eprints.nottingham.ac.uk/49209/1/Thesis.pdf

Copyright and reuse:

The Nottingham ePrints service makes this work by researchers of the University of Nottingham available open access under the following conditions.

This article is made available under the University of Nottingham End User licence and may be reused according to the conditions of the licence. For more details see: http://eprints.nottingham.ac.uk/end_user_agreement.pdf

For more information, please contact eprints@nottingham.ac.uk

End Winding Mount Integrated Motor Drive

by

Robert Abebe MEng (Hons)

Thesis submitted to the University of Nottingham for the degree of Doctor of Philosophy

September 2017

Abstract

With increased need for high power density, high efficiency and high temperature capabilities in Aerospace and Automotive applications, Integrated Motor Drives (IMD) offer a potential solution. . A number of IMD configurations already exist, each with their respective merits, drawbacks and industrial applications. Despite these potential benefits of IMDs, thermo-mechanical concerns remain over the close coupling integration of the power module and machine

This thesis presents a novel end winding mount Integrated Motor Drive. CFD simulations are performed for thermal analysis of the proposed concept and investigation of the effects of the cooling systems in IMDs. The thermal, mechanical and electrical effects of close coupling integration are investigated and solutions proposed. The design and manufacture of a working End Winding mount IMD prototype is also described with particular attention to the thermal effects and temperature distribution in the manufactured prototype.

Acknowledgments

I would like to express my sincere gratitude to my supervisors Prof. Mark Johnson and Prof. Chris Gerada for the opportunity to start this journey and the support provided. Special thanks especially to Prof. Mark Johnson, for your patience and guidance during the course of the project – I couldn't have wished for a better mentor and supervisor for my PhD.

My heartfelt thanks and appreciation go to Dr. Giovanni Lo Calzo, Dr. Gaurang Vakil and Dr. Bassem Mouawad. You guys went above and beyond to support me and counting on you as colleagues and more importantly, friends, has made this whole experience enjoyable – I am forever grateful!

To Lee and Lilliana, Tom Cox and Jian Feng – my deepest gratitude for all your help and guidance even when you didn't have to. To the rest of my colleagues in the PEMC group, it has been a privilege to work with you.

To my parents and family, your trust and patience during this period has been immeasurable. George, for the quiet conversations and unwavering motivation, I thank you.

Finally and most importantly, to Viktorija, words cannot express my gratitude. I certainly couldn't have done this without you!

Table of Contents

1. Introduction

1.1. Introduction 1

1.2. Project Aims and Objectives 5

1.2.1. Aims. 5

1.2.2. Objectives 5

1.3. Thesis Structure. 6

2. Literature Review 8

2.1. Principal Types of IMD 8

2.1.1. Surface mount integration 9

2.1.2. End plate mount integration 11

2.1.3. Stator iron mount integration 14

2.2. Cooling Systems 17

2.3. High Temperature Devices 22

2.3.1. Wide Band Gap Materials 22

2.3.2. Silicon Carbide vs Gallium Nitride 25

2.4. Modular Integration 28

2.5. Converter Topologies for IMD 29

2.5.1. Matrix Converter 30

2.5.2. Two-Level Full Bridge Converter 31

2.5.3. Three-level Neutral Point Clamped (NPC) converter . 32

2.5.4. Multiphase full bridge converter 33

2.6. Passive Components 35

2.6.1. Ceramic Capacitors 36

2.6.2. Electrolytic Capacitors 37
2.6.3. Film Capacitors 39
2.6.4. Electro Chemical Double Layer Capacitors 39
2.7. Packaging of Power Electronics Module 40
2.7.1. Interconnects 41
2.7.2. Die attachment 43
2.7.3. Encapsulant 44
2.7.4. Substrate 44
2.8. Challenges in IMD Design 46
2.9. Future Trends 48
3. End Winding Mount IMD 52
3.1. Introduction 52
3.2. End winding Mount IMD 52
3.2.1. Thermal Challenges 58
3.2.2. Mechanical Challenges 58
3.2.3. Electrical Challenges 59
3.3. End Winding IMD Prototype 1 60
3.3.1. Software simulations 61
3.3.1.1. Lumped Parameter Models 61
3.3.1.2. Computational Fluid Dynamics (CFD) and FEA Analysis 68
3.3.2. Experimental Results 77
3.3.2.1. E-core Sample 78
3.3.2.2. Power Electronics 81
3.3.2.3. Sintering Process 84
3.3.2.4. Winding Mount Power Electronics 85
3.4. Conclusion 91

4. Prototype 1 optimization 94
4.1. Introduction 94
4.2. Prototype 1 optimization 95
4.2.1. Motorette winding 95
4.2.2. Attachment joint 98
4.2.2.1. Pressure Assisted Sintering 98
4.2.2.2. Pressure-less Sintering 109
4.2.2.3. Solder 112
4.3. Conclusion 117
5. CFD Simulations for E. Winding Mount IMD Prototype 2. 120
5.1. Introduction 120
5.2. Geometry Design for End Winding Mount IMD Prototype 2 122
5.2.1. Geometry Design 122
5.2.2. CFD Analysis 128
5.3. Conclusion 144
6. Experimental Validation of Prototype 2 147
6.1. Introduction 147
6.2. Prototype components 147
6.2.1. Motorette Back Iron 147
6.2.2. Copper winding 149
6.2.3. PE Module 151
6.2.4. DBC Substrate 152
6.2.5. SiC MOSFETs 154
6.2.6. Motorette Assembly Process 155
6.2.7. Motorette Housing 159

6.2.8. Current Sensing 162
6.3. Thermal Tests 163
6.4. Switching Test 187
6.5. Conclusion 201
7. Comparison of Experimental and Simulation Results . . 203
7.1. Introduction 203
7.2. Comparison of Experimental and Simulation Results 204
7.2.1. Bare dies 204
7.2.2. Substrate 207
7.2.3. Copper Winding 209
7.3. Conclusion 212
8. Conclusion and Future Work 214
8.1. Conclusion 214
8.2. Future Work 219

List of Figures

Figure 2.1: Surface mount integration (a) Simple addition of PE case on electric motor (b) Modularised converter units mounted on motor housing 9

Figure 2.2: (a) Danfoss VLT DriveMotor LCM 300 (b) Siemens SIVITEC MSA 3300 11

Figure 2.3: Endplate mount integration. Redesigned finned endplate with Converter Loss Simulation Resistors 12

Figure 2.4: (a) UQM PowerPhase HD 250 (b) Bonfiglioli Electric Power train 600D 13

Figure 2.5: Back iron mount integration. (a). Power electronics mounted on Stator Back Iron. (b) Stator pole module consisting of an iron pole piece and a power converter module 14

Figure 2.6: (a) Unsprung assembly Protean in-wheel motor. (b) Cross section of Protean in-wheel motor 15

Figure 2.7: Showing parallel and series cooling paths (a) Axial View of PE mounted on Endplate – parallel path. (b) Simplified layout of water pipes through machine housing – series path 19

Figure 2.8: (a) Temperature gradient in a standard cooling system (b) Danfoss Showerpower cooling concept showing the finned baseplate and vents for coolant input and output 21

Figure 2.9: Matrix converter 30

Figure 2.10: Two-Level full bridge converter 32

Figure 2.11: 3-Level NPC full bridge converter 33

Figure 2.12: Multiphase full bridge converter 34

Figure 3.1: End Winding Mount IMD concept 54

Figure 3.2: Input parameters for thermal resistance 64

Figure 3.3: Transient thermal graph showing the temperatures of the lumped parameter modelled wound E-core at 25 W 65

Figure 3.4: Transient thermal graph showing the temperatures of the lumped parameter modelled wound E-core at 50 W 65

Figure 3.5: Transient thermal graph showing the temperatures of the lumped parameter modelled sintered JFET on end windings 66

Figure 3.6: Simscape thermal resistance model of end winding mounted 67

Figure 3.7: Geometry of motorette in casing 69

Figure 3.8: CFD analysis showing air velocity over the end windings 71

Figure 3.9: Steady state temperature distribution of E-wound core at 25W losses 72

Figure 3.10: Steady state temperature distribution of E-wound core at 50W losses 72

Figure 3.11: Steady state temperature distribution of JFET sintered on AlN substrate at 5W losses 73

Figure 3.12: Temperature distribution of JFET sintered on AlN substrate at 65W motorette losses and 16W JFET losses 74

Figure 3.13: Seady state and transient temperatures of the ANSYS modelled IMD section 77

Figure 3.14: Characterised motorette without power electronics attached 78

Figure 3.15: Motor Housing 78

Figure 3.16: Motorette mounted on 3D printed supports 79

Figure 3.17: Motorette in fan-mounted housing 79

Figure 3.18: Temperatures of motorette components at 25W 80

Figure 3.19: Temperatures of the motorette components at 50W . . 81

Figure 3.20: SiC JFET with aluminium wire bond 82

Figure 3.21: Etched bottom side of substrate 82

Figure 3.22: Wires soldered on top-side copper 83

Figure 3.23: Temperatures of the substrate and JFET at 5W losses .83

Figure 3.24: Spaced out and pressed copper end windings 84

Figure 3.25: shows the manual screen-printing system used to apply the paste 84

Figure 3.26: Cover for die and wire bond during sintering 84

Figure 3.27: Power electronics unit and wound E- core in sintering press 85

Figure 3.28: Power electronics unit sintered on end windings of wound E-core 85

Figure 3.29: Experimental setup of JFET sintered on end windings of motorette and energised separately 86

Figure 3.30: Transient thermal graph showing the temperatures of the IMD components at 65W copper losses and 16W JFET losses 87

Figure 4.1: End winding profile cut with a CNC cutter 96

Figure 4.2: Copper winding machined from a block of copper 95

Figure 4.3: Dummy end winding and AlN substrate created for testing attachment processes 97

Figure 4.4: Steel stencil for sinter paste deposition 98

Figure 4.5: SEM X-ray of pressure-assisted silver sinter layer 99

Figure 4.6: Steel rods glued on the sintered sample 101

Figure 4.7: Detached substrate from end winding dummy after mechanical pull test 102

Figure 4.8: Tensile strength test of the sinter layer 103

Figure 4.9: PVD silver coated end winding dummy samples 105

Figure 4.10: Silver coated end winding dummy and substrate profile 106

Figure 4.11: Tensile strength test of silver coated sinter layer (pressure assisted) 107

Figure 4.12: Temperature profile used for the pressure-less silver sintering process 109

Figure 4.13: Tensile strength test of silver coated sinter layer (pressure-less) 110

Figure 4.14: X-ray SEM of solder layer 112

Figure 4.15: Detached substrate from end winding dummy after mechanical pull test 114

Figure 4.16: Tensile strength test of solder 114

Figure 5.1: CFD geometry of Prototype 2 with mounting support . 124

Figure 5.2: Complete CFD geometry 124

Figure 5.3: Velocity profile of coolant at 10% fan speed 128

Figure 5.4: Y-Axis view of coolant velocity profile at 10% fan speed 129

Figure 5.5: Temperature profile of Prototype 2 components at 10% fan speed 130

Figure 5.6: Z-axis view of Prototype 2's temperature profile at 10% fan speed 130

Figure 5.7: Velocity profile at 50% fan speed 131

Figure 5.8: Temperature profile at 50% fan speed 132

Figure 5.9: Velocity profile at 100% fan speed 132

Figure 5.10: Temperature profile at 100% fan speed 133

Figure 5.11: Winding temperature at 10% fan speed 134

Figure 5.12: Winding temperature at 50% fan speed 135

Figure 5.13: Winding temperature at 100% fan speed 135

Figure 5.14: Probe locations on the Winding and Back Iron 136

Figure 5.15: Solder layer temperature at 10% fan speed 137

Figure 5.16: Component temperature difference utilising solder and silver sinter attachment layers at varying fan speeds 138

Figure 5.17: Steady state temperatures for IMD components at varying fan speed 140

Figure 5.18: Water velocity profile at 10% flow rate 142

Figure 6.1: Kapton taped Back Iron and Tooth laminations 148

Figure 6.2: Side view of motorette winding with 1 mm spacing between turns 149

Figure 6.3: Schematic of the H-Bridge circuit 151

Figure 6.4: Top and bottom side of AlN substrate with vias 153

Figure 6.5: Top and bottom side of SiC MOSFET 154

Figure 6.6: Sintered MOSFETs on the top side of the AlN substrate 155

Figure 6.7: AlN substrate soldered on copper windings 156

Figure 6.8: Assembled PE Module mounted on copper winding . . 157

Figure 6.9: Assembled PE Module and winding in Motorette Back Iron 158

Figure 6.10: 3D printed motorette housing with fan attached on the back side 159

Figure 6.11: Motorette housing and PLA support 160

Figure 6.12: Complete assembly of Prototype 2 161

Figure 6.13: SEM image of solder layer 163

Figure 6.14: Schematic drawing of thermal test rig 164

Figure 6.15: PE module sprayed with non-conductive coating (red coating) 166

Figure 6.16: Test rig for experimental validation 167

Figure 6.17: Prototype 2 component temperatures at 10% fan speed (a) PE module temperature (b) Motorette temperature 170

Figure 6.18: Prototype 2 component temperatures at 20% fan speed (a) PE module temperature (b) Motorette temperature 171

Figure 6.19: Prototype 2 component temperatures at 30% fan speed (a) PE module temperature (b) Motorette temperature 172

Figure 6.20: Prototype 2 component temperatures at 40% fan speed (a) PE module temperature (b) Motorette temperature 173

Figure 6.21: Prototype 2 component temperatures at 50% fan speed (a) PE module temperature (b) Motorette temperature 174

Figure 6.22: Prototype 2 component temperatures at 60% fan speed (a) PE module temperature (b) Motorette temperature 175

Figure 6.23: Prototype 2 component temperatures at 70% fan speed (a) PE module temperature (b) Motorette temperature 176

Figure 6.24: Prototype 2 component temperatures at 80% fan speed (a) PE module temperature (b) Motorette temperature 177

Figure 6.25: Prototype 2 component temperatures at 90% fan speed (a) PE module temperature (b) Motorette temperature 178

Figure 6.26: Prototype 2 component temperatures at 100% fan speed (a) PE module temperature (b) Motorette temperature 179

Figure 6.27: Prototype 2 component temperatures at varying flow rates 180

Figure 6.28: Junction to Inlet thermal resistance vs Flow rate . . . 184

Figure 6.29: Switching test at 50% Duty Cycle (10.3V; 5.4A) (a) PE module temperature (b) 2A Ripple Current; 12.2A mean winding current 191

Figure 6.30: Switching test at 60% Duty Cycle (10.3V; 9.2A) (a) PE module temperature (b) 2A Ripple Current; 17.7A mean winding current 192

Figure 6.31: Switching test at 80% Duty Cycle (10.3V; 9.7A) (a) PE module temperature (b) 2.1A Ripple Current; 18A mean winding current 193

Figure 6.32: Switching test at 82% Duty Cycle (10.3V; 9.6A) (a) PE module temperature (b) 2.2A Ripple Current; 18.4A mean winding current 194

Figure 6.33: Switching test at 86% Duty Cycle (10.3V; 11.6A) (a) PE module temperature (b) 2.2A Ripple Current; 20A mean winding current 195

Figure 6.34: Switching test at 87% Duty Cycle (10.3V; 13.2A) (a) PE module temperature (b) 2A Ripple Current; 22A mean winding current 196

Figure 6.35: Switching test at 87.5% Duty Cycle (10.3V; 14A) (a) PE module temperature (b) 2.1A Ripple Current; 23.6A mean winding current 197

Figure 6.36: Component temperature with varying Duty Cycle . . . 198

Figure 7.1: Differences in temperature between CFD and Experimental results for the bare dies 205

Figure 7.2: Differences in temperature between CFD and Experimental results for the Substrate 209

Figure 7.3: Differences in temperature between CFD and Experimental results for the Windings 210

Figure 7.4: Differences in temperature between CFD and Experimental results for the Back Iron 211

List of Tables

Table 2.1: Commercially available IMDs and their target applications 16

Table 2.2: Material properties of Si, SiC, GaN and Diamond 24

Table 3.1: Temperature distribution of IMD components from MATLAB, ANSYS Steady State and transient simulation results. . 74

Table 3.2: FEA and experimental results showing maximum temperatures of individual IMD components at 25W and 50W . . . 80

Table 3.3: Steady state temperature distribution of IMD components from MATLAB, ANSYS and experimental results 88

Table 3.4: Experiments and Test conditions performed 92

Table 4.1: Comparison of the attachment methods analysed 116

Table 5.1: Air speed at varying fan speed 123

Table 5.2: Prototype components and materials 125

Table 6.1: Measured winding inductance in air and laminated core .150

Table 6.2: Steady state Temperature of Prototype 2 components at different flow rates 181

Table 6.3: Steady state Temperature of Prototype 2 components at different Duty Cycles 189

Nomenclature

Symbol	**Description**	**Units**
A	surface area	m^2
d	diameter	m
h	heat transfer coefficient	W/m^2k
Hz	frequency	Hertz
I	current	amps
k	thermal conductivity	W/mk
l	length	metres
L	Material thickness	metres
p	pressure	Pa
P	power	Watts
Q	heat	Watts
R	resistance	ohms
Re	Reynolds number	
Nu	Nusselt's number	
Pr	Prandtl number	
T	temperature	K
u	velocity	m/s
x	distance	m

Abbreviation	**Description**
2D	2 dimensional
3D	3 dimensional
AC	Alternating current
AlN	Aluminium Nitride
CAD	Computer Aided Design
CCM	Continuous Conduction Mode
CFD	Computational Fluid Dynamics
DCM	Discontinuous Conduction Mode
DPC	Direct Power Converter
ECDL	Electro-Chemical Double Layer
EV	Electric Vehicle
EMI	Electromagnetic Interference
FCOC	Flip-Chip-ON-Chip
FEA	Finite Element Analysis
GaN	Gallium Nitrite
IGBT	Insulated Gate Bipolar Transistor
IMD	Integrated Motor Drive
MLCC	Multi-Layer Ceramic Capacitors

MOSFET	Metal Oxide Semiconductor Field Effect Transistor
NPC	Neutral Point Clamped
PE	Power Electronics
SiC	Silicon Carbide

Chapter 1

Introduction

1.1 Introduction

Over the last two decades there has been a shift from traditional physically separated motor and drive systems to more compact, power dense, motor-drive combinations [1]. This new power-dense motor-drive structure combines both the motor and its associated control and drive circuitry within a single enclosure. The earliest records of commercially available motor-drive systems were manufactured by Grundfos in 1991 and Franz Morat KG in 1993 [2].

These compact systems have been called a variety of names from 'smart motors' to 'integrated motors', the latter forming the foundation for the new moniker currently identified with these systems [3]. The term 'integrated motor drive (IMD)' is the latest associated with this class of products and is as a result of the success of a TB Woods Inc. manufactured motor-drive registered under the same name [3].

IMDs are increasingly being developed and produced by machine manufacturers due to the significant potential benefits they offer. The most significant of these benefits include direct replacement of inefficient direct on line motors, increased power density, lower losses and lower costs compared with separate motor and drive solutions. Technological advancements over the last decade have led to the development of robust electronic components able to withstand the harsh environments required by some forms of integration [4]. By eliminating separate enclosures and

long cable runs, the integrated approach promises to lower system costs by 20 to 40% [5].

Development of converter technology, more efficient and robust passive components (especially capacitors), reliability and packaging as well as advancements in research of high-temperature power semiconductor materials such as silicon carbide (SiC) and gallium nitride (GaN), will enable power electronics to meet the harsh and rigorous environmental conditions the converter faces in an IMD.

Despite the attractive benefits IMDs present, reservations still exist on them being the future in motor drives technology. Simple addition of power electronics to the machine adds volume to the combination if the structures are not properly physically integrated. Unlike the machine, the PE is not known for its robustness – mechanically or thermally. Without proper thermal management, placing the PE close to the motor (heat source) might cause irreparable damage to the drive. There are also problems of vibrations which could damage the internal electrical connections of the converter and decrease the expected PE lifetime. Limitations due to lack of available space in the motor and the need to adapt the power converter to the electromagnetic field stresses inside the motor housing also pose major problems [5].

Elimination of transmission cables has economic advantages, including increased reliability due to the removal of the output filter commonly required for long cables. Removal of long cable runs and integration into a single package will also significantly reduce potential electromagnetic interference (EMI). This allows for EMI testing and prevention measures to be applied to the overall package at the point of manufacture. The space requirement for a separate converter will be eliminated and overall system size may be reduced compared with a traditional separated solution [6, 7]. Commissioning and testing time can also be potentially reduced by performance testing of the converter and machine as a single unit [6, 8, 9]. This will also eliminate the need for inverter control rooms and ventilation equipment as the integrated motor and drive can also utilise a singular cooling system, further reducing size and cost of the IMD compared with a separated solution [10]. Integrating the motor and drive will also allow for increased automation of the manufacturing process [11].

Various power electronic integration approaches have been proposed in the literature ranging from a simple mounting of the converter on the machine housing to high levels of modular integration.

To take advantage of the benefits of an IMD it is important to define what it is. For the purpose of this work – an IMD is the result of the functional and structural integration of the power electronics (PE) converter with the machine as a single unit taking into consideration the

electrical and structural and thermal impacts both components have on each other and the system as a whole.

All IMD units fulfil the functional electrical integration of the PE with the machine, as this is a defining feature of an IMD. However, the structural integration is a design problem which requires careful mechanical and thermal analysis of the converter and machine as a single unit. This is a challenge for designing and manufacturing an IMD. Despite the attractive benefits IMDs present, reservations still exist about their widespread use. A simple addition of PE to the machine adds volume to the combination if the structures are not properly physically integrated. Having the PE in close proximity to the machine (anywhere on or inside the housing) poses a thermal management problem for the entire system. Until recently, above 7.5 kW output, the effects of heating from both machine and drive build up significantly and present a practical limit for the manufacture of higher power drives [3, 6]. The physical size of the converter also limits the practical power rating of commercial IMD units up to the 7.5 kW limit. Commercialisation of higher power and larger size IMDs will require more complex designs and impact product costs [1, 4]. Above this 7.5 kW threshold, traditional separated motor-drive systems might offer a better alternative hence the dearth in high power commercially available IMDs. Without proper thermal management, placing the PE close to the machine (the prominent heat source) might cause irreparable damage to the drive. There are also problems of vibrations which could damage the internal electrical connections of the

converter and decrease the expected PE lifetime. Limitations due to lack of available space in the motor and the need to adapt the power converter to the electromagnetic field stresses inside the motor housing also pose major issues.

This thesis presents a novel integrated motor drive concept – Winding Mounted Integrated Motor Drive. Experimental and CFD analysis on the thermal behaviours of both converter and machine in close proximity is also presented.

1.2 Project Aims and Objectives

1.2.1 Aims

The aim of this project is to research, design and develop a novel motor drive solution that offers benefits in power density, maximum operating temperature and potential lower lifetime and maintenance costs.

1.2.2 Objectives

The main objectives of this project are to

- Analyse existing motor drive solutions outlining their respective advantages and disadvantages as well as industrial applications.

- Present the novel motor drive solution, its configuration and how it differs from already established motor drive options.
- Use software simulation packages to design and analyse the temperature distribution in the motor drive concept.
- Manufacture a working prototype to validate the software simulations.
- Optimise the prototype.
- Design and manufacture a final prototype incorporating optimisation recommendations from the first prototype.

1.3 Thesis Structure

- Chapter 2 presents a literature review of existing integrated motor drive configurations and their industrial applications. High temperature devices and the passive components and interconnect materials utilised in PE module manufacture are also analysed. Cooling systems and packaging technologies for IMDs are also investigated.
- Chapter 3 introduces a novel End winding mount IMD concept and details the software and experimental results from the first prototype
- Chapter 4 details the optimisation of the end winding mount IMD prototype investigated in Chapter 3 to tackle the thermos-mechanical challenges encountered.

- Chapter 5 presents CFD simulations of the final manufactured prototype with assumptions made for the boundary conditions
- Chapter 6 provides details on the experimental validation of the final end winding mount IMD manufactured.
- Chapter 7 compares the experimental and simulation results for the final prototype of the end winding mount IMD concept.
- Chapter 8 makes conclusions and recommendations for future works on the IMD concept introduced.

Chapter 2

Literature Review

2.1 Principal Types of IMD

Despite significant awareness of IMDs in industry, extensive research and literature on the topic, very little work exists on complete PE and machine integration. The majority of literature and research exists as reviews of present IMD technologies and market perspective [12–16], finite element analysis (computer simulations) [17, 18] and functional integration [19]. Due to spatial restrictions for physical integration of PE on or inside the motor housing, the complete structural PE integration research and documentation can be divided into three major categories namely – surface mount integration, end plate mount integration and stator iron mount integration.

2.1.1 Surface mount integration

This involves the physical mounting of the power converter on the motor housing. Different variations of this concept have been proposed – from a simple mount of the PE on the case of the motor to modularising the power converter and mounting the smaller converter units on the motor housing [19–24]. In Fig. 2.1a, a simple addition of PE on the motor is shown while Fig. 2.1b shows a modularised converter mounted on the motor housing. A shared or separate cooling system could be adopted depending on application and power density requirements. This mode of

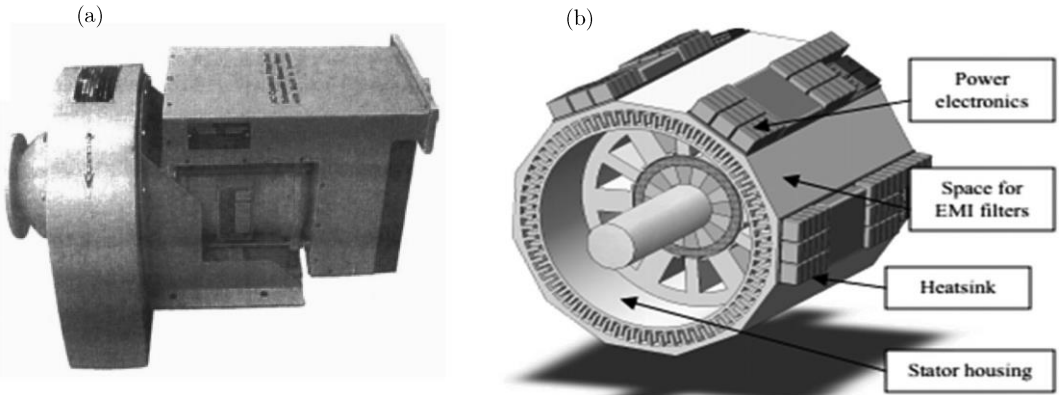


Fig. 2.1 Surface mount integration (a) Simple addition of PE case on electric motor [21] (b) Modularised converter units mounted on motor housing [22]

integration is particularly attractive because of its simplicity, low cost of manufacturing and relative ease of implementation [16, 23]. The housing acts as a thermal barrier providing thermal isolation between the converter and the machine (particularly the stator windings – a major heat source). The thermal management of the casing must guarantee full absorption of all of the power electronic heating loss and all of the radially conducted heating loss from the machine. By redesigning the housing to

accommodate an active cooling system [20], it can also act as a heat sink for the PE and converter (common thermal node) by offering a larger surface area for heat transfer and dissipation. The housing also provides mechanical stability and a mounting surface for the converter [21]. Extra thermal management and cooling mechanisms can be adopted for high power density motors where stator winding temperatures reach and sometimes exceed 200°C. Forced air cooling using fins embedded in the stator housing is employed in [20, 22] utilises a liquid cooling system by running water pipes through the stator housing.

Numerous commercially available surface mounted IMD configurations exist, with the majority focused on pumps, fans and compressor applications. Low power ratings are available, with Schneider offering the Lexium 32i range with power ratings from 0.4–2.2 kW [25]. Danfoss offer mid power range IMDs up to 7.5 kW [26] and VEM Motors [27] offers a line of IMDs (compact Line) with power ratings up to 30 kW. High power IMDs are also commercially available with the Siemens SIVETEC series for electric vehicles (EV) offering surface mount IMD systems from 30–200 kW range with power densities up to 2.6 kg/W [28]. This large range of power ratings highlights the numerous possibilities available when adopting this configuration, with limitations largely being application dependent (Fig. 2.2).

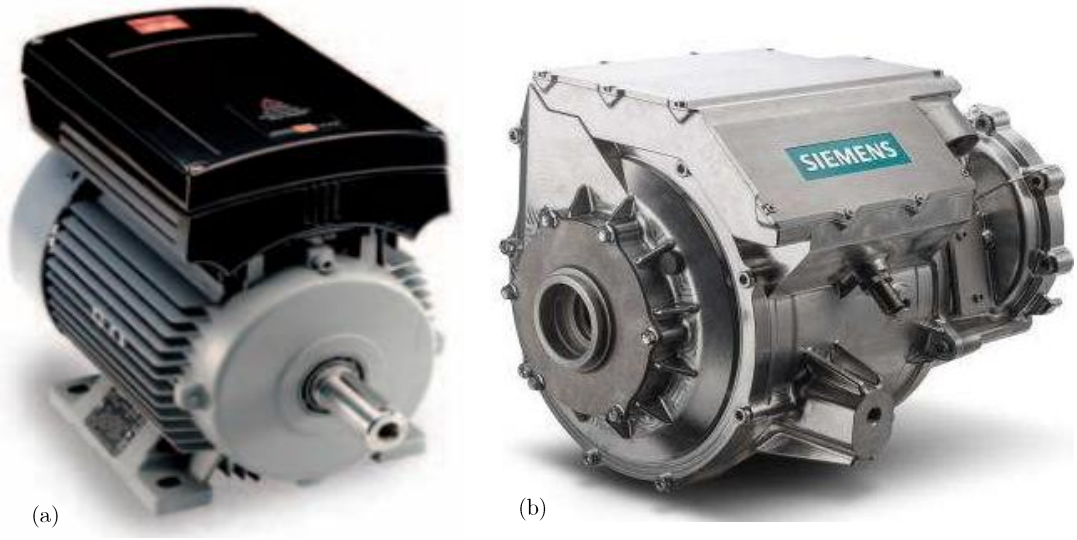


Fig. 2.2 (a) Danfoss VLT DriveMotor LCM 300 [26] (b) Siemens SIVITEC MSA 3300 [28]

Recent commercially available surface mount IMDs suggest a shift from a more centralised surface mounted converter to a modular structure. Lenze offer modular low to mid-range IMDs with power ratings ranging from 0.4–7.5 kW [29]. Commercial high power modular IMDs with ratings up to 16.5 MW are currently manufactured by Siemens under the integrated drive systems range [30].

2.1.2 End plate mount integration

This is a variation of the surface (radial) mount configuration with converter mounting position dependent on available space in the axial direction. Like the surface mount, the end plate mount configuration provides a stable mechanical platform for the converter. It also provides thermal isolation of the PE from the machine. In the example published in literature [31], a 30 kW specialised configuration is manufactured

wholly dependent on the available space for mounting and the cooling system adopted. The endplate is redesigned to accommodate the PE and any extra cooling mechanism (cooling fins) added. This design aims to protect the PE by placing them before the motor in the cooling air flow [31]. However, the machine suffers in this regard due to the redesigned end plate restricting adequate ventilation and cooling since all end winding losses must now be conducted radially. It is generally assumed that the machine robustness means it is able to withstand elevated temperatures compared with the converter. Figure 2.3 shows an endplate mounted PE integration configuration.



Fig. 2.3 Endplate mount integration. Redesigned finned endplate with Converter Loss Simulation Resistors [31]

In a very high speed machine it may be difficult to adequately ventilate the rotor if adopting this design. An extra cooling mechanism may be necessary if the IMD in question is operated at high torque and low voltage [31]. The PE position in [31] is necessary due to the available space in a predefined motor and the cooling system adopted. The PE unit was mounted on a redesigned endplate which was used as a heat sink for

the power modules. Due to the lack of available space for mounting, a matrix converter was used in order to avoid the bulky energy storage elements and DC-link circuits used in traditional converter configurations [32]. The fan is redesigned (increased diameter) to compensate for the reduced air flow to the motor. Figure 2.4 shows industrial examples of endplate mounted IMD.

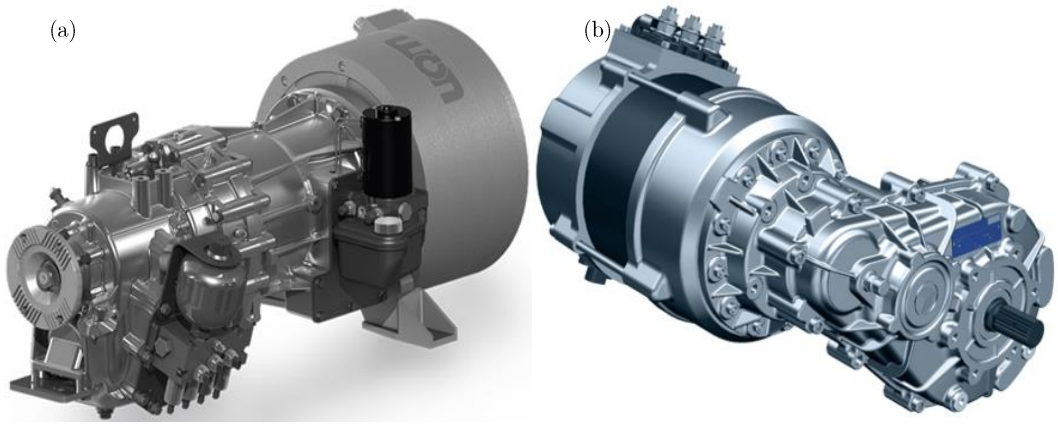


Fig. 2.4. (a) UQM PowerPhase HD 250 [33]. (b) Bonfiglioli Electric Power train 600D [34]

Commercial endplate mounted configurations include the UQM PowerPhase HD 250 with NexDrive EV3-850 [33] and Bonfiglioli Electric PowerTrain 600D [34]. Both IMDs are for electric vehicle applications with high power ratings of 250 and 45 kW, respectively. Other manufacturers include TB Woods and ABB with a mid-range power rating portfolio between 3.7 to 7.5 kW [35, 36]. Typical applications include EV where surface integration is difficult due to lack of space in the radial direction

2.1.3 Stator iron mount integration

This configuration is aimed at producing a more compact, high power density IMD. The power converter is mounted on the stator back iron as shown in Fig. 2.5 [6]. This concept is particularly beneficial when the height of the converter components (especially the DC-link capacitor) is small. The converter can fit into the space between the stator back iron and endplate.

(a)

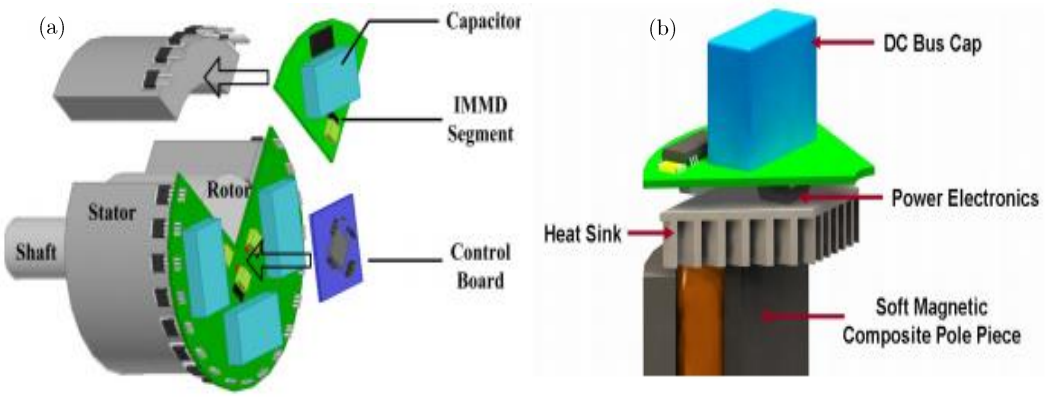


Fig 2.5 Back iron mount integration. (a). Power electronics mounted on Stator Back Iron [6]. (b) Stator pole module consisting of an iron pole piece and a power converter module [11].

The power converter may be segmented (modularised) around the back iron and the individual modules connected in series. The converter modules supply independent machine windings – akin to a switched reluctance machine method of energising the windings [6] or a concentrated winding. A similar design is utilised in [11] with the power converter also modularised. However, the use of silicon based PE required the need for a heat sink in every module thereby increasing the overall volume of the module. The 83 kW protean electric wheel [37, 38] is one of the very few commercially available manufactured IMD adopting this

approach (Fig. 2.6). The benefit of having a more compact IMD due to the integration of the converter in the machine housing presents a few problems. The complexity of efficiently integrating the relatively fragile converter within the machine housing is amplified by the high vibration and shock loads the converter is subjected to in the machine enclosure [38]. The limited space within the enclosure, places the converter in close proximity to the windings. This requires careful thermal analysis to ensure the PE can withstand the localised high temperature [39]. A liquid cooling system is adopted in [38] with an axial and orthogonal path to facilitate heat transfer and improve heat dissipation – cooling both the PE and windings simultaneously.

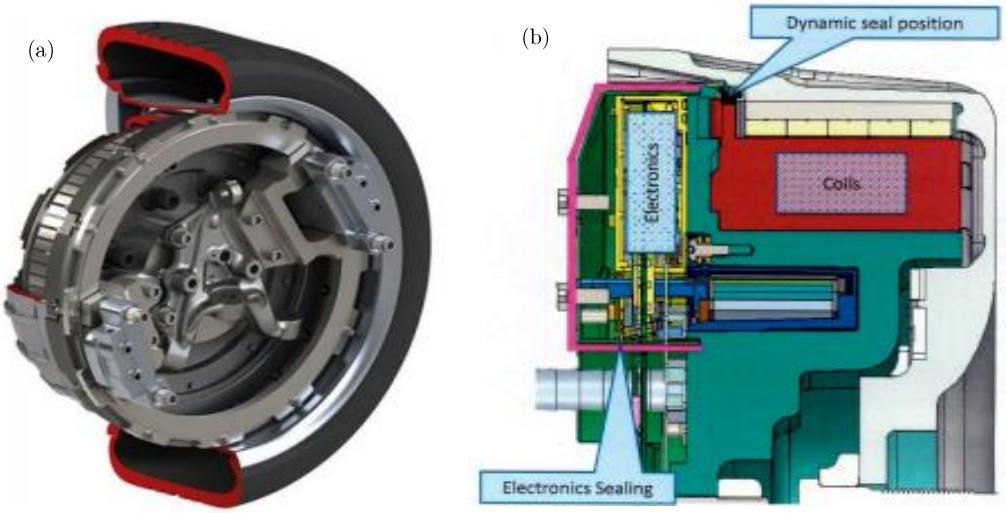


Fig. 2.6. (a) Unsprung assembly Protean in-wheel motor [37]. (b) Cross section of Protean in-wheel motor [38]

Table 2.1: Commercially available IMDs and their target applications

	Power rating (kW)	Mounting Position	Product	Application
Yaskawa	1.5-4	Surface	IE4MD [40]	-
Danfoss	0.5- 7.5	Surface	VLT FCM 300 [26]	Pumps, conveyors
Baldor	0.75-7.5	Surface	SmartMotor [41]	Fans
Lenze	7.5	Surface	8400 motec [29] [42]	Fans and pumps
Grundfoss	0.75-22	Surface	Grundfoss E-pump [43]	Pump
VEM Group	0.5-30	Surface	VEMoDRIVE compact [27]	Pump
Rockwell Automation	1-1.4	Surface	Kinetix 6000M [44]	Food packaging
Leroy-Somer	5.5-7.5	Surface	VARMECA 14 [45]	Hoisting
Schneider	0.6 -2.2	Surface	Lexium 32i [25]	Materials processing
Sew-Eurodrive	0.37 - 4	Surface	MOVIMOT [46]	Packaging and conveyor systems
Lenze	Up to 11kW	Surface	Smart Motor M300 [47]	Materials processing
Siemens	30- 200	Surface	SIVETEC MRS/MRI [28]	Electric vehicles
Ford	45 – 70	Surface	Hybrid Escape [48]	Electric vehicles
Alpha	Up to 0.2	Endplate	ASX series [49]	-
INMOCO	0.05-0.3	Endplate	Pegasus Integrated Motion system [50]	Material processing

AXOR	0.3 – 1.47	Endplate	Fast Back [51]	Material Processing
TB Woods	0.75 – 3.7	Endplate	E-trAC IMD [35]	-
ABB	0.75-7.5	Endplate	Integral Motor [36]	Pump and fan
UQM	140-250	Endplate	Polyphase HD with NexDrive EV3-850 [33]	Electric Vehicles
Bonfliglioli	45	Endplate	Electric Powertrain 600D [34]	Electric Vehicles
Protean	83	Stator Iron	Brabus E Class [37]	Electric Vehicle wheel

2.2 Cooling Systems

Close proximity integration demands power devices and modules capable of operating in harsh conditions, with elevated temperatures and thermal cycling – both active and passive. Various commercial products are unable to meet these demands and it is imperative an efficient cooling system is implemented. Cooling the integrated converter requires extensive thermal analysis of the converter and machine individually and as a unit. Adopting separate cooling systems for the converter and machine potentially increases the volume, cost and maintenance demands of the IMD.

In IMDs, the converter is mounted on or in the machine enclosure; this combines both thermal and mechanical requirements of these components

into a single design problem. Combining the physical structure of both converter and machine in a single housing reduces the physical size of the motor drive and reduces duplication. Adopting a unified cooling system instead of the traditional separated option tackles the thermal demands of both converter and machine simultaneously. However, since the thermal demands of the PE and machine vary (due to the large heat flux of the PE compared to the machine) a unified cooling system that efficiently accommodates both PE and machine is complicated [52]. The use of a combination of active and passive cooling systems is inevitable in modern IMDs due to the rigorous thermal demands of the system [53]. Using an active cooling system involves forced convection cooling of the power module and machine [54] [55]. This increases the overall weight and volume of the system whilst adversely impacting overall system performance. The substrate or base plate (heat spreader) of the converter is in direct contact with the coolant which increases the heat transfer coefficient between the converter and coolant aiding heat dissipation. The increased cost and added maintenance of the cooling system is also a drawback.

In most industrial drives and IMDs in literature, when a unified active cooling system is adopted, the thermal path can be arranged in parallel or series. In a parallel path, both heat sources- the machine and PE are independent of each other. When implemented in an IMD where the heat sources are in close proximity, isolation is required. Isolation involves sectioning the power module away from heat sources in an

environmentally controlled compartment but the closer the converter is to heat sources like the stator windings and iron, the harder it is to isolate [56]. This thermal path arrangement is implemented in [31] [57] with the more fragile PE sectioned off from the machine by the redesigned end plate. Emphasis is on protecting the PE, as the machine is usually viewed as thermally 'robust' enough to handle elevated temperatures.

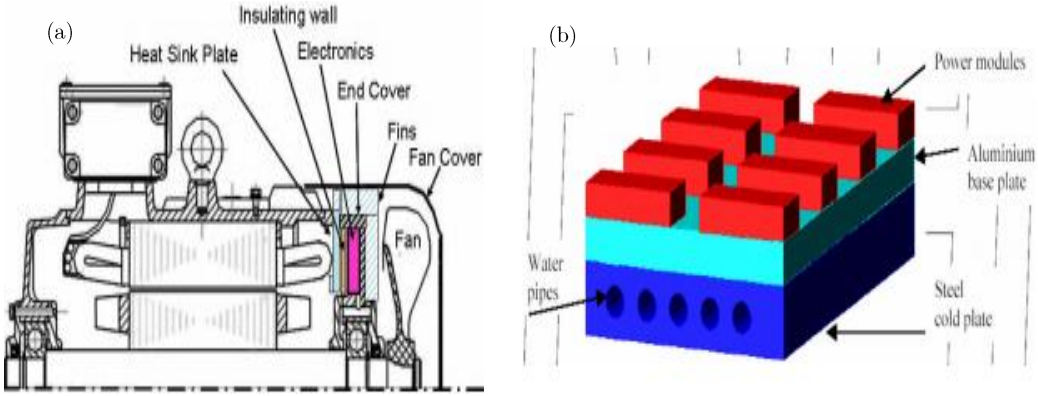


Fig 2.7: Showing parallel and series cooling paths (a) Axial View of PE mounted on Endplate – parallel path [31] (b) Simplified layout of water pipes through machine housing – series path [20]

A series/unified path for the machine and converter offers a common path for heat flow. The thermal path is from the coolant to the PE then machine (or machine before PE). The varying thermal demands of both PE and machine and the large temperature gradient of the thermal path makes its implementation complicated. Most IMDs adopt either a fully parallel cooling path or a hybrid of both parallel and series cooling.

In [20] and [24], both converter and machine share a common thermal node for heat dissipation – the machine housing. Forced convection cooling using water pipes machined through the machine housing is

incorporated. The drawback with this arrangement is the large pressure drops in the coolers and large temperature gradient that exists in the common thermal path due to the difference in thermal demands of heat sources. A series-parallel hybrid cooling system is adopted in [31], with the fan cooling the sectioned PE unit first before the rest of the machine.

In a passive cooling system, no external cooling system is utilised and heat dissipation is achieved through a combination of - natural convection, use of a thermal mass (heat sink), ventilation and thermal isolation. Thermal management using a passive cooling system can also be achieved by reducing the overall power ratings of the system, utilising high temperature operating components and increasing efficiency - in order to reduce system losses.

Converter cooling ranges from a simple heat sink or heat spreader to an advanced convection cooling system. Heat sinks and spreaders offer a cheap and simple cooling option but as the required operating temperature of the IMD increases a more efficient cooling system is required. Heat sinks and spreaders are often large compared to the cooled devices. Novel cooling concepts have been proposed for IMD for improving heat transfer [53], [58-62].

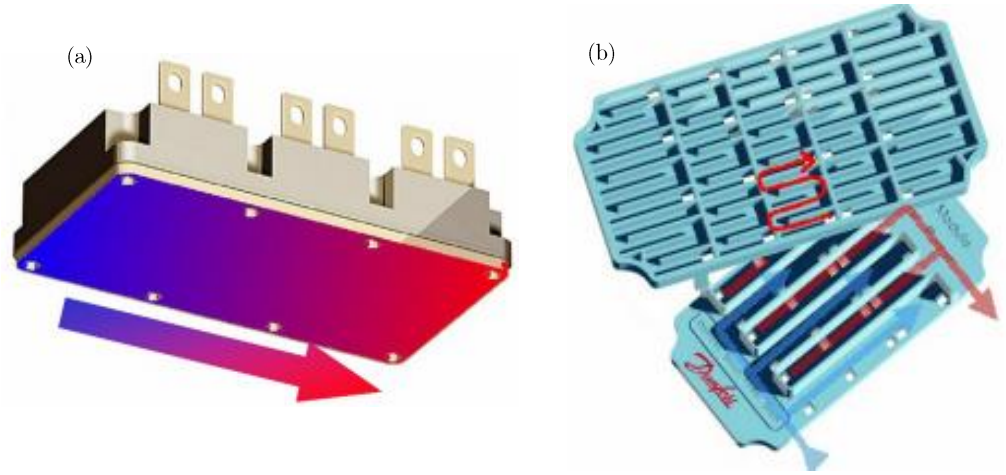


Fig. 2.8. (a) Temperature gradient in a standard cooling system (b) Danfoss Showerpower cooling concept showing the finned baseplate and vents for coolant input and output [53]

In [53] [58], Danfoss presents an improvement on the standard jet impingement cooling system by removing the coolant from the thermal path before it starts to warm up. This eliminates the temperature inhomogeneity usually associated with a 'series path' cooling. A similar concept is adopted in [62] where an active cooling substrate for the PE is manufactured by machining a synthetic. In [59], a water-cooled, finned common node between the converter and machine is manufactured similar to [53]. The surface area of the common thermal path is both increased and cooled, further reducing the temperature gradient of the common sink. Infineon presents a novel parallel cooling system in [61] for EV applications. The converter module is designed to provide optimum temperature dissipation from the module and isolation from the rest of the system. A combination of active and passive cooling approaches is utilised in [61] where the power device operating temperature is reduced and the power module is redesigned to allow liquid cooling between its

mounting plates. These novel concepts are aimed at improving heat transfer in PE modules.

A combination of forced convection (active) and passive cooling presents the only realistic cooling option for a power dense, closely integrated IMD system. This is due to the high heat transfer coefficient and low thermal resistance it offers aiding a more efficient cooling. Although low power systems will reduce thermal management demands in IMDs, close proximity integration and the shift to high power applications in recently manufactured IMDs suggests low power systems do not offer a realistic solution to the problems encountered in close proximity integration. By utilising materials that can withstand high temperatures and harsh conditions, both active and passive cooling can be utilised without compromising on power ratings.

2.3 High Temperature Devices

2.3.1 Wide Band Gap Materials

With increasing demand for more efficient, higher power and higher temperature operation of power electronic converters, the challenge of increasing the efficiency and power density of converters has become more urgent for design engineers to solve [63]. Presently, silicon power devices are the dominant semiconductor choice in industry [64] [65]. However,

due to basic physical restrictions, silicon power devices have reached their limits in terms of further development and scaling [66]. They also have a maximum temperature for the device junction in the range of 125-150°C [66].

Wide band gap semiconductors have been championed as the future in semiconductor technology since the 1950s [67]. High temperature and low conduction & switching losses are some of the advantages of wide band gap semiconductors in power devices [68]. Their ability to operate at higher power densities, voltages and frequencies are also potential advantages that make them beneficial in power device applications.

Table 2.2 shows the material properties of the most common wide band gap semiconductors compared to silicon. The wide band gap semiconductor devices exhibit superior physical properties compared to silicon devices [70-74]. Diamond potentially exhibits much better properties compared to SiC or GaN. However, there has been a lack of development due to financial cost of implementation, material availability and its low coefficient of thermal expansion (CTE) [75]. There are also significant manufacturing issues due to a lack of efficient methods to create conventional devices that rely on doped layers.

Table 2.2: Material properties of Si, SiC, GaN and Diamond [69]

Property	Si	6H-SiC	4H-SiC	GaN	Diamond
Bandgap Eg (eV)	1.1	3.03	3.26	3.45	5.45
Dielectric Constant, ε_r	11.9	9.66	10.1	9	5.5
Breakdown Field, E_c (kV/cm)	300	2500	2200	2000	10000
Electron mobility, µn (cm^2/Vs)	1500	500	1000	2000	2200
Hole mobility µn (cm^2/Vs)	600	101	115	850	850
Thermal conductivity, λ (W/cmK)	1.5	4.9	4.9	1.3	22
Thermal Expansion (x10^{-6})/ °K	2.6	3.8	4.2	5.6	1-2
Saturated E-Drift Velocity, Vsat (x10^7 cm/s)	1	2	2	2.2	2.7

For packaging, it is essential that the CTE of the semiconductor material matches the electrically insulating ceramic board [76]. This allows the semiconductor material to be easily adapted for higher temperature applications. GaN and SiC are a technically and commercially realistic competitor for Si in the power semiconductor market compared to diamond and are becoming widely available [77-81].

2.3.2 Silicon Carbide vs Gallium Nitride

SiC and GaN are two important wide band gap materials for future switching and RF power applications. SiC and GaN both exhibit higher thermal conductivity and bandgap energy compared to Si [82]. With GaN's higher electron mobility compared to SiC and Si, GaN should ultimately be the best device to provide lower losses at higher frequencies [83]. High frequency operation allows for smaller passive components, especially DC-DC capacitors. This leads to a reduction in the overall volume and increase in power density of an IMD incorporating GaN power devices.

The energy band gap of silicon carbide is lower than GaN. Since a larger band gap results in a smaller generation of carriers in the depletion regions of devices, it is favourable for reducing the leakage current of devices which utilize P-N junctions to support voltages. The larger band gap is also favourable for producing Metal-Semiconductor contacts with larger Schottky barrier heights. This means GaN in theory can produce thinner devices for a rated voltage compared to SiC [84]. For a given voltage rating both GaN and SiC will produce smaller devices compared to Si, making them highly beneficial for IMDs due to the limited space available for integration.

In power devices, the breakdown electric field strength determines how high the largest field in the material is before breakdown occurs. This

allows SiC and GaN to operate at much higher voltages and lower leakage currents compared to Si. With SiC and GaN exhibiting significantly higher values compared to Si, higher power rated devices can be produced. This is particularly beneficial in IMDs where power density is important. SiC and GaN can produce smaller devices with higher power ratings compared to Si.

The maximum operational temperature of a semiconductor material is determined by the bandgap. The temperature limit is reached when the number of intrinsic carriers approaches the number of purposely added (extrinsic) carriers. Therefore, semiconductors with wider bandgaps can operate at higher temperatures. In IMDs that demand operating temperatures higher than 150°C, SiC and GaN provide a realistic integration option since they can produce devices with a practical temperature limit of 600°C compared to Si with a temperature limit of 225°C [57].

The thermal conductivity of the material determines how quickly and efficiently it conducts heat to its surroundings [85], however, packaging limits restrict the overall maximum operating temperature. SiC has a higher thermal conductivity compared to GaN and so SiC can theoretically operate at higher power densities compared to GaN devices. Efficient heat dissipation is important in IMDs, especially the converter unit due to the high heat flux it produces over a small area (compared to the machine). By utilising SiC PE devices, the converter module

temperature can be reduced further decreasing the overall IMD temperature.

Manufacturers argue that both devices do not overlap in competition but have distinct benefits for specific applications. GaN is thought to be the obvious choice for low voltage applications (<600V) and SiC better for high voltage applications (>1000V) [86]. However, between 600V-1000V the choice between SiC and GaN is application dependent.

SiC poses significant advantages over GaN in power device application due to a number of reasons. Some of them include [87-91] –

- The lack of native oxide in GaN restricts production of GaN MOS devices. However, SiC uses SiO2 as a native oxide.
- GaN as a material possesses a lower thermal conductivity (about one-fourth) compared to SiC. For high power, high temperature operation applications, this is particularly important as heat needs to be dissipated quickly and efficiently.
- The cost of manufacturing pure GaN wafers due to the difficulty in growing GaN boules is higher than that of SiC. GaN wafers are usually grown on SiC or Sapphire. However, recently, GaN wafers are grown on Si producing potentially cheaper devices compared to SiC [88]. GaN on Si offers a relatively low-cost route to low voltage devices (under 1000V). GaN has also been shown to exhibit a better trade-off between on-state and switching loss than SiC.

The epitaxial growth of GaN on the silicon wafer is the sole cost disadvantage.

2.4 Modular Integration

Modular integration involves segmenting the power electronics into smaller modules that control dedicated stator winding sections. These modules are physically independent of each other and are usually connected together in series or parallel for the purpose of control. An active voltage (or current if connected in parallel) balancer is usually required to balance and regulate the segment voltages during unbalanced or asymmetrical load conditions. Advantages of modular systems include fault tolerance, better thermal capabilities, power rating scalability and a possible reduction in the overall size and cost of the PE.

Drive modularisation is independent of converter position as mounting can occur on the motor housing [22] on the stator iron [6], [10] or on the end plate [31]. Fault tolerance is one obvious advantage as multiple modules exist which form a unit as opposed to a centralised power electronics module. The system can be designed to allow for individual module failure. Current and voltage loading stress is also reduced in the PE as lower rated components are used in the modules to form a much larger rated unit [92].

The size of the components can also be reduced as the ratings for independent modules and their passive component sizes are a lot lower compared to a central PE unit.

Improved thermal capability is another possible advantage. This is as a result of having individual lower rated components and more evenly distributed heat dissipation [93].

Due to these potential benefits, modular drives are very beneficial for IMD design. In [6], both machine and drive are modularised (one converter phase leg per machine pole) and the benefits include – better thermal performance due to lower rated devices, increase in machine lifespan as a result of low voltage change in the slot insulation layer, lower maintenance cost and fault tolerance. A similar concept termed "site of action integration" is applied in [13] for EV integration with resulting benefits of shorter connecting wires. The possible drawbacks are the necessity for a complex control system for the individual power modules and the difficulty of mechanically and structurally integrating the modules with the motor [94].

2.5 Converter Topologies for IMD

Power electronic converter configurations and topologies have been analysed extensively in [95]. The topologies analysed include;

- 3 phase buck converter
- Vienna Rectifier

- Discontinuous Conduction-Mode (DCM) boost converter
- Continuous Conduction-Mode (CCM) boost converter
- Matrix converter
- Two-stage Direct Power Converter (DPC) with Reverse Blocking (RB)-IGBTs in the rectification stage

As the results of converter topology comparison are application-dependant, it is not possible to determine a single best topology for any IMD. The pros and cons of each topology are investigated below, focusing mainly on aspects more related to possible integration.

2.5.1 Matrix Converter

The matrix converter is a forced commutated direct ac-ac converter that uses an array of nine controlled bidirectional switches as the main power elements to create a variable output voltage system with unrestricted frequency [32]. The conceptual scheme of a matrix converter is depicted in Fig. 2.9.

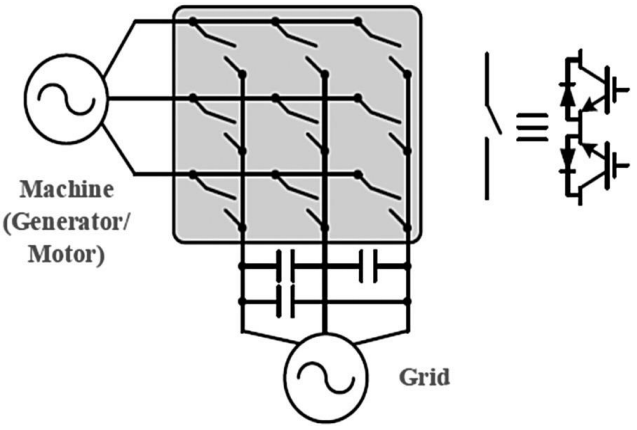


Fig. 2.9. Matrix converter

The potential advantages of this topology include a relatively compact size (no need for dc-link capacitors), sinusoidal input current, bi-directional power flow (power regeneration capability) and a controllable input power factor [32]. It is an attractive prospect in applications where volume, reliability and weight are important – particularly in IMDs.

Its main disadvantages are a low voltage transfer ratio of 0.86, the necessity of an additional clamping circuit for protection and of a mainly capacitive input filter. Moreover, it suffers from high cost due to the large amount of switching devices (18 IGBTs and 18 diodes) and due to the non-conventional arrangement requiring custom made power modules. The absence of a dc-link capacitor means no decoupling between the input and output, and also the complete absence of ride-through capabilities [96].

2.5.2 Two-Level Full Bridge Converter

The 2-Level full bridge topology is the workhorse of Power Electronics as we know it. It is a very well-known structure (Fig. 2.10), relatively simple to drive and flexibly controllable with different algorithms to suit the application. It can be used in both inverter and rectifier mode (bidirectional power flow). Being so common, power modules with this arrangement are easily available on the market, with power ratings ranging from a few hundred Watts to MWs, and both based on Si

(MOSFETs and IGBTs) and SiC technologies (MOSFETs and JFETs), thus a custom designed power module is not required.

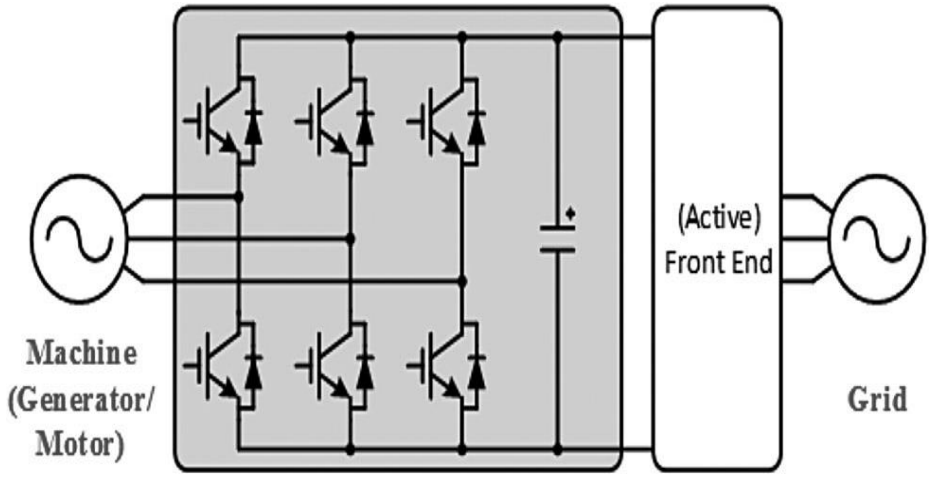


Fig 2.10. Two-Level full bridge converter

2.5.3 Three-level Neutral Point Clamped (NPC) converter

The Three-Level NPC topology is probably the most known of the 3-Level AC/DC converter topologies and it is gaining strong industrial acceptance. The main benefit of using a multilevel converter structure is the reduced current THD which can be achieved when compared to conventional 2-Level structure operated at the same switching frequencies. This will naturally lead to higher achievable fundamental frequencies making this configuration desirable for high speed applications. Additional benefits in terms of conversion efficiency gains may occur if the converter is designed such that lower voltage rating devices are used, which in turn would lead to reduced switching losses. A reduction in the current THD is also closely related to a reduction in

machine losses, and can potentially ease the IMD overall thermal management.

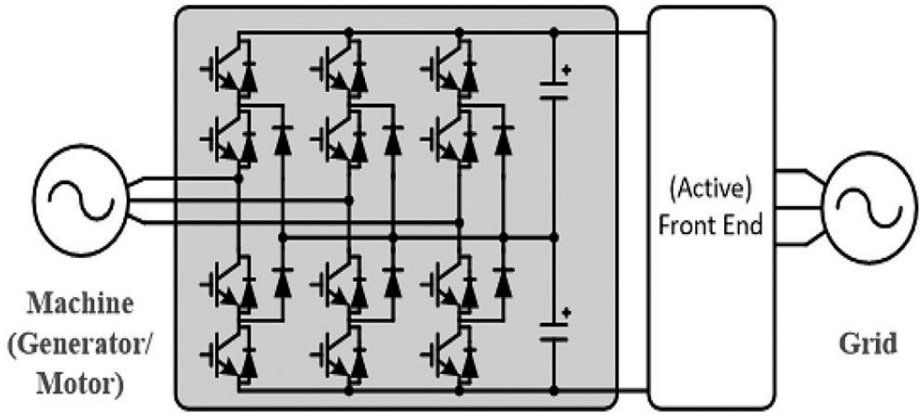


Fig 2.11. 3-Level NPC full bridge converter

The main drawbacks of this arrangement is the necessity to balance the DC-Link midpoint (using relatively complex control algorithms) and the high number of active devices, resulting in a lower reliability, added complexity and an increased cost. As this topology is gaining popularity for a range of energy conversion applications including automotive and industrial, there is a reasonable selection of commercially available power modules for this topology. The structure of the 3-Level NPC full bridge is depicted in Fig 2.11.

2.5.4 Multiphase full bridge converter

Multiphase full bridge topology (Fig. 2.12) is derived from the conventional full bridge arrangement. With respect to this it presents a potentially more complex control algorithm (depending on machine windings arrangement and number), however it also presents a number

of advantages such as increased fault tolerance as well as increased power processing partitioning (feature highly desirable in an IMD). As full bridge converters, multiphase full bridges can be used in both inverter and rectifier mode (bidirectional power flow) and suffers from the same drawbacks. The same considerations can be made for PE modules and technologies.

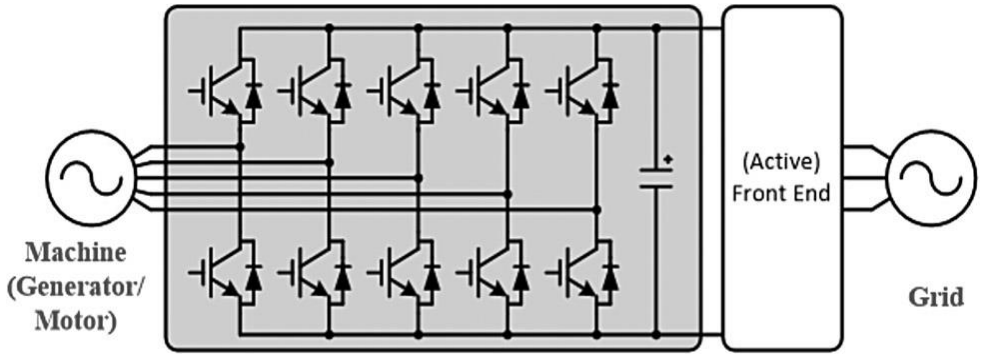


Fig 2.12. Multiphase full bridge converter

The number of phases in electrical drives is typically three, driven partly by convention and partly by a compromise between number of devices and machine utilisation. Three phases represents the best compromise between the two in most conventional scenarios. The following are some considerations whilst selecting the number of phases:

- Single phase: this represents a very cheap converter solution however the machine is typically characterised by very high torque ripple, vibration and losses. This is due to the inability of establishing a rotating field in the machine.

- Two phase: a two phase drive can be fully functional and effective when compared with three and higher phase number alternatives as in all cases a rotating field can be established. It can be a suitable solution for high speed drives especially for cost-sensitive applications without high torque requirements. The downside of such a drive is the typically lower torque density of the machine and higher torque ripple.
- Four-phase and higher: will present a solution with an improved torque density and lower torque ripple when compared with three phase machine drives. However this comes at the extra cost of having more components. Higher phase numbers are however attractive when high power drives are to be connected to low voltage networks such in automotive applications. Channelling the power through more phases limits the current requirements of devices and thus their size, allowing for an easier structural integration into the machine, as well for more spatially distributed PE-related losses.

2.6 Passive Components

Passive components (especially capacitors and inductors) account for a considerable amount of the material cost and volume of a power electronic system. Fig. 2.13 gives a graphical illustration of the material costs and volume of passive components compared with other components in a PE system. At high temperatures capacitors are particularly challenging due

to thermal limits of many common capacitor materials. Leakage currents also occur at high temperatures making it hard for the capacitor to hold charge [57]. The DC link capacitor helps avoid over-voltage during commutation and provides a low impedance path for the switching harmonics, effectively buffering the ripple current, but passive DC-link capacitors are often bulky and expensive. There are four main capacitor technologies available

- Multi-layer ceramic capacitors (MLCC)
- Electrolytic capacitors
- Film capacitors
- Electro-chemical double layer (ECDL)

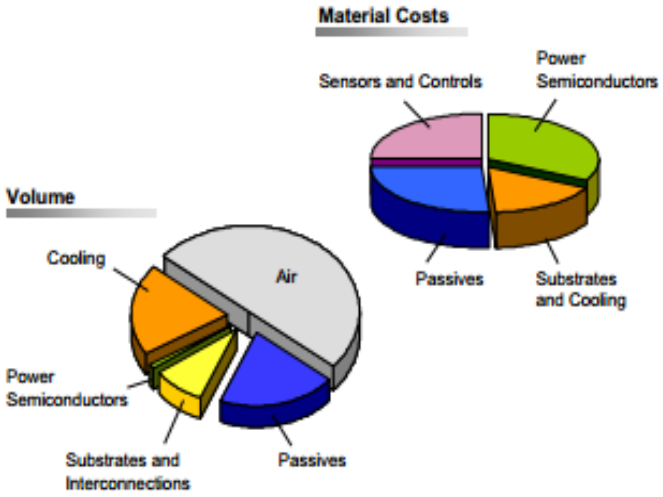


Figure 2.13: Typical Material Cost and Volume Distribution in Power Electronics System [13]

2.6.1 Ceramic Capacitors

The MLCC is the most dominant form of ceramic capacitor. Its most important attributes are its high capacitance and compactness [97–99].

The most expensive of the four capacitor options, ceramic capacitors offer very high AC current ratings, high temperature operation (up to 200°C) and small size. It is also the most widely used passive component in modern electronics [100] and has high energy density.

Ceramic capacitors are not limited to MLCCs. Bespoke capacitors exist with unique capabilities lacking in other capacitor technologies [100]. High temperature ceramic capacitors that can withstand temperatures of up to 250°C exist [101]. Ceramic capacitors are used mostly for high temperature and high voltage applications [102]. The major disadvantages are the high cost and the brittle nature of ceramic capacitors [103, 104]. In IMD traction applications where shock and vibration is prominent, reliability issues arise over the mechanical stability of ceramic capacitors. Moreover, the low energy density of ceramic capacitors mean several components have to be paralleled up to achieve the necessary ratings required. This further increases the overall cost of the IMD system.

2.6.2 Electrolytic Capacitors

These capacitors are mostly used in the rectification stage of switched mode power supplies [105]. The cheapest and most popular of the four options, electrolytic capacitors achieve the highest storage densities (up to 1 J/cm3) but have the lowest AC current ratings. Operating temperature is usually up to 120°C [106]. Although electrolytic capacitors

are the standard choice for DC link storage in conventional motor drives, their limited current handling capabilities and operating temperature restricts their use in integrated drives. In addition, due to their physical construction, they show a relatively high equivalent series resistance and equivalent series inductance, thus posing a limit at the converter maximum switching frequency of operation. The thermal limitation is a problem especially in IMDs due to the compact nature of the unit.

Theoretically the maximum voltage for electrolytic capacitors is 800 V. However, practically the maximum voltage is 600 V [107]. This makes electrolytic capacitors susceptible to voltage surges. Electrolytic capacitors are also polarity dependent thus restricting their applications to DC circuits. Thermal degradation of the electrolytic capacitor is a heat triggered electrochemical reaction [108, 109].

Thermal degradation causes a relatively short life time of electrolytic capacitors compared with ceramic and film capacitors [110]. Although electrolytic capacitors have very high energy densities, In IMD integration, their bulky size and short life time due to thermal degradation means they hardly feature as passive components. This is due to the high operating temperatures and limited integration space in the IMD enclosure.

2.6.3 Film Capacitors

Polymer film capacitors are the most flexible in device geometry of the aforementioned capacitor technologies. They combine the advantages of low losses and mechanical robustness with high volume capacitance. They are also polarity independent providing true bipolar operation. Typical applications include high frequency inverters and solid state switch snubbers. They are also capable of operating at higher voltages (up to 100 kV) [111]. Their ability to work under high electric field coupled with their high energy density is an advantage [112, 113]. Theoretical operating temperatures can reach up to 220°C, however, commercially available film capacitors operate at temperatures up to 170°C [114]. They also exhibit higher life time and higher ripple current capability compared with electrolytic capacitors [115].

Their main disadvantages include their high cost, lower capacitance per volume compared with electrolytic capacitors and low-medium operating temperatures. Despite these disadvantages, film capacitors offer a realistic capacitor choice in IMDs due to its small size and longer life time compared with electrolytic capacitors and its mechanical robustness and high energy storage density compared with ceramic capacitors.

2.6.4 Electro Chemical Double Layer Capacitors

Chemical double layer capacitors also known as 'supercapacitors' are low energy (compared with electrochemical batteries), high power density

storage devices [116]. Although not as prominent as the aforementioned types of capacitors, they have been commercially available for decades [117]. Typical applications include backup and recovery systems and as energy storage for EV [118].

The relatively high cost [119] and high self-discharging rate [120] are potential drawbacks of the ECDL. Its low operating temperatures compared with other types of capacitor also makes ECDL capacitors unlikely to see successful application in IMD. They also have a very low operating voltage per cell which means that large numbers of cells connected in series are required as well as complex balancing circuits to ensure that the cell voltages remain equalised throughout the stack [121].

2.7 Packaging of Power Electronics Module

In an IMD, the converter is arguably the most sensitive component in the system. The growing demand for an efficient, high temperature operable converter has led to advancement in research on wide band gap devices [122]. High temperature environments like combustion engines in aircraft and automobiles could benefit from a high temperature integrated power module. The ability for a power module to operate at a high temperature results in a smaller system size of the IMD and reduced costs of the cooling system.

Wide band gap devices like SiC and GaN can theoretically operate at temperatures above 500°C while Si is restricted to junction temperatures lower than 175°C [123–125]. Above 200°C Si devices experience latch-up at reverse bias junctions and leakages [57]. SiC power devices exist with operating temperatures up to 200°C [126–129], but the maximum temperature of a SiC power module for example is limited to about 150°C [130, 131]. A commercial high temperature SiC module has been reported operating at 250°C [132]; however, reservations exist over its reliability above 200°C.

The packaging of the PE module primarily restricts its maximum operating temperature [133, 134]. The module undergoes high thermal and thermo-mechanical stresses at high temperatures leading to critical failures in the system [135, 136]. Degradation of polymeric materials used in the module packaging as well as the creation of intermetallic compounds, which may weaken the joints also occur at high temperatures [124, 137, 138]. Categories of interest in power module packaging are – interconnects, die attachment, substrate choice and encapsulation [139].

2.7.1 Interconnects

Conventional power modules use aluminium, copper or gold wire bonds as the main current path for interconnection [140, 141] and the wire bond is arguably the weakest part of the power module [142, 143].

At temperatures above 200°C, the reliability and mechanical stability of aluminium bonds is drastically reduced [87, 142] with wire bond lift-off or wire bond breakages the most common failures [144]. These failures usually occur at the heel of the wire bond – where the most stress occurs [145, 146]. The thermal resistance of the wire bonds also increase at high currents and temperatures [61, 147].

Alternative interconnect options that offer high temperature operation and reliability over 200°C will improve the life time of PE modules in IMDs. Large diameter platinum wires have been investigated for high temperature application integration. Despite exhibiting exceptional mechanical strength at high temperatures, CTE mismatch with the semiconductor and low electric conductivity are some of its disadvantages [148]. Silver alloy wire bonds have also been investigated for high temperature operation [149]. Its high thermal conductivity is also beneficial in IMD applications [150]. Flip chip technology can also potentially replace standard interconnections by connecting the power devices directly to the package through conductive metallic bumps [151]. In [152], a highly power dense, wireless converter module for IMD integration is presented using flip chip on flex (FCOC) technology with improved thermal performance.

2.7.2 Die attachment

The die attachment is the connecting interface between the substrate and the die ensuring that the die is mechanically stable on the substrate and thermally efficient in heat transfer to the substrate [153].

Materials used for die attachment ranges from high lead and lead free solders to silver sintered layers [154–158]. Solders are the most common die attachment but often have a low working temperature. However, Sn based solder alloys have been reported to possess working temperatures more than 280°C [159–161]. However, its low thermal conductivity restricts efficient heat transfer in power modules. Zinc alloy solders have also been reported to operate at temperatures above 200°C [162].

Sintering offers the best die attachment option boasting working temperatures up to 650°C and thermal conductivity orders of magnitude higher than solder [163–167], properties particularly beneficial for IMD integration. However, a very high pressure (around 30 MPa) is required to achieve sintering leading to potential cracks or possible destruction of the relatively fragile ceramic substrate. Silver particle pressure-less bonding has been reported in literature and provides an alternative for silver sintering without the substrate subjected to high pressures [168].

2.7.3 Encapsulant

The encapsulant acts as a protective barrier for the power chip and components from hostile environments. It also acts as a heat spreader and can prevent arcing at high voltages [169, 170]. In close proximity drive integration (like back iron mount integration), the PE encapsulant will be subjected to high ambient and operating temperatures. It is therefore important the chosen encapsulant can withstand such high temperatures and harsh environment. Typical encapsulation materials are silicone gel, epoxy and parylene with the later showing high working temperatures more than 200°C. Several encapsulants claim to have working temperatures more than 250°C [171–181]; however, reliability studies claim encapsulants slowly degrade before reaching 250°C [137, 182].

2.7.4 Substrate

The substrate provides electrical isolation, mechanical support and thermal conductivity for the circuitry of the power module. It consists of a thin ceramic substrate sandwiched between two layers of copper or aluminium metallisation. Popular ceramic materials are – alumina, aluminium nitride, silicon nitride and Beryllia. Alumina is the cheapest and most common option but has the lowest thermal conductivity compared with others [183, 184]. Aluminium nitride (AlN) possesses a higher thermal conductivity and its CTE matches SiC [185, 186]. However, its mechanical strength is poor [187]. Beryllia although exhibiting an excellent thermal conductivity is a toxic material raising

health and environmental issues. Silicon nitride (Si_3N_4) is fairly new hence its limited supply. It has average thermal and electrical characteristics but excellent mechanical properties.

In IMD integration, high mechanical strength, high thermal conductivity and a close CTE to the power devices utilised are some of the properties required. The choice between Si_3N_4 and AlN is application dependent with AlN used for a power dense IMD where efficient heat dissipation in paramount. In applications with high vibration levels (close proximity integration applications), Si_3N_4 is a better option for IMD integration with fracture toughness levels twice AlN's [140].

Other packaging technologies have been investigated in search of a more compact high temperature operation. Flip chip technologies present a compact wireless configuration [188–191] but reservations exist over its mechanical stability and mechanical stress at high temperatures [143, 192]. Flip-Chip On-Chip (FCOC) substrates [193] have also been reported to reduce stress between solder joints, devices and substrates. Flex substrates also provide the flexibility of producing power modules with distinct shapes especially beneficial in IMD integration due to the lack of available mounting space [194]. Another wireless packaging technique – a variant of FCOC, utilising a 'SKiN' flex layer is presented in [195] promising improved thermal capabilities and power density compared with a standard power converter. Pressure contact technology has also been investigated as a possible replacement for aluminium wire bonds for

high temperature applications [196, 197]. Its high manufacturing costs and complicated manufacturing process remain drawbacks in manufacturing. Careful selection of materials in the module is also important to avoid CTE mismatch. CTE mismatch can lead to die fracture, fatigue and lifting, horizontal crack propagation, delamination and cracking of the ceramic substrate [57, 198-199].

The thermal and mechanical properties of standard PE module components will limit its successful integration in a machine. Manufacturing a specialised power module by utilising WBG devices like SiC and GaN with high temperature operating die attaches, encapsulants and interconnects will aid successful close proximity integration. Moreover, adopting specialised packaging techniques like FCOC and 'slot-module' [94] can improve power density and heat dissipation in the power module.

2.8 Challenges in IMD Design

The emphasis on smaller, more efficient and power dense converters has led to rapid development in converter technologies. Devices able to switch at higher frequencies allow for a reduction in size of power devices like magnetics and capacitors. Compared with the machine, the converter has a much higher power density with typically in the range of 50–500 W/cm^2 for power semiconductor devices, compared with 0.1–3 W/cm^2 for

magnetic components and less than 0.1 W/cm^2 for capacitors [200]. This is due to its smaller volume and high power handling capabilities [201].

The converter losses are concentrated over a smaller area leading to localised high temperatures (hot spots). This leads to complications in converter cooling and thermal management especially in close proximity to other heat sources such as stator windings [202]. Losses in the machine frame also increase the overall temperature of the IMD system. This limits the power dissipated by the converter, consequently decreasing its power handling capabilities [203].

Poor thermal contact between the converter baseplate or substrate and the mounting position could potentially be problematic depending on the quality of both surfaces [20, 24]. A poor thermal contact between both surfaces will increase the thermal resistance and cause poor heat transfer between the converter and machine. This is particularly troublesome when a singular cooling system is adopted in the IMD as the housing area is used as a heat sink for the converter and efficient heat transfer between the machine and PE is important.

The complexity and cost of installing a cooling system to efficiently dissipate heat from the converter and machine is also challenging.

Vibration and mechanical stability also pose reliability issues in drive integration. Machines that operate in hostile environments such as

traction applications are exposed to high shock and vibration levels. Mounting the converter on or in the housing of these machines exposes the converter to significant vibration problems [6, 22]. Reliability of attachment methods such as thermal-joint compounds and screws may be severely affected by high vibration levels [22].

To tackle the pressing thermal and mechanical issues encountered in IMD design, future research in the following options should be considered -

- Advancements and efficient implementation of an active cooling system
- Manufacture of bespoke modularised converters
- Utilising high temperature devices.

Future research into these topics will help adapt the cooling system, converter and machine components to the rigorous thermal and mechanical demands of an IMD system.

2.9 Future Trends

Major challenges associated with PE integration include limited available installation space, high thermal and mechanical stresses on devices and machine components and the complex cooling systems needed. Current IMDs are as a result of a pre-defined converter installation space on or around the machine housing, usually as a result of the mechanical requirements of the machine, with little to no consideration on the converter needs. Increasing the power density, reliability and efficiency of

IMDs whilst reducing the overall manufacturing cost, has led to active research and development of smaller, more efficient power modules.

By exploiting the benefits of wide band gap devices, manufacturers have been able to produce devices that can withstand the rigorous thermal, mechanical and electrical demands of close coupling integration. GaN and SiC are expected to phase out Si as choice semiconductors in IMD applications. Compared with GaN, SiC has a distinct time and technology advantage in discreet power devices and module commercialisation and is expected to feature in future IMDs as the choice converter module or power device. 'Full' SiC power modules already exist providing high efficiency, temperature operation and power density whilst maintaining a small volume for machine integration. However, with GaN's ability to operate at higher frequencies compared with SiC and ongoing research in cheaper alternatives on growing GaN boules, GaN is expected to compete fiercely in power device manufacturing with SiC. Diamond although exhibiting superior properties compared with SiC or GaN is still decades away from commercialisation and is not expected to feature in PE modules in the near future.

Advancements in passives technology has also led to smaller high temperature operation devices with ceramic capacitors exhibiting operating temperature greater than 200°C. It is expected that the compactness, high capacitance and thermal capabilities of the ceramic and film capacitors will see them feature heavily in IMD converter

modules in future. Aluminium nitride is expected to remain the choice ceramic for power modules; however, research into silicon nitride (Si3N4) which possesses better mechanical properties should provide competition for AlN in the next few years. Currently, the copper layer on the ceramic substrate is usually nickel and/or gold plated in other to avoid oxidation of the copper layer. However, at very high temperatures (above 400°C) breakdown of this oxidation layer occurs – compromising reliability [187]. Extensive ongoing research into alternate finish materials like titanium, lead and molybdenum could offer realistic alternatives to gold and nickel finishes.

These advancements in material and packaging technologies have led to more production of commercial high power IMDs. This suggest the 7.5 kW limit previously recognised as the threshold practical power rating of commercial IMDs has increased and will continue to do so. A shift from low/mid power rated IMDs to high power rated IMDs is also expected as WBG devices, improved component materials and better packaging techniques are properly incorporated in power modules and IMDs. Moreover, recently manufactured IMDs suggest a shift from the popular surface mount configuration to more close proximity integration with the converter integrated in the machine housing. Bespoke modular converter units enable close proximity integration and will see an increase in more power dense IMDs manufactured.

Typical IMD applications include pump and fans, however, high power rated IMDs capable of high temperature operation currently feature heavily in EV and HEV application. It is expected that IMDs will continue to feature in electric vehicular systems especially 'under-the-hood' and motor tire environments where limited space and high operating temperatures exist.

CHAPTER 3

End Winding Mount IMD

3.1 Introduction

This chapter introduces the end winding mounted Integrated Motor Drive (IMD) concept. An initial prototype is presented which aims to solve the thermal problem of having the power module and machine windings (both heat sources) in close proximity

3.2 End Winding Mount IMD

Conventional IMD units are based on sectioning the power electronics away from the machine to prevent failures attributed to temperature rise

of converter components due to close proximity integration in or around the machine housing. The drawback of adopting this integration approach is the overall increase of IMD volume due to compartmentalising both machine and converter. This inherently leads to a reduction in power density of the system.

The thermal challenges of having the power electronics unit in close proximity to the machine heat sources (copper windings, Iron and rotor) still pose the major hindrance in close integration. In IMDs, cooling the PE and machine is complicated due to the varying thermal demands of the PE and machine. The PE unit generates significant losses in the motor drive and also possesses the highest power density of all the IMD components. Its significant thermal management demands are also increased with the maximum operating temperature of most commercially available power modules around 150°C. This temperature limit is as a result of a few reasons including –

- The power device (IGBT, MOSFET or JFET) composite material. Silicon is restricted to junction temperatures lower than 175°C while wide band gap devices like Silicon Carbide (SiC) and Gallium Nitride (GaN) can theoretically operate at temperatures above 500°C [18-20].
- The interconnecting materials like Aluminium wire bonds (the most common) have been reported to experience reliability and mechanical stability issues above 200°C [21, 22]. Wire bond

breakage and lift off are the most common failures in a power module at high temperature [23].

- The efficiency and power capacity of the PE module is reduced at higher temperatures [11].

To alleviate the thermal issues associated with close proximity integration of IMDs, the following steps have been proposed in literature -

- In-depth electrical, thermal and mechanical analysis of the machine and converter
- Efficient design and packaging of the IMD components as a single unit.
- Utilising wide band gap devices like SiC and GaN
- Adopting an efficient forced convection cooling system

Taking into account the design limitations of close proximity integration of power electronics in the machine enclosure, an integrated motor drive is proposed with the power electronics converter module mounted on the machine's end windings.

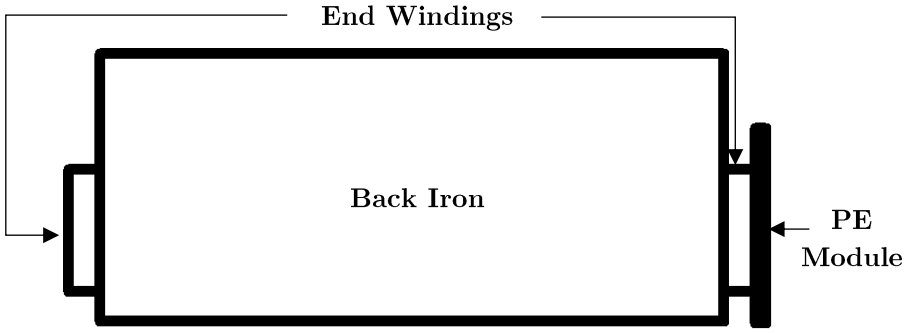


Fig 3.1: End Winding Mount IMD concept

For high temperature capability, the module consists of wide band gap devices like Silicon Carbide (SiC) or Gallium Nitride (GaN), high temperature capable ceramic capacitors, Aluminium Nitride ceramic substrate and electrical connections (wire bond interconnects between the devices and the copper layer on the substrate). The AlN substrate provides mechanical stability for mounting the SiC devices and passives on the windings, a good thermal path for heat transfer between the power electronic devices and machine windings and electrical connection between the devices and windings.

Electrical connection between the devices and the windings is achieved by copper tracks at the bottom of the substrate which mirror individual winding coils. This prevents short circuit in the end windings by providing isolation between the copper windings. The individual power modules mounted on specific tooth windings can energise specific winding segments providing an opportunity for modularity and fault tolerance in the system. With converter modularity adopted in the system, the temperature distribution the power electronics have on the overall system can be improved due to lower thermal stresses per module. Also, with the individual PE modules consisting of lower rated devices, the losses from individual modules are reduced. The cooling system required to accommodate the lower rated power modules is also less power demanding. This is because the cooling system can afford to be less effective in terms its ability to deal with high heat flux over a large area.

This means less heat spreading required hence smaller overall volume potentially reducing the cost and overall size of the system.

The ceramic substrate is mounted on the end windings by silver-sintering, soldering or mechanical clamping. Sintering involves forming a thin interconnecting layer of silver by high pressure and temperature between the substrate and end windings. The choice of substrate is very important as it plays a major role in mechanical stability, reliability and heat dissipation in the system.

The machine windings act as a heat sink for the power electronics by providing a large thermal mass for heat dissipation. This is particularly crucial during transient mode (quick changes in temperature) as the windings can absorb any increase in temperature of the power electronic devices. With the machine windings acting as a heat sink, it is important that its temperature is lower than temperature of the power module. This is to ensure heat flow is from the power module to the heat sink. There is no thermal barrier between the converter and motor (strong thermal coupling). Mounting the PE on a heat source (windings) will require a robust converter that can operate at very high temperatures.

This is particularly challenging as both heat sources are in close proximity inside the machine housing. The cooling system is a critical design aspect as efficient cooling systems can significantly reduce thermal resistances to produce a better temperature distribution in the IMD. Also, utilising high

temperature devices will aid in better thermal distribution and high temperature operating capability of the overall system.

Other potential benefits of adopting this mounting configuration include –

- Lower EMI due to shorter connecting wires between the PE devices and energised windings
- An increase in power density of the motor drive by having the power electronics module closely integrated inside the machine housing resulting in a smaller, more efficient motor drive.
- A unified cooling system adopted as opposed to a separate option adopted in a traditional motor drive which potentially reduces cost and increase the overall power density of the system
- Reduced current and voltage stress on the PE as lower rated devices are used in the module.
- Potential fault tolerant benefits since all the modules are independent.
- Utilizing fast switching, wide band gap devices like SiC or GaN allows for high frequency operation. Depending on the circuit topologies implemented, at low frequencies, the size of magnetics makes up the majority of the overall converter size. This means at high frequencies, the PE module size can be reduced, further increasing the overall power density of the IMD.

Despite the potential benefits of the end winding mounted IMD concept outlined above, a few reservations still exist in its successful implementation and demonstration of a working prototype. The initial challenges identified are highlighted below

3.2.1 Thermal challenges

Arguably the most complicated challenge in implementing the end winding mounted IMD concept, positioning the PE module in the machine housing poses a very complicated thermal problem. As earlier stated, both PE module and machine windings are heat sources. Placing them in close proximity poses a problem in IMD thermal distribution. Standalone, the copper windings are the hottest component in the machine. With the power electronics mounted on the windings and efficient thermal management system is imperative.

3.2.2 Mechanical challenges

Attaching the module to the copper windings poses a genuine problem in successfully implementing this concept. The attachment joint not only has to provide a thermal path for heat transfer from the power module to the copper windings (heat sink). It also has to provide a robust mechanical joint for potential vibrations in the machine enclosure.

3.2.3 Electrical challenges

The power module mounted on the copper end windings presents a possibility to reduce the length of connecting wires between PE and windings. However, the physical arrangement of the connecting wires between the PE module and copper windings remain a question.

The production of a working prototype that fully demonstrates the end winding mount IMD concept is both complicated and novel? The packaging/assembly of the IMD and its cooling system was anticipated as the most crucial points in the prototype manufacturing. In order to reduce manufacturing errors - especially in unfamiliar processes like pressure sintering and reduce overall manufacturing costs, the manufacturing process was split into two parts –

- Prototype 1
- Prototype 2

The first Prototype was manufactured to validate the initial thermal and mechanical concept of the End winding mount IMD. It consists of a simple heat source (PE module) mounted on the end winding of a motorette. It aims to investigate and analyse the heat distribution in the IMD system with the PE module mounted on the end winding. It also investigates the mechanical challenges of physically attaching the PE module to the copper end winding.

The second prototype (Prototype 2) improves on the first by manufacturing a fully functional PE module and mounting it on the end winding. The mechanical mounting process for this prototype incorporates optimisation recommendations detailed in Chapter 4. The thermos-mechanical challenges encountered from manufacturing the first prototype are solved and the solutions implemented in Prototype 2. The design, manufacture thermal and electrical results from Prototype 2 are detailed in Chapter 6.

3.3 End Winding IMD Prototype 1

The aim of this prototype was to validate the thermal concept of the power module mounted on the end windings of the machine. It was also used to investigate silver sintering as a potential attachment method for the power module on the end windings and fine tune the process if necessary. Being a fairly rudimentary stage, the power module and machine are viewed solely as heat sources hence no electrical connection existed between then. Both components were energised independently and their temperature distribution analysed.

A lumped parameter model of the PE module attached to the end winding was created to represent the effective thermal resistances of the individual components. At the concept stage, lumped parameter models offer an easier, less complicated technique compared to numerical methods like Computational Fluid Dynamics (CFD) or Finite Element Analysis (FEA)

[207]. However, for larger scale models, they can be complicated to manage and rely heavily on input data at boundary. Another disadvantage of this model is the difficulty in identifying the correct heat transfer coefficients – which is also an important parameter that influences the quality of the model. The heat transfer coefficients are dependent on the geometry and flow characteristics.

3.3.1 Software Simulations

3.3.1.1 Lumped parameter models

Before modelling, a quick thermal analysis was performed to investigate the feasibility of the proposed concept. Using (3.1), the temperature of the winding was calculated with the bare die as the primary heat source (16W loss).

$$Q = hA(\Delta T) \qquad (3.1)$$

(where h = Heat transfer coefficient, A = Area, ΔT = Change in component temperature)

Natural convection was assumed as the only heat dissipation mechanism and the ambient temperature was set as 25°C. This resulted in a maximum temperature of 80°C. However, with the windings energised at 25W, the maximum temperature calculated was 165°C. With the calculated temperature well above the maximum die temperature of 150°C, an external cooling system is required to dissipate the heat.

Assuming a heat transfer coefficient of 35 W/m^2K for low speed, forced convection cooling, the calculated maximum temperature was 60°C. Although the calculated temperature values are heavily dependent on assumed heat transfer coefficient values, this highlights the importance of an additional cooling system to the realisation of the proposed concept.

Using MATLAB Simscape, lumped parameter models of an E-core, copper wound motorette and a JFET sintered on Aluminium Nitride (AlN) substrate were created. The total surface area of the Motorette and copper windings were $3.85e^{-2}$ m^2 and $5.84e^{-2}$ m^2 respectively. Thermal resistances of individual components and heat transfer coefficients due to convection (natural and forced) were modelled. The lumped parameter model of thermal resistances and nodes present a simplistic and fast thermal analysis of the systems modelled. The heat transfer coefficient due to natural convection on the back iron and hot end winding was assumed to be 5 W/m^2K. A forced convection heat transfer coefficient value on the cold end winding side was calculated by calculating the effective thermal resistance between the copper insulation and forced air using (3.2).

$$(R_{th} = \frac{L}{kA} = \frac{1}{hA}) \qquad (3.2)$$

(Where L = thickness of material; A= Area; k = thermal conductivity; h = heat transfer coefficient)

For each thermal resistance, values for the thermal conductivity, thickness and area of the material are inputted as shown in Figure 3.2.

For heat transfer by conduction and forced convection, Equations 3.3 and 3.4 apply respectively.

Conduction -

$$R_{th.conduction} = \frac{L}{kA} \qquad (3.3)$$

(Where L = thickness of material; A= Area; k = thermal conductivity)

Forced convection –

$$R_{th.convection} = \frac{1}{hA} \qquad (3.4)$$

(h = heat transfer coefficient)

The calculated heat transfer coefficient on the cold end windings was 54.3 W/m^2K. The thermal distribution of the E-core components at 25W and 50W can be observed in Figures 3.3 and 3.4. The maximum temperature almost doubles with an increase in losses from 25W to 50W.

A 7.3 mm^2 SiC bare die device was modelled on an Aluminium Nitride (AlN) substrate to represent the power electronics device attached to the motorette end windings. Using E-core losses of 50W and bare die losses of 16W, the thermal distribution of the bare die sintered on the E-core end windings was analysed to investigate their respective maximum temperatures when in close proximity. The temperature distribution and thermal coupling effects between the power electronics device and E-core windings is shown in Figure 3.5. The maximum temperature of the IMD system was recorded on the bare die - 188℃. The hot and cold end

winding temperatures also increased from 155℃ and 153℃ to 179℃ and 173℃ respectively.

Although the lumped parameter models offer a quick and fairly accurate estimation of the temperature distribution of the IMD components, probing specific points on individual components is difficult. Also, hot spots in the system cannot be observed and the model assumes a uniform temperature across a body which in reality has a temperature gradient. Also, as shown in Figure 3.6, the large scale of the model makes it complicated to manage with numerous thermal nodes and resistances. The model is also heavily reliant on the heat transfer coefficients inputted

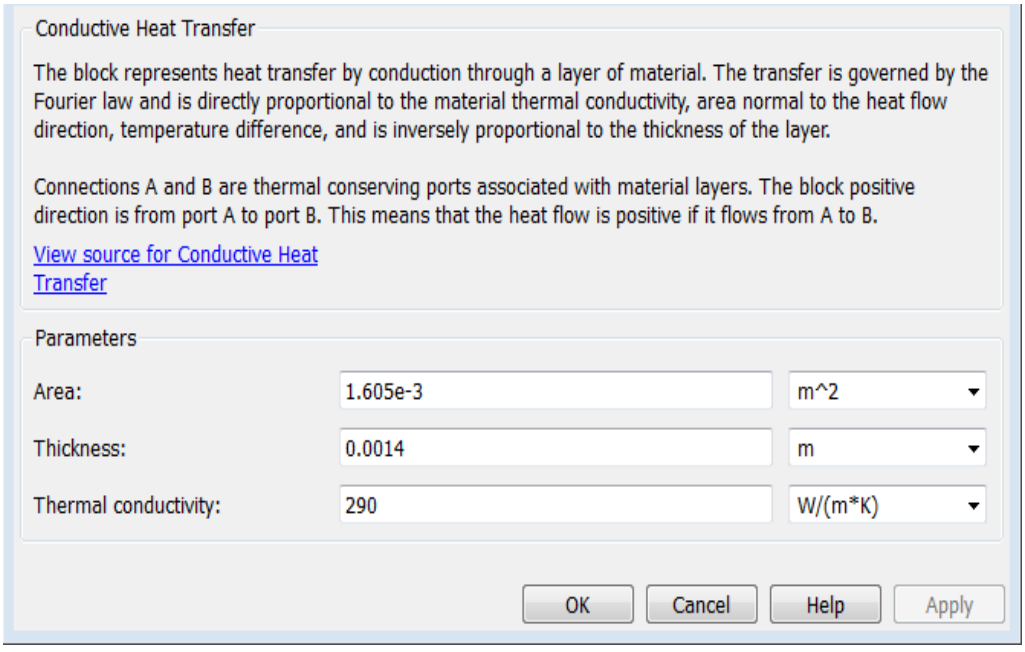


Fig.3.2: Input parameters for thermal resistance

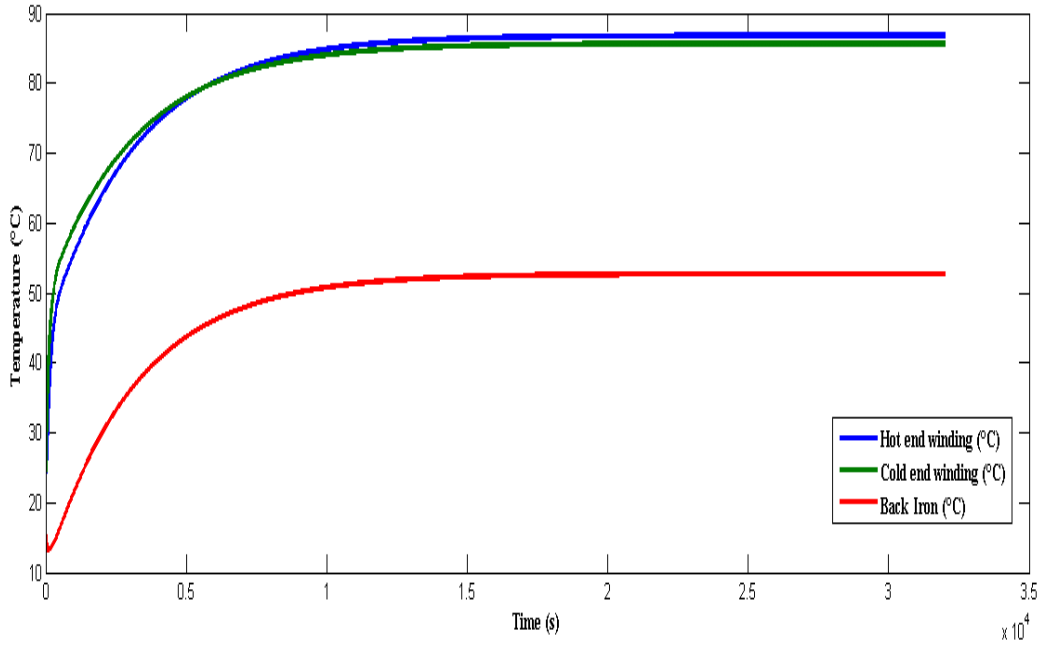


Figure 3.3: Transient thermal graph showing the temperatures of the lumped parameter modelled wound E-core at 25 W

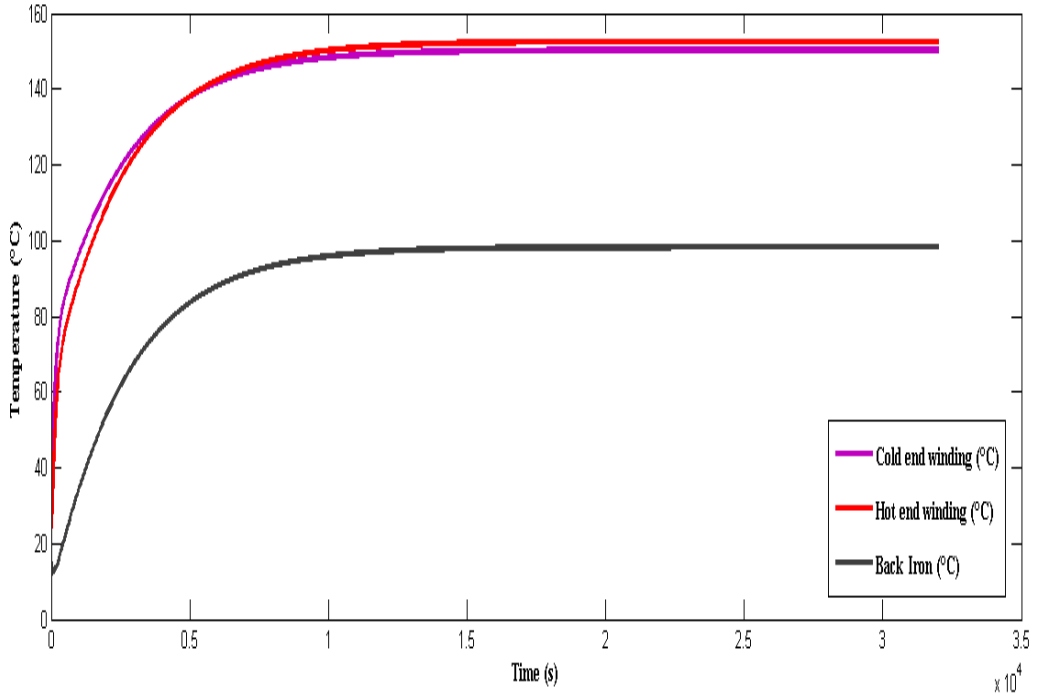


Figure 3.4: Transient thermal graph showing the temperatures of the lumped parameter modelled wound E-core at 50 W

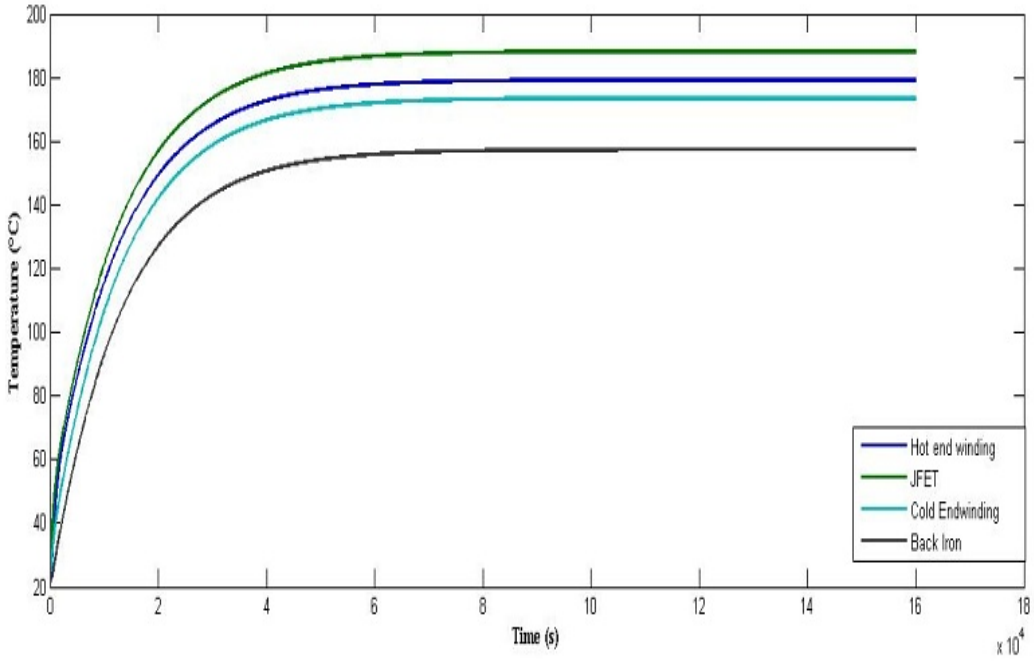


Figure 3.5: Transient thermal graph showing the temperatures of the lumped parameter modelled sintered JFET on end windings

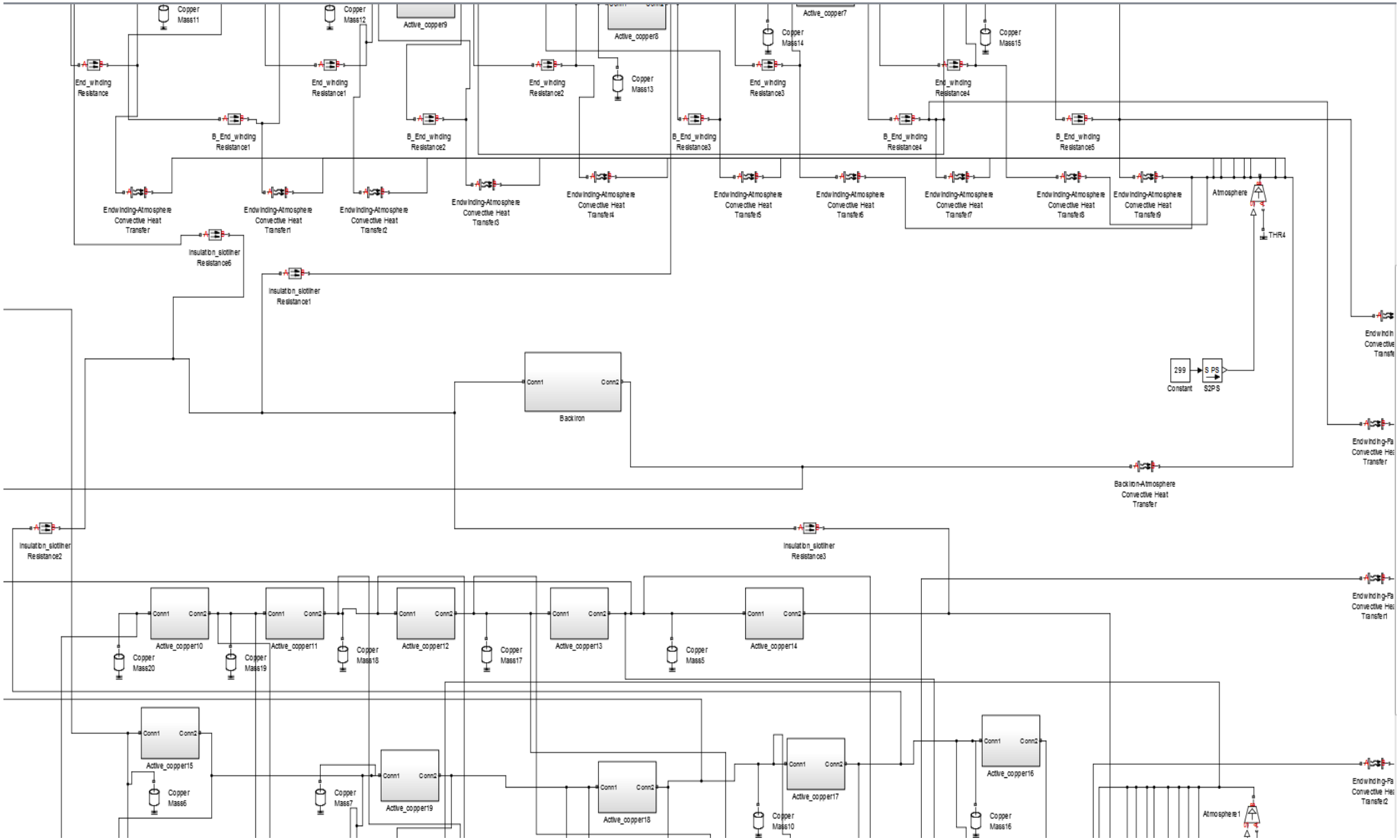


Fig. 3.6: Simscape thermal resistance model of end winding mounted IMD

3.3.1.2 Computational Fluid Dynamics (CFD) and FEA Analysis

FEA thermal analysis using ANSYS steady state and transient temperature packages were used to model the wound E-core and JFET- separately and as an IMD unit. Compared to the lumped parameter model analysis, FEA allows for a more in depth thermal analysis, investigation of critical thermal paths in a system and observing potential hot spots in the system. FEA is commonly used for thermal analysis especially due to conduction. The computational cost compared to lumped parameter model is however higher. For thermal analysis on motor drives especially when modelling the cooling effects on a geometry, FEA analysis is overly dependent on the heat transfer coefficient values inputted. For a 3D model, the heat transfer coefficient on a surface is non-uniform and dependent on the surface contact with the coolant. This makes it difficult to input accurate HTC values.

CFD offers a more accurate numerical modelling option compared to both FEA analysis and Lumped Parameter models. CFD allows for air flow and heat transfer to be modelled in the same package – overcoming the shortcomings of both FEA and Lumped Parameter method. However, the computational cost is high compared to the other simulation methods.

The stack length of the back iron was 100mm and it represented $1/6^{th}$ of a full stator back iron. The copper winding was 1.25mm thick with an insulation layer thickness of 0.1mm. Two layers of 5 turns of copper

windings were modelled to fill the slot area. Figure 3.7 shows the geometry of the E-core wound motorette with standing supports and housing. The design of the support and outlet holes was intended to replicate the MATLAB thermal resistance model which cools only one side of the end copper windings with the support blocking air flowing through the slots.

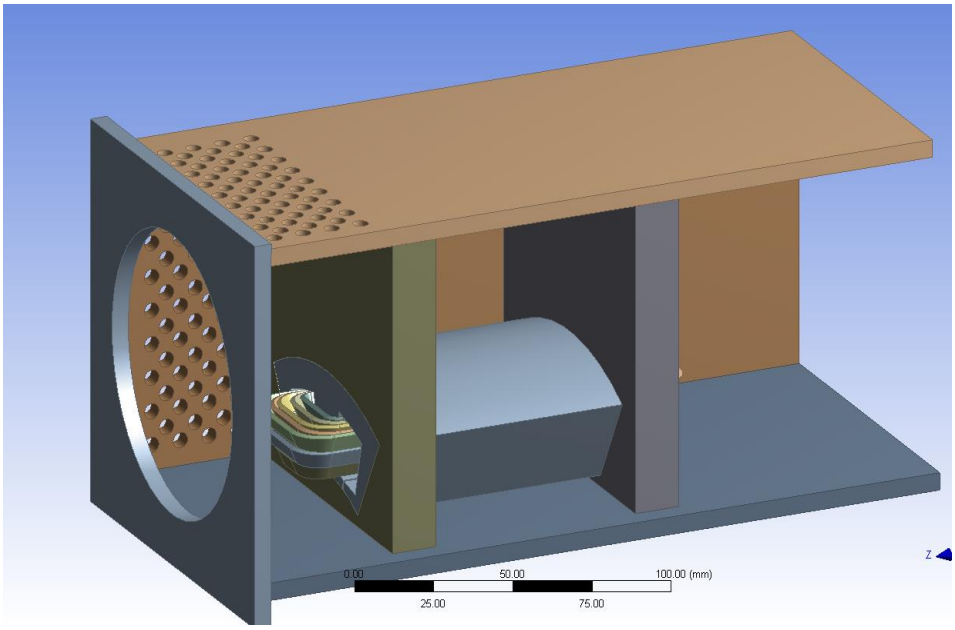


Fig 3.7: Geometry of motorette in casing

The same boundary conditions from the lumped parameter model were set for the steady state and transient temperature analysis. However, for the heat transfer coefficient due to forced convection on the end windings, CFD was used to calculate the value. FLUENT CFD package was used to find the air velocity over the end windings at different points. Although, FLUENT can calculate energy equations – like the steady state and transient temperature packages in ANSYS, the computational time for calculating both fluid dynamics and energy equation is large. This is particularly disadvantageous when numerous

geometries have to be analysed. ANSYS FLUENT was therefore only used for CFD analysis and ANSYS steady state and transient packages where used to analyse the temperature distribution in the IMD after the initial boundary conditions were set. Figure 3.8 shows the air velocity profile over the end windings.

Using (3.4), the air velocity from the CFD analysis was used to calculate the Reynolds number. The Prandtl number – dependent on the fluid (air) material property was also calculated using (3.5). The end windings are assumed to be a flat plate with a steady stream flow of air perpendicular to its surface. The Nusselt's number can be calculated by using the expression – Nu = 0.0296 Re (4/5) Pr (1/3).

$$\mathrm{Re} = \frac{Dv\rho}{\mu} \qquad (3.4)$$

(Where D = surface area of plate; v = air velocity; ρ = dynamic viscosity of air; μ = air density)

$$\mathrm{Pr} = \frac{\mu C_p}{k} \qquad (3.5)$$

(Where μ = dynamic viscosity; C_p = specific heat; k = thermal conductivity of air)

The calculated heat transfer coefficient was 61.5 W/m²K. This was set as the forced convection heat transfer coefficient boundary condition for steady state and transient temperature analysis in ANSYS's thermal packages. The E-wound core and JFET with substrate were analysed individually and as an IMD unit using the steady state and transient temperature analysis. This was to observe the effect of the

winding as a heat sink and the thermal coupling effects of the windings and PE module on the IMD system.

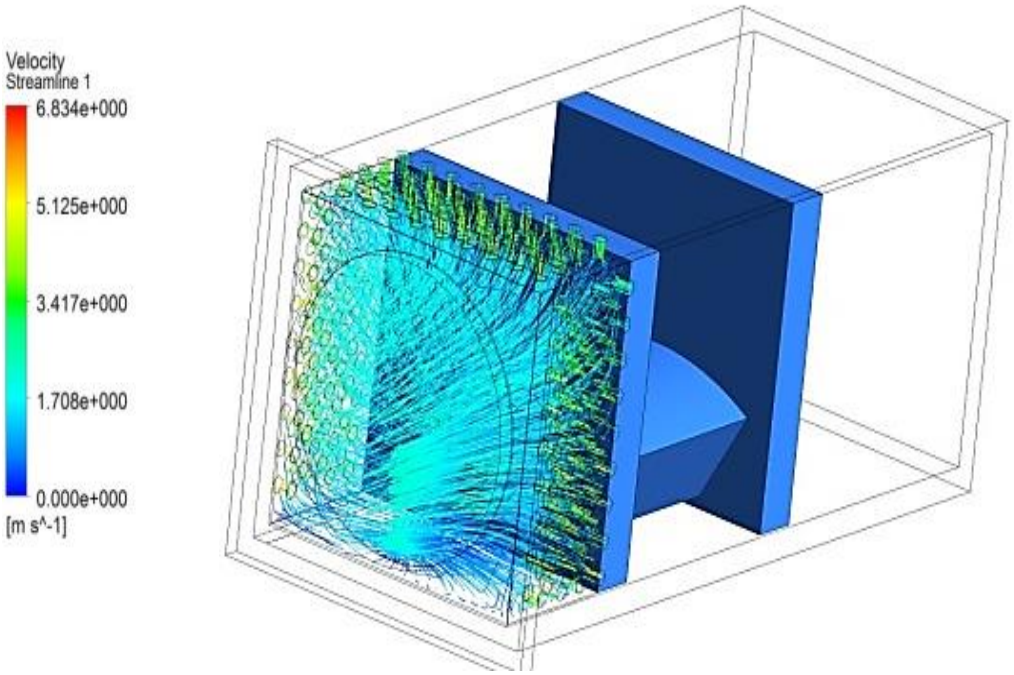


Fig. 3.8: CFD analysis showing air velocity over the end windings

Figures 3.9 and 3.10 show the temperature distribution on the motorette at 25W and 50W respectively. Unlike the thermal resistance model, the FEA model shows a more realistic temperature distribution on both the copper windings and back iron respectively. This is because the individual components are not treated as bulk materials. The temperature gradient between hot and cold end windings is also greater compared to the Lumped parameter model.

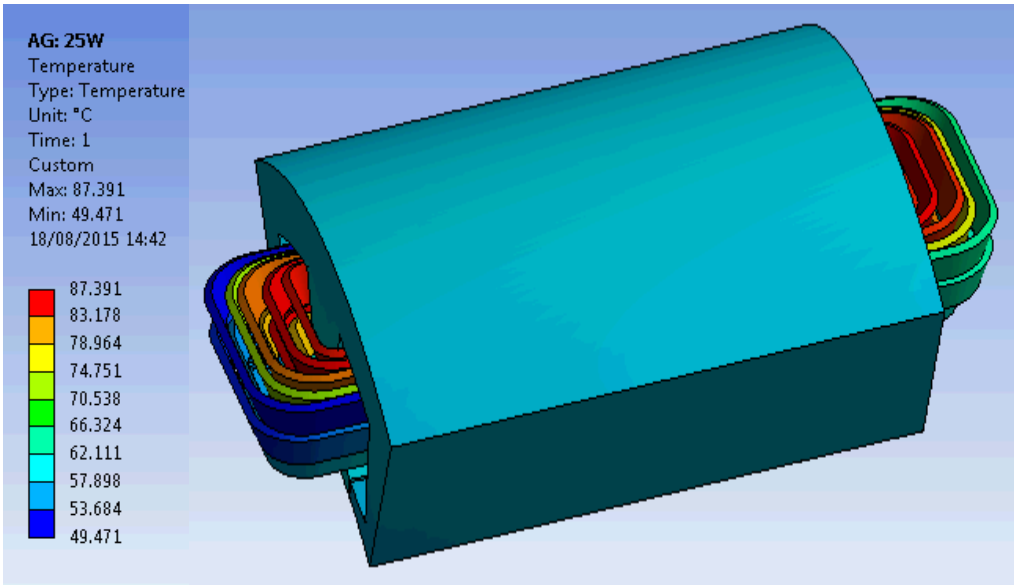


Fig. 3.9: Steady state temperature distribution of E-wound core at 25W losses

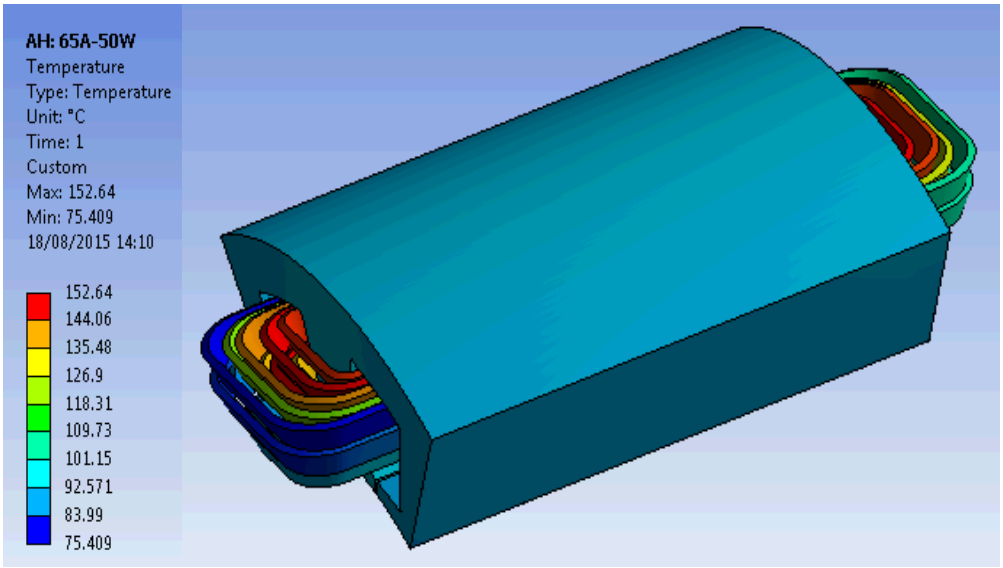


Fig. 3.10: Steady state temperature distribution of E-wound core at 50W losses

The JFET sintered on Aluminium Nitrite (AlN) substrate was also modelled and analysed. A natural convection boundary condition setting was applied on the JFET and top copper side of the substrate. A value of 5 W/m^{2}K was assumed to be the heat transfer coefficient due to natural convection.

The JFET was characterised individually to ascertain the maximum temperature under natural convection conditions. Simulating 5W losses, the temperature of the die was approximately 153°C. The high temperature even under low load conditions was due to the restriction in heat dissipation due to the inefficient utilization of natural convection and a relatively small substrate area for heat spreading.

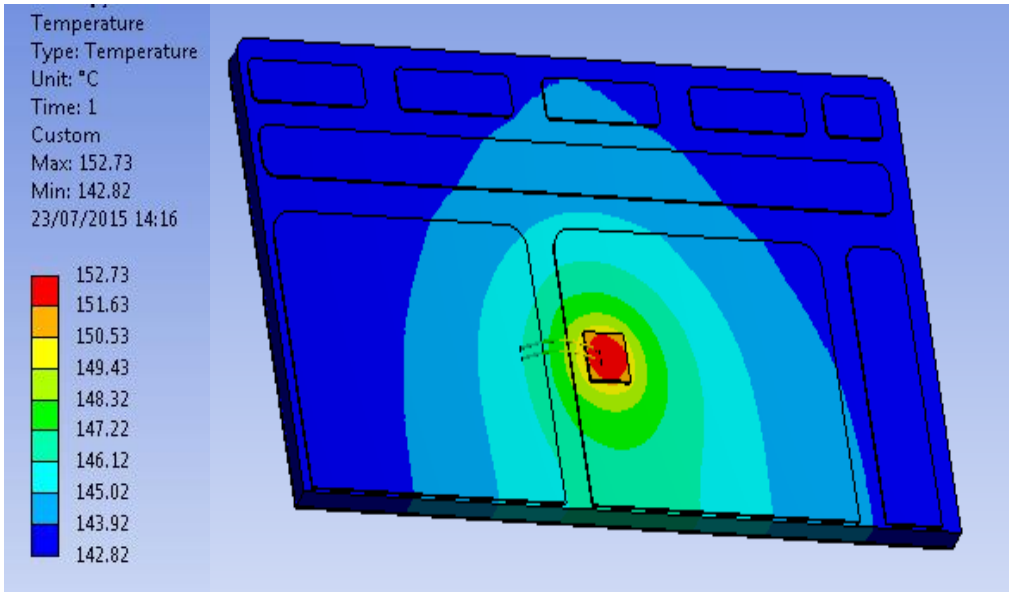


Fig. 3.11: Steady state temperature distribution of JFET sintered on AlN substrate at 5W losses

The IMD unit – JFET on AlN substrate sintered on E-wound core, was also analysed using the steady state and transient temperature packages. This was to compare with the Lumped Parameter model results and investigate critical thermal paths in the system. The ease of changing the geometry and material properties of the system is also an added advantage. Losses of 50W for the E-wound core and 16W for the JFET were simulated to achieve maximum temperatures of 186°C and 174°C for the JFET and end windings respectively. The steady

state temperature distribution for the IMD unit can be observed in Figure 3.12.

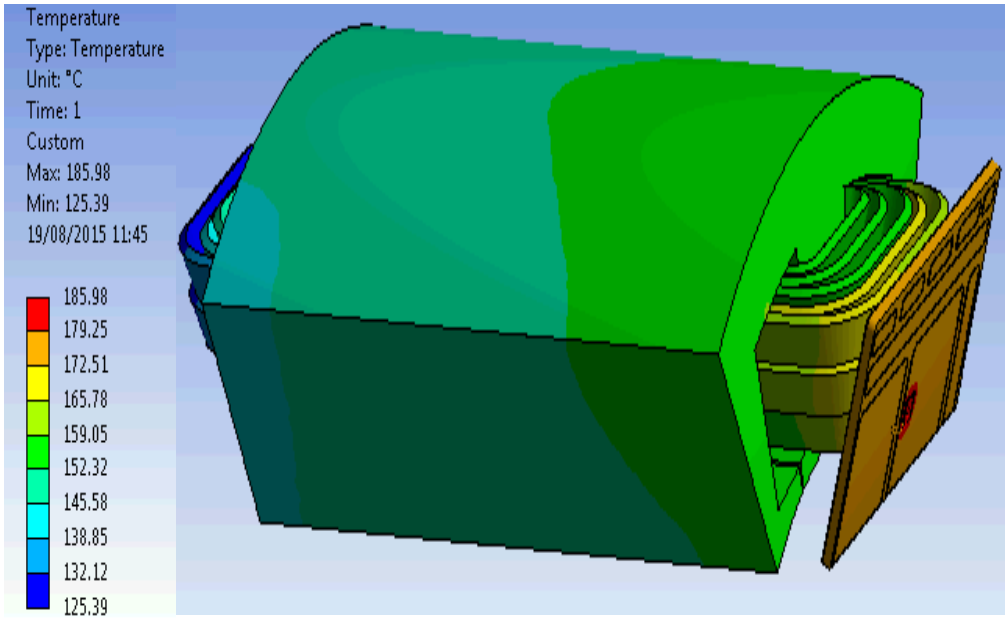


Fig. 3.12: Temperature distribution of JFET sintered on AlN substrate at 65W motorette losses and 16W JFET losses

A transient model was also created using the same boundary conditions as the steady state model. Table 3.1 shows the temperatures of the IMD components using different analytical packages. The results from the steady state and transient thermal ANSYS packages are very similar indicating high consistency in the FEA models. The MATLAB model also shows similar results for the JFET and hot end winding temperatures compared to the FEA models. However, the cold end winding and Back Iron temperatures for the MATLAB model shows an increase of 24°C and 32°C respectively compared to the FEA models. This highlights the drawback of utilising a lumped parameter model. The accuracy of the model is heavily dependent on the parameters inputted and assumptions made. Furthermore, the temperature gradient across a geometry is not realistically embodied

in a lumped parameter model – especially in a complicated layered body like the motorette windings. The assumptions made in the lumped parameter model (simplifying the layered winding coils into a whole copper block) also reduce the accuracy of the model compared to the FEA models. For the high Back Iron temperature reading for the lumped parameter model, this was due to the thermal contact assumption between the copper windings and the back iron. The lumped parameter model assumes the copper block model is in full contact with the Back Iron. However, only a fraction of the copper windings is in actual contact with the Back Iron. This erroneously gives a higher heat transfer between the windings and Back Iron, leading to a higher temperature reading on the Back Iron compared to the FEA models.

Table 3.1: Temperature distribution of IMD components from MATLAB, ANSYS Steady State and transient simulation results

	JFET (°C)	**Hot EW (°C)**	**Cold EW 1 (°C)**	**Cold EW 2 (°C)**	**Back Iron (°C)**
MATLAB	188	179	173	-	157
ANSYS (Transient)	185	173.4	149	147.7	125
ANSYS (Steady state)	186	174	150	148	125

Although, Table 3.1 shows a limited number of temperature readings from the different IMD components, the FEA model allows for greater flexibility in choosing probe points in the geometry. This allows temperature readings from any desired point on the geometry to be recorded. The lumped parameter model is highly restrictive on the probe points that can be accessed. Despite the possibility of implementing more probe points in the lumped parameter model, the high complexity and large size of the model makes this prohibitive. The similarities in results between all the three models show a high accuracy in the simulation results. However, the discrepancies in temperature for the cold end winding and back iron readings between the FEA and lumped parameter models

After steady state temperatures of 186°C and 174°C were reached for the JFET and end windings respectively, the inputted copper loss was reduced to 21W. The JFET losses were left unchanged. This was to analyse the thermal distribution of the IMD components and how quickly the system responded to the changes in temperature of specific components. Figure 3.12 shows the temperature distribution of the IMD components at steady state and transient temperatures at 65W and 21W copper losses.

From Figure 3.13, the thermal coupling between the individual IMD components can be observed. It highlights the high accuracy between the steady state anf transient thermal packages. It also highlights the individual component thermal constants and how it affects heat dissipation. With a reduction in JFET losses, the temperatures of the

individual IMD compontents reduce despite the losses remaining constant. The success of the end winding mounted IMD concept hinges on a good thermal coupling between the PE and the copper windings and the initial results show good thermal coupling between the individual components. Therefore, with the end windings adequately cooled, the PE can be efficiently cooled as well.

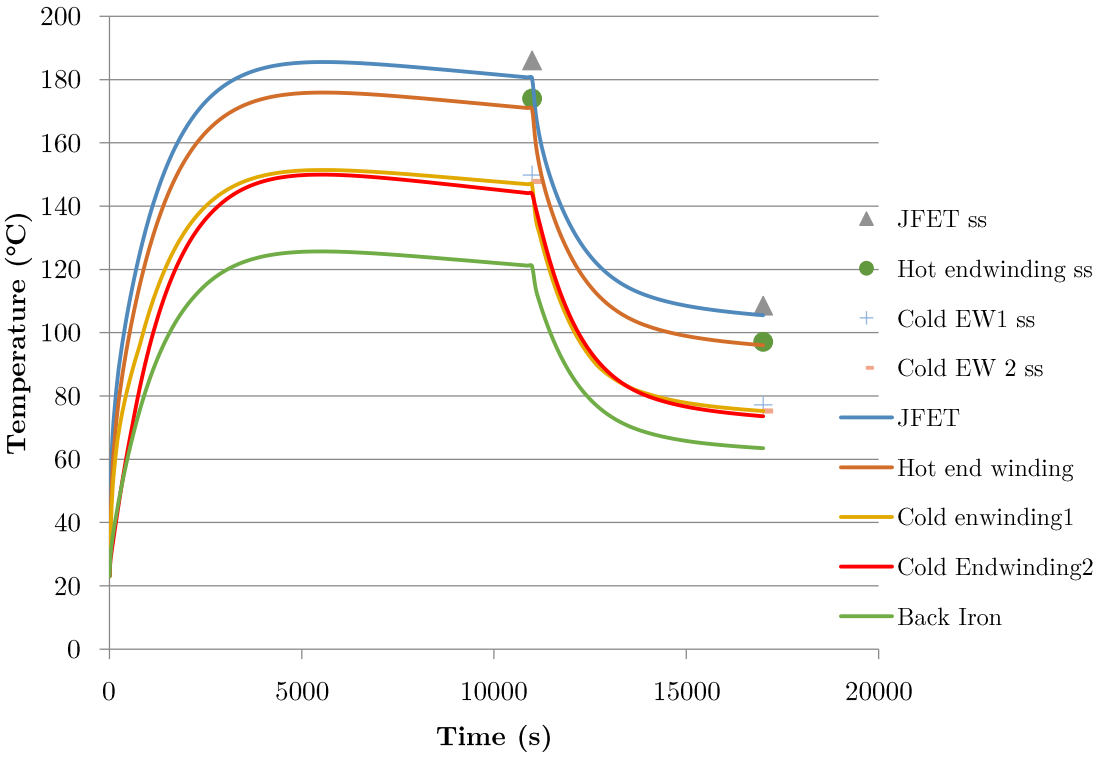


Figure 3.13: Steady state and transient temperatures of the ANSYS modelled IMD section

3.3.2 Experimental Results

For the experimental results, the individual IMD components were manufactured for prototype 1. The aim of this prototype was to -

- To validate the simulation results

- Investigate the mechanical feasibility of mounting the PE module on the motorette end windings
- Address any unforeseen arising issues – especially with the attachment of the PE on the winding

To ensure the experimental sample was similar to the FEA simulation geometry, added components were manufactured. An enclosure to channel the air flow and 3D printed supports for the Back Iron were also manufactured.

3.3.2.1 E-core Sample

A solid stack E-core back iron sample shown in Figure 3.14 was manufactured to validate the simulation results. Although a laminated core would have reflected more accurately a machine's Back Iron, a solid core was both cheaper and less time consuming to procure compared to the laminated core. For the initial concept validation, a solid core would suffice. Moreover, the solid core was modelled in the FEA simulations so both geometries (FEA and experimental) are more comparable. The samples were manufactured to reflect the simulation geometries as accurately as possible. This was used to investigate the manufacturability of the proposed concept. Initial thermal analysis of



Fig. 3.14: Characterised motorette without power electronics attached



Fig. 3.15: Motor Housing

the E-core was performed without attaching the substrate and power device to characterise independently. This was aimed at characterising both components individually. This would aid in the analysis of the thermal coupling effects both components have on each other.

The Back Iron was wound with a Nomex insulated flat copper winding of 2 mm thickness. The core was wound to ensure a maximum slot fill. Figure 3.14 clearly shows the wound E-core with a filled slot area. The top winding row consists of 5 turns, the middle and bottom rows, 3 and 2 turns respectively. The 3D printed support attached to the Back Iron was manufactured to assist with the winding process. The support prevents the copper winding insulation from breaking on the sharp edge of the Back Iron during winding.

A motor housing shown in Figure 3.15 was built from Perspex sheets for the E-core for protection and to channel air flow on the appropriate components. 3D supports printed from Polylactic Acid (PLA) were manufactured as a mounting platform for the E-core and to isolate the back iron from fan air flow. Figure 3.16 shows the solid stack E-core mounted on the 3D printed supports. An FD9225-N mountable fan



Fig. 3.16: Motorette mounted on 3D printed supports

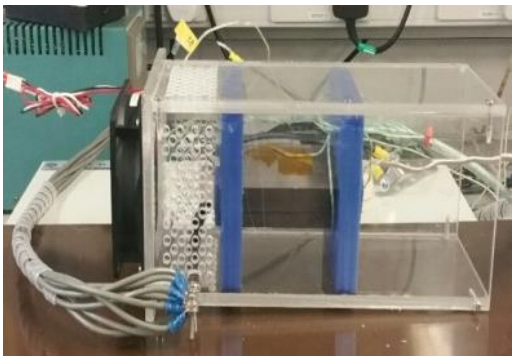


Fig. 3.17: Motorette in fan-mounted housing

with a maximum rated air flow of 48.7 CFM was attached to the motorette housing to represent a forced convection cooling system.

The thermal analysis carried out aimed at investigating the interaction between different heat sources in close proximity. Iron losses were not considered in the thermal analysis making the motorette copper windings the primary heat source. The windings were energised by a high current-low voltage DC power source. The power source used was an 'Agilent Technologies N8732A 10V/330A' DC power supply. Temperature readings were measured and recorded using K-thermocouples and a PICO USB TC-08 datalogger. Six thermocouples were attached to different components on the prototype. Figures 3.18 and 3.19 show the temperature distribution of the motorette components at 25W and 50W copper losses respectively.

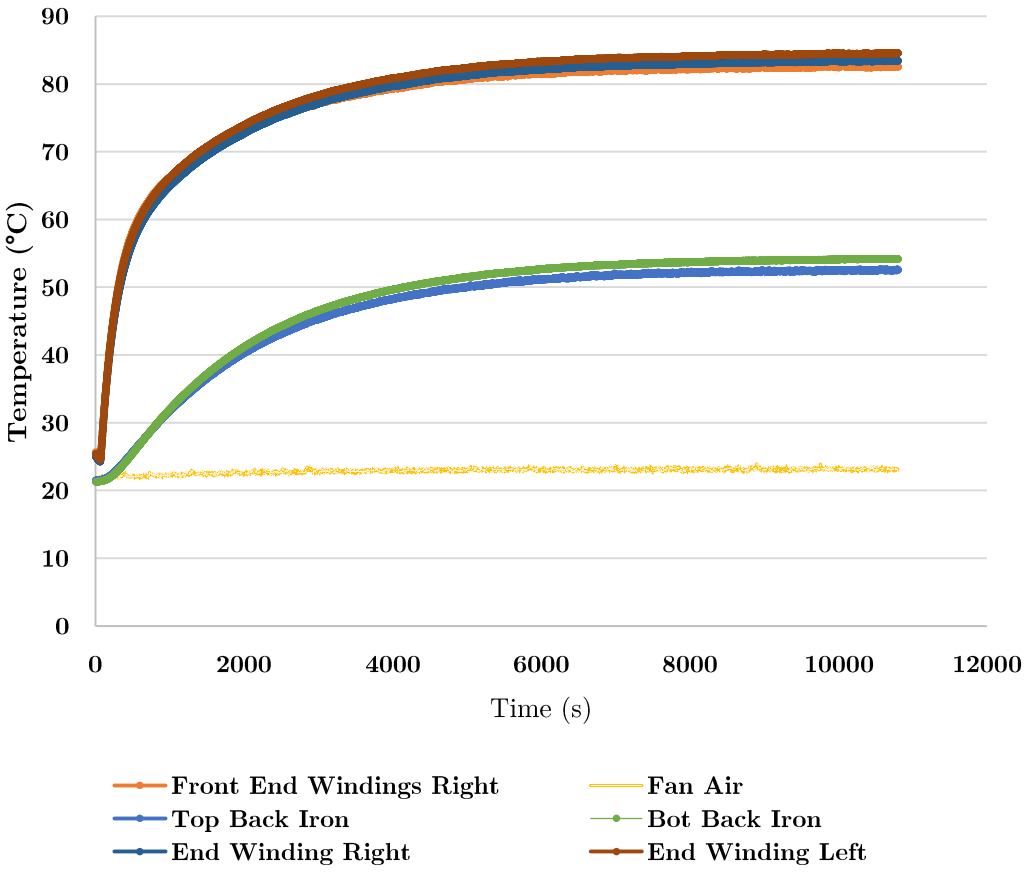


Figure 3.18: Temperatures of motorette components at 25W

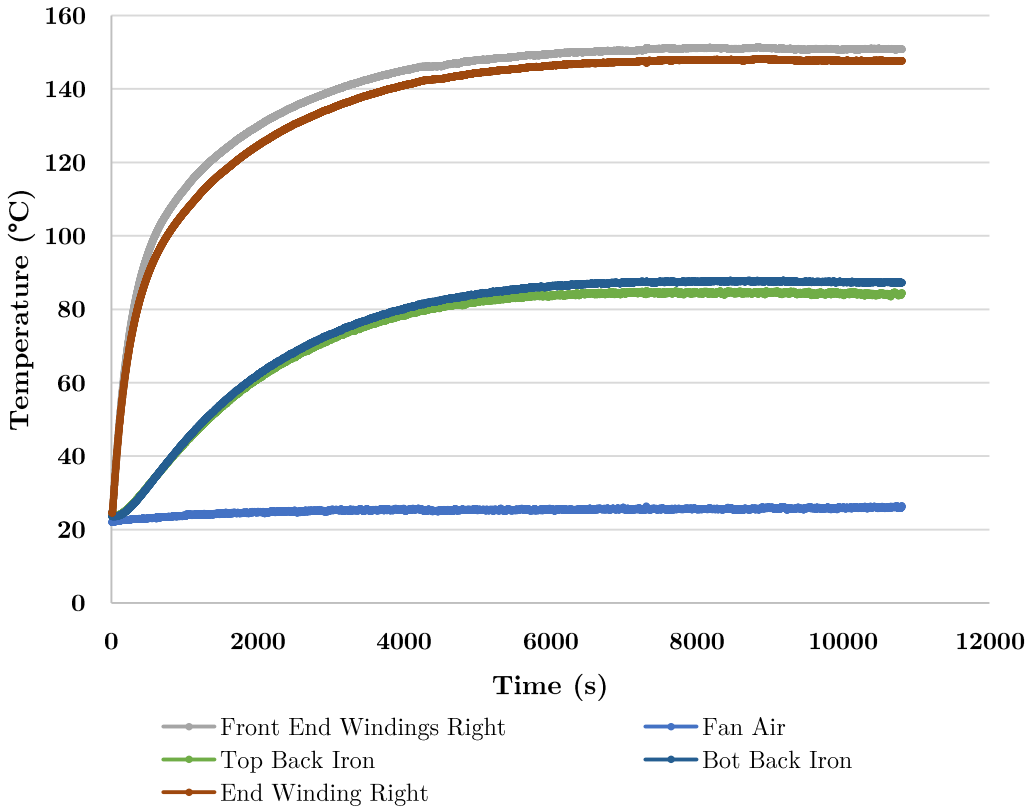


Figure 3.19: Temperatures of the motorette components at 50W

Table 3.2: FEA and experimental results showing maximum temperatures of individual IMD components at 25W and 50W

	End windings (°C)	**Back Iron (°C)**
FEA (ANSYS) 25W	87.4	57
Experimental 25W	84.6	54.2
FEA (ANSYS) 50W	152.6	91
Experimental 50W	150	87

3.3.2.2 Power Electronics

A SiC Infineon JFET was sintered on an Aluminium Nitride ceramic substrate to represent the power electronics unit. The JFET dimensions were 2.7x2.7x0.2 mm and the substrate had a ceramic thickness of 1.25 mm and top and bottom copper layers' thickness of 0.15 mm each. The bottom copper layer was etched to provide isolation and prevent shorting the end winding turns the substrate will eventually be mounted on. The JFET – considered solely as a heat source has no gate connections. Aluminium wire bonds are attached to the source and the drain is sintered on the copper tracks. Two wires are soldered on the top copper layer to energise the normally on JFET.

The PE module was characterised individually before mounting on the motorette end winding. The maximum operating junction temperature for the SiC bare die JFET was 175°C; however, the tests performed on the JFET were without a heat sink or base plate and with natural

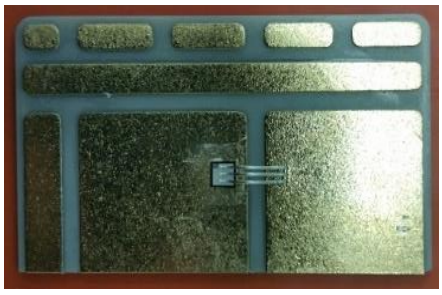


Fig. 3.20: SiC JFET with aluminium wire bond



Fig. 3.21: Etched bottom side of substrate

convection as the only cooling system. Figure 3.23 shows the temperature distribution on the substrate and die at 5W losses. The high heat flux the power device produces due to its small area compared to the copper windings emphasises their varying thermal management demands. It is also important the interconnect layer

between the substrate and end windings has a high thermal conductivity for better heat transfer.

The choice of interconnect material was between high temperature solders and silver sintering. Silver sintering was chosen due to its higher thermal conductivity, higher melting point and operating temperature compared to high temperature solders [39-40].

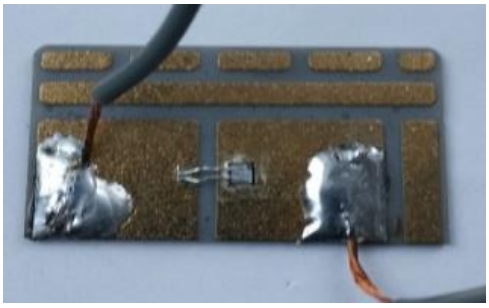


Fig. 3.22: Wires soldered on top-side copper

The calculated junction-ambient ($R_{thJ\text{-}A}$) and junction-case thermal resistances ($R_{thJ\text{-}C}$) due to natural convection from experimental results were 25°C/W and 4°C/W respectively. However, these resistances are highly package dependent and when a heat sink or base plate is attached to the substrate $R_{thJ\text{-}C}$ is significantly reduced.

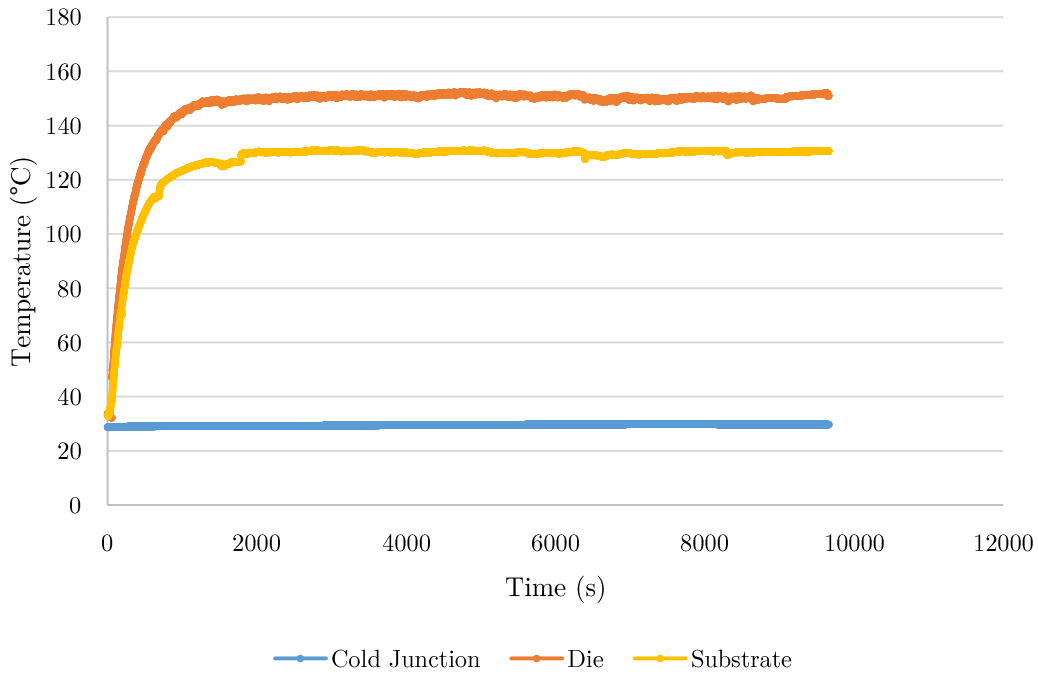


Figure 3.23: Temperatures of the substrate and JFET at 5W losses

3.3.2.3 Sintering Process

The ceramic substrate was attached to the copper end windings by sintering. Both surfaces were treated before sintering was performed. The insulation around the copper end windings to be attached to the substrate was removed and the windings were pressed in a rig to produce a flat surface for sintering. The coils were also separated to avoid short circuiting. Figure 3.24 shows the wound E-core after pressing the windings, spacing and cleaning the coils.



Fig. 3.24: Spaced out and pressed copper end windings

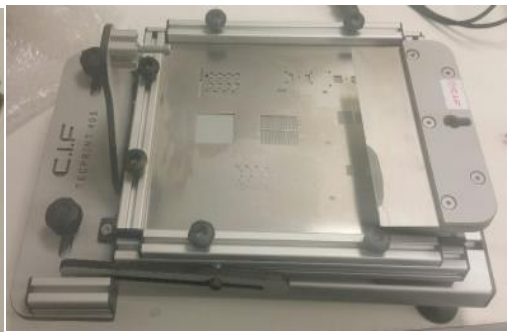


Figure 3.25: shows the manual screen-printing system used to apply the paste

The silver paste was stencil printed to the end windings. A 100µm stencil was used to ensure a uniform distribution of silver paste on the end windings. An aluminium protection for the die and wire bond was manufactured (shown in Figure 3.26) to shield the delicate power device and bond wires from the high-pressure press.

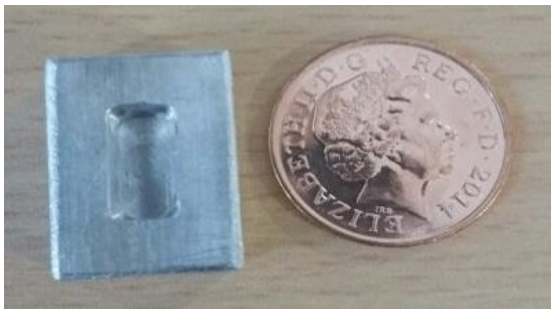


Figure 3.26: Cover for die and wire bond during sintering

The minimum pressure required to achieve a good bond layer is 5 MPa [41]. At this pressure, the sinter ability increases tremendously due to the increased active contact area between the individual silver particles [40]. It is essential to have a very smooth surface between both contact areas (the bottom copper layer of the substrate and end windings) as

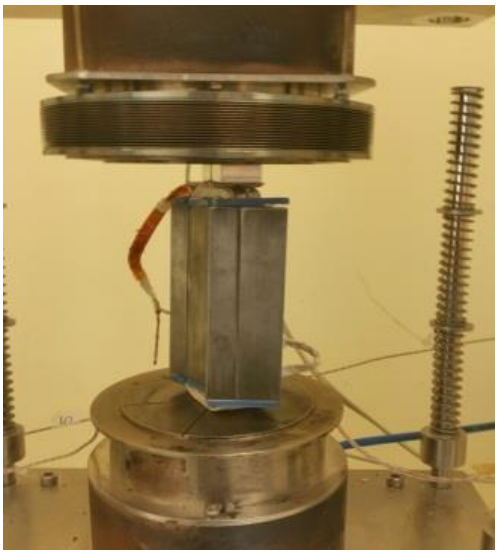


Fig. 3.27: Power electronics unit and wound E- core in sintering press



Fig. 3.28: Power electronics unit sintered on end windings of wound E-core

even the slightest irregularities can lead to cracking or breaking of the ceramic substrate at high pressures. Typical temperatures for sintering start around 250°C [42]. The sintering process was performed at 10 MPa and a temperature of 280° for 30 minutes. The higher temperature of 280°C (compared to the 250°C in literature) and longer time was aimed at compensating for the low pressure applied. This produced a decent attachment between the substrate and copper winding.

3.3.2.4 Winding Mount Power Electronics

The SiC JFET and E-core copper windings were energised separately. The experiment was aimed at investigating the response time of the copper windings (heat sink) to changes in temperature in the JFET. The critical thermal paths in the system were also investigated. Thermocouples were placed on critical thermal points in the system – back iron, JFET, end windings and the fan air. Figure 3.29 shows the experimental rig for testing. Using a fixed heating current of 65A and 8A for the windings and JFET respectively, the voltage ratings over the course of the experiment increased due to an increase in temperature of the respective components. Increase in temperature over time leads to an increase in component resistance which ultimately leads to higher power dissipation. The voltage increased by 0.1V and 0.3V for the windings and JFET respectively over the course of the experiment. The voltage rise produced a final power dissipation of 65W and 16W for the windings and JFET at steady state.

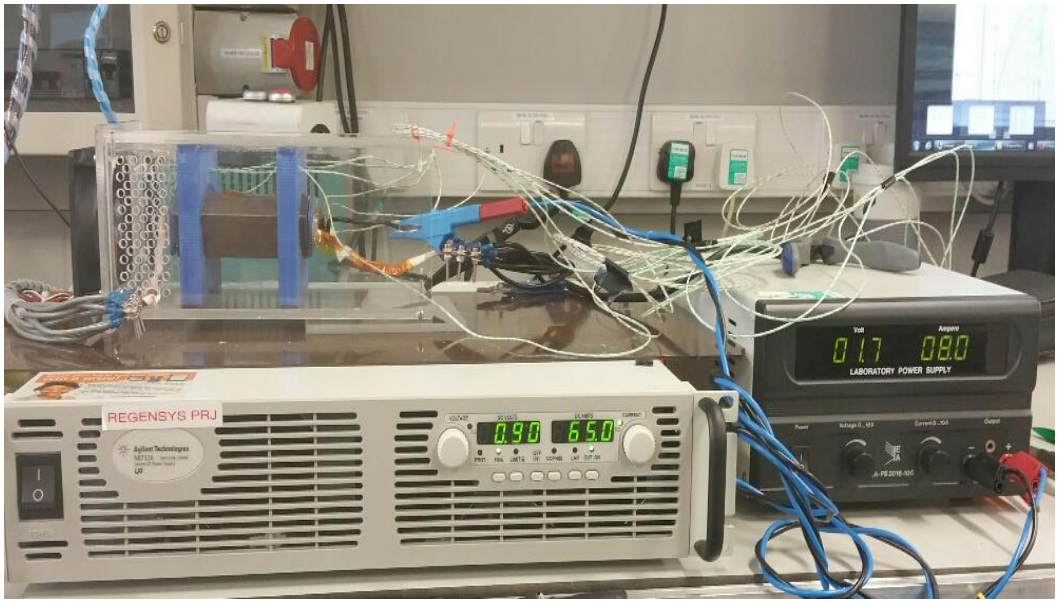


Fig. 3.29: Experimental setup of JFET sintered on end windings of motorette and energised separately

Component temperatures of the IMD system were recorded at steady state. The input power for the copper windings was reduced by 44W and the JFET losses were left constant. This was to validate the simulation results and analyse the assumptions for boundary conditions set in the simulation models. Figure 3.30 shows the changes in temperature of the IMD components at initial input losses (65W and 16W for the windings and JFET respectively) and after the copper losses are reduced.

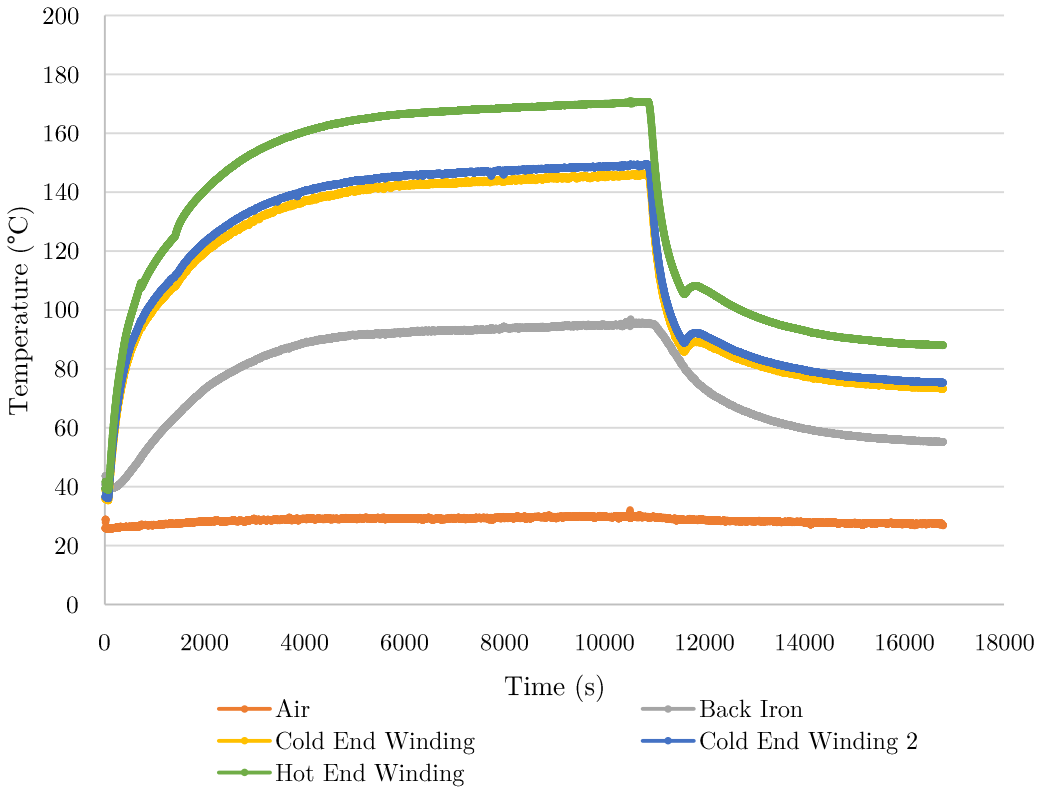


Figure 3.30: Transient thermal graph showing the temperatures of the IMD components at 65W copper losses and 16W JFET losses

The thermocouple labelled 'hot end winding' was placed on the copper windings directly behind the substrate – completely isolated from the forced air cooling from the fan. The 'cold end winding' labelled thermocouples were placed on the copper windings in direct contact with forced air from the fan. The junction to ambient and junction to case resistances are 9.81°C/W and 0.625°C/W respectively. Table 3.3 shows the temperature distribution of the IMD components from the MATLAB and ANSYS models, and the experimental model.

The MATLAB model has higher component temperatures compared to both ANSYS and experimental results due to the lumped parameter method of analysis. The maximum component temperature is recorded

for each IMD component in the MATLAB model and specific points on the IMD cannot be probed. However, the ANSYS model allows for probing specific points on the model analysed. The thermocouples on the experimental sample were placed on the exact points the ANSYS thermal probe. End windings and JFET temperatures of the experimental sample and simulation models similar which indicated the assumptions made for the heat transfer coefficients on the JFET and end windings were accurate.

For the Back Iron temperature, the experimental and simulation results greatly differ. This is due contact region modelled between the copper windings and the back iron in the simulation geometry. The MATLAB and ANSYS models assume good contact between the active copper windings in the slot and the E-core tooth. The MATLAB model assumes the two bodies in perfect contact with each other and the results from Table 3.3 show the best heat transfer between the copper windings and back iron. The ANSYS model allows for a slightly imperfect contact between the windings and back iron – to reflect a more realistic scenario. However, due to the thickness and mechanical strength of the copper windings in the experimental sample, it was difficult to achieve good contact between the active copper and the back iron. This makes heat transfer between the copper windings and the back iron very poor – hence the low temperature recorded in the experimental results.

Table 3.3: Steady state temperature distribution of IMD components from MATLAB, ANSYS and experimental results

	JFET	**Hot EW**	**Cold EW**	**Cold EW2**	**Back Iron**
MATLAB	188	179	173	-	157
ANSYS	186	174	150	148	125
Experimental	180	171	149	146	94

The first prototype although validating the End Winding Mounted IMD concept from a thermal perspective left a few questions unanswered. The electrical connection between the power module and motorette winding – an essential requirement for functioning machines is not demonstrated in Prototype 1. Furthermore, silver sintering as an attachment method raised doubts as the choice attachment method for this IMD concept. The sintering process being undeveloped especially in large surface and irregular areas resulted in many damaged substrates. The high pressures the brittle substrates were subjected to, produced cracks in some substrates and in others destroyed the substrate. The uneven surface of the jig-pressed motorette windings also aided in the damage of substrates.

The issues raised from the first prototype had to be rectified before manufacturing the second one. The first step was to address the manufacturing issues from the first prototype. The main mechanical problem was the attachment method used for connecting the power

module to the motorette windings. Pressure silver sintering as an attachment method was reconsidered by analysing other processes. Pressure-less sintering and high temperature soldering was considered alongside pressure assisted sintering. Although it is envisaged silver sintering as a process will offer the best results in terms of heat transfer from substrate to windings and mechanical stability at high temperatures, implementing the process outside die attachments remain unproven.

3.4 Conclusion

The end winding mount configuration potentially offers an increase in power density of the IMD and reduced system EMI compared to conventional IMDs. The results – both simulation and experimental, demonstrate the feasibility of the winding mount configuration as a viable option for drive integration. Although the experiment was solely from a thermal perspective, it addresses the erroneous assumption that the power electronics fails near other heat sources. The manufacturability of this concept using silver sintering as a heat transfer interface and attachment between the coper windings and the substrate is also investigated. The pressure-assisted sintering process proved unsuitable for the end winding mount IMD concept with several substrates damaged in the process.

The results show the copper windings act as a heat sink for the power electronics unit providing a large thermal mass for heat dissipation. The IMD unit also utilises a single cooling system which could

potentially reduce overall cost. With simulation and experimental results fairly similar, this demonstrates the accuracy of the boundary condition assumptions made for the simulation models. These could be extrapolated and adopted in future models with varying geometries and material properties.

Table 3.4: Experiments and Test conditions performed

Manufacturing Process	**Manufacturing tools/Test Vehicles**
Wind solid core Back Iron	Copper winding wound on back iron (6 turns)
Design and manufacture motorette housing	Motorete housing manufactured using Perspex sheets
Design and manufacture motorette supports	3D printed platforms for motorette support and thermal isolation
Integrate cooling system	A fan is mounted on the Perspex motorette housing for forced convection cooling of the windings
Integrate temperature sensors	K-type thermocouples are attached to the individual motorette components to measure temperature
PE module attachment to winding	The PE module is sintered by pressure-assisted silver sintering on the copper winding
Excite individual heat sources and record component temperature	The windings and diode are excited by a DC power supply

The thermal challenges of having the power electronics unit near the machine heat sources (copper windings, Iron and rotor) still pose the major hindrance in close integration. In IMDs, cooling the PE and machine is complicated due to the varying thermal demands of the PE and machine. The PE unit generates the most losses in the motor drive

and possesses the highest power density of all the IMD components. Its significant thermal management demands are also increased with the maximum operating temperature of most commercially available power modules around 150°C.

Despite the encouraging initial results, more work still has to be done on designing and analysing the electrical connections between the windings and the PE unit. The experiment does not account for the PE unit energising the copper windings. The next prototype looks to address the issues encountered during manufacture especially the substrate to windings attachment. Electrical connections between the windings and PE for combined electrical and thermal analysis of the winding mount configuration will also be implemented in the next prototype.

The next chapter presents optimisation options on Prototype 1. Different motorette to winding attachment processes are investigated as a result of the problems encountered during the sintering process in this prototype.

CHAPTER 4

PROTOTYPE 1 OPTIMIZATION

4.1. Introduction

This chapter analyses the different substrate to motorette winding attachment processes investigated as a result of the problems encountered during the sintering process in the first prototype. The mechanical stability of the different processes is also investigated. The flatness of the motorette windings which contributed to damaging substrates during the pressure-assisted sintering process is also addressed.

4.2. Prototype 1 Optimization

4.2.1. Motorette winding

During manufacture of the first prototype, many problems were encountered especially with the attachment of the power module to the motorette end windings. The end windings as a mounting platform proved problematic due to the surface roughness and flatness. For pressure-assisted silver sintering, a minimum surface roughness of 5µm is required for bonding. However, this value cannot be guaranteed after jig pressing the copper end windings flat. Also, with the jig-pressed end windings, a perfectly flat surface for sintering cannot be assured. Furthermore, the curvature around the bend of the end winding reduces the available surface area for attaching the PE module. There's also a possibility of compromising the copper insulation during the jig press process.

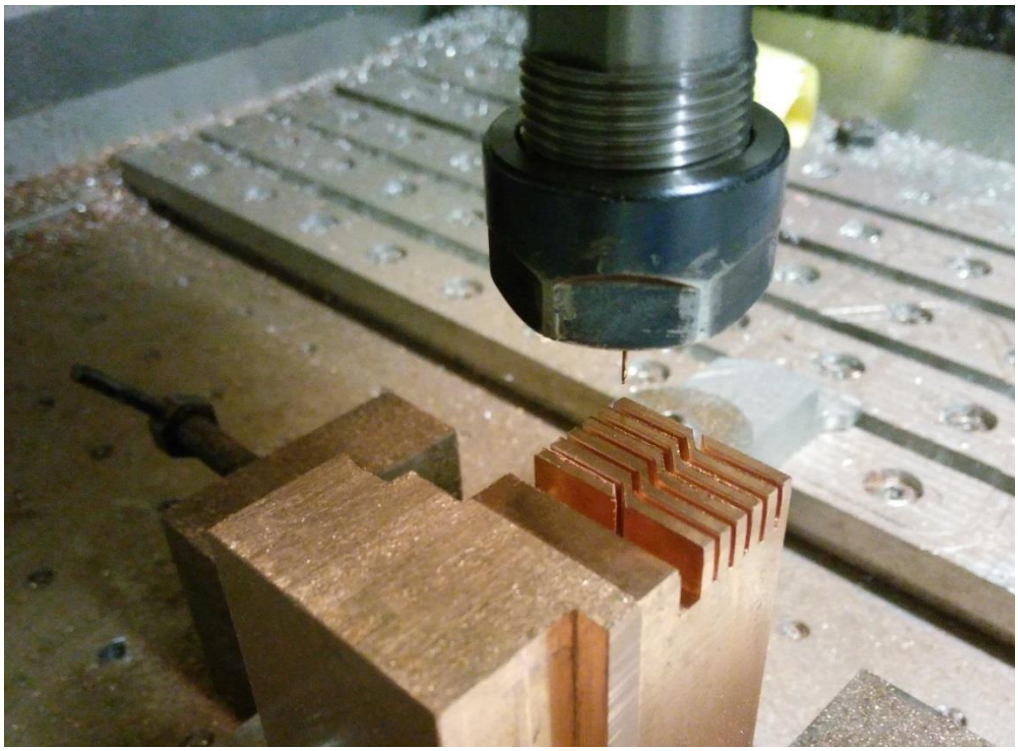


Fig 4.1: End winding profile cut with a CNC cutter

Taking these challenges into consideration, it was immediately apparent that using a commercially available copper winding will require some modifications to the windings before implementing in the end winding mount IMD concept. A preformed solid copper winding with a low number of turns was chosen for manufacture. The low number of turns was due to a restriction in the manufacturing process. The copper winding was cut from a single block of copper and could only produce one layer of turns per tooth. However, the benefits of adopting this winding structure is the spacing between each turn can be controlled. This is especially important when mounting the substrate on the winding.



Fig 4.2: Copper winding machined from a block of copper

The copper tracks on the substrate can be easily aligned on the pre formed copper winding. Low number of turns is also very common in high speed machines. The back EMF of a machine is proportional to its speed and number of turns therefore at high speeds the back EMF increases. This requires the converter to supply a very high voltage for the corresponding high back EMF. To regulate the back EMF, a low number of turns is required. Manufacturing a pre-formed motorette winding will also ensure a flat and smooth surface for mounting the PE module.

With the motorette windings manufactured, the next step was to analyse the attachment processes for the substrate to end winding joint. As earlier stated, the pressure assisted silver sintering process adopted during

manufacture of the first prototype raised concerns about its mechanical stability and reliability. Also, with the high costs accrued due to damaged ceramic substrates, the sintering process had to be optimised for large surface areas and other attachment processes were investigated.

4.2.2. Attachment Joint

For testing the attachment processes identified, a dummy copper end winding was manufactured. This was aimed at saving both cost and time in the manufacture of a full end winding. The dummy end winding was designed to replicate the end winding profile used as a mounting platform for the substrate. The bottom copper layer of a gold finish AlN substrate was mechanically etched to match the end winding profile.

The attachment processes analysed were –

- Pressure-assisted silver sintering
- Pressure-less silver sintering
- Soldering

4.2.2.1. Pressure assisted sintering

In the first prototype, pressure assisted sintering was utilised and a few challenges were encountered that questioned its suitability as an attachment method especially in large areas. Although compared to solder

pressure assisted sintering offers much higher temperature operation and better heat transfer, its mechanical stability for larger areas remains problematic. Also, during the sintering process, the high pressures the substrate is subjected through can cause irreparable damage to the fragile substrate.

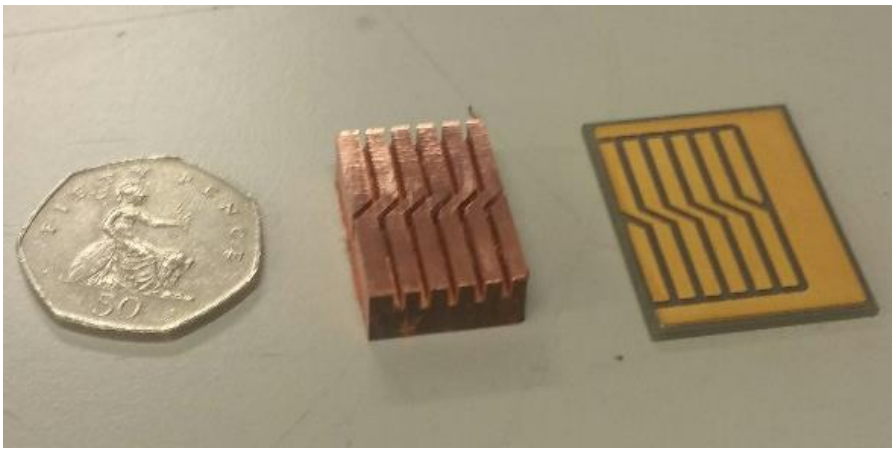


Fig 4.3: Dummy end winding and AlN substrate created for testing attachment processes

The sintering process was carried out using the end winding dummy and corresponding substrate shown in Fig 4.3 to represent the motorette end winding and power module respectively. The silver sintering paste used was the Heraeus Sinter Paste ASP. The end winding dummy was polished and treated in an ultrasonic bath to remove organic and loose deposits on the sample in preparation for the sintering process. The substrate was also treated in an ultrasonic bath to remove organic material.

Using a 100µm steel stencil shown in Figure 4.4, an even layer of silver paste was deposited on the end winding dummy. The silver paste on the

end winding dummy was dried in the oven for 3 minutes at 150°C. This is aimed at removing inorganic materials and helps coat the end winding layer to be sintered on. Another thin layer of silver paste is then applied on the dried silver layer on the end winding dummy. This two-step sintering process supposedly gives better results for larger area sintering [206].

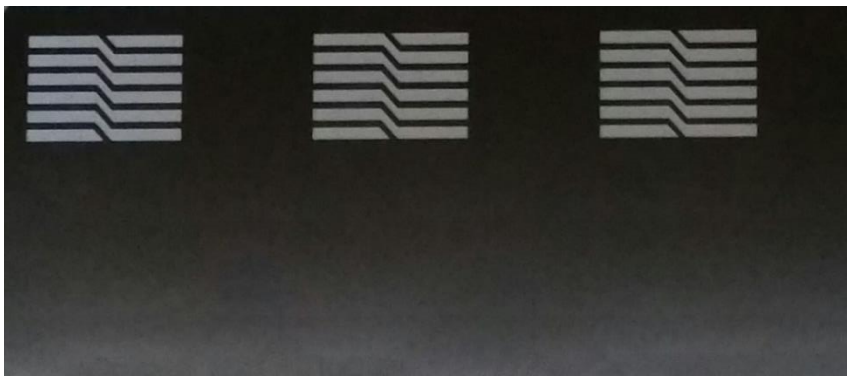


Fig 4.4: Steel stencil for sinter paste deposition

The AlN substrate was placed on the sinter layer on the end winding dummy – carefully aligning the copper tracks on the substrate to the sinter layer on the end winding dummy. The sample was placed in the sintering rig and subjected to pressure conditions of 10 MPa with a temperature profile similar to the one described in the sintering process of the first prototype.

With the sintering process completed, the next step was to investigate the quality of the sinter layer and analyse its mechanical strength. To analyse he inaccessible sinter layer (blocked by the substrate and end

winding dummy), a Scanning Electron Microscope (SEM) machine was used. This works by scanning electron beams across the surface of the sample analysed. When these electron beams hit the surface of the sample, they produce signals which are detected to generate an image of the sample scanned. Typical electron producing signals include X-rays, backscattered electrons and secondary electrons. To produce high quality imaging, especially with the sinter layer sandwiched between two different materials of varying thickness, an X-ray SEM was used. Using X-ray signals allow for qualitative and quantitative analysis especially in mapping and profiling a sample's structure and composition.

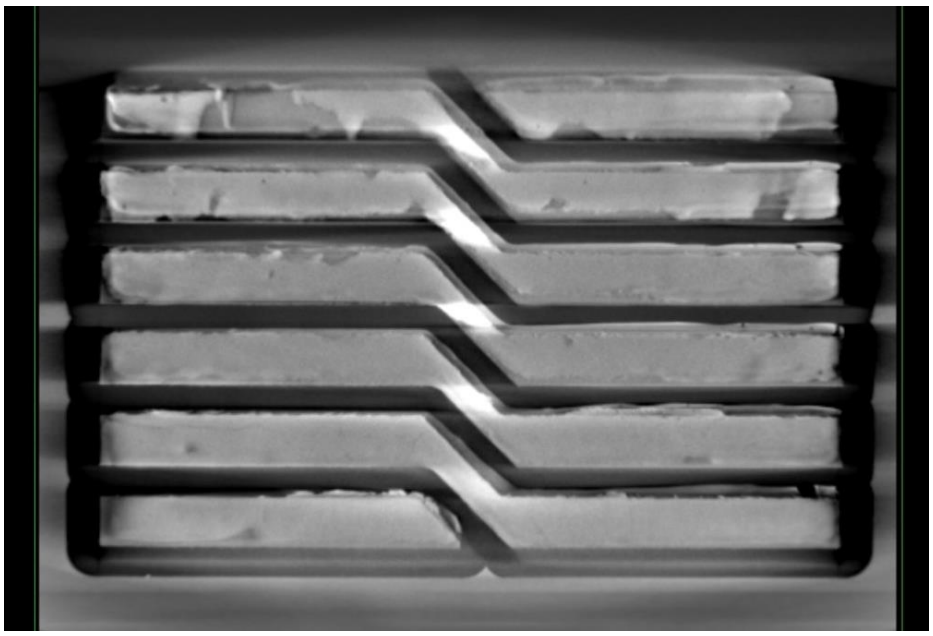


Fig 4.5: SEM X-ray of pressure-assisted silver sinter layer

Figure 4.5 shows the resultant X-ray imaging after the SEM scan of the pressure assisted sinter sample. A fairly uniform silver layer can be

observed with very few areas of no bond. These are usually around the edges of the bond area. The top right winding also features a large patch of missing silver layer. The 'no-bond' areas ultimately weaken the overall structure of the attachment joint and reduce the reliability of the IMD. More importantly, the thermal resistance of the silver sinter layer increases with increasing holes and voids in the structure. With the silver joint layer being a critical thermal junction in the IMD system, it is important to reduce its thermal resistance for efficient heat transfer from the PE module to the end windings (heatsink). With a heat transfer coefficient of over 200 W/m^2K, silver sintering offers an efficient heat transfer from the power module to copper windings. With very few voids present in the attachment layer, the heat distribution from power module to winding is also further improved. Furthermore, the pressure application helps to ensure a uniform layer thickness on the sinter layer. This reduces the chances of having a slant or slightly uneven substrate attached to the winding.

The next step was to investigate the strength of the sinter layer. With the power electronics module mounted on the end windings and in the machine housing, it is envisaged that the module will be subjected to high vibration levels. This is due to electromagnetic forces acting on the copper windings. From a reliability perspective, it is imperative the attachment joint between the substrate and end windings is mechanically strong enough to withstand these vibrations.

To investigate the strength of the sinter layer joint, a mechanical pull test was performed. This is usually done to test the tensile or shear strength of a coating on a material. Two cylindrical rods were attached to the substrate and end winding dummy respectively. The rods were attached to both the substrate and end winding dummy as shown in Figure 4.6 using a cyanoacrylate one-component epoxy adhesive, E1100S.

The adhesive is a welding substitute with very high tensile and shear strength. The surfaces of the sample (both substrate and winding dummy) were degreased and treated. The glue was applied on both surfaces and then oven cured at 130°C for 60 minutes. Using a calibrated hydraulic pump, the sample was pulled apart till detachment.



Fig 4.6: Steel rods glued on the sintered sample

From Fig 4.7, it can be observed that the silver layer is mostly on the gold finish AlN substrate with very little on the end winding dummy. With the silver layer not bonding on the end winding dummy, the attachment joint is weaker overall. This signifies a weak adhesion between the silver layer and the copper end winding. It also suggests that the silver paste did not properly diffuse into the surface of the copper end winding. An oxidation layer can also be observed on the end winding dummy. This oxidation layer prevents a good adhesion of the silver layer on the copper surface. [204] shows that the degree of oxidation between the silver sinter surfaces is directly related to the sinter bond shear strength – with a higher degree of oxidation resulting in lower shear strength values and vice versa. Fig 4.8 shows the force the sinter layer was subjected under till failure.



Fig 4.7: Detached substrate from end winding dummy after mechanical pull test

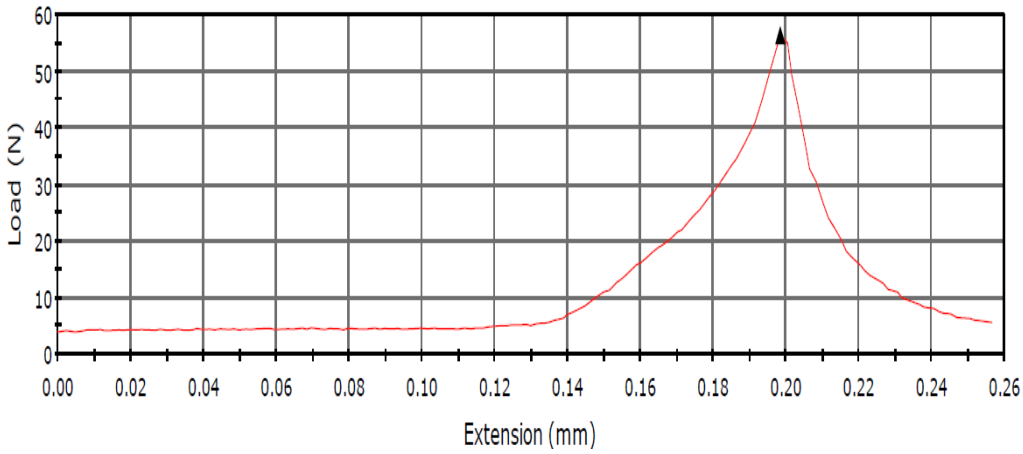


Fig 4.8: Tensile strength test of the sinter layer

A force of 56N was required to detach the substrate from the end winding. Based on the bo nd surface area, the tensile strength of the sinter bond layer was 2.3 MPa. Compared to conventional high temperature solders with typical tensile strength values up to 30 MPa, the recorded tensile strength of this sinter layer is considerably low. The shear strength can be assumed to be 0.577 – 0.6 the value of the tensile strength using Tresca or von Mises criterion [205]. This gives a shear strength value of 1.4 MPa for the sinter layer. In literature, the shear strength of silver sintering is quoted at over 70 MPa [206]. However, this value was recorded for a small bond area of 2.7 x 2.7 mm^2. A good bond quality of the sinter layer over larger areas cannot be guaranteed using sintering techniques optimised for small bond areas. This is because homogenous pressure cannot be guaranteed applied across the sample area due to its large size. This prevents the restructuring of the silver particles and removal of air from the sinter layer which ultimately leads to a weaker silver sinter layer.

The strength of the sinter bond ultimately depends on the quality of adhesion of the sinter layer to the copper end winding sample. The high pressure applied on the sample is supposed to aid in the densification of the silver films and reduction of pores/voids found in the sinter layer. A 6 MPa applied pressure produced bonds with shear stress values of over 70 MPa in literature [206]. This shows that the 10 MPa applied pressure utilised in the pressure assisted sinter process was sufficient to produce a much stronger bond than the 2.8 MPa shear strength realised. The weakness of the silver joint is as a result of the oxidation layer formed on the end winding dummy at high temperature.

To prevent this oxidation layer from forming on the copper surface and improve the strength of the attachment joint, the sintering process can be performed in a vacuum or the copper surface can be coated. The latter was the only realistic option available due to the unavailability of a suitable vacuum sinter rig.



Fig 4.9: PVD silver coated end winding dummy samples

The surface of the dummy copper winding used as a mounting platform for the power module was coated with silver by the process pf Physical Vapour Deposition (PVD). PVD is a vacuum deposition method that produces thin films by creating a vapour of the material to be deposited. The material to be coated (copper winding) is covered in an even layer of 1 µm silver coat. Figures 4.9 and 4.10 show the dummy end windings coated in silver.

Using sputter deposition method (one of various PVD processes), high melting materials like silver can be easily deposited on the copper sample. Sputter deposition PVD has the advantage of stronger adhesion to the target material and corrosion resistance compared to electroplating. Compared to electroplating, PVD coatings also have high durability and

high temperature operation. It also has the added advantage of being more environmentally friendly compared to traditional processes like electroplating (which usually produces harmful by-products).

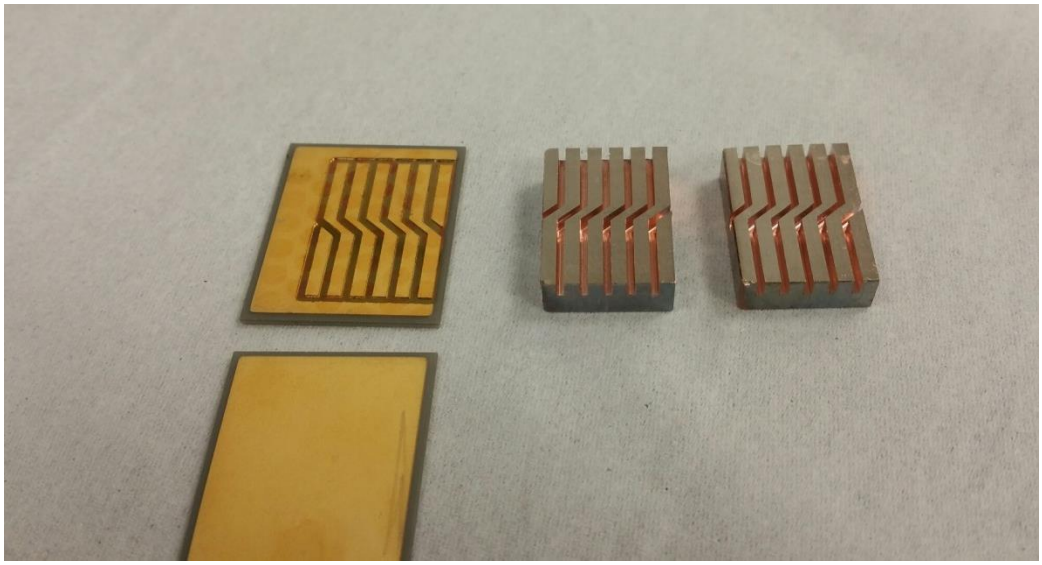


Fig 4.10: Silver coated end winding dummy and substrate profile

With the end winding coated with a 1 µm silver layer, the silver sintering process was repeated. The mechanical stability of the sinter bond was again investigated using the mechanical pull test. Fig 52 shows the tensile strength of the silver bond layer.

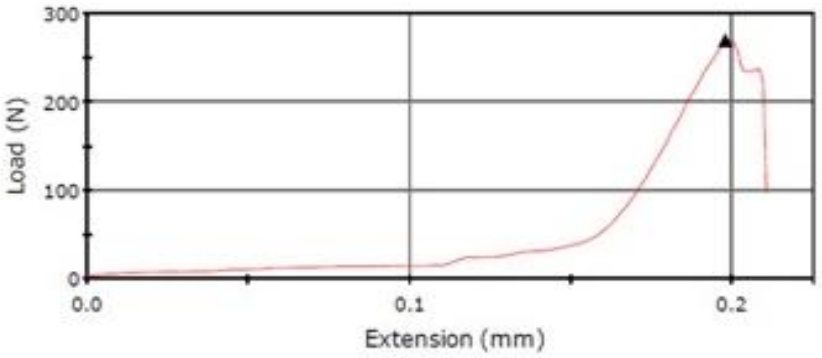


Fig 4.11: Tensile strength test of silver coated sinter layer (pressure assisted)

A force of 269N was required to detach the substrate from the end winding dummy. This shows a remarkable improvement on the mechanical strength of the silver sinter layer after coating the end winding surface with silver. The tensile strength and shear strength of the new sinter layer was 10.9 MPa and 6.6 MPa respectively – more than double the values recorded for the first sample.

4.2.2.2. Pressure-less sintering

From the results of the pressure sintered sample, the overall mechanical strength of the silver sinter bond improved by coating the mounting surface of the winding with silver. This reduced the degree of oxidation on the copper winding surface allowing the silver particles properly diffuse into both copper surfaces.

Although it is well documented to be worse off in both mechanical stability and thermal performance compared to pressure-assisted sintering [204], pressure-less sintering has its merits compared to pressure assisted sintering. The high pressure which the die and substrate is subjected under is the major disadvantage of pressure assisted sintering compared to the pressure-less option. Severe damage to both device and substrate due to high pressure is very common during the manufacturing process of pressure assisted sintering. Furthermore, pressure-less sintering offers a less complicated overall manufacturing process. A specialised rig is essential in pressure assisted silver sintering in order to apply the required pressure. This is both complicated and expensive due to the high sintering pressures (up to 30 MPa) required and the potential additional costs of damaged components during the sintering process.

Pressure-less silver sintering offers a cheaper, less complicated, silver sintering alternative. However, the major drawback is the overall mechanical strength and stability of the bond layer it produces compared to pressure assisted silver sintering. The absence of the high pressures required to restructure the silver particles (in pressure assisted sintering) creates a less compact silver sinter layer in pressure-less sintering. Additionally, the high pressures help in the removal of pores in the silver layer. This in turn increases the overall thermal conductivity and stability of the structure especially under high temperature and pressure conditions. Pressure-less silver sinter attachment layers suffer in this

regard, with an overall less mechanically stable and thermally efficient structure compared to pressure assisted sintering.

The pressure-less sintering copper winding sample was prepared in the same way the pressure assisted silver sintering sample was – polished, treated and PVD coated with silver. The silver paste used was Heraeus ASP 295 – 79P2 (D1). The silver paste was applied on the silver coated copper winding surface using a 100µm stencil. Fig 4.12 shows the temperature profile for the sintering process. In the initial drying stage of the process, the sample was placed in the oven for 30 minutes at 50℃ then another 30 minutes at 100℃. This process was to remove 'organics' from the silver paste. The temperature was then ramped up to 285℃ in increments of 20℃ per minute. In the final sintering step, the temperature was maintained at 285℃ for 1 hour. At this stage, the silver particles are restructured and diffuse into both copper winding and substrate surfaces.

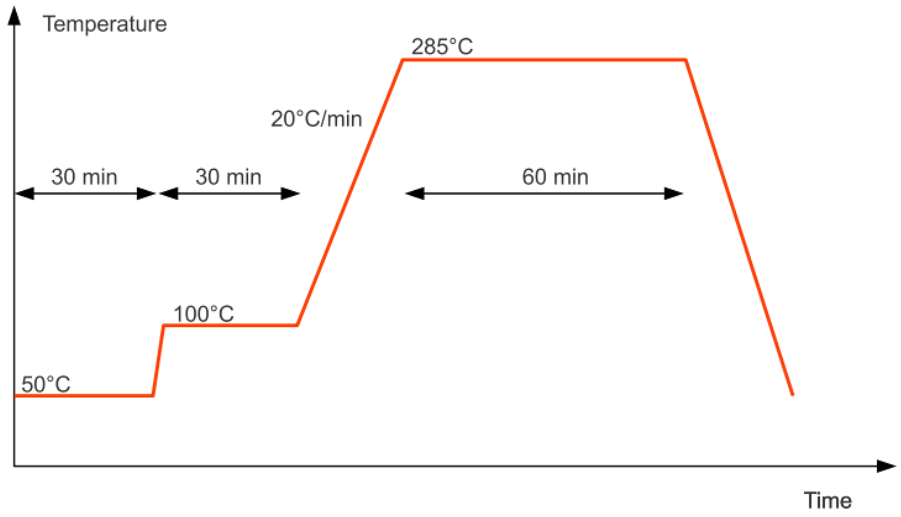


Fig 4.12: Temperature profile used for the pressure-less silver sintering process

The tensile strength of the sinter bond was examined using the procedure carried out with the pressure assisted sintering. Two steel rods were attached to the sample like in Fig 4.6 and pulled apart. Fig 4.13 shows the stress profile of the pressure-less sintered bond.

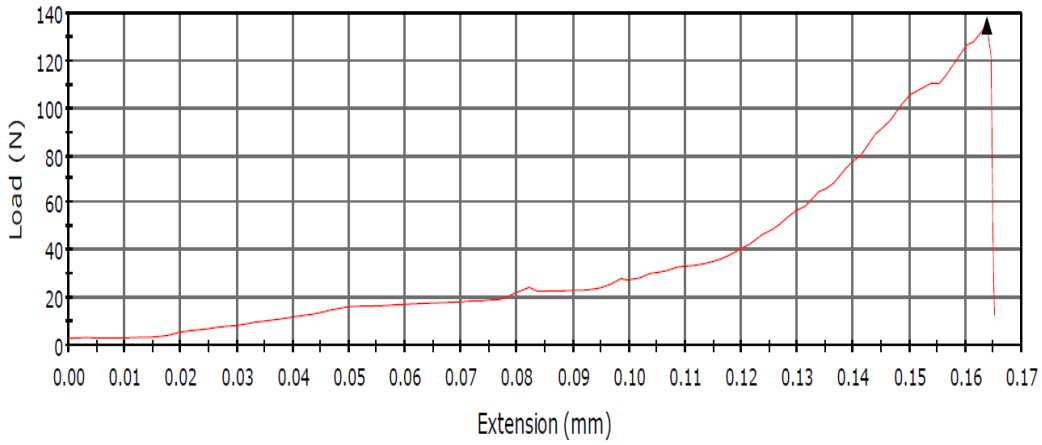


Fig 4.13: Tensile strength test of silver coated sinter layer (pressure-less)

The sample failed at 135N load. This equates to tensile and shear strengths of 5.5 MPa and 3.3 MPa respectively. Compared to the pressure assisted option, this shows a reduction in the mechanical strength of the structure by half.

4.2.2.3. Solder

Another attachment method investigated for attaching the power module to the end winding was soldering. Of all three attachment processes investigated, soldering presents the most established attachment method. Where high mechanical strength and electrical connectivity is required,

soldering presents the most popular choice in industry. Its low cost compared to the sintering alternative is also an added advantage.

The flux in the solder also helps to prevent oxidation on the copper end winding at high temperatures. It also helps remove impurities that can form on the metal surfaces to be soldered at high temperatures. This increases the overall strength of the solder bond. Furthermore, for the geometry being analysed, the 1 mm spacing between the turns presents the chance of short circuiting – especially when aligning the substrate copper tracks with the end winding profile. By utilising solder, this short circuit chance is mitigated due to the flux in the solder improving the wetting characteristic of the solder. This improves adhesion between metal surfaces in contact with the solder and the solder layer. In the eventuality of too much paste being applied, the solder sticks to the substrate metallisation and end winding.

Using the substrate and end winding profile adopted for the pressure assisted sintering process, the soldering process was implemented. The solder paste used was Loctite RM89– a lead-free, Tin-Silver alloy, high temperature solder. The choice of solder was due to its high melting point of 210°C which is essential for high temperature operation capability. The paste was applied on the end winding sample using a squeegee and a laser-cut 200 µm stencil. The sample was placed in the oven for 3 mins at 220°C.

Using the X-ray SEM machine, the solder joint was examined. Fig 4.14 shows the solder joint layer after SEM examination. Compared to the sinter layer, it can be observed that the solder layer contains a large amount of voids in the structure.

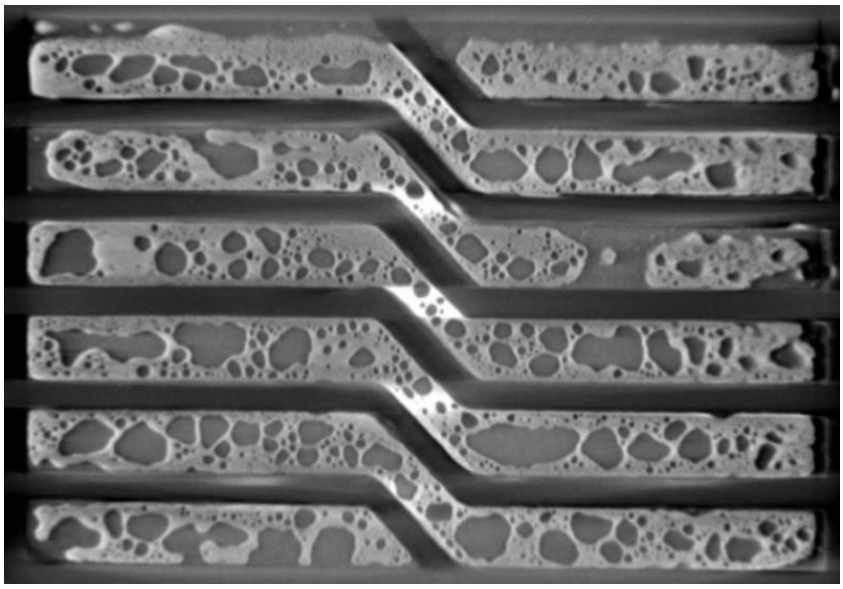


Fig 4.14: X-ray SEM of solder layer

The presence of these voids in the solder structure increases the temperature resistance of the layer. This is detrimental to an efficient heat transfer between substrate and coper windings (heat sink). Although the solder layer can be optimised to reduce the void size, the sinter layer will always possess a smoother layer with fewer voids/ no bond areas. This means the solder joint layer will be less efficient in heat transfer between substrate and motorette windings compared to the sinter layer.

The thermal conductivity of silver sinter (> 200 W/m^{2}K) compared to solder (60 W/m^{2}K) also points to silver being the superior attachment material – in terms of heat transfer. Although the sinter layer possess a lower heat transfer coefficient (about 200 W/m^{2}K) compared to pure silver, it is still significantly higher than solder. However, solder presents a more stable attachment joint due to its high mechanical stability for larger bonding areas compared to silver sinter.

A tensile pull test was performed on the soldered winding dummy and substrate to investigate its mechanical stability. The conditions for the pull test were similar to those under which the pressure assisted sinter pull test was performed. This was to ensure a more accurate comparison between both processes. From Fig 4.15, it can be observed that the solder exhibits a significantly stronger bond compared to both silver sintering options. The copper tracks on the substrate were completely detached from the ceramic. This shows, the substrate itself was damaged and the solder layer left uncompromised.

The results of the pull test for the solder layer is shown in Fig 4.16. It can be observed that the solder layer failed at 716N, producing a tensile strength of 29 MPa and shear strength of about 17 MPa. Compared to pressure assisted and pressure-less silver sintering, this shows solder has tensile and shear strengths two and half and five times more than pressure assisted silver sintering for large areas.

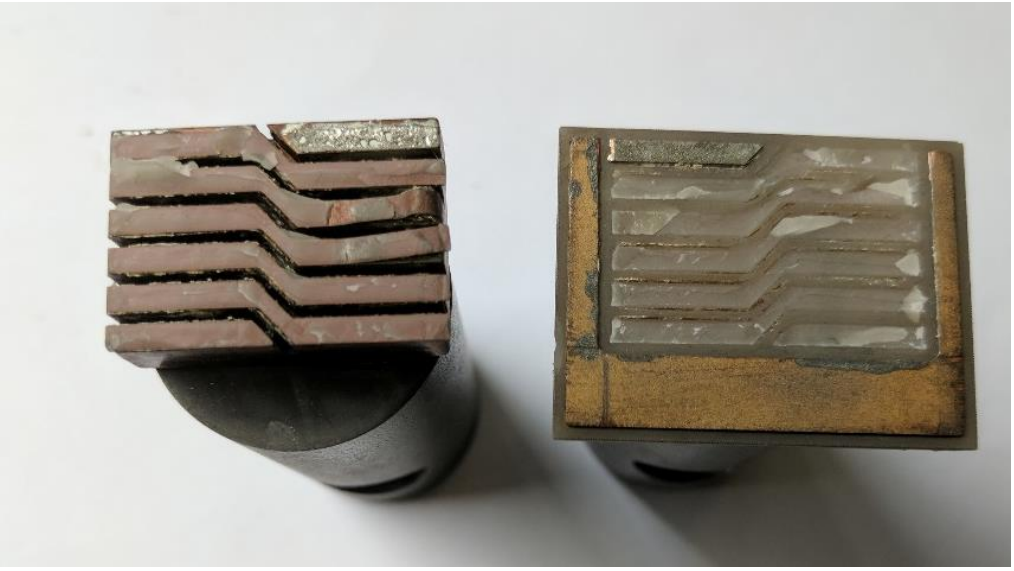


Fig 4.15: Detached substrate from end winding dummy after mechanical pull test

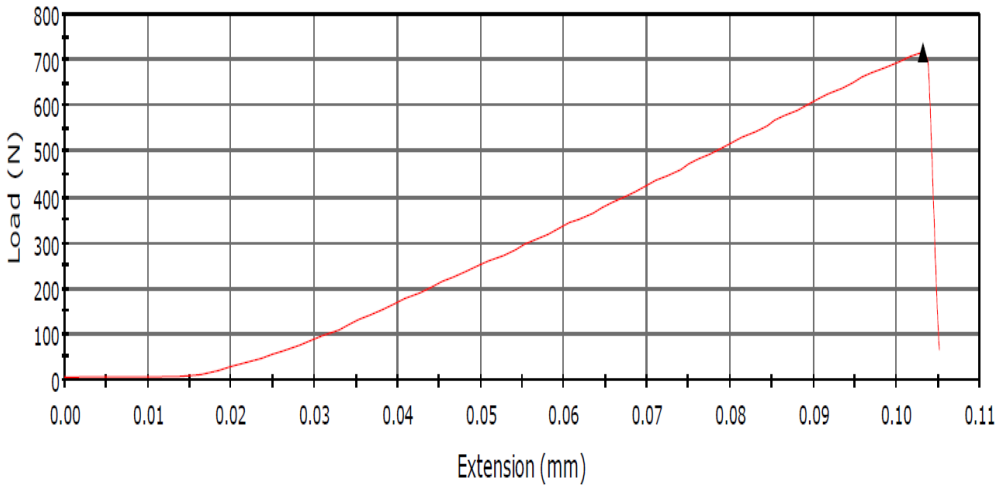


Fig 4.16: Tensile strength test of solder

The high mechanical strength of the solder joint layer ultimately leads to a more reliable end winding mount IMD compared to pressure-assisted sintering. During high vibration levels and thermal cycling, the joint layer

is subjected to high stress levels. Solder offers a more mechanically stable option under these conditions. Although, the thermal performance of the solder layer will be worse off compared to sinter, the realisation of the end winding mount IMD concept greatly hinges on a good attachment between the winding and substrate.

4.3. Conclusion

This chapter investigates more efficient and reliable methods of implementing the PE odule on end winding mouned IMD. From the first prototype, the major problem encountered was correctly mounting the delicate PE module on the motorette end winding. Pressure-assisted siler sintering proved too problematic initially and the uneven surface of the end windings also complicated the mounting process.

A bespoke motorette winding was manufactured from a single block of copper in order to provide a flat stable mounting surface for the PE module.

Three PE module to end winding attachment methods were also analysed to determine the best option for the end winding mounted IMD concept. Pressure-assisted silver sintering, Pressure-less silver sintering and Soldering were the options considered. Although each had their individual

merits and faults, the solder option was ultimately decided upon as the best option. Compared to both sintering options, the thermal conductivity of solder (high temperature) is considerably less. This suggests an inferior heat transfer from PE module to winding utilising solder as an attachment option. However, with its superior mechanical stability compared to both pressure assisted and pressure-less silver sinter, solder offers a more reliableattachment option for proff of the IMD concept. Table 4.1 compares the different attachment
options analysed.

Table 4.1: Comparison of the attachment methods analysed

	Ease of Implementation	**Thermal conductivity (W/m^2K)**	**Mechanical stability**	**Max. Operating temperature**
Pressure assisted sintering	Hard	> 200	Low	700
Pressure-less sintering	Easy	> 200	Very low	700
Solder	Easy	< 60	High	200

In future, silver sintering should be considered as an attachment option for the end winding mounted concept. However, being a relatively undeveloped process especially for large area attachment, it is too early to implement it as an attachment method. Even pressure-less sintering if properly controlled can provide a reliable attachment layer for this concept.

The next chapter presents a working end winding mount IMD prototype utilising the bespoke copper windings manufactured. Additionally, solder will be used for attaching the PE module on the winding. Although primarily this project investigates the thermal and mechanical feasibility of the proposed IMD concept, a functional power module will be designed and manufactured to be mounted on the motorette end winding. A laminated Back Iron will also be used instead of a solid core. This is to replicate a real machne Back Iron and also reduce core losses especially during switching.

CHAPTER 5

CFD Simulations for End Winding Mount IMD Prototype 2

5.1 Introduction

This chapter analyses the heat distribution in Prototype 2 (introduced in Chapter 2) using CFD analysis. The optimisation choices from the previous chapter are taken into consideration when designing the sample

geometry. The fluid dynamics and cooling effects of the fan on the windings are analysed.

The CFD analysis focuses on the heat transfer from the PE module to ambient via the fan cooled winding under varying losses conditions. It also investigates the effects of varying fan speed on temperature distribution in the sample.

The ease of analysing the effects of changes in material in the sample is one of the major advantages of utilising software simulations before experimental validation. In this chapter, the effects of implementing silver sintering as a substrate to end winding attachment material on heat transfer from the PE module to winding is also investigated. Although from Chapter 3 it was concluded that the complexity of adopting silver sintering for attachment renders it unfeasible, its thermal effects on the sample can be analysed using CFD. Also, forced convection cooling using water is simulated to investigate its effects on the temperature distribution in comparison to air.

5.2 CFD Simulations for End Winding Mount IMD Prototype 2

5.2.1 Geometry Design

The simulated geometry for Prototype 2 was designed to closely replicate the physical design of the sample to be manufactured. Dimensions of the copper winding (Figures 42 and 43), SiC MOSFET and AlN substrate (Figure 63) were modelled to match the experimental sample. However, some assumptions were made to some specific components due to the complexity of modelling these components. The assumptions made were –

- **Back Iron**: The shape and dimensions of the Back Iron closely match the physical sample. An insulation layer was also modelled around the teeth to closely replicate the experimental set up. However, the geometry was designed as a solid core instead of stacked 0.1mm steel laminations. This is because the Back Iron is not a critical path for heat dissipation in the system. Furthermore, the large computational time and complexity of modelling the laminations will produce very little improvement, if any, in the accuracy of the simulation results.
- **Solder Layer:** The SEM image of the solder layer in Figure 55 shows an uneven solder layer riddled with voids and no bond areas. These voids will invariably affect the thermal resistance and heat transfer between the PE module and windings. A uniform, void-free solder layer

was modelled instead. A more optimistic temperature distribution is expected in the simulation results compared to the experimental values.

- **Clearances in Back Iron Support:** The 3D printed support for the Back Iron was designed with 0.5mm clearances to ensure the sample slides easily through the opening. These clearances also exist for the support to housing. Although these small clearances will be sealed with silicone gel for the experimental tests, the gel introduces a new material which is absent in the CFD geometry.
- **Fan:** The cooling fan was modelled as a flat surface with streamlined air flow. To reduce the error in measuring the initial inlet air speed, the air speed was recorded at different points around the fan enclosure. Using a velocity probe, the air speed was measured at the fan inlet and 6cm from the inlet (when the flow is streamlined). Table 8 shows the air flow speed at different duty cycles. The inlet air speed set was the streamlined air speed measured.
- **Wire bonds:** The Aluminium wire bonds from the device to the substrate metallisation were not modelled because they play a very small role (if any) in heat transfer from the die to the substrate.

Table 5.1: Air speed at varying fan speed

Fan speed (%)	**Air Speed (ms^{-1})**	**Air Speed at 6 cm from fan (ms^{-1})**
10	2.9	4.6
20	3.5	6.9
30	5.8	8.0
40	6.0	9.2
50	6.9	10.2
60	7.2	11.0
70	8.0	12.3
80	9.1	13.5
90	10.0	14.3
100	11.0	14.6

Despite these slight variations in the CAD geometry compared to the final manufactured prototype, a high accuracy is expected in the simulation results. Figure 5.1 shows the CAD geometry of Prototype 2 without the mounting supports and Figure 5.2 shows the complete CFD geometry with Housing.

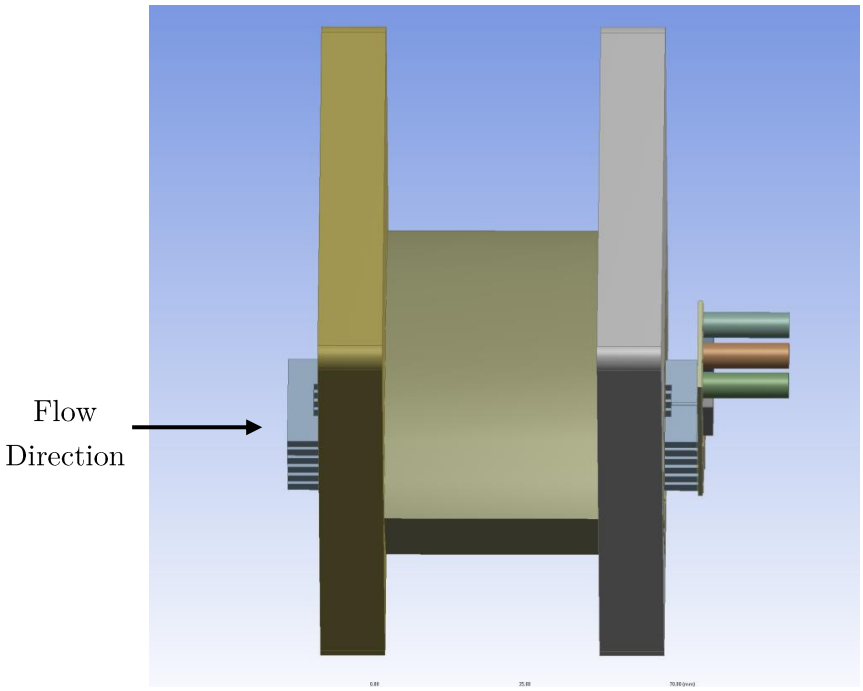


Fig 5.1: CFD geometry of Prototype 2 with mounting support

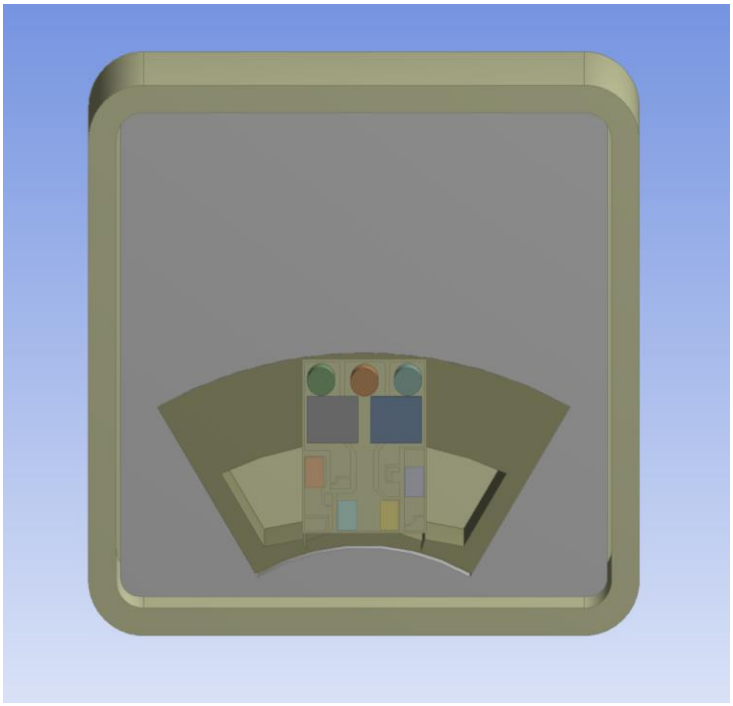


Fig 5.2: Complete CFD geometry

The ceramic capacitors and connecting steel rods were also modelled. This was to ensure the capacitor remains within the operating temperature conditions due to the heating effects of the SiC devices. Table 5.2 shows the prototype components modelled and the material properties assigned.

Table 5.2: Prototype components and materials

Component	**Material**
Back Iron	Steel
Winding	Copper
Substrate	AlN (1mm); 2 copper layers (0.2mm each)
Capacitors	Ceramic
Housing	Polylactic Acid (PLA)
Support	Polylactic Acid (PLA)
Bare Die	SiC
Insulation layer	Kapton tape
Solder Layer	Solder

Heat distribution in the model between the PE module and winding as well as heat transfer from the winding to coolant accounts for the primary heat transfer in this model. To ensure accurate meshing of the geometry, mesh manipulation at the interfaces between two bodies, proximities and curvatures was performed. A refined mesh was adopted between the interface layers between bodies and gaps between then windings using

contact sizing and inflation mesh manipulation techniques. The mesh for the air geometry was also refined, especially around faces in contact with the copper winding. A mesh growth rate of 1.23 was set to effectively capture narrow gaps between the winding turns. The total element count for the model was 11.8 million. Although, the element count suggests a fairly large model ultimately leading to a higher computational cost, the accuracy of the model is greatly improved.

With the mesh and pre-processing conditions set, the model was exported to Fluent to set boundary conditions and solve. The solver was steady state, Pressure-Based with an Absolute Velocity Formulation. The Absolute option is usually utilised for a non-rotating flow while the Relative option is suited for rotating flows. The k-epsilon fluid viscous model was set with an Enhanced Wall Function option. The cell zones were set with air being the only Fluid zone and the rest of the motorette components set as solids. Losses are inputted on the SiC devices body as Internal heat Generation (W/m^3) using the Source Terms option. Coupled wall thermal interface layers were created between individual motorotte components and their corresponding contact components. The copper winding to Back Iron interface region is set as a Winding-Air-Back Iron contact region to allow for poor contact between both components. The inlet was set as a Velocity Inlet with the airspeed and temperature set using the data from Table 5.1. The flow outlet was set as an Outflow. This option is chosen when the outlet pressure and flow velocity is unknown.

With the pre-processing and boundary conditions set, the first CFD test was to analyse the temperature changes in the geometry (especially the PE module) under varying fan speed conditions. This was to investigate how responsive the cooling system was to increased power losses. Furthermore, the flow direction is observed under different fan speed conditions to investigate if any changes occur.

5.2.2. CFD Analysis

Starting with the lowest fan speed to simulate the worst-case scenario, the losses inputted for the bare dies were distributed evenly across all four devices. Although in reality the individual device losses will vary slightly due to each device's on-state resistance, the losses are expected to be similar. An overall loss of 87W was set for the bare dies (representing 22W per device). Taking into account the solder layer was modelled without voids and a perfect contact with the winding and the PE module, the input losses were conservative to ensure the MOSFET maximum operating temperature was not exceeded during the experimental validation.

The inlet air temperature was set at 24°C - measured from the fan. Figure 5.3 shows the coolant velocity profile at 10% fan speed (lowest fan speed). As expected, there is some turbulence around the stator support. However, this has little effect on heat dissipation in the system. Streamlined airflow is primarily through the slot opening resulting in heat

dissipation from the heat sink (windings). Due to the restricted space for air flow, the air speed increases in the slot up to three times the inlet speed. The airflow also passes through the 1mm spacing between the turns. However, due to the high flow resistance the turn spacing presents, only a small percentage of air flows through this path. The coolant contact on the winding is primarily on the top and bottom turns and both sides of the winding. Fig 5.4 shows the Y-axis of the coolant velocity profile at 10% fan speed.

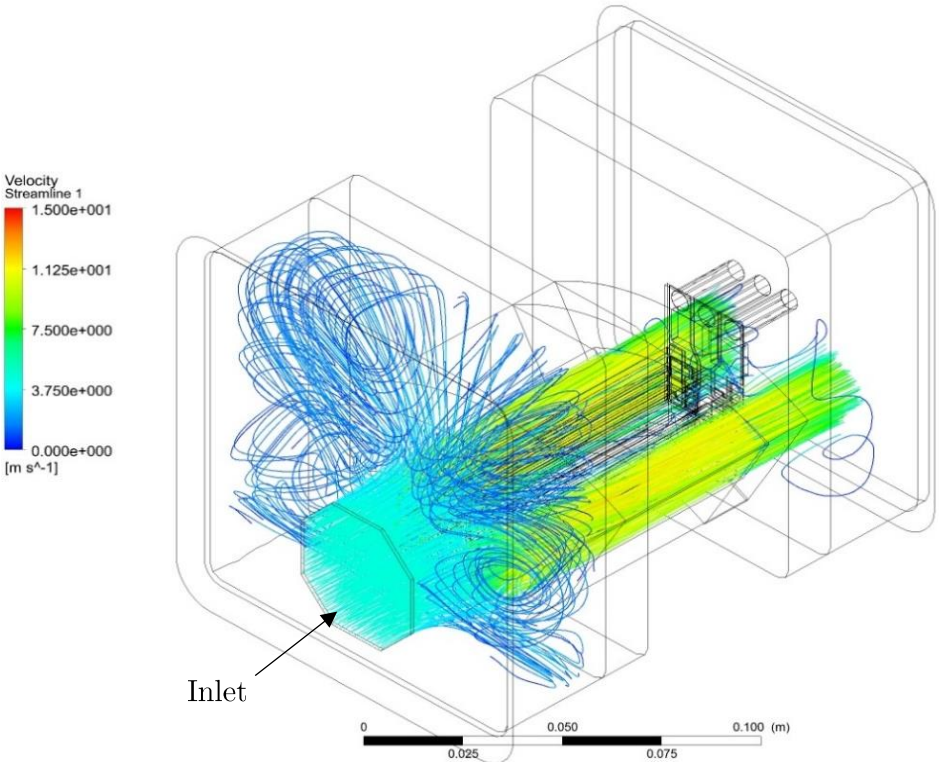


Fig 5.3: Velocity profile of coolant at 10% fan speed

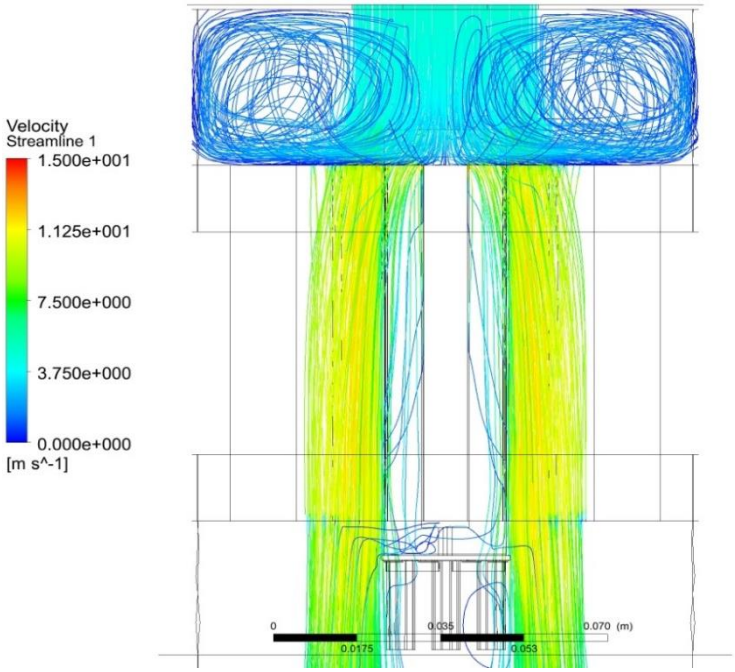


Fig 5.4: Y-Axis view of coolant velocity profile at 10% fan speed

Figure 5.5 and 5.6 show the temperature of the PE module and motorette components at 10% fan speed conditions. Q1 and Q2 have the maximum temperatures at 148℃ and Q3 and Q4 with slightly lower temperatures of 142℃ and 143℃ respectively. Q1 and Q2's higher temperatures are due to the effect of having two heat sources in close proximity. Despite this, the overall temperatures of all four bare dies are similar with a maximum difference of 4℃ between the dies. This result highlights the effect of the copper winding in heat dissipation from the PE module. Although the AlN substrate acts as a heat spreader in the module, it is evident that heat transfer is primarily from the devices to the copper winding. This is advantageous when only specific devices are switched on; the neighbouring OFF devices are not subjected to high temperatures due to

the heating effects of the ON devices. It also suggests that more devices could potentially be added to the PE module with minimal thermal coupling between the devices.

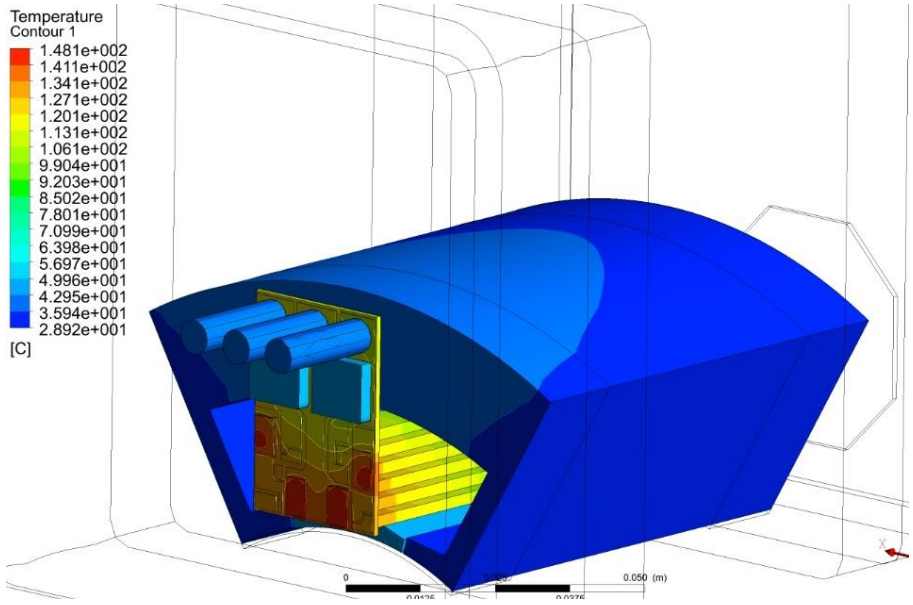


Fig 5.5: Temperature profile of Prototype 2 components at 10% fan speed

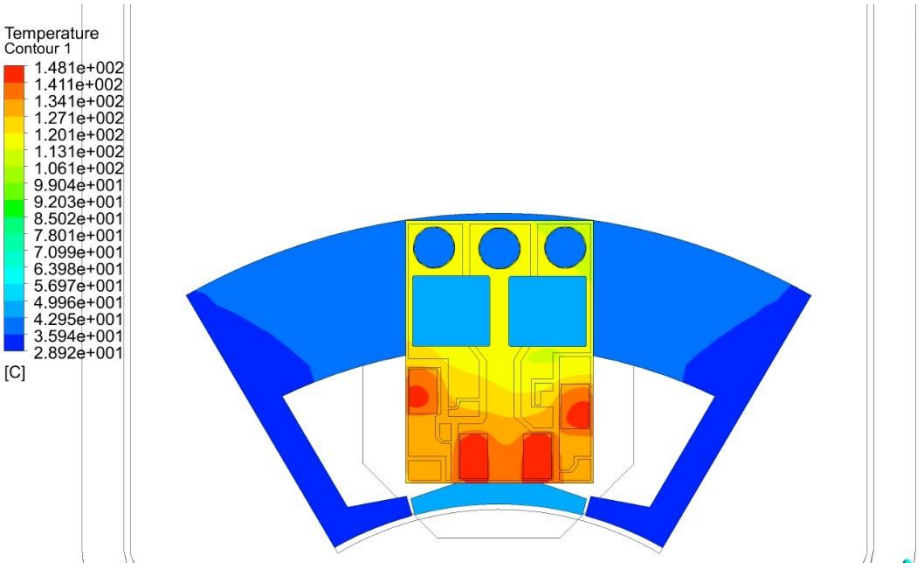


Fig 5.6: Z-axis view of Prototype 2's temperature profile at 10% fan speed

Figures 5.7 to 5.10 show the temperature and velocity profiles of the sample at 50% and 100% fan speed respectively. The coolant direction remains unchanged over different fan speed. However, its speed increases with increasing input fan speed. Furthermore the temperature distribution remains similar – with Q1 and Q2 producing the highest temperatures compared to Q3 and Q4. The Back Iron has the lowest temperature due to the insulation layer between the winding and teeth restricting heat transfer between both components.

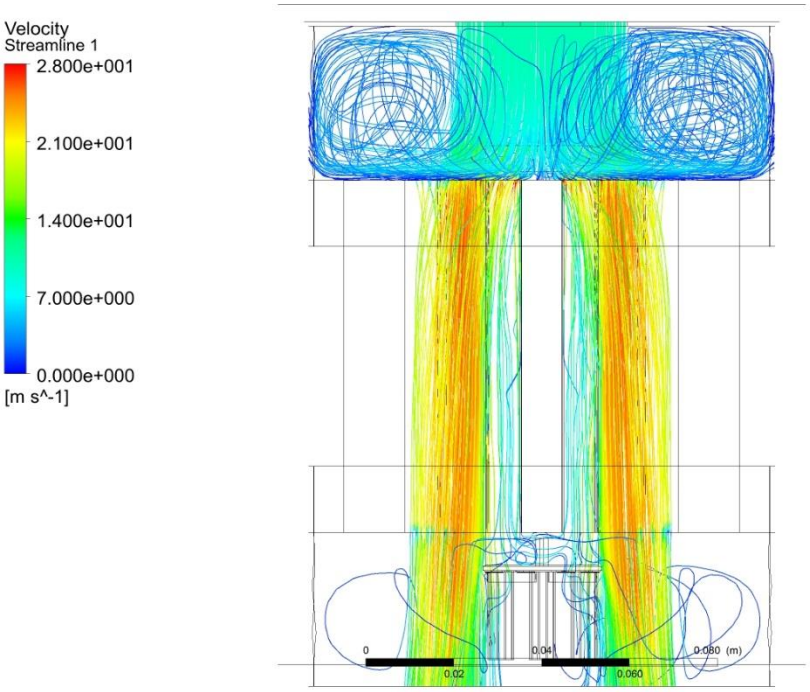


Fig 5.7: Velocity profile at 50% fan speed

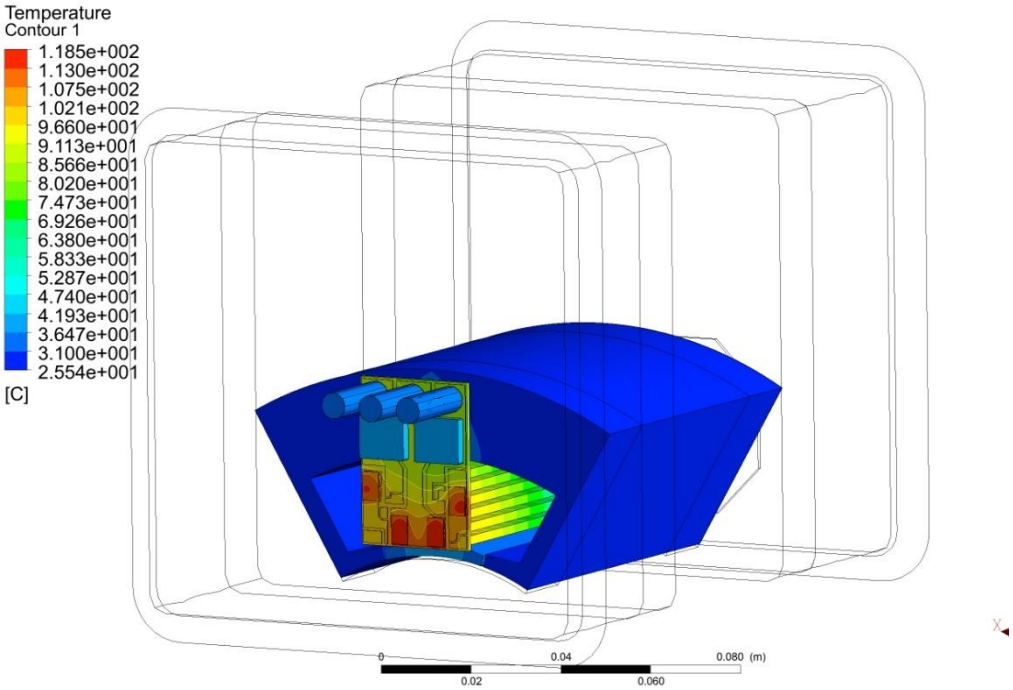


Fig 5.8: Temperature profile at 50% fan speed

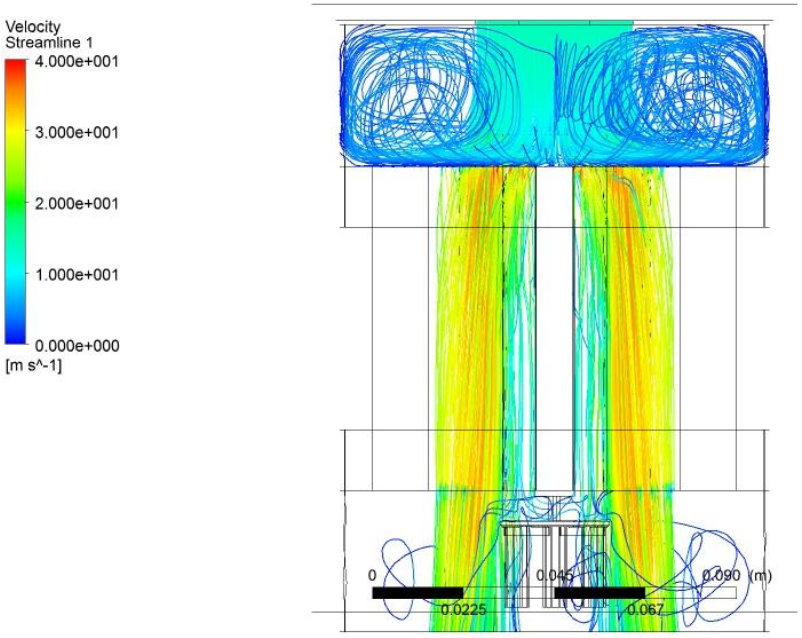


Fig 5.9: Velocity profile at 100% fan speed

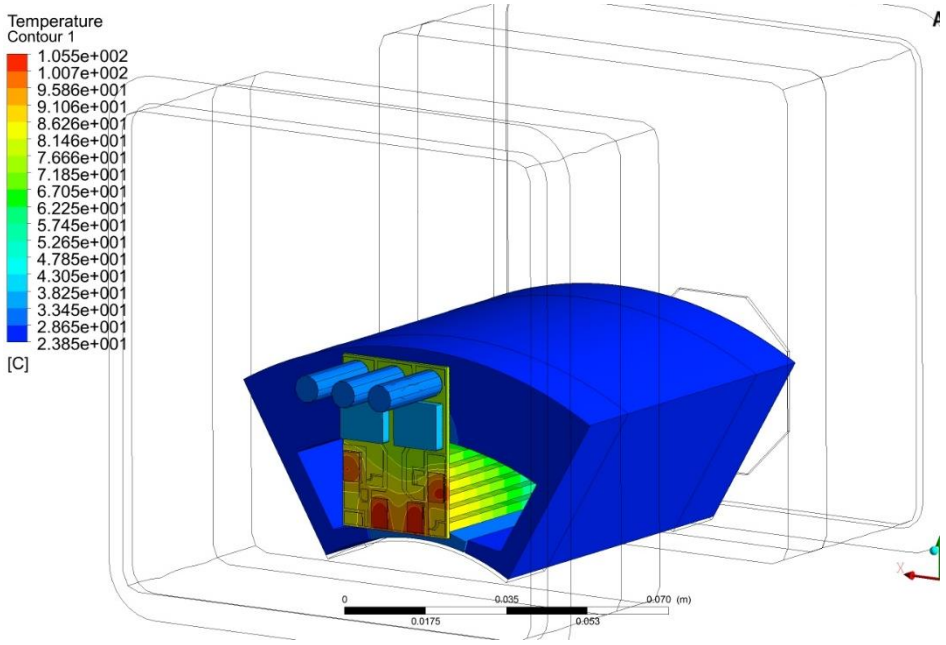


Fig 5.10: Temperature profile at 100% fan speed

The winding temperature exhibits a large thermal gradient with an average temperature difference of 67℃ between the hot and cold end windings for all fan speed. Large thermal gradients over fairly small areas are normal for forced air convection cooling, especially when the body is a heat source or in direct contact with one. Figure 5.11 to 5.13 show the winding temperature at 10%, 50% and 100% fan speed. The hottest part of the winding is located just behind the substrate – specifically behind devices Q1 and Q2. Furthermore, devices Q1 and Q2 are located on two copper turns respectively. However, Q3 and Q4 have three copper turns for heat dissipation respectively. With more copper area for heat

dissipation, Q3 and Q4 exhibit lower temperatures for similar input losses compared to Q1 and Q2.

However from the winding temperature images, the hottest location will be inaccessible for temperature probing during experimental validation. For comparison with the experimental results, specific accessible locations on the winding were therefore probed for the simulated hot and cold end winding temperatures. Figure 5.14 shows probe locations for hot and cold end winding temperatures and Back Iron.

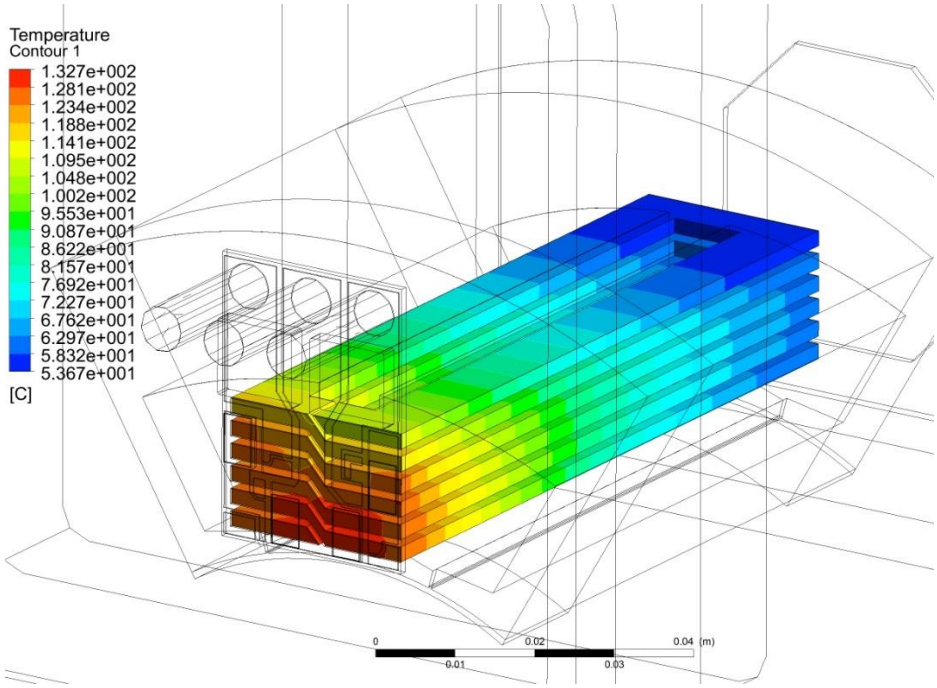


Fig 5.11: Winding temperature at 10% fan speed

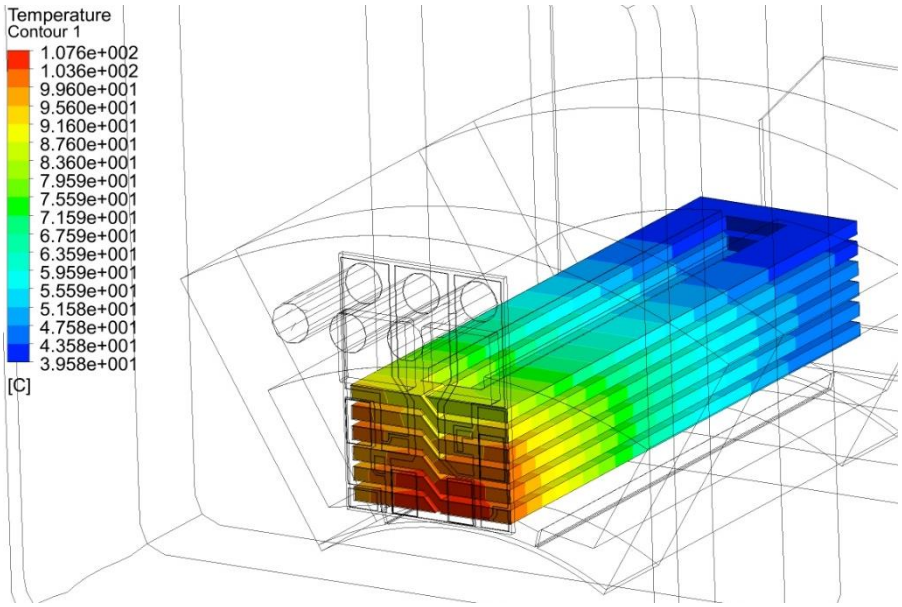


Fig 5.12: Winding temperature at 50% fan speed

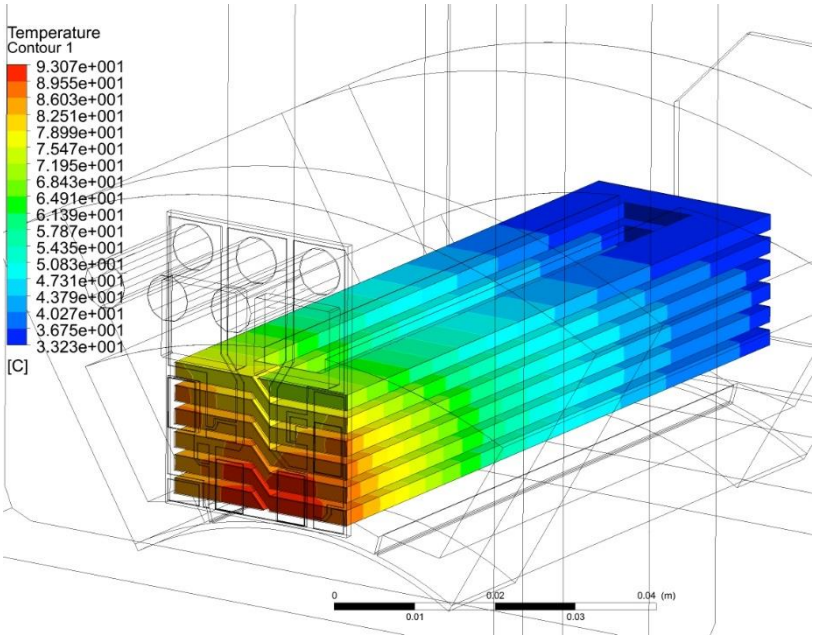


Fig 5.13: Winding temperature at 100% fan speed

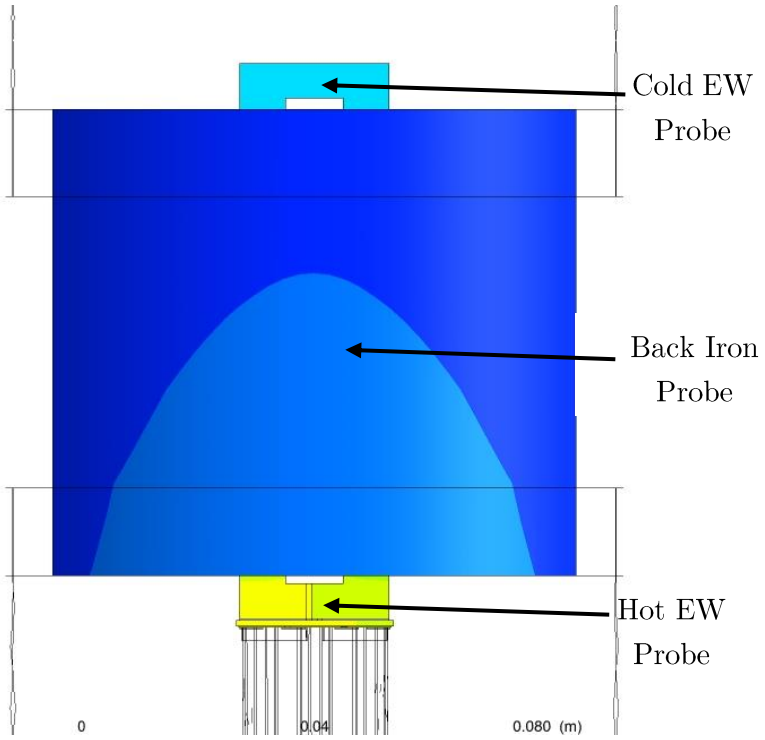


Fig 5.14: Probe locations on the Winding and Back Iron

The solder temperature at 10% fan speed was also measured to ensure its maximum operating temperature is not exceeded. Figure 5.15 shows the solder layer temperature at 10% fan speed. The maximum solder temperature stands at only 5°C higher than the winding temperature. This suggests good thermal coupling between the solder layer and copper winding. However, in reality, a higher temperature is expected for the solder layer due to the presence of voids in the structure and an uneven layer. The lowest temperature recorded for the solder layer is at a location with no contact with the power devices. This low temperature solder layer region is where the Vias are situated hence the absence of any device mounted on it. This further highlights the large temperature gradient

across very small areas with a temperature difference of almost 30℃ across 17mm.



Fig 5.15: Solder layer temperature at 10% fan speed

With silver exhibiting a higher thermal conductivity compared to solder, the effects of adopting a different attachment layer was simulated. To investigate the criticality of the solder layer, the material properties for that region was changed. The boundary conditions, geometry and other material properties were kept unchanged. However, the solder layer was changed from solder to silver sinter. Figure 5.16 shows the component temperature difference utilising silver and solder as attachment layers for different fan speeds. It shows the reduction in temperature using silver sinter as an attachment layer compared to solder.

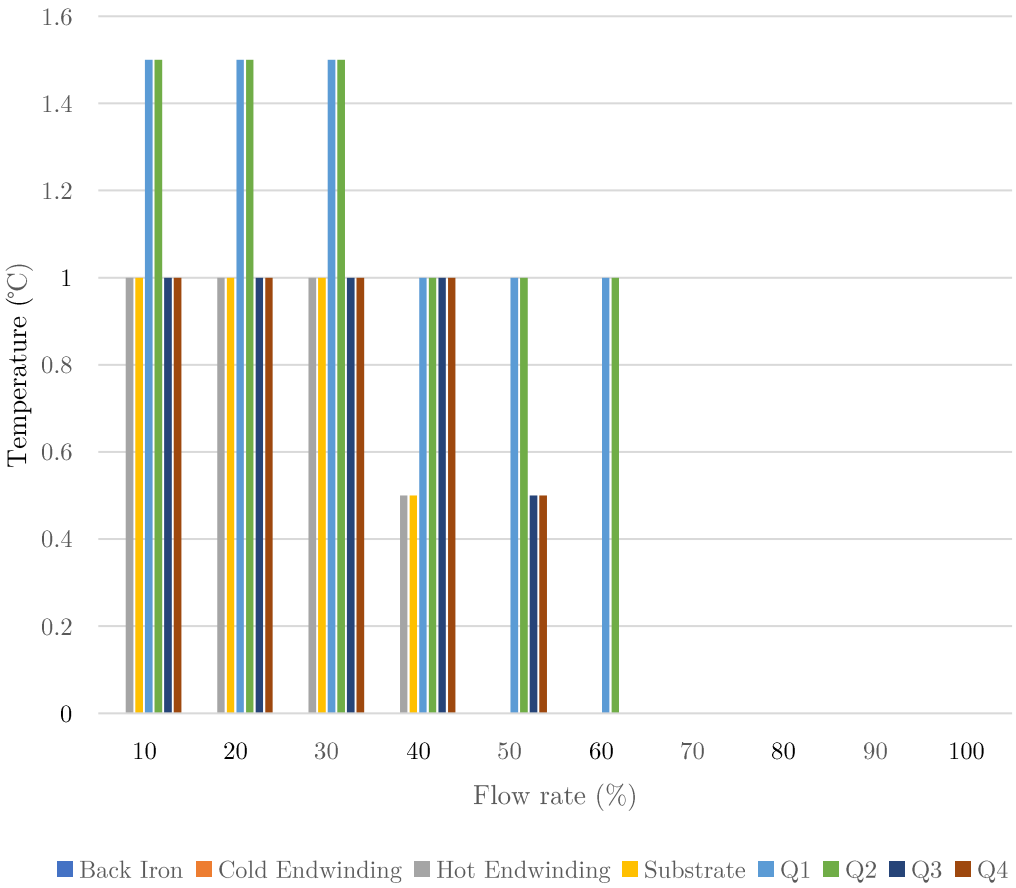


Fig 5.16: Component temperature difference utilising solder and silver sinter attachment layers at varying fan speeds

The graph shows a resolution of 0.5℃ with a maximum temperature of 1.5℃. The sinter layer reduces the temperatures of the individual components by a maximum of 1.5℃. For the Back Iron and Cold End winding, there is no change in temperatures with a silver sinter attachment layer. Q1 and Q2 (hottest components) show a reduction in temperature of 1.5℃ till 30% fan speed – after which the temperature reduces by only 0.5℃. Above 60% fan speed, no temperature changes

occur suggesting no thermal benefits in utilising silver sinter instead of solder.

The power devices are the only components with any temperature reduction at 50% duty cycle. This shows that although silver offers a higher thermal conductivity compared to solder, the size of the layer also dictates its heat dissipation. Furthermore, heat dissipation by convection is more prominent compared to conduction, therefore, the cooling fluid heavily dictates heat transfer from the PE module to windings. This result also shows the quality of the attachment layer is more important than its material choice. With no voids present in the solder layer, its performance is on par with silver. However, in reality, producing a void-free solder layer smooth enough to rival one produced by silver sinter is challenging.

Using the probe points as reference, Figure 5.17 shows the steady state temperature recorded for individual components of the sample at varying fan speed. The Back Iron, hot and cold end winding temperatures recorded are from the probe locations in Figure 5.17. Although this does not represent the maximum temperature for these components, it allows for comparison with the experimental results.

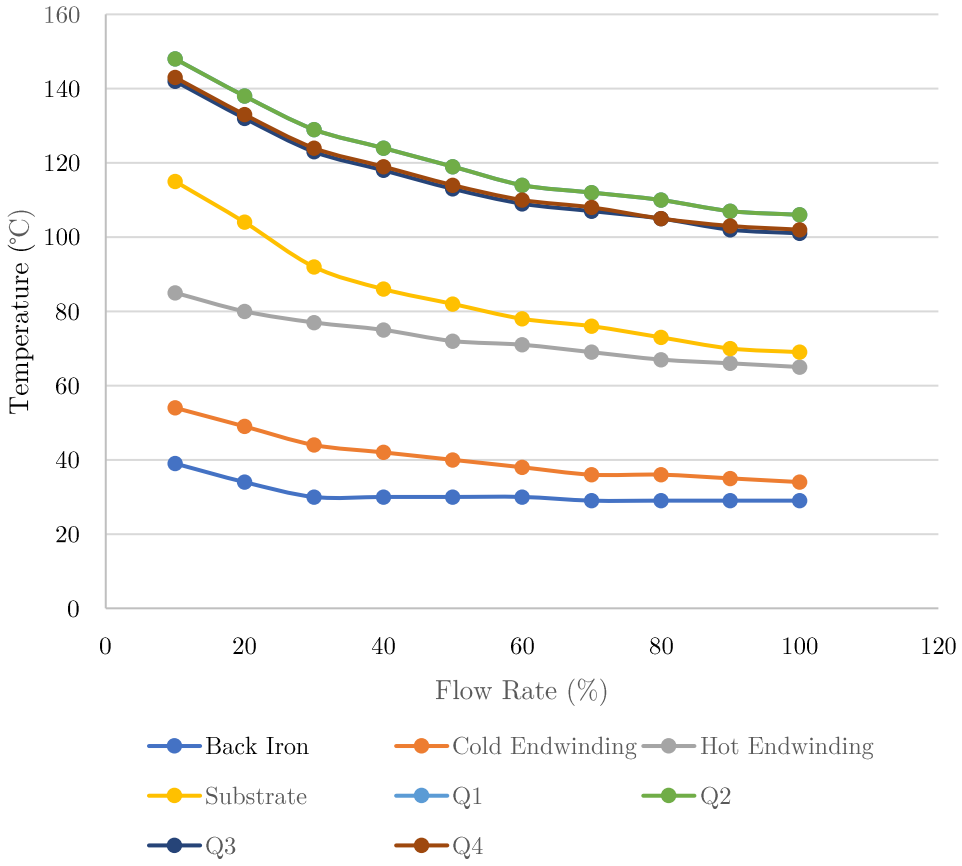


Fig 5.17: Steady state temperatures for IMD components at varying fan speed

From 50% fan speed, the temperature changes with increasing fan speed are minimal for the all components analysed. The maximum fall in steady state temperature between 50% and 100% flow rate is recorded at the Substrate, Q1 and Q2 and is 13°C representing a change of 14% in thermal resistance. The Back Iron temperature only decreases by 1°C and both end winding temperatures decrease by 7°C doubling the flow rate from 50% to 100%. This suggests heat dissipation in the system is restricted

by the coolant utilised. After 50% fan speed, further increase in the coolant speed leads to limited improvement in thermal performance.

To investigate the potential benefits of adopting a higher thermal conductivity coolant, air was replaced with Deionised water as a coolant. With a thermal conductivity of above 0.6 W/(m^{2}K) compared to air's 0.02 W/(m^{2}K), deionised water offers a better coolant for heat dissipation. However, it is usually more complicated to implement and its dedicated pump and piping system usually adds to the overall volume and cost of the motor drive. Furthermore, sealing and containment of the fluid is complicated and pressure drop concerns have to be managed efficiently. For the purposes of comparison, the prototype geometry is left unchanged with only the coolant changed. The simulation was performed at 10% fan speed to simulate the worst-case scenario. The flow speed for the deionised water was set at 4.6ms^{-1} – representing 10% fan speed of the forced air coolant. In reality, higher losses are expected for forced water cooling compared to forced air cooling at similar flow speeds. This is due to the increased pumping power required to reach those speeds for forced di-water cooling.

The velocity profile of the coolant is shown in Figure 5.18. The velocity profile compared to the air velocity profile has very little flow through the winding turns. This is due to thicker, more developed boundary layer as a result of the higher density and viscosity of water compared to air. However, the maximum flow speed is slightly lower compared to air. The die temperatures (maximum component temperatures) also drop from

148℃ to 36℃ - a 92% reduction in thermal resistance. This highlights the importance of the cooling system, more specifically, the coolant used, on the effectiveness of the end winding mounted IMD.

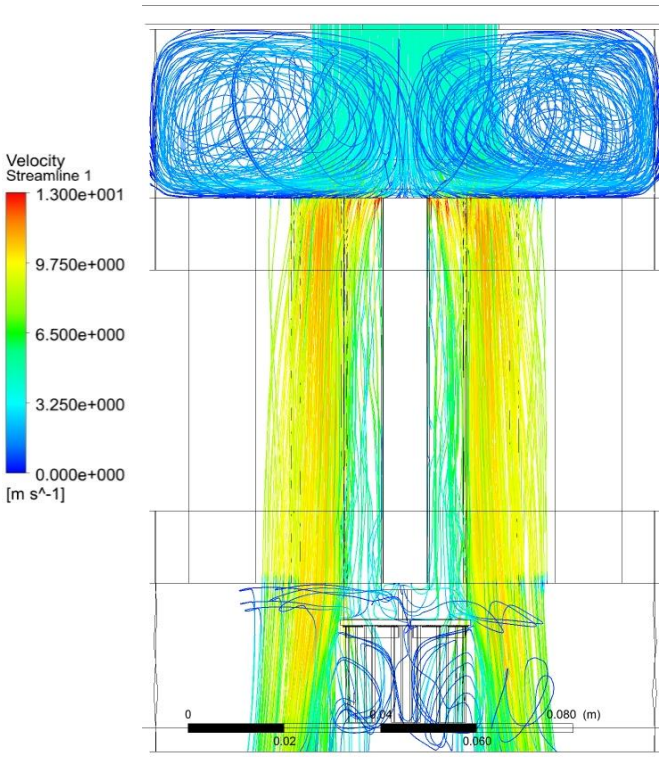


Fig 5.18: Water velocity profile at 10% flow rate

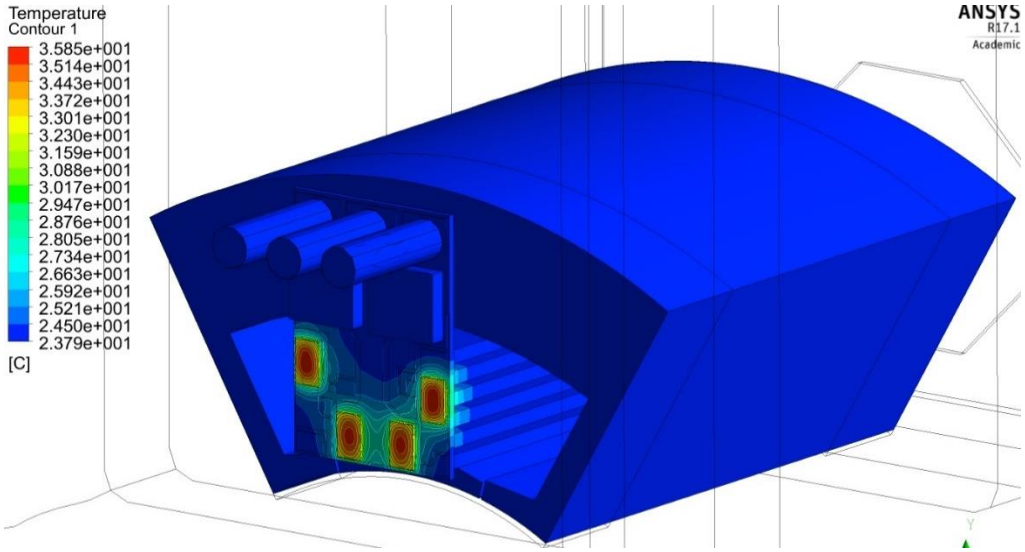


Fig 5.19: Temperature distribution of IMD using water coolant

5.3. Conclusion

This chapter detailed the CFD analysis of the final prototype designed incorporating optimisation recommendations from the previous chapter for the geometry design. The simulated geometry was designed to closely replicate the sample manufactured taking into account some assumptions on the CAD geometry design to reduce computational time. The Back Iron, Solder layer and fan geometries were simplified. The wire bonds on the substrate were not modelled as they are assumed to have little influence on temperature distribution in the system.

The overall system losses were assumed to be produced by the SiC devices, however, in reality, the Back Iron and copper windings also produce some losses. In the case of the prototype, these losses can be assumed to be negligible due to the low current density of the winding and the high quality of the motorette laminations.

Equal Losses were assumed for the individual MOSFETs and the temperature distribution across the IMD components was analysed for different flow rates. The maximum component temperature was measured at Q1 and Q2 due to the devices being close to each other. Q3 and Q4 recorded slightly lower temperatures compared to Q1 and Q2. Increasing the flow rate of the coolant greatly improved heat dissipation in the system up till 50% fan speed– after which changes in temperature were minimal. This highlights the limitation of air as a coolant choice – despite the increase in flow speed, improvements in heat dissipation was minimal. It also suggests the size of the substrate could be reduced reducing system volume and increasing power density. The fan size could also be reduced further increasing power density.

The solder layer as a critical thermal interface was analysed. Due to the absence of voids in the simulated structure, the solder layer plays a lesser role in heat transfer from the PE module to the winding. The heat transfer between the bare dies and ambient is governed more importantly by the forced convection cooling variables – coolant material, flow rate etc. Changing the PE module to winding attachment material from solder to silver sinter only produced minor improvements in heat dissipation.

However, changing the coolant from air to water produced substantial changes in the overall temperature of the IMD components.

The next chapter focuses on the experimental validation of the thermal tests performed. Furthermore, switching tests are also performed to analyse the bare dies' operation at high frequencies.

Chapter 6

Experimental Validation of Prototype 2

6.1. Introduction

This chapter presents an end winding mounted IMD taking into account the improvements made to Prototype 1. Furthermore, it demonstrates the validation of the CFD model from the previous chapter using experimental results. The individual prototype components are presented and how they differ from the earlier prototype outlined.

A power module is also designed and mounted on the end windings. Unlike the first prototype where the representative power module was a SiC device acting purely as a heat source, the new power module will act both as a heat source and drive current through the motorette windings. The experimental tests presented in this chapter will focus heavily on the thermal interaction between the power module and the motorette copper windings. The tests carried out in this chapter were –

- Thermal test – to investigate the heat transfer from the heat source (PE module) to heat sink (copper winding) and ambient.
- Switching test – to investigate the MOSFETs behaviour under switching conditions. Also, it helps investigate the thermal behaviour of the PE module and motorette components when the devices are unevenly thermally stressed.

6.2. Prototype 2 Components

6.2.1. Motorette Back Iron

A high silicon steel sheet (JNHF 600) was used with lamination thickness of 0.1 mm. The motorette stack length was 80 mm. This high frequency grade lamination was used in order to carry out tests at high frequency (up to 100 kHz) and reduce the Iron losses at those frequencies. The

individual laminations were stacked together using Pedigree 12-0-12 High Temperature Electrical Insulating Varnish with an operating temperature up to 220°C. The inside of the back iron was lined with Kapton tape for electrical insulation from the copper winding. The tooth was also covered with Kapton tape for the same reason. Figure 6.1 shows the stacked motorette lamination and corresponding tooth.

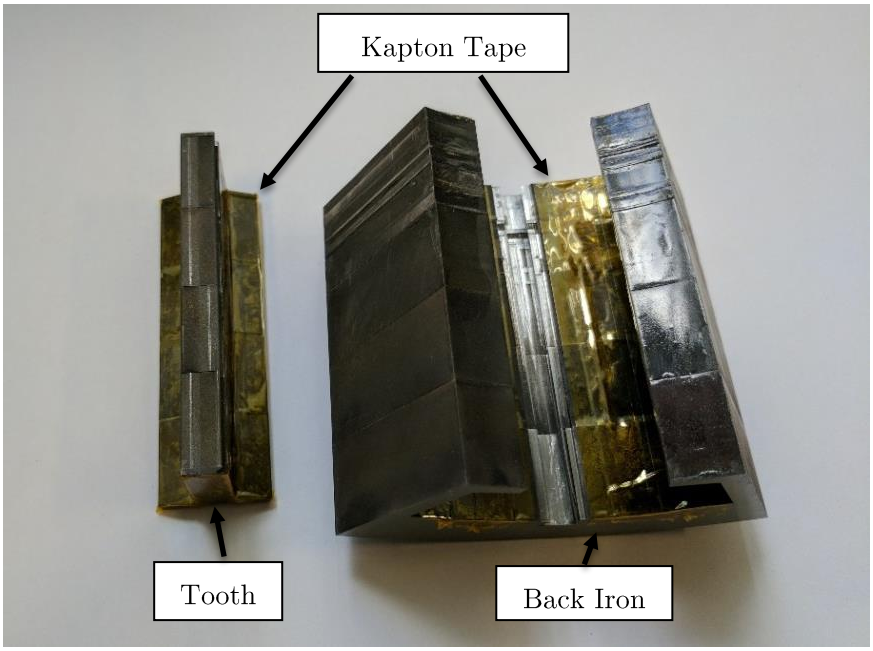


Fig 6.1: Kapton taped Back Iron and Tooth laminations

6.2.2. Copper Winding

To ensure a flat mounting surface for the PE module, the motorotte winding was cut from a single block of copper. The winding had spacings of 1 mm between turns. Individual turns were cut with a thickness of 2 mm. The length of the winding was 95.5 mm with an end winding length of 6 mm.

Tolerances of 1 mm and 0.5 mm were added to the spacing between the winding and tooth and the individual winding turns respectively. After cutting the winding, due to the elasticity of copper and residual stresses after machining, the winding behaves like a spring. There is a chance of potential short circuit since the winding is elastic and the individual turns are not mechanically secured. This is also compounded by the small 1 mm spacing between the turns. To rectify this potential problem, winding spacers were 3D printed to ensure the 1 mm spacing between turns remain uncompromised. Figure 6.2 shows the motorette copper winding with 1 mm spacing between the turns.

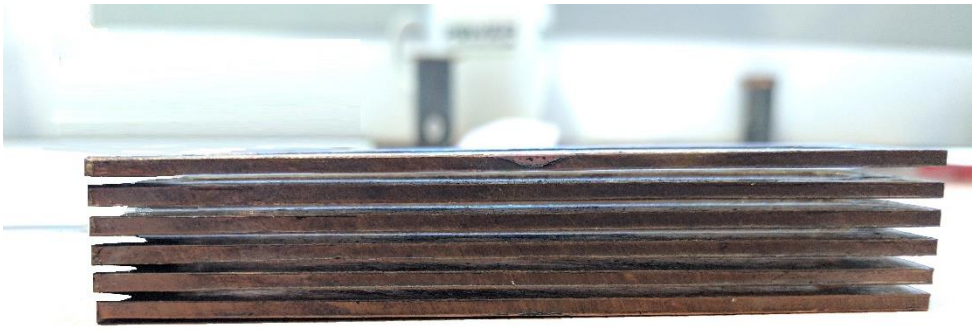


Fig 6.2: Side view of motorette winding with 1 mm spacing between turns

The resistance of the winding was also measured along with its inductance at varying frequencies. The bespoke copper wire measured a resistance of 5mΩ. Table 6.1 shows the measured inductance of the winding at different frequencies.

Table 6.1: Measured winding inductance in air and laminated core

Frequency (kHz)	**Inductance of wire in air (µH)**	**Inductance of wire in motorette core (µH)**
1	1.59	32.8
5	1.45	32.3
10	1.40	32
15	1.39	31.8
20	1.37	31.7
30	1.35	31.3
40	1.35	31.3
50	1.34	31.2
100	1.32	30.6

6.2.3. PE Module

The PE module attached to the copper winding was designed to be compact enough to sit on the copper end winding without interfering with or obstructing potential neighbouring power modules. SiC Bare die MOSFETs were sintered on the DBC substrate to represent an H-bridge circuit. Figure 6.3 represents a schematic of the device arrangement in the circuit. Ceramic capacitors were also mounted on the DBC substrate to provide some local DC decoupling capacitance and reduce the ripple voltage and overshoot at switching frequencies.

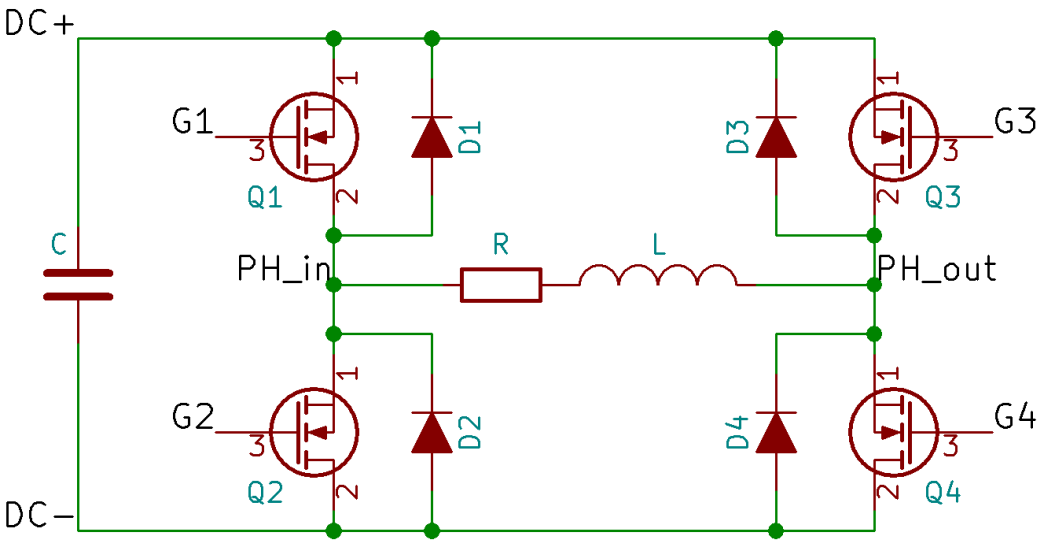


Fig 6.3: Schematic of the H-Bridge circuit

Compared to the representative PE module presented in Chapter 3 for Prototype 1, the new Prototype 2 module consisted of –

- An Aluminium Nitride (AlN) DBC substrate with filled vias
- Four SiC MOSFETs
- Two ceramic capacitors (68nF each)
- Three steel connectors

6.2.4. DBC Substrate

The AlN – based substrate was supplied by REMTEC. It consists of a Direct Bonded Copper (DBC) substrate with an AlN ceramic sandwiched between two copper layers. The thickness of the copper layers was 0.2mm

each and the AlN was 1mm thick. The AlN ceramic was selected for its high thermal performance – above 150 W/m^2K. Also, its CTE is well matched to SiC, reducing thermally induced stress during operation.

The overall dimension of the DBC substrate was 37.77 x 27 x 1.4 mm^3. The copper layer was finished with 4.064µm Electroless nickel and 0.152µm of immersion copper. The gold finish is especially desirable for good wire bond adhesion and die silver sintering. Figure 6.4 shows the top and bottom sides of the substrate. For electrical connection between the top and bottom copper tracks of the substrate, vias were laser drilled in the substrate and filled with copper to create an electrical connection. The end winding mount IMD concept relies on the power devices on the substrate directly driving the copper windings hence the presence of the filled vias. The four vias shown in Figure 6.4 are 0.51 mm diameter, each with a 0.76 mm clearance between individual vias in a pair.

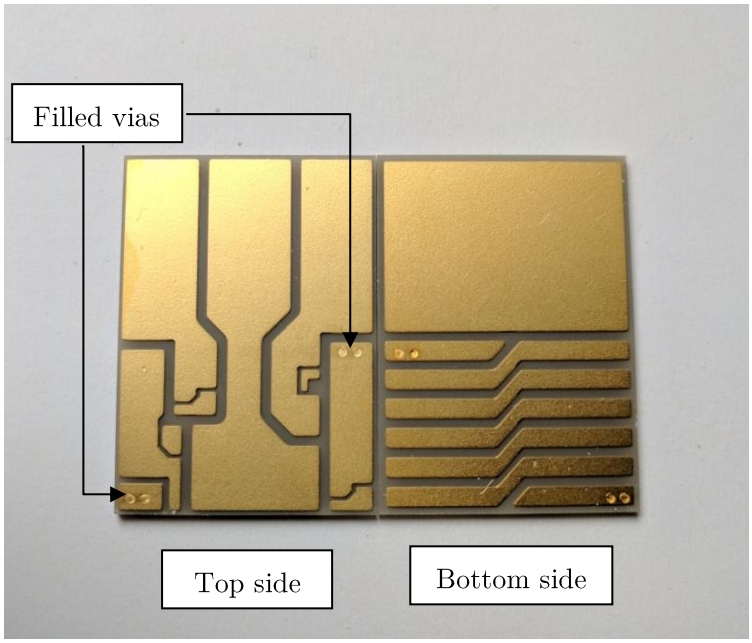


Fig 6.4: Top and bottom side of AlN substrate with vias

6.2.5. SiC MOSFET

The power devices used (shown in Figure 6.5) were CREE CPM2-1200-0025B Silicon Carbide Power MOSFET. The devices were rated at 1200V, 98A (71A at 100°C) with dimensions of 6.44 x 4.04 x 0.2 mm. The gate pad dimensions were 0.5 x 0.8 mm with the drain located at the bottom of the die and the source pad on the top. The source and gate pad metallisation was Aluminium, with a thickness of 4 µm. The drain metallisation was finished with Nickel and Silver with a total thickness of 8 µm. This enabled it suitable for soldering and silver sintering on the gold finished copper layer of the substrate.

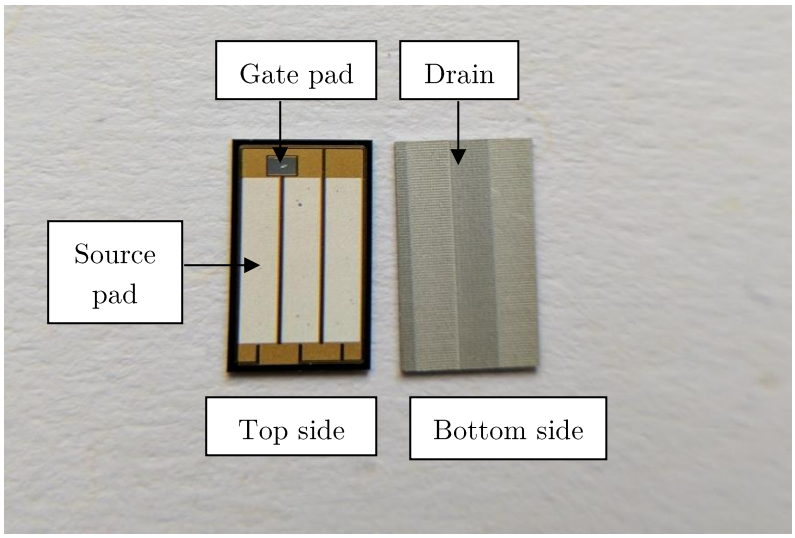


Fig 6.5: Top and bottom side of SiC MOSFET

6.2.6. Motorette Assembly Process

The SiC MOSFETs were bonded on the substrate using a Datacon 2200 Evo Die Bonder. It allows the dies to be picked and placed accurately on any position on the substrate using temperature and pressure to form the bond. The SiC MOSFETs were first dipped on a dried silver film at 130℃ in order to transfer the silver on the backside of the device. They are then placed on their corresponding positions on the DBC substrate. Each MOSFET was sintered at 270℃ using 10MPa for 5 minutes. Figure 6.6 shows the bare die sintered on the AlN substrate. Compared to soldering, sintering offers superior heat transfer between the power device and substrate. Also, for small surface areas, the reliability and strength of the

sinter bond is dependable – with shear strength values up to 70 MPa [204].

With the devices sintered on the substrate, the next step was attaching wire bonds for electrical connection. Due to the small size of the gate pad, the size of the wire bond used was 375 µm. Aluminium wire wedge bonds were attached by ultrasonic energy and vibration using an F&S Delvotec 5650 Semi-Automatic Heavy Wire Wedge Bonder. The wire bond can be seen in Figure 6.7.

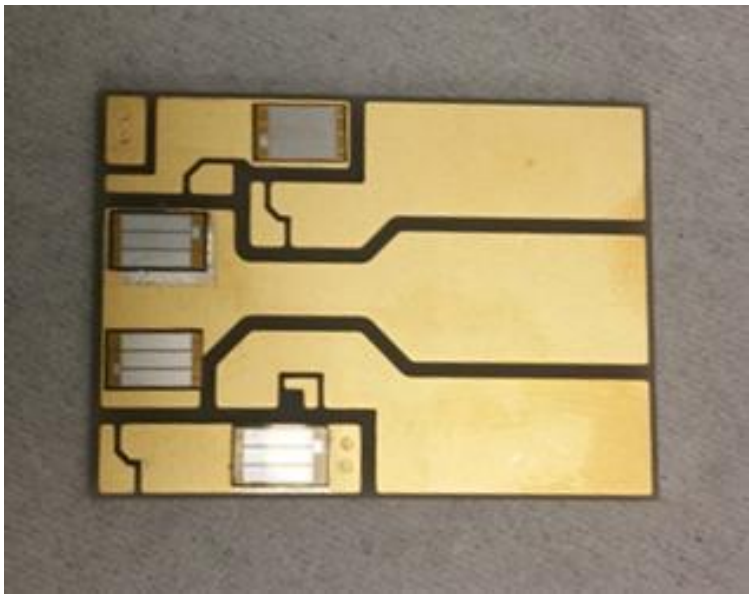


Fig 6.6: Sintered MOSFETs on the top side of the AlN substrate

The next manufacturing step was the attachment of the substrate on the end winding of the copper windings. Using the 100 µm stainless steel stencil, the solder paste was applied on the end winding. The stencil used had an offset of 0.2 mm around the edges to avoid the solder paste seeping

into the 1 mm spacing between the turns. The solder used was Multicore Loctite RM89 – a lead free, Tin-Silver, high temperature solder with a maximum operating temperature up to 200℃. Steel plates of 1 mm were cut and placed between the winding turns to ensure the spacing remains consistent – especially during the soldering process at high temperature. The sample was placed in the oven for 3 minutes at 210℃. Figure 6.7 shows the substrate soldered on the copper windings.



Fig 6.7: AlN substrate soldered on copper windings

The high frequency decoupling capacitors and steel connectors were manually soldered on the top side of the substrate. The capacitors used were Kemet 68nF Multilayer Ceramic Capacitors (MLCC) (P/N C4540H683JDGACT05). The maximum operating temperature was

200°C – robust enough to handle high temperature operation. An annotated diagram of the PE module attached to the winding is shown in Figure 6.8. The steel connectors used were soldered on the substrate by preheating the substrate and using a wide tip soldering iron.

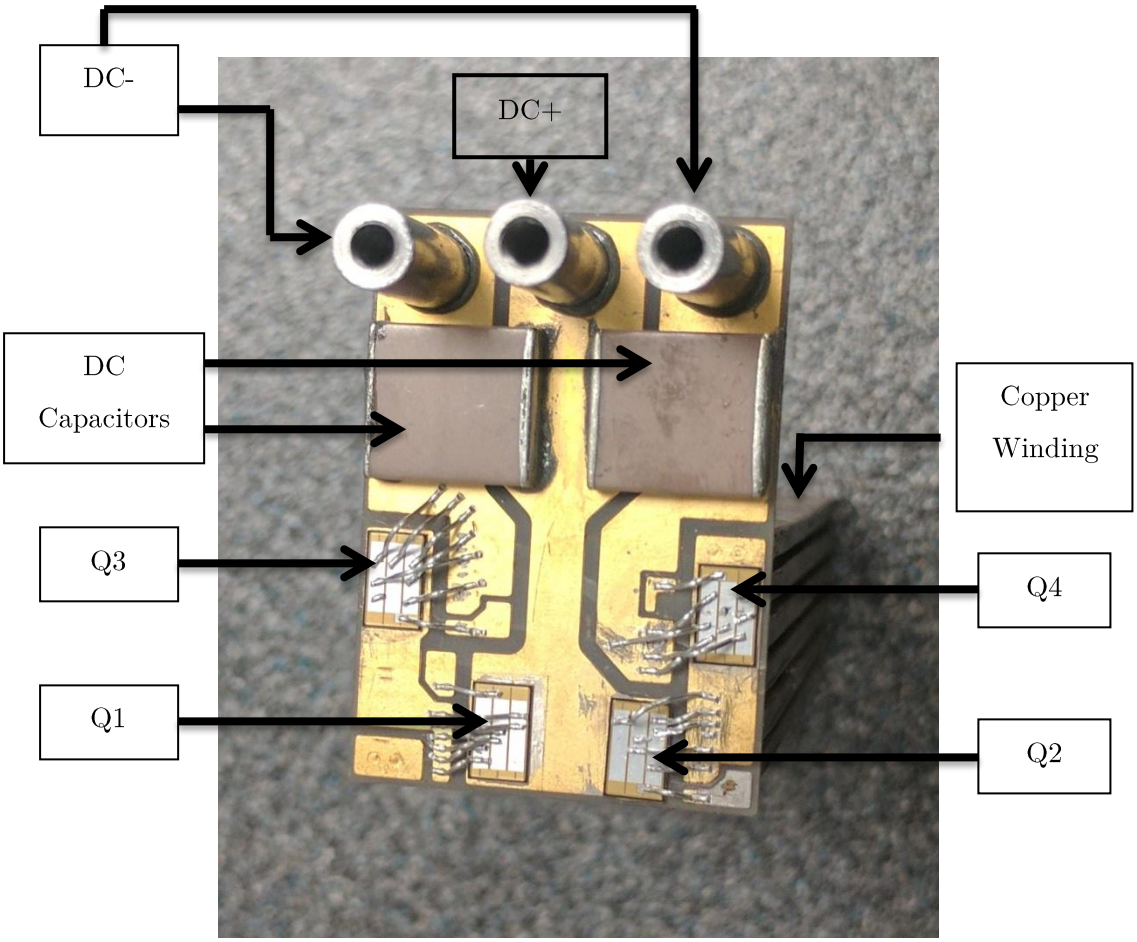


Fig 6.8: Assembled PE Module mounted on copper winding

The Back Iron, copper winding and end winding mounted substrate assembly is shown in Figure 6.9. The motorette tooth was inserted into the copper winding spacing with the PE module attached.

The 3D spacers were fixed on the opposite end of the copper winding. This was to ensure the PLA spacers are in direct contact with the fan. With PLA known to get soft and melt around 60°C, positioning the spacers as close to the fan as possible will ensure they remain under 60°C.

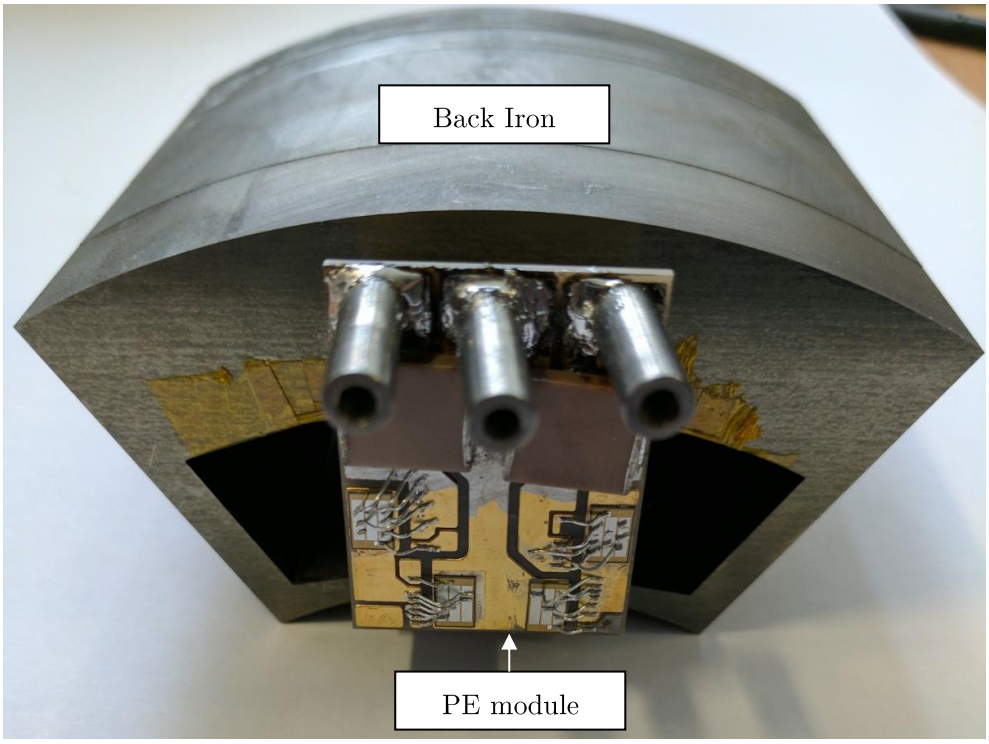


Fig 6.9: Assembled PE Module and winding in Motorette Back Iron

6.2.7. Motorette Housing

The motorette housing was designed to support and accommodate the sample as well as the cooling fan. The cooling fan used was a counter rotating San Ace 40 9CRE0412P5J03 axial fan with a flow rate of approximately 32 cubic feet per minute (CFM). The fan was chosen for

its relatively small size, high flow rate, PWM speed control and a small fan dead spot. The fan also allows for a streamlined flow with high speed from 6cm from the fan blades. This was particularly important in ensuring a streamlined air flow, similar to a realistic fan cooled machine. Furthermore, the streamlined air flow is achieved without the need for integrating an air channel to direct the airflow.

The motorette housing was 3D printed using PLA material. The dimensions of the housing were 120 x 120 x 150 mm with a layer thickness of 6mm for extra stability. The housing also contained a fan stand designed to sit directly in front of the end winding. Figure 6.10 shows the motorette housing with the fan attached.

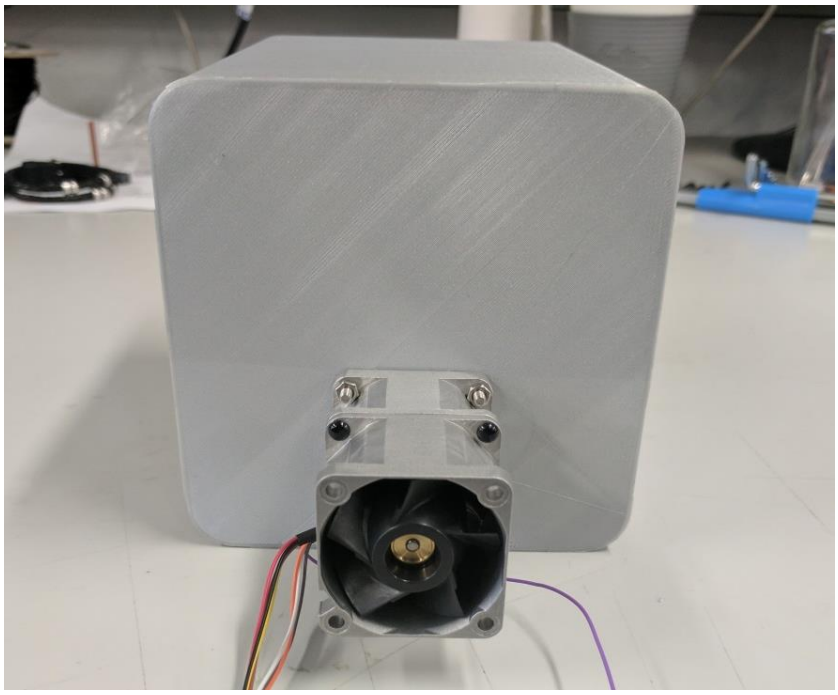


Fig 6.10: 3D printed motorette housing with fan attached on the back side

Support platforms were also 3D printed for the motorette Back Iron. This was to ensure the copper windings were aligned with the fan. The supports were 15mm thick each – rigid enough to support the weight of the sample. Clearances of 0.5mm were also incorporated in the design to allow the motorette to slide easily through the support opening. The PLA support was also used in isolating the Back Iron from the air flow. It ensured the air only flowed through the slot opening. Four 6cm M4 screws were attached to one of the supports to ensure a fixed distance from the fan. The 0.5 mm clearances were sealed with silicone gel after inserting the motorette in the support opening. Fig 6.11 shows the motorette mounted and sealed in the 3D support with the screws attached for spacing.

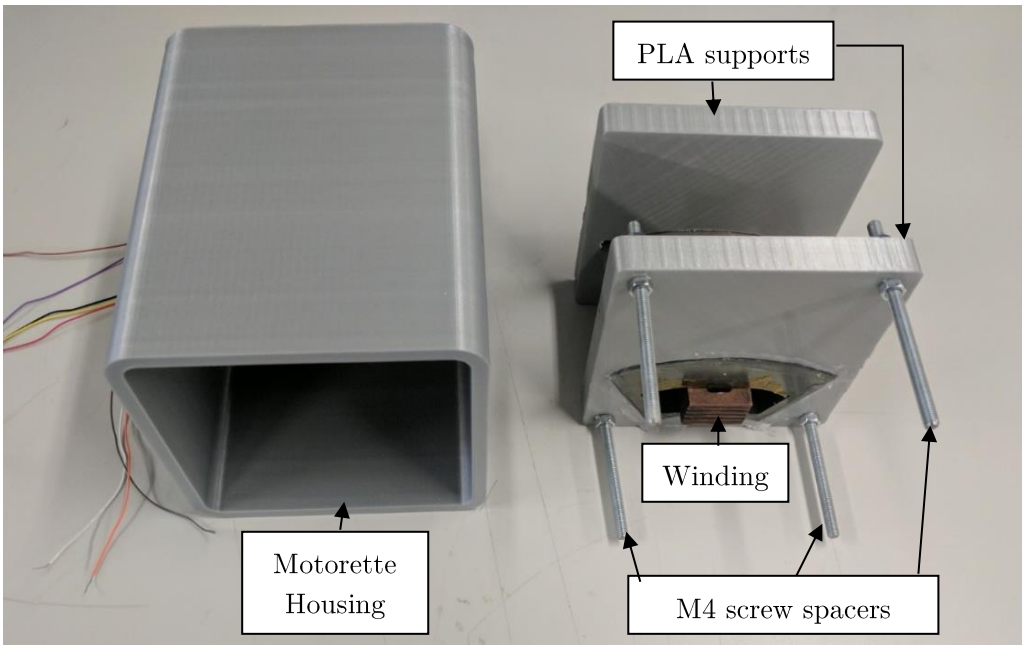


Fig 6.11: Motorette housing and PLA support

6.2.8. Current Sensing

The last step was to integrate a current sensor in the circuit. A copper wire loop was soldered on the substrate between the two legs of the H-Bridge as shown in Figure 6.12. This was to understand the current distribution between the devices. Gate connections were also soldered on the substrate. The connectors used were the Samtec SMD connector header FTMH-102-03-L-DV.

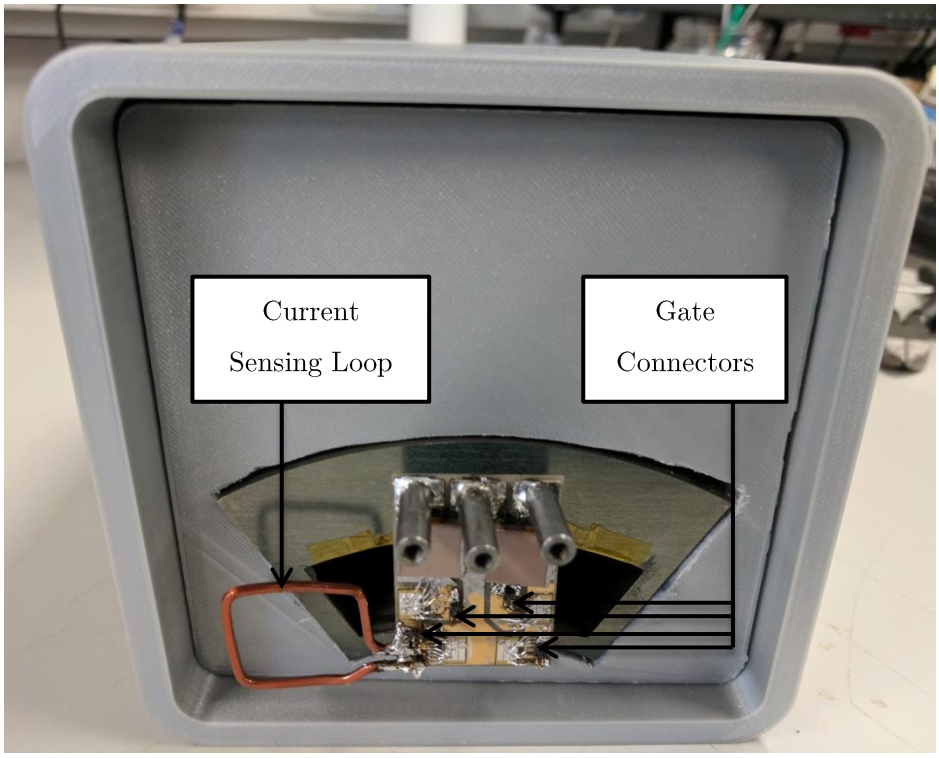


Fig 6.12: Complete assembly of Prototype 2

With the prototype fully assembled, the experimental rig was set up for thermal and electrical tests, as detailed below.

6.3. Thermal tests

The aim of the thermal test was to investigate the temperature distribution between the individual IMD components. It also aims to investigate improvements (if any) in temperature distribution between Prototypes 1 and 2.

The thermal tests were focused on how efficiently the fan and copper windings dissipated heat from the PE module. The anti-parallel body diodes of the MOSFETs are used as heat sources for this test. With the parasitic diodes not optimised for current conduction compared to the MOSFET, the diodes have more losses compared to the MOSFETs hence producing higher device temperatures with lower input current and representing a worst case scenario. Furthermore, the gate of the MOSFET does not need to be energised for the diodes to conduct hence its choice as the current path in this test.

Before setting up the experimental test rig, an X-ray of the solder layer (shown in Figure 6.13) was carried out. This was to determine the amount of voids present in the solder layer. Figure 6.13 is a mirror image of the solder layer with Q2 and Q4 on the left side; Q1 and Q3 on the right side. It shows a 2D image of an X-ray projection of the solder layer between the DBC substrate and copper winding.

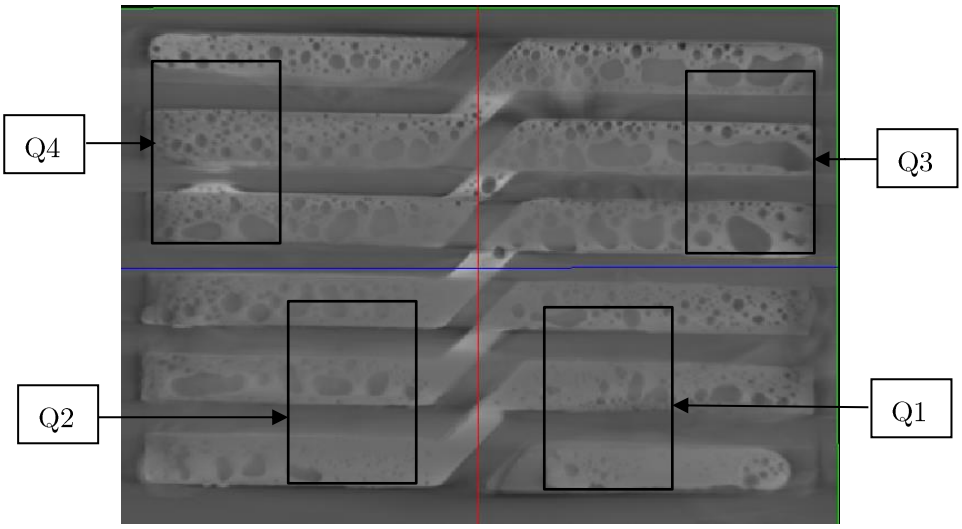


Fig 6.13: SEM image of solder layer

With the presence of voids directly related to the thermal resistance of the layer, it is expected that dies Q3 and Q4 will have temperatures compared to Q1 and Q2 for similar losses. This is due to the large number of voids in that location compared to the bottom half layer.

An appropriate rig was set up for the test as per the schematic shown in Figure 6.14.

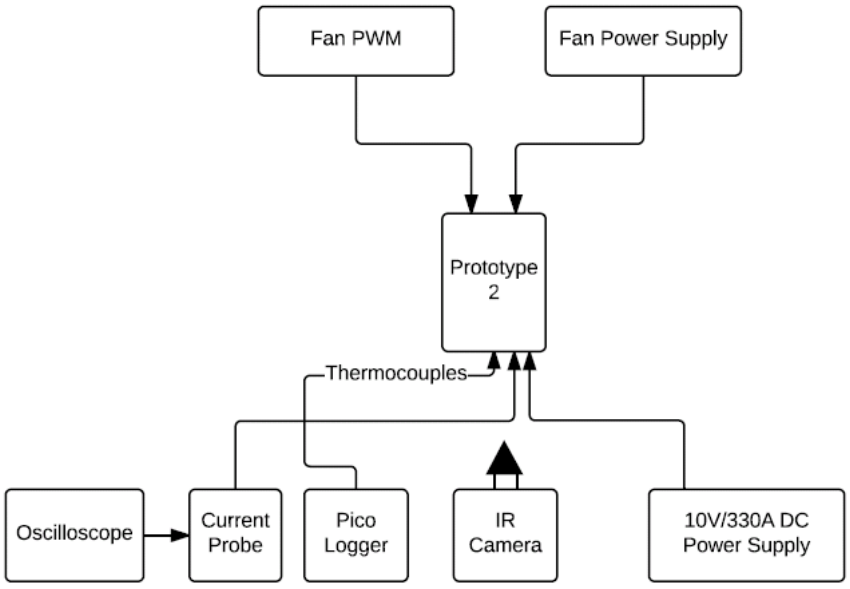


Fig 6.14: Schematic drawing of thermal test rig

K- Thermocouples were placed on the Substrate, Back Iron and both end windings – shown in Figure 5.14 in Chapter 5. These thermocouples were connected to a Pico-Logger to monitor the temperature of the IMD components. The fan was connected to a power supply of 12V/1.3A (15.6W at full power) and a Pulse Width Modulator (PWM) (Tektronix AFG3052C Function Generator) was used to regulate the fan speed.

To monitor the diode temperature, a Fluke Ti25 Infrared Thermal Image Camera was used. Due to the reflective surface of the substrate, the potential readings from the thermal camera could be erroneous. To counteract this potential problem, the substrate was coated with a conformal layer to reduce reflectivity. The conformal coating used was an

Electrolube Red Aerosol DCR200H. With a maximum operating temperature of 250°C, the spray was appropriate as a high temperature coating. More importantly, this specific coating was chosen because of its non-conductive qualities. With a high dielectric strength of 90kV/mm, the entire substrate could be coated without short-circuiting the individual copper tracks. The published emissivity of the red coating was 0.96 and this was used on the thermal imager to obtain a more accurate reading.

The thermal camera was calibrated by using coating a resistor with the conformal spray and attaching a K- thermocouple to the resistor. The thermocouple was connected to a hand held Tenma 72-7715 Thermometer. Current was passed through the resistor and the temperature changes monitored on the thermometer and thermal camera. The results were very positive with a +/- 1℃ temperature difference between both readings.

Figure 6.15 shows the PE module coated with the non-conductive conformal coating. The gate connections of the MOSFET are shorted with thin copper wires to ensure the gate voltages are clamped at zero to eliminate parasitic turn on of the MOSFET.

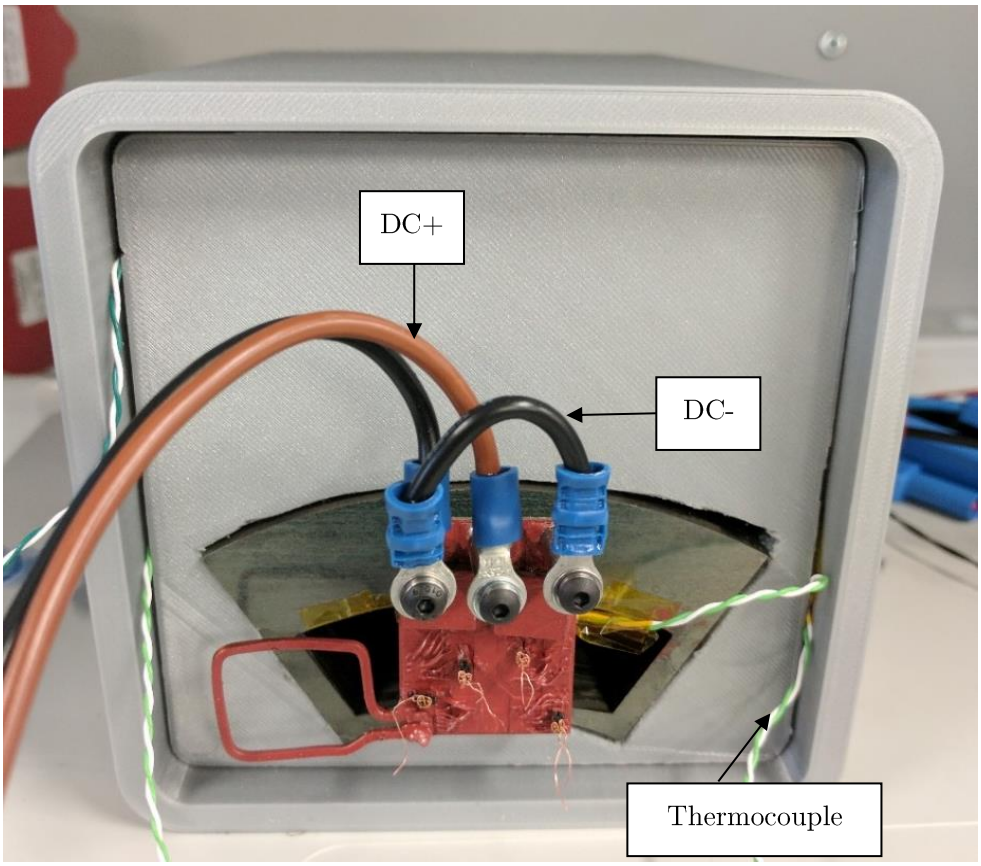


Fig 6.15: PE module sprayed with non-conductive coating (red coating)

The fan speed was measured using a Testo 425 Compact Thermal Anemometer. The speed was varied using the PWM to vary the flow rate of the coolant. The experimental rig was set up as shown in Figure 6.16.

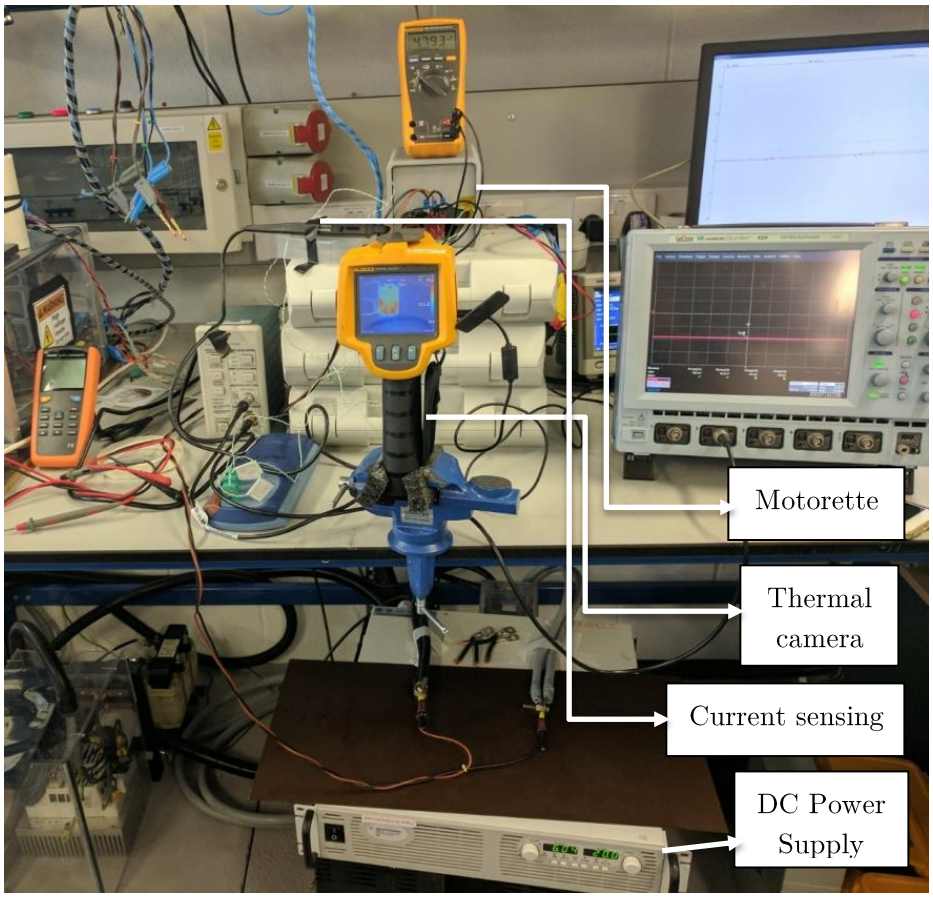


Fig 6.16: Test rig for experimental validation

The first test was to investigate the temperature distribution in the IMD system due to varying flow rates. This helps analyse how effectively, the cooling system (fan and heat sink) works to dissipate heat from the PE module. It also allows the thermal resistances between different components to be determined based on the varying flow rates.

The diodes were powered by the DC power supply at -5 V with 17A current. Starting at the maximum fan speed, the temperatures of the individual components are measured and recorded. Figure 6.17 – 6.26

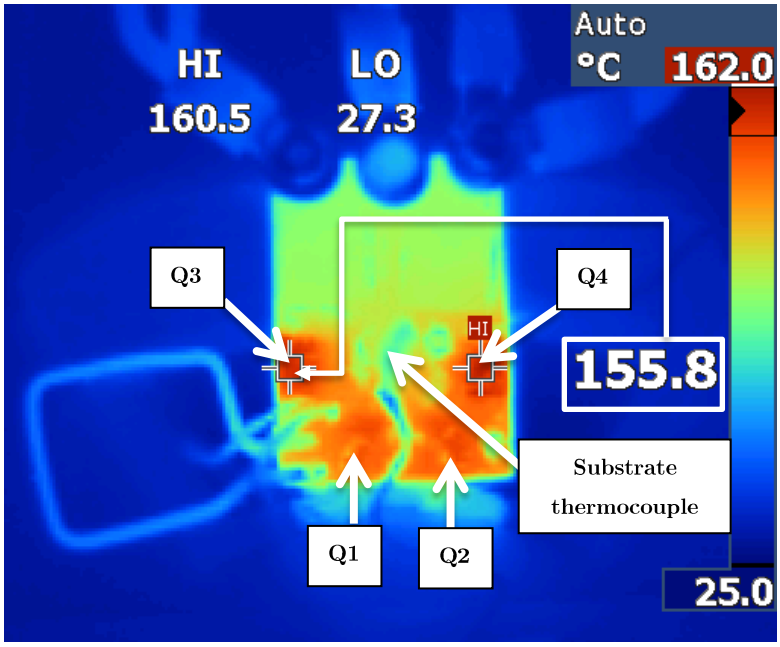
show the temperature reading of the PE module and the motorette components from the thermal camera and thermocouples for the different flow rates analysed. It can be observed that the temperature of the IMD components increase with a reduction in flow rate. Figure 6.27 shows the maximum component temperature with respect to flow rate.

The difference in hot and cold end winding temperatures average 32°C for the flow rates analysed. For a single component with no interface layer, the large temperature gradient recorded – especially for a good thermal conductor (copper) could be as a result of –

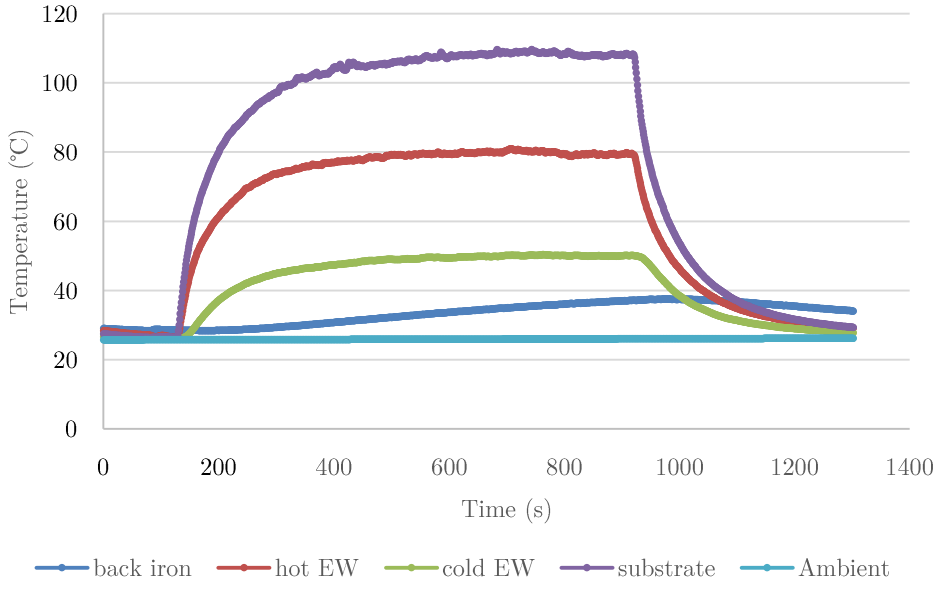
- The position of the thermocouples: The thermocouple measures the temperature of the surface of the body. With the Cold End winding thermocouple placed directly in front of the fan, the temperature of that surface is heavily influenced by the coolant temperature (26°C).
- Forced convection cooling: Without implementing a forced convection cooling system in the sample (natural convection), the temperature distribution in the copper winding would have been more uniform. However, with one end of the winding forced cooled and the other heated by the substrate, a large temperature difference is measured between both ends of the winding.
- Coolant material: The consistent difference between the hot and cold end winding temperatures is as a result of the heat transfer coefficient (HTC) of forced air cooling. The HTC of this cooling

system is limited by the material of the coolant utilised (air). Employing a different coolant like water or oil will produce higher HTC leading to a larger temperature gradient across the winding.

10% Flow rate



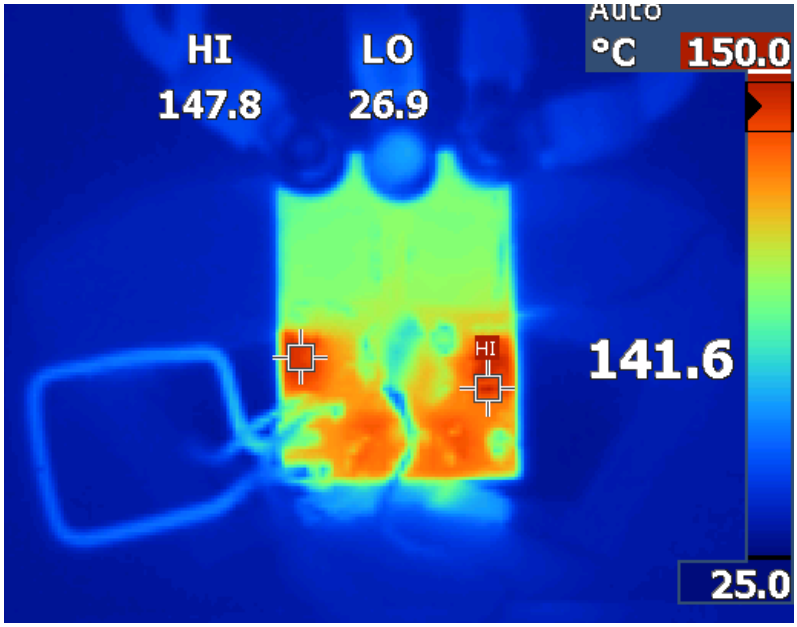
(a)



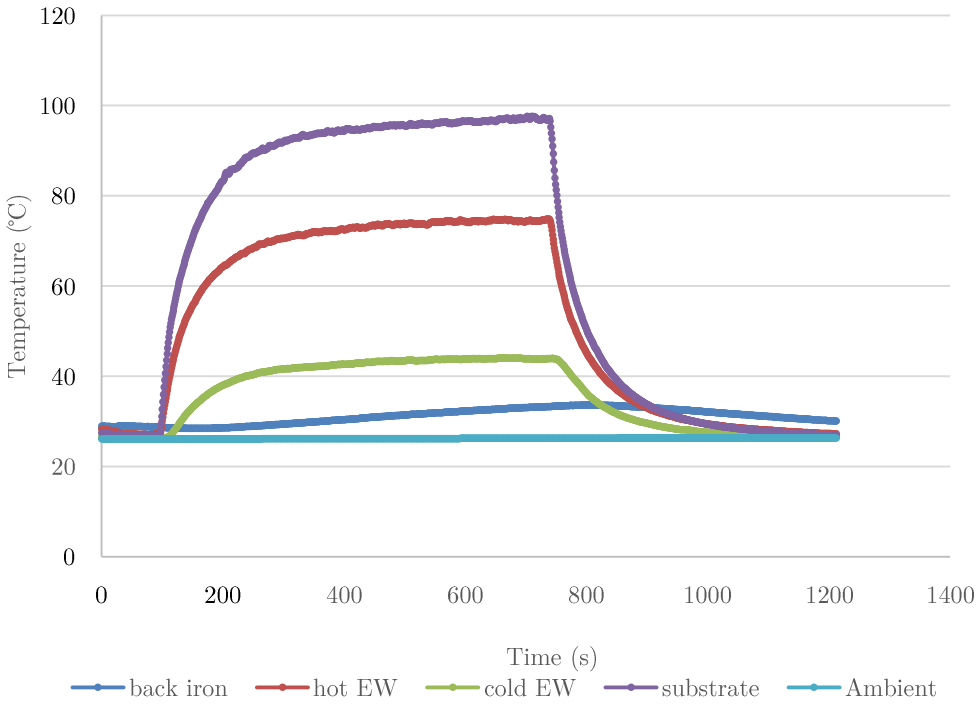
(b)

Fig 6.17: Prototype 2 component temperatures at 10% fan speed (a) PE module temperature (b) Motorette temperature

20% Flow rate



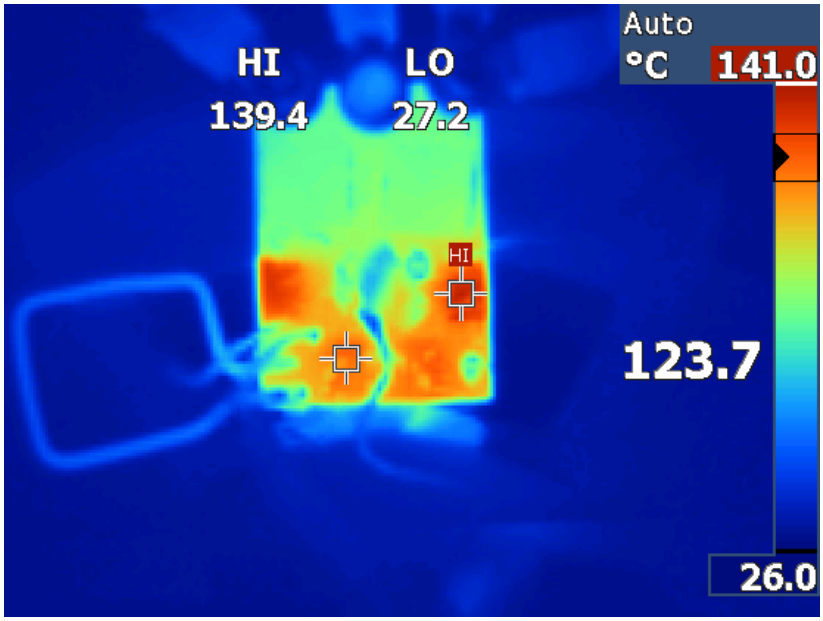
(a)



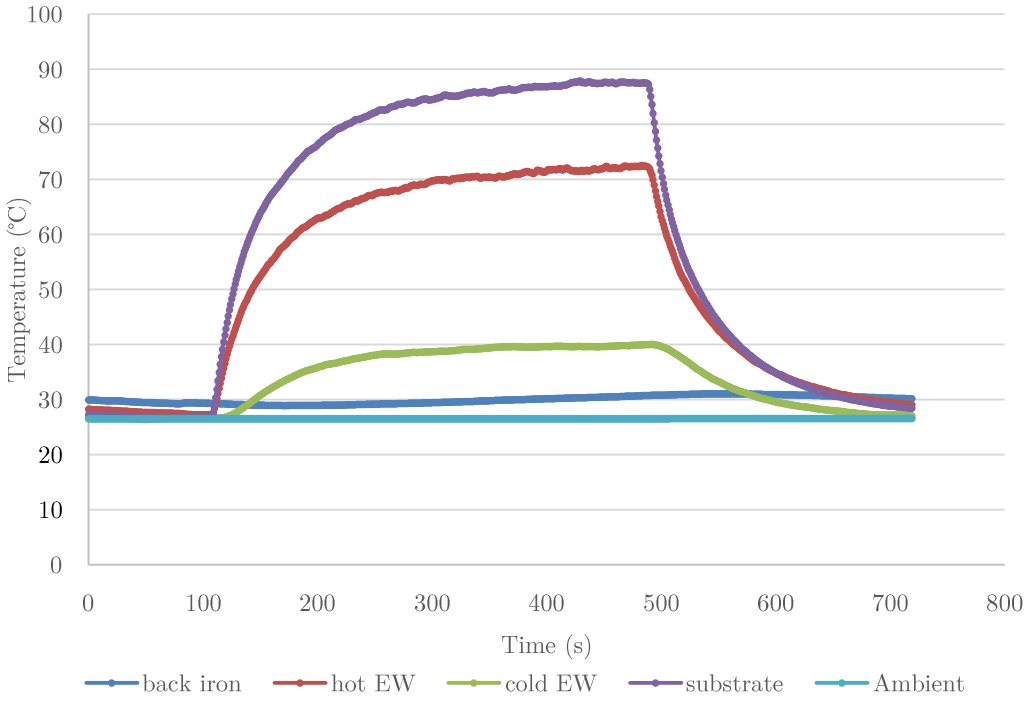
(b)

Fig 6.18: Prototype 2 component temperatures at 20% fan speed (a) PE module temperature (b) Motorette temperature

30% Flow rate



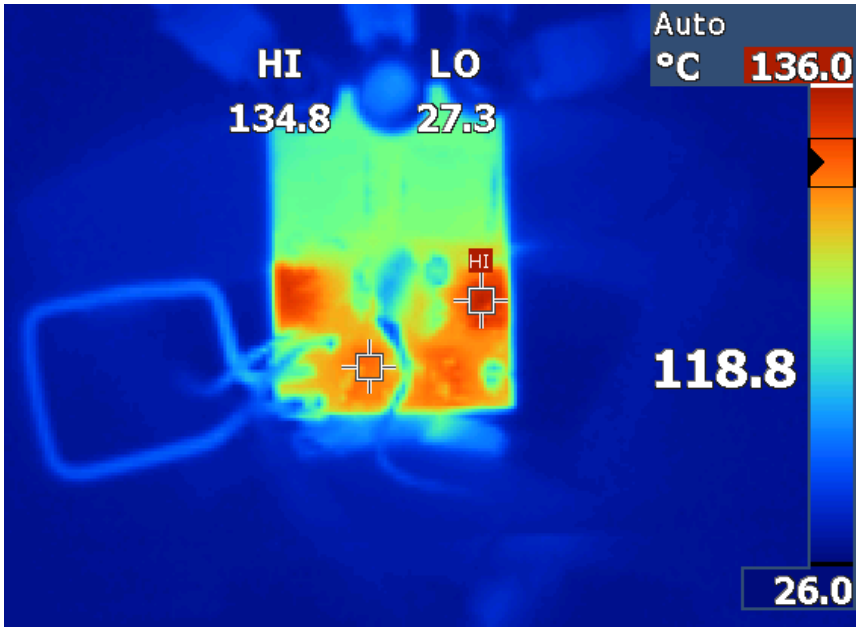
(a)



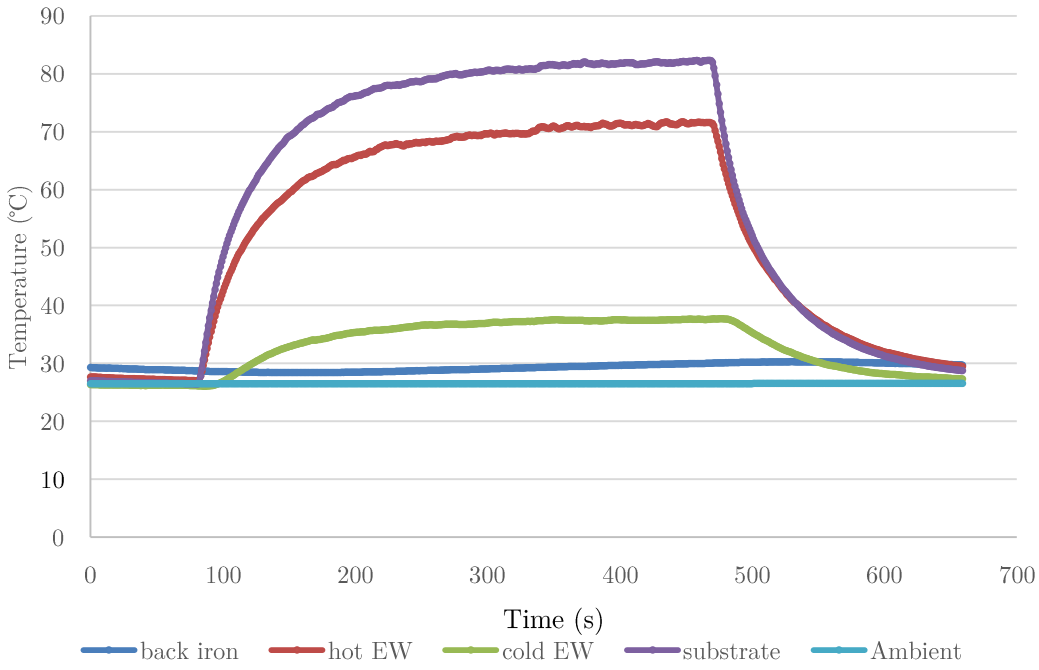
(b)

Fig 6.19: Prototype 2 component temperatures at 30% fan speed (a) PE module temperature (b) Motorette temperature

40% Flow rate



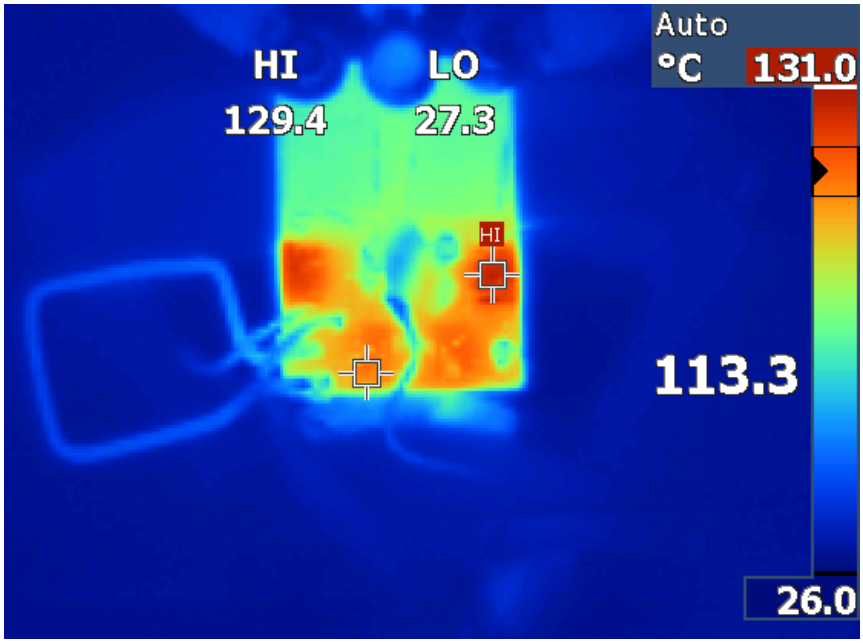
(a)



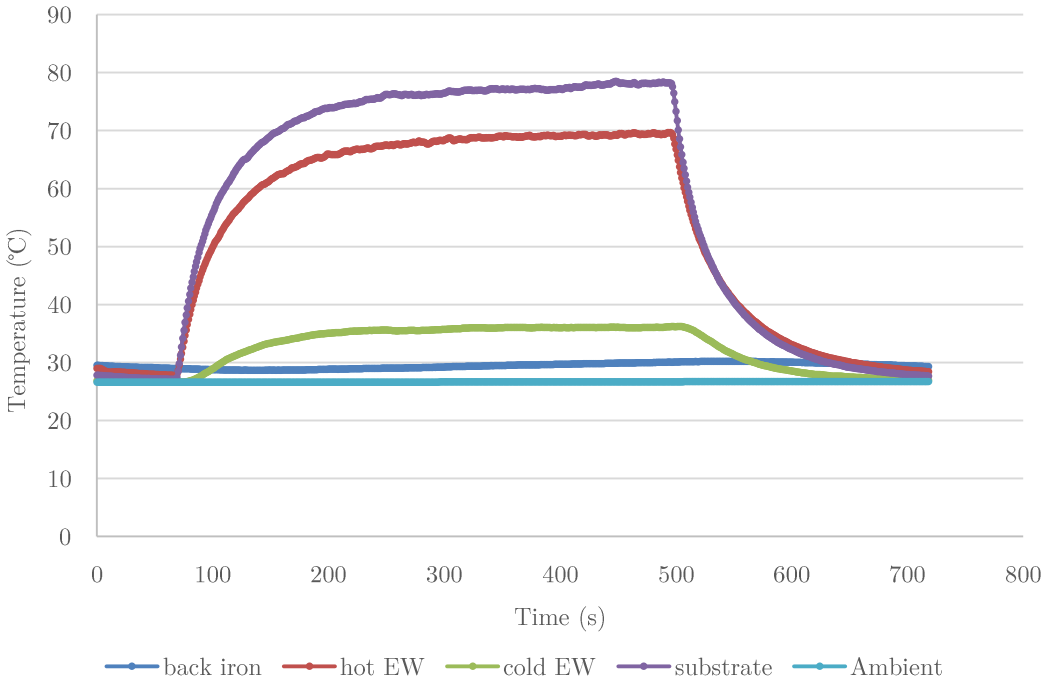
(b)

Fig 6.20: Prototype 2 component temperatures at 40% fan speed (a) PE module temperature (b) Motorette temperature

50% Flow rate



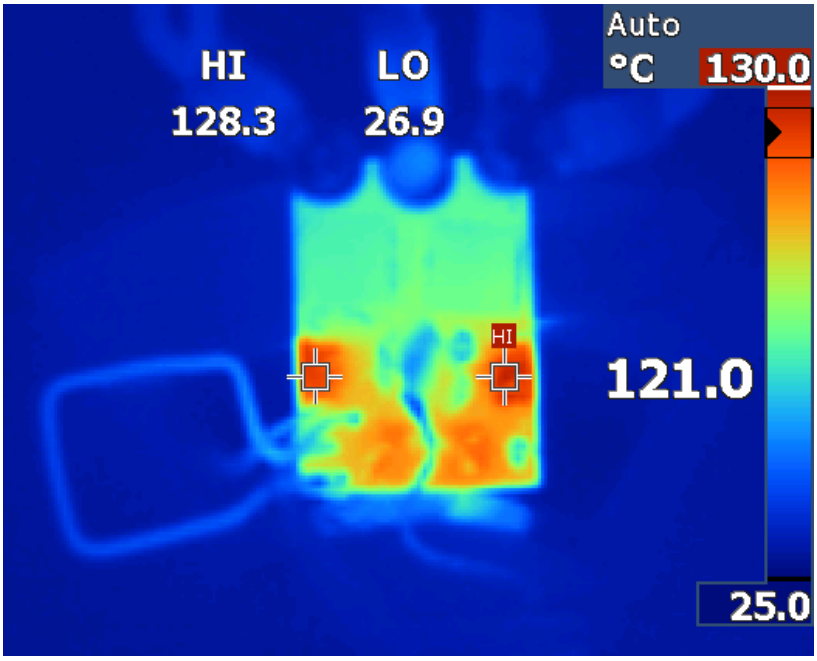
(a)



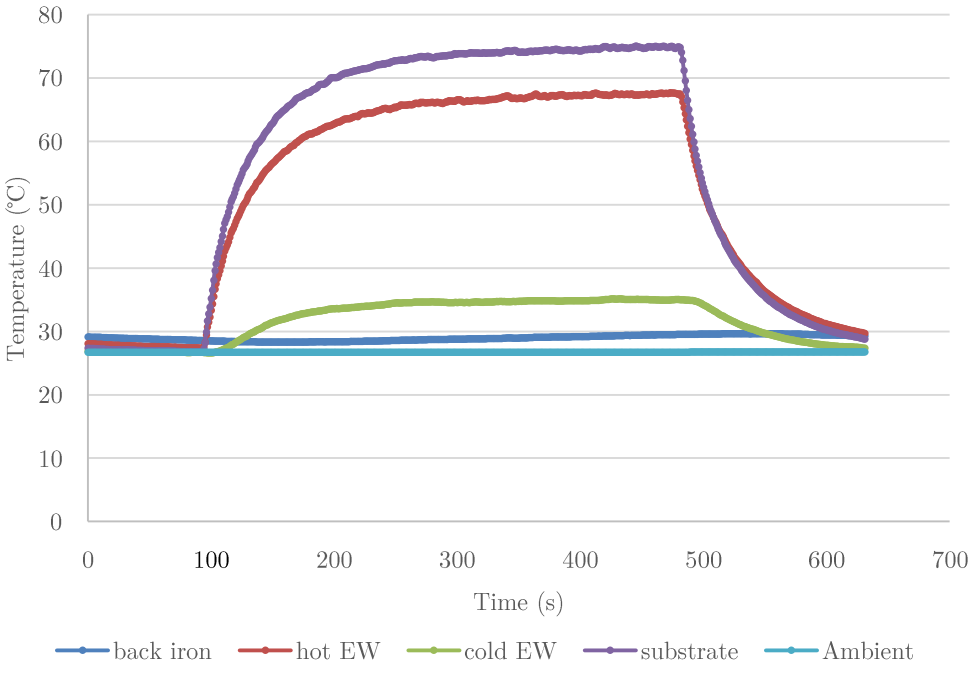
(b)

Fig 6.21: Prototype 2 component temperatures at 50% fan speed (a) PE module temperature (b) Motorette temperature

60% Flow rate



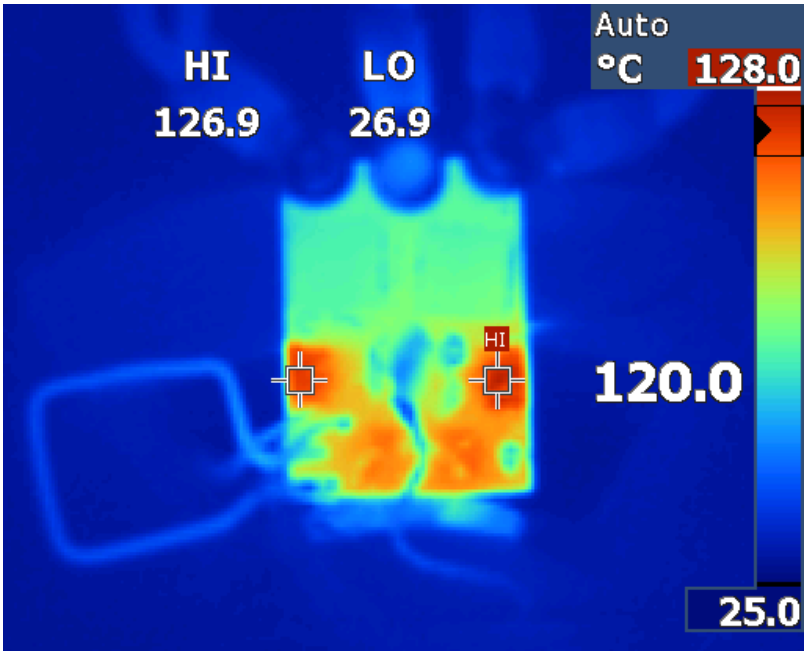
(a)



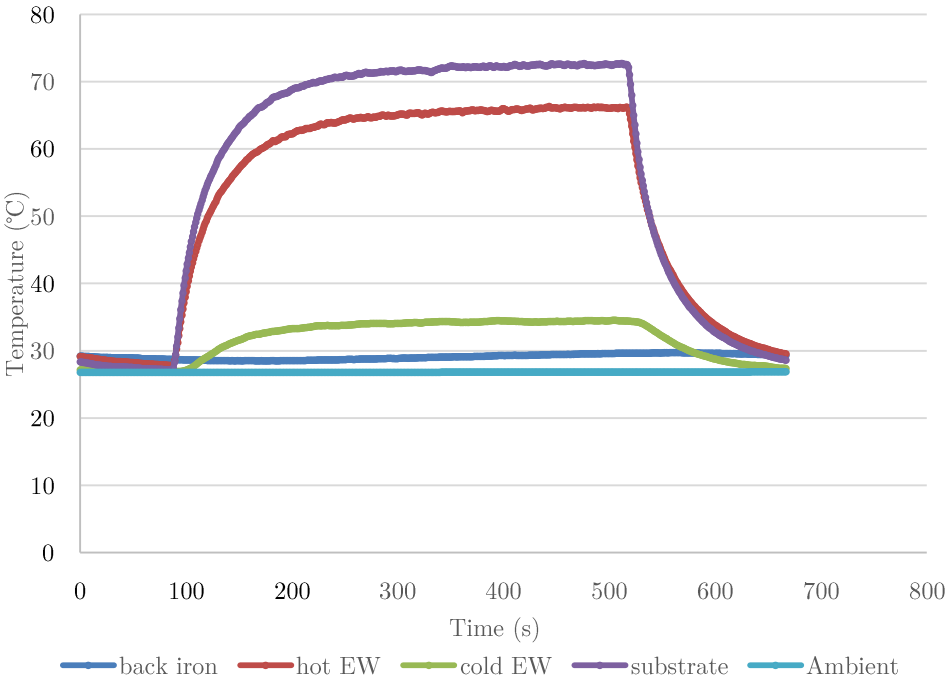
(b)

Fig 6.22: Prototype 2 component temperatures at 60% fan speed (a) PE module temperature (b) Motorette temperature

70% Flow rate



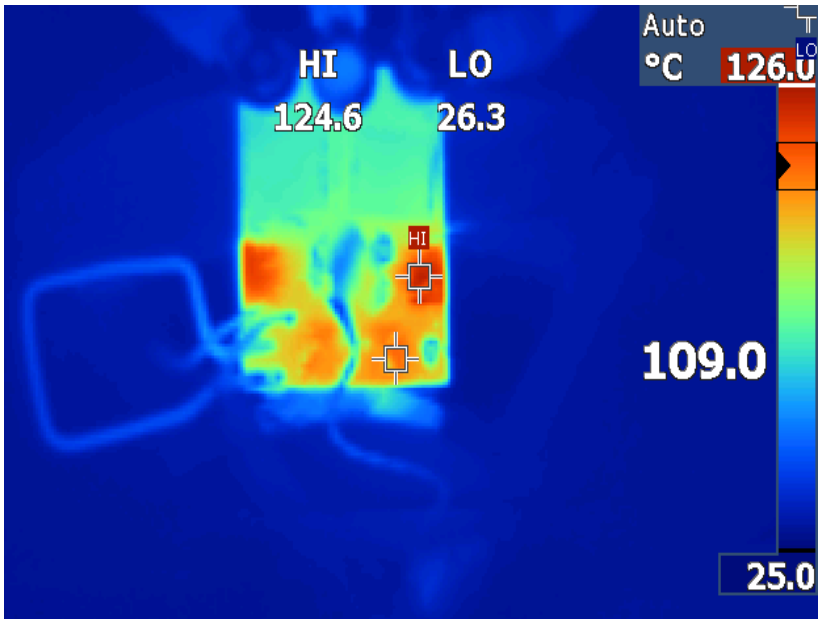
(a)



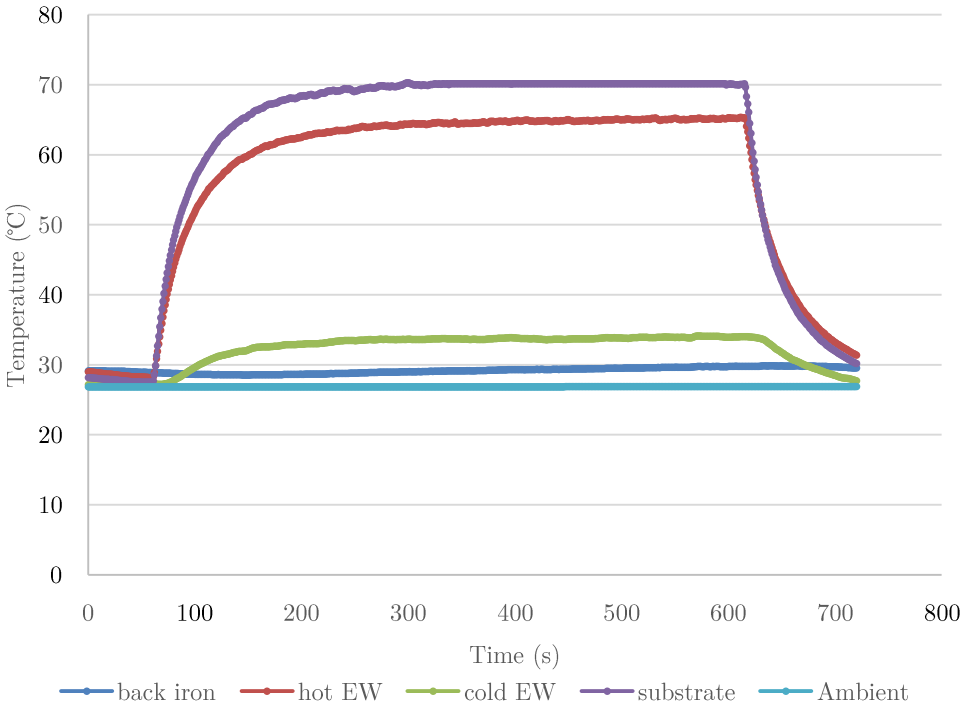
(b)

Fig 6.23: Prototype 2 component temperatures at 70% fan speed (a) PE module temperature (b) Motorette temperature

80% Flow rate



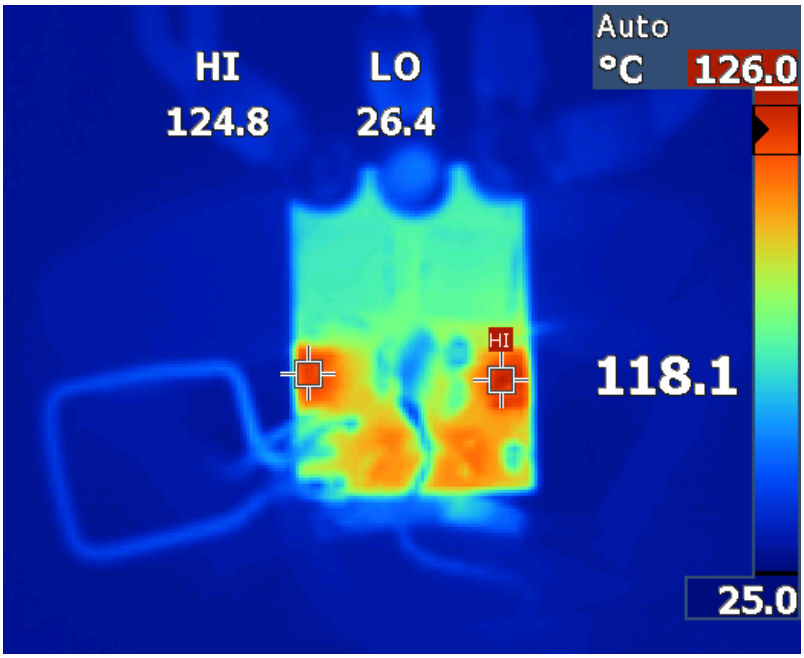
(a)



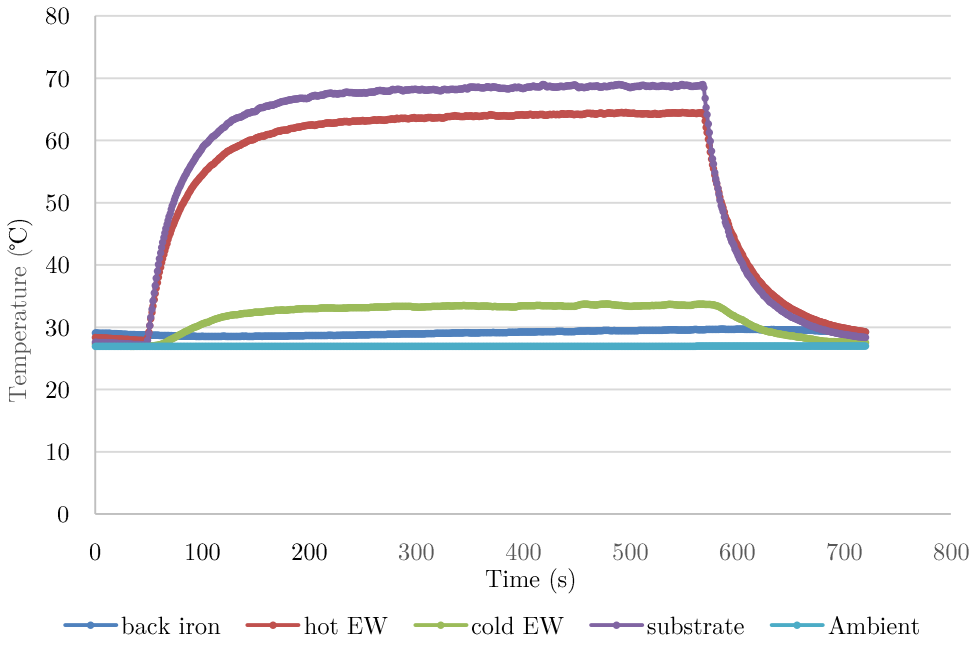
(b)

Fig 6.24: Prototype 2 component temperatures at 80% fan speed (a) PE module temperature (b) Motorette temperature

90% Flow rate



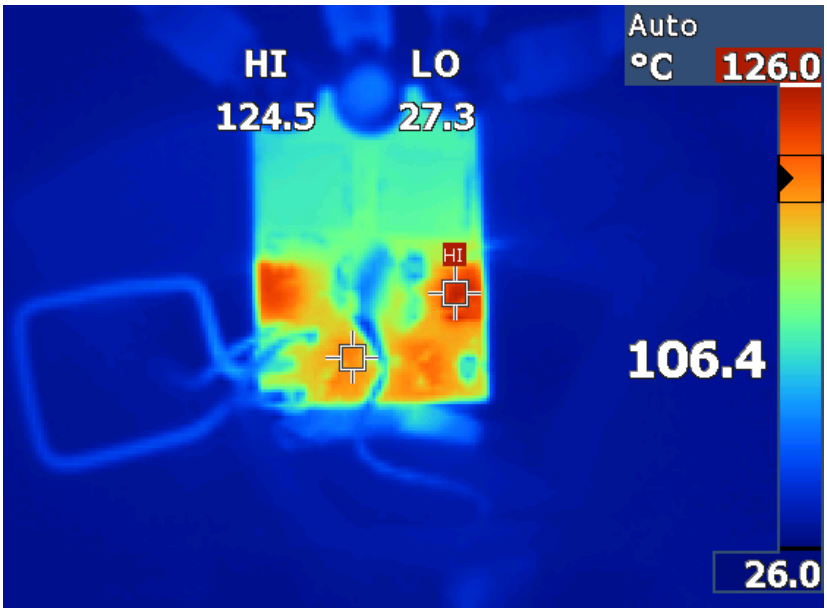
(a)



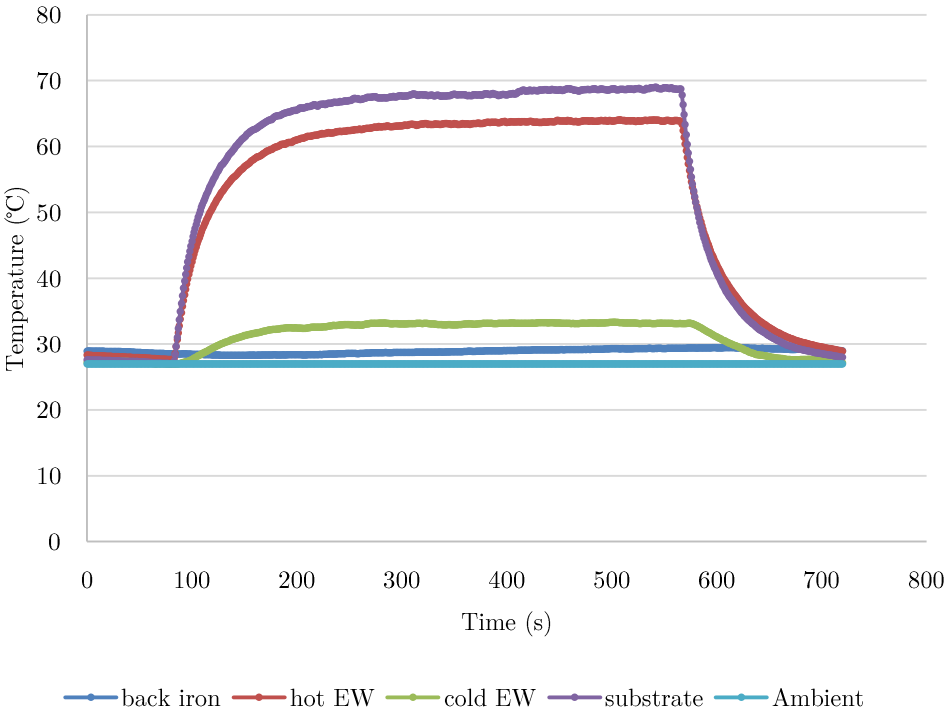
(b)

Fig 6.25: Prototype 2 component temperatures at 90% fan speed (a) PE module temperature (b) Motorette temperature

100% Flow rate



(a)



(b)

Fig 6.26: Prototype 2 component temperatures at 100% fan speed (a) PE module temperature (b) Motorette temperature

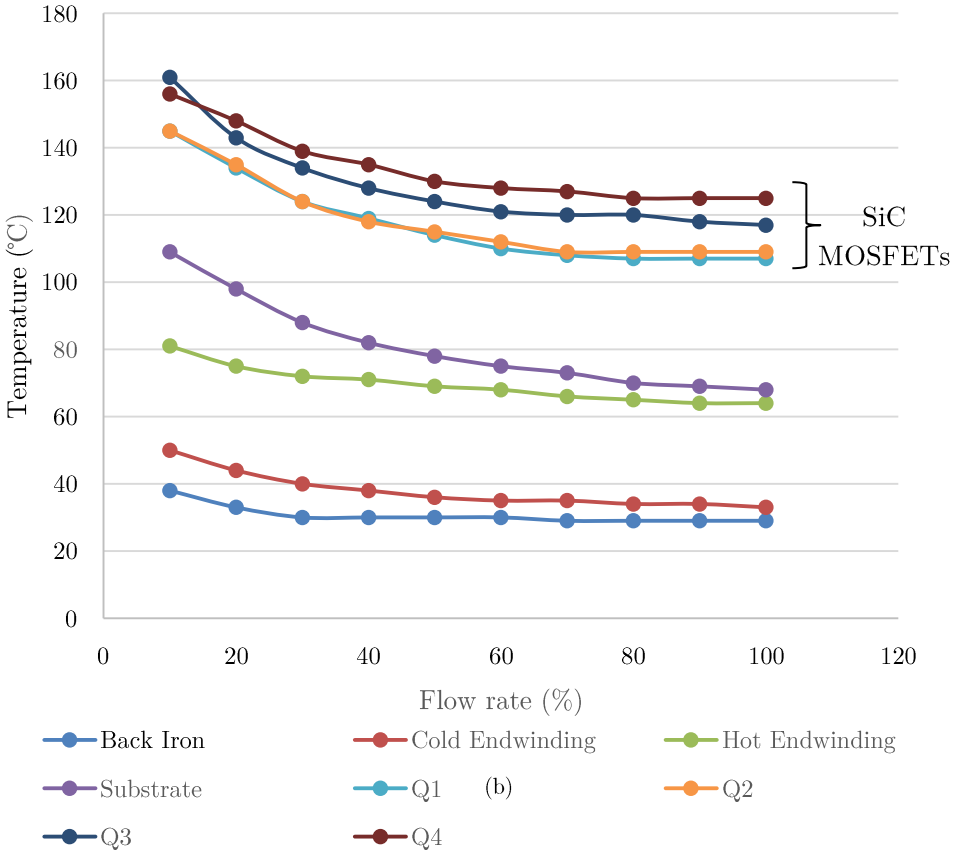


Fig 6.27: Prototype 2 component temperatures at varying flow rates

The Back Iron temperature remains fairly constant across different flow rates. This is as a result of the large thermal mass of the steel Back Iron – which requires a longer time to reach thermal equilibrium compared to the other motorette components. However, and more importantly, the poor thermal contact between the copper winding and the Back Iron means the heat transfer from the former to later is limited. The Kapton tape insulation between the windings and Back Iron reduces the heat transfer between the windings and the Back Iron. From Table 6.2, the Back Iron temperature after 30% flow rate remains fairly constant at only 4°C above inlet temperature.

Table 6.2: Steady state Temperature of Prototype 2 components at different flow rates

Flow Rate (%)	**Back Iron (°C)**	**Cold EW (°C)**	**Hot EW (°C)**	**Sub (°C)**	**Q1 (°C)**	**Q2 (°C)**	**Q3 (°C)**	**Q4 (°C)**	**Inlet (°C)**
10	38	50	81	109	145	145	161	156	25.75
20	33	44	75	98	134	135	143	148	25.75
30	30	40	72	88	124	124	134	139	25.75
40	30	38	71	82	119	118	128	135	25.75
50	30	36	69	78	114	115	124	130	25.75
60	30	35	68	75	110	112	121	128	25.75
70	29	35	66	73	108	109	120	127	25.75
80	29	34	65	70	107	109	120	125	25.75
90	29	34	64	69	107	109	118	125	25.75
100	29	33	64	68	107	109	117	125	25.75

The hottest components are diodes Q3 and Q4. This is in part due to the slight differences in the individual device forward voltage, leading to different device losses. However – and more importantly, from Figure 70, the X-ray image of the solder layer shows voids and pores present in the structure. The top half of the winding, where Q3 and Q4 are located,

shoes a larger number of voids and pores compared to the bottom half (where Q1 and Q2 are located). This will lead to a higher thermal resistance between the top devices (Q3 and Q4) and the winding ultimately resulting in higher temperatures for Q3 and Q4. This highlights the importance of the solder layer not only for mechanical attachment but also for heat transfer.

Diodes Q1 and Q2 have similar temperature readings for all flow rate measurements with a maximum of 2°C difference in temperature. With similar losses across all four devices, this suggests the increased temperature recorded for Q3 and Q4 is as a result of the poor thermal path between the PE module and winding at that location. A difference of 28°C between the substrate and copper winding at 10% flow rate suggests good thermal coupling between both components. This is further highlighted by a 4°C difference between both components at maximum flow rate. As the flow rate (fan speed) increases, the effective heat transfer performance of each winding will be improved resulting in a change in the heat flux distribution; heat will tend to flow vertically from the die into the nearest windings rather than spreading across the substrate

From Figure 6.27, the changes in temperature for the Prototype components remain virtually constant after 50% flow rate. Even with an increase in flow rate, the temperature changes are minimal. This shows that although the voids in the solder layer influence temperature

distribution between PE module and windings, the main restriction in thermal dissipation for the sample remains the coolant material. Furthermore, the power density can be increased and losses decreased by implementing a lower rated fan without adversely affecting thermal performance. The thermal tests also highlight the uneven temperature distribution across the substrate. Although the substrate acts as a heat spreader, the maximum temperatures are concentrated around the devices (lower half of the substrate). This shows forced convection cooling is prominent in heat transfer compared to conduction with the fan cooled windings dissipating the most heat from the PE module.

For forced convection cooling, especially where heat dissipation is primarily from a heat sink to a cooling system, heat dissipation from power device to ambient is minimal. This is due to a high junction to ambient thermal resistance ($R_{th\ (j\text{-}a)}$) resulting in only a very small percentage of heat dissipated from the die to ambient. Furthermore, with the large temperature gradient in the heatsink (copper windings), the junction to case thermal resistance is difficult to measure. This is because in thermal resistance measurements, the body temperature is assumed to be uniform. This means, for the winding temperature, an average temperature value is assumed. This gives an inaccurate temperature reading for the winding, hence an erroneous $R_{th(j\text{-}c)}$. Also, using the hot end winding temperature as a representation of the overall winding body temperature will be inaccurate. This is because the temperature is non-

uniform and mainly reflects the local substrate (on the back side of the substrate) temperature. A more appropriate thermal resistance measurement is the die to coolant inlet temperature. This provides a more realistic representation of how effectively the PE module cooling system operates. Figure 6.28 shows a graph of the die (junction) to inlet thermal resistance ($R_{th\,(j\text{-}i)}$) variation with flow rate.

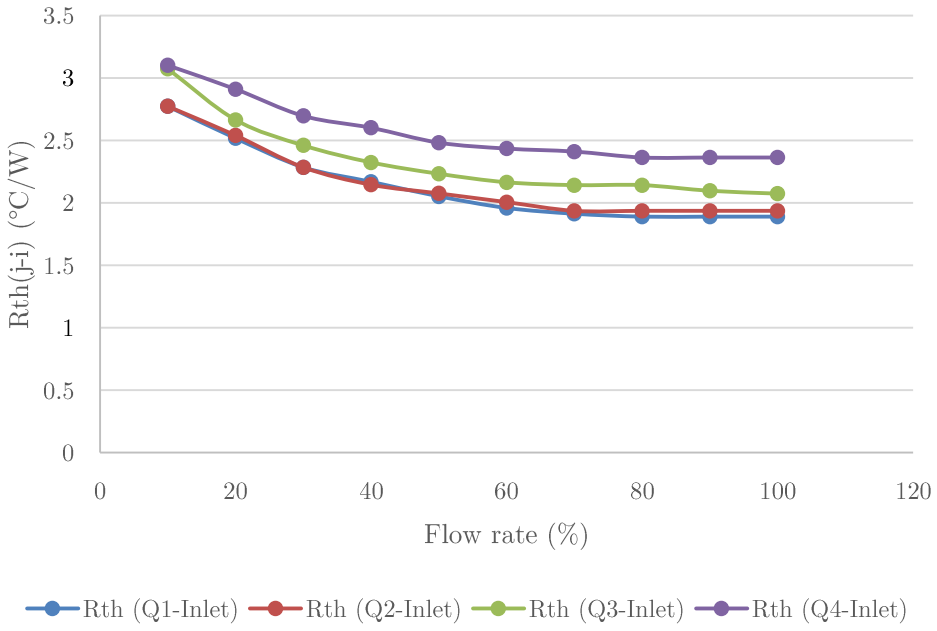


Fig 6.28: Junction to Inlet thermal resistance vs Flow rate

The average junction to inlet thermal resistances for all four diodes at maximum and minimum flow rates are 2.1°C/W and 3°C/W respectively. These thermal resistance values are dependent on a number of factors, namely –

- **Contact between the bare dies and substrate:** The contact between the die and the substrate influences the efficiency of heat

dissipation from the die to substrate with a higher contact area resulting lower temperature drop and vice versa. Furthermore, the choice of material between both components (bare die and substrate) also determines how efficiently heat is dissipated from the die.

- **Contact between the substrate and heat sink (copper windings)**: Like the contact between the bare die and substrate, the substrate to windings contact is vital in heat dissipation from die to windings. With voids present in the solder layer, heat transfer between the heat source and heat sink is not as efficient resulting in an increase in $R_{th(j-i)}$. Also, the thermal conductivity of solder restricts the heat transfer capability of the layer, further increasing $R_{th(j-i)}$. By reducing the voids present in the solder layer (in Fig 6.13) or using a different attachment material (like sintered silver), the thermal resistance between die and fan can be reduced.
- **Choice of coolant**: The thermal conductivity of air limits its heat transfer capability. Although a higher flow speed increases the heat transfer coefficient of air, this value is limited by the realistic air speeds that can be achieved. The thermal resistance between junction and inlet can be reduced by using a different coolant like water.

With these factors taken into consideration, an average Rth(j-i) value of 2.1°C/W at maximum flow rate represents a favourable result. The next step was the switching tests to investigate the PE module operating not only as a heat source but a functional power module with the devices switching and current passing through the windings. A detailed comparison between these experimental results and its corresponding simulation results are presented in the next chapter.

6.4. Switching Test

The aim of this test was to investigate the system performance switching at high frequencies and the effective temperature distribution in the PE module and motorette components. The circuit is similar to Figure 6.3 with the inductive load between Phase in and Phase out. The inductance of the coil is lower than desired due to the limited number of turns in the coil. Equation 6.1 shows the relationship between the Back EMF, Current, Inductance and Switching frequency.

$$\varepsilon = i(2\Pi f)L \qquad 6.1$$

(Where ε= Back EMF; I = current; f = Frequency; L = Inductance)

With the Inductance value fixed, to increase the load Back EMF, the current through the winding or the switching frequency have to increase.

However, increasing the current through the windings will lead to increased copper losses. This in turn results in higher temperatures in the copper windings. With the windings acting as a heat sink for the PE module, it is important to maintain low copper losses, ensuring a low component temperature. So, to generate a large enough Back EMF without increasing the current through the windings, a high switching frequency is required. To reduce the ripple current, there is a trade-off between additional switching losses and reduced conduction losses as the switching frequency increases. Although the current ripple reduces by increasing the switching frequency, the switching losses increases at higher switching frequency.

A chopper circuit was used for the test with MOSFET Q1 modulated; Q4 always on and Q2 always off. With only two devices conducting at once, the body diode of Q3 allows current flow when Q1 is off. In the absence of a suitable gate driver, the gate connections on the devices were excited with +/- 5V from the Function Generator. A Tektronix TCPA300 current probe was connected to the copper loop shown in Figure 6.12 to measure the current through the winding.

The tests were performed at 100 kHz switching frequency to investigate the high frequency operation of the prototype. To simulate a worst-case scenario, a duty cycle of 50% was used. This is because maximum ripple current was expected at this duty cycle. To increase the losses in the

devices, the duty cycle was further increased. This is because current increases with an increase in duty cycle and conduction losses increase with a square of current. Figure 6.29 – 6.35 show the PE module temperature distribution at 50%, 60%, 80%, 82%, 86%, 87% and 87.5% duty cycles. All tests were performed at 100 kHz duty cycle with a fixed supply of 10.3V.

At 50% duty cycle, Q3 is the hottest device in the PE module. This is because with Q1 off half the time, the diode on Q3 recycles current in the circuit. With the diode more lossy compared to the MOSFET, the temperature on Q3 is highest for the same current. Q2 remains off throughout the test and the temperature profile captured in its location is as a result of heat propagation from the conducting devices (Q1, Q3 and Q4). Table 6.3 shows the maximum temperatures of the PE module and motorette from 50% to 87.5% duty cycles at 100 kHz.

Table 6.3: Steady state Temperature of Prototype 2 components at different Duty Cycles

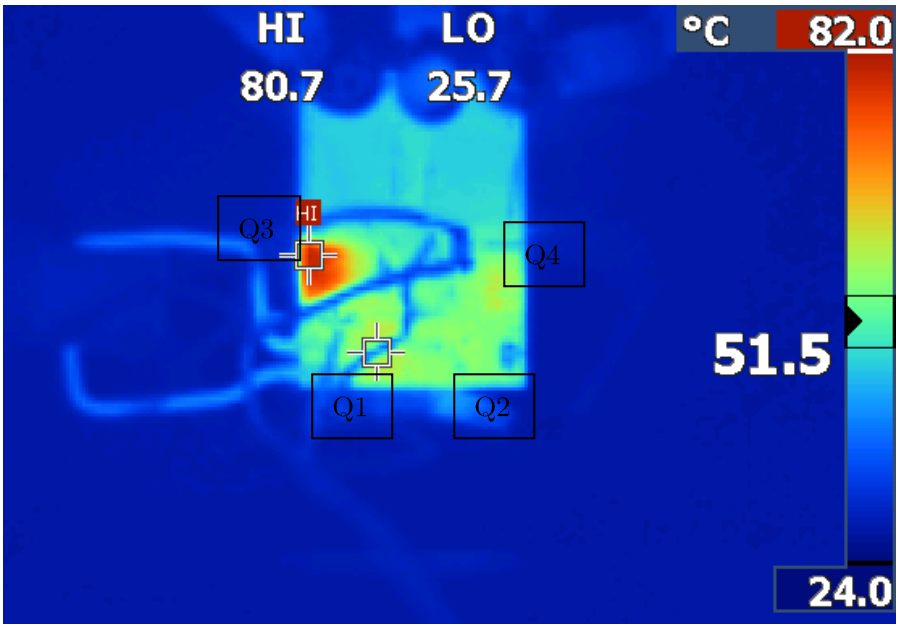
Duty cycle (%)	**Cold EW (°C)**	**Hot EW (°C)**	**Substrate (°C)**	**Back Iron (°C)**	**Q1 (°C)**	**Q2 (°C)**	**Q3 (°C)**	**Q4 (°C)**
50	29	44	42	26	52	44	81	64
60	31	59	54	27	81	74	109	91
80	31	61	54	27	82	73	104	91
82	31	61	53	27	82	73	105	92
86	33	71	65	29	117	97	114	121
87	34	78	67	29	140	112	127	143
87.5	37	86	74	30	157	120	133	169

As the duty cycle and current increases, the losses through the devices increases – evident in the high temperatures measured. However, the losses distribution in the devices changes with an increase in duty cycle. From 50%- 82% duty cycle, Q3 is the hottest device due to the conducting lossy body diode and poor thermal path due to voids in the solder joint, Q4 the second hottest because it is constantly on and Q1 being the least hottest of the conducting devices. However, from 86% duty cycle, Q4 becomes the hottest devices with Q1 and Q3 next. This is because with a current of 20A through the constantly on Q4, its losses are high. Furthermore, Q1 is ON for a longer time and the diode on Q3 conducting

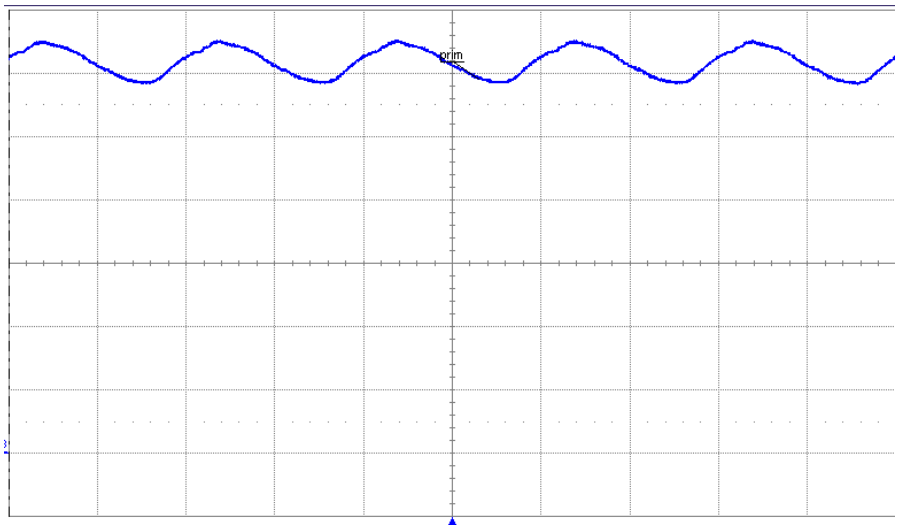
for a shorter period. At 87.5% duty cycle (Figure 6.35), a maximum temperature of 170°C was recorded for Q4 and 157°C for Q1.

The hot End winding temperature is higher than the substrate temperature due to the position of the thermocouples for both components. Furthermore, with only specific devices conducting, the overall temperature of the substrate is reduced. The effective heat transfer performance of the copper winding is also higher compared to the substrate. This is due to the high fan speed (100%) resulting in a change in the heat flux distribution in the winding compared to the substrate. Heat therefore flows vertically from the die into the nearest windings rather than spreading across the substrate resulting in a higher temperature reading for the End winding compared to the substrate.

50% Duty Cycle



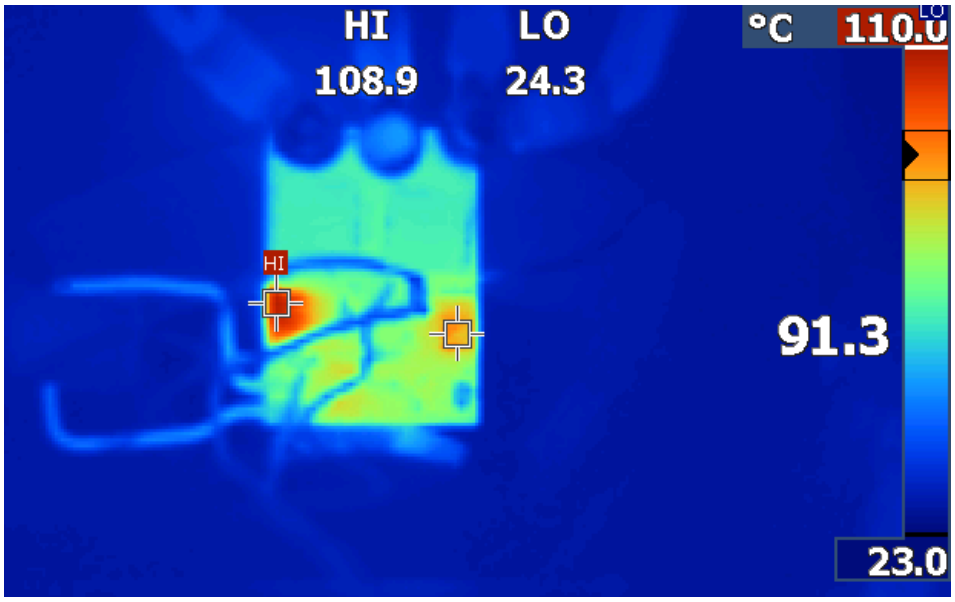
(a)



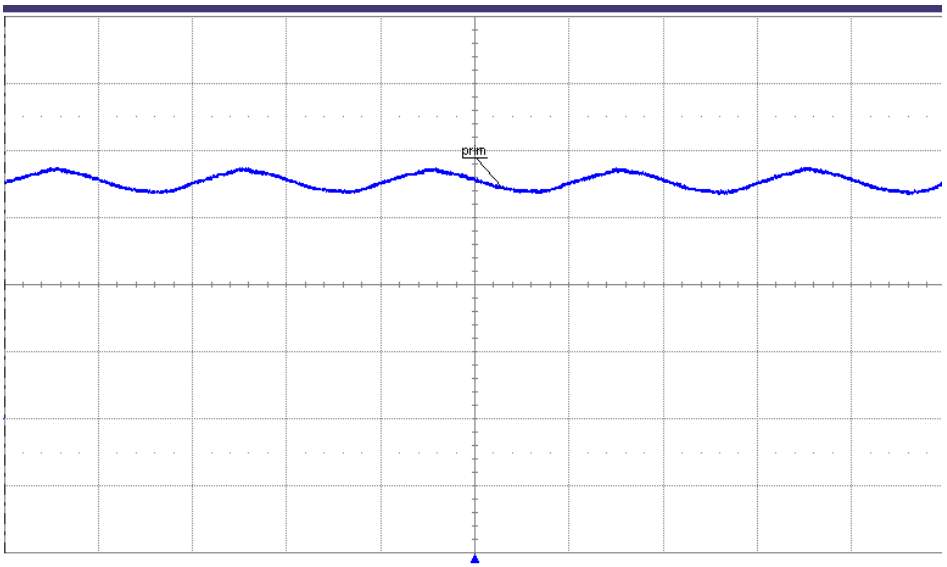
(b)

Fig 6.29: Switching test at 50% Duty Cycle (10.3V; 5.4A) **(a)** PE module temperature **(b)** 2A Ripple Current; 12.2A mean winding current

60% Duty Cycle



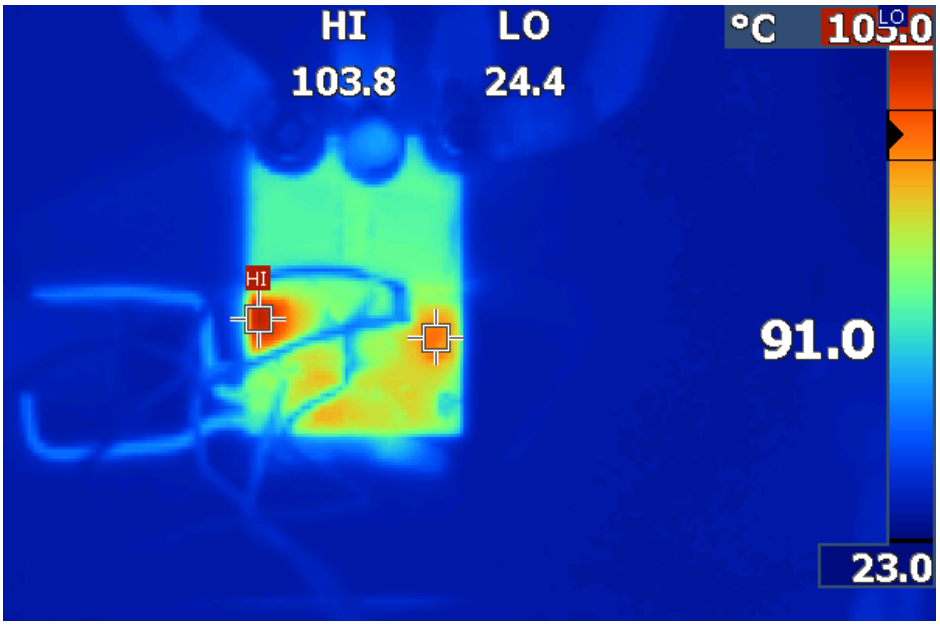
(a)



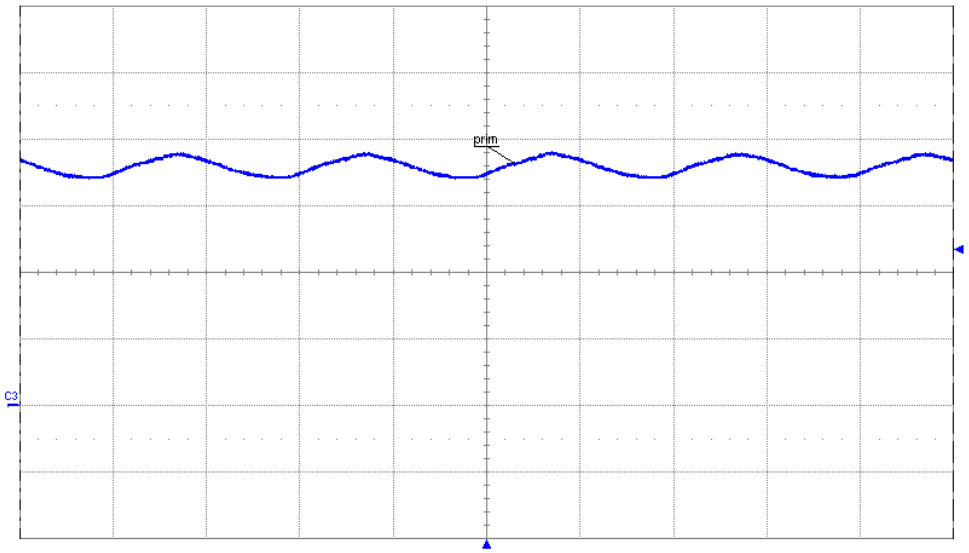
(b)

Fig 6.30: Switching test at 60% Duty Cycle (10.3V; 9.2A) **(a)** PE module temperature **(b)** 2A Ripple Current; 17.7A mean winding current

80% Duty Cycle



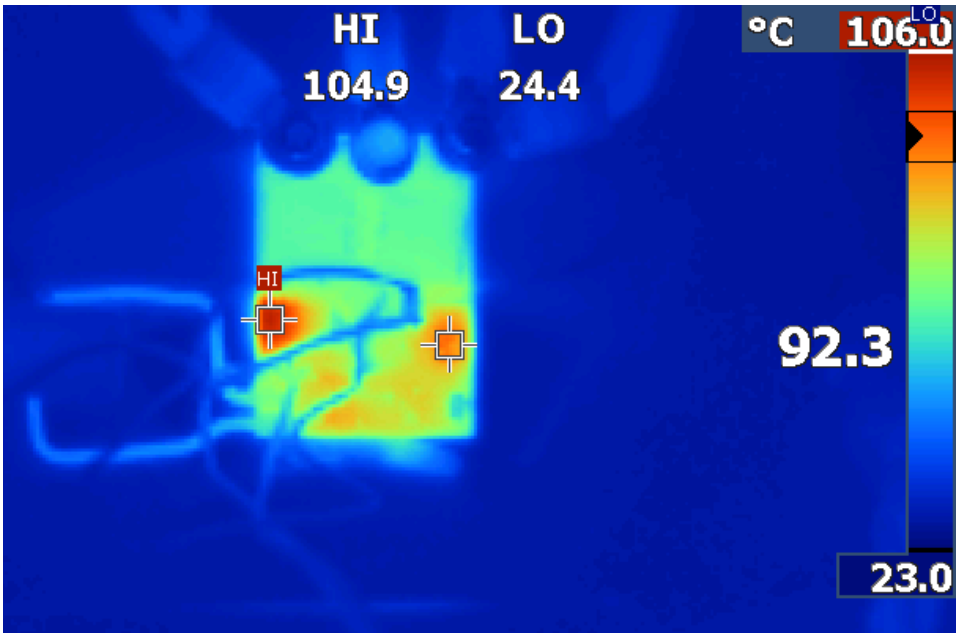
(a)



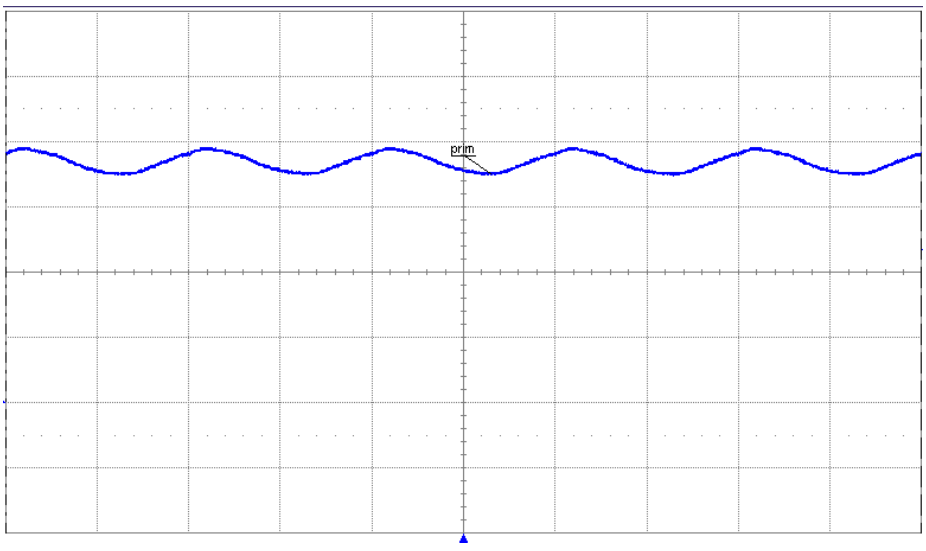
(b)

Fig 6.31: Switching test at 80% Duty Cycle (10.3V; 9.7A) **(a)** PE module temperature **(b)** 2.1A Ripple Current; 18A mean winding current

82% Duty Cycle



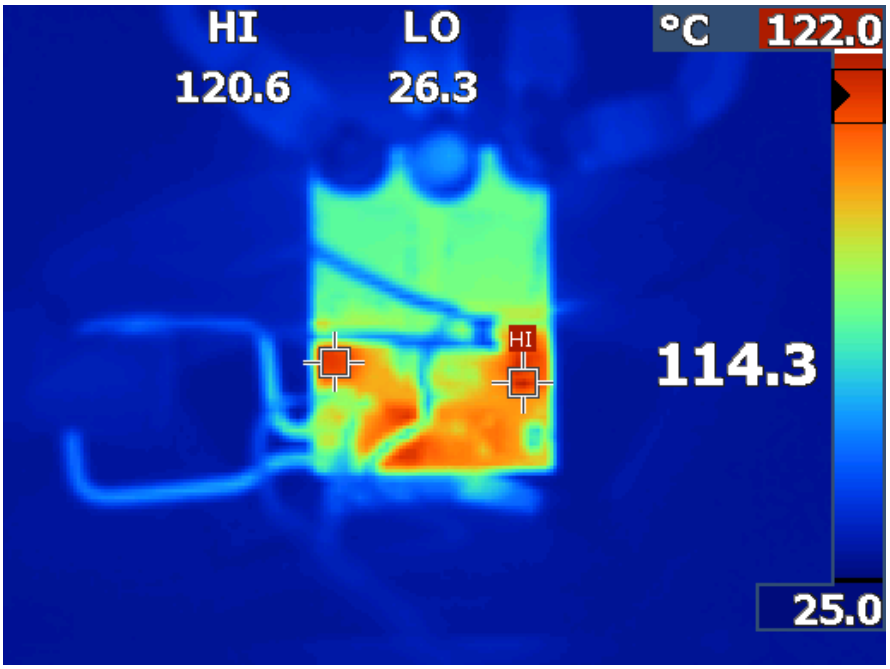
(a)



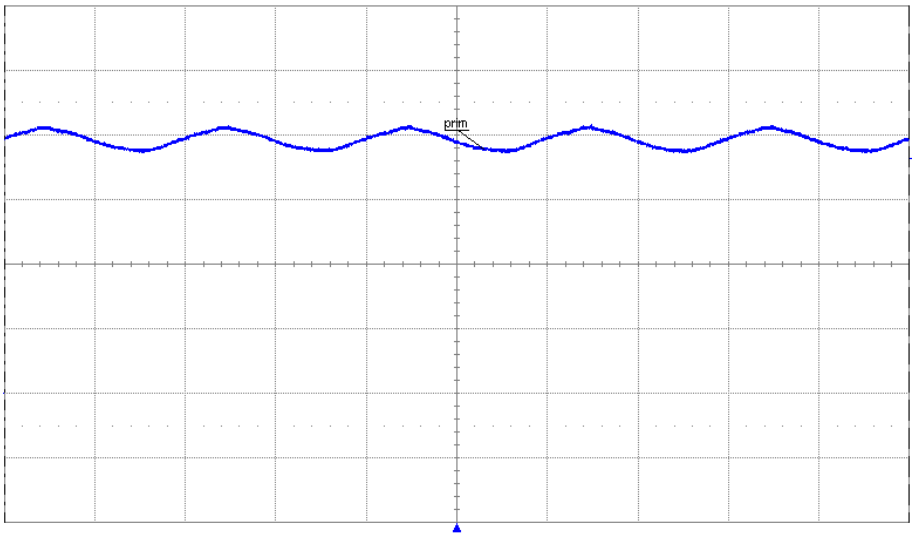
(b)

Fig 6.32: Switching test at 82% Duty Cycle (10.3V; 9.6A) **(a)** PE module temperature **(b)** 2.2A Ripple Current; 18.4A mean winding current

86% Duty Cycle



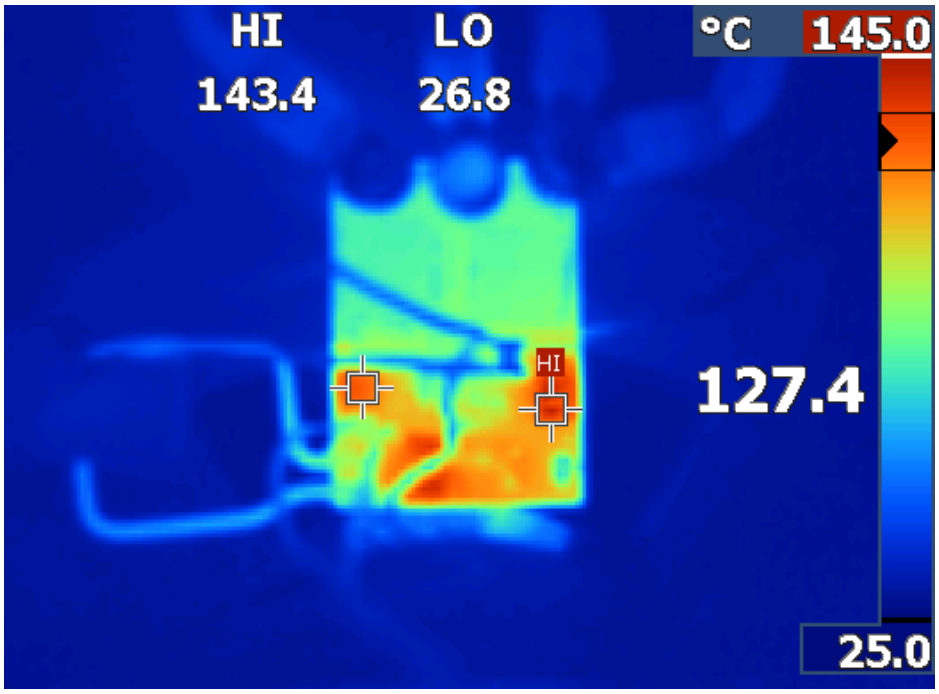
(a)



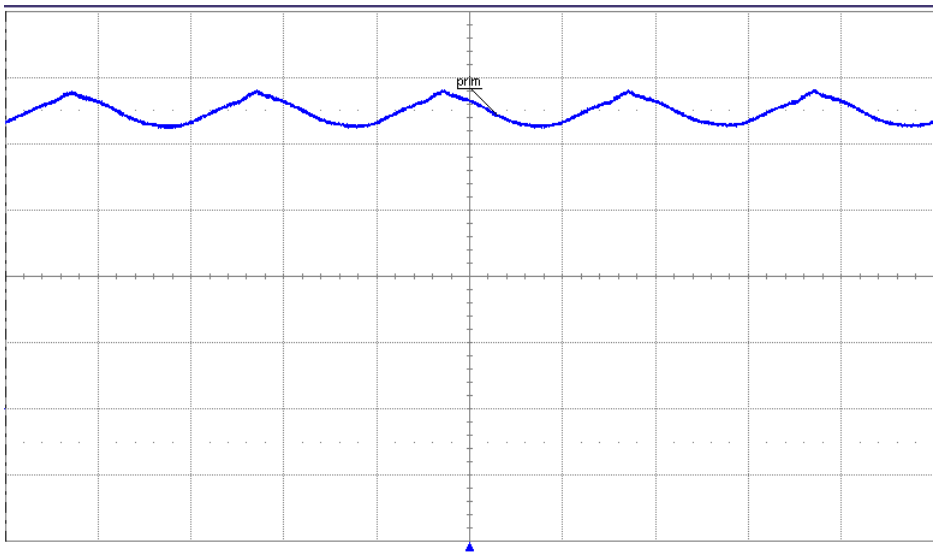
(b)

Fig 6.33: Switching test at 86% Duty Cycle (10.3V; 11.6A) **(a)** PE module temperature **(b)** 2.2A Ripple Current; 20A mean winding current

87% Duty Cycle



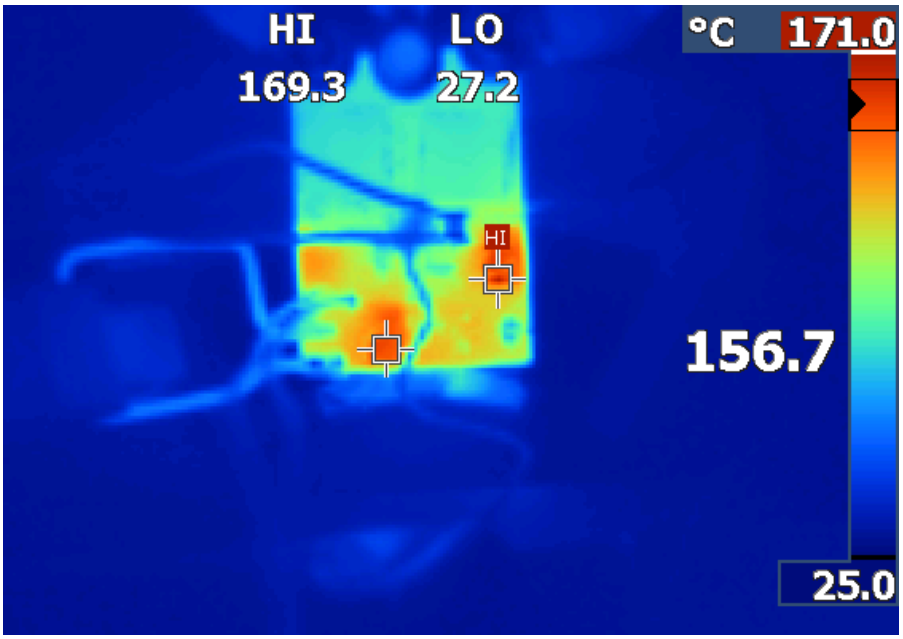
(a)



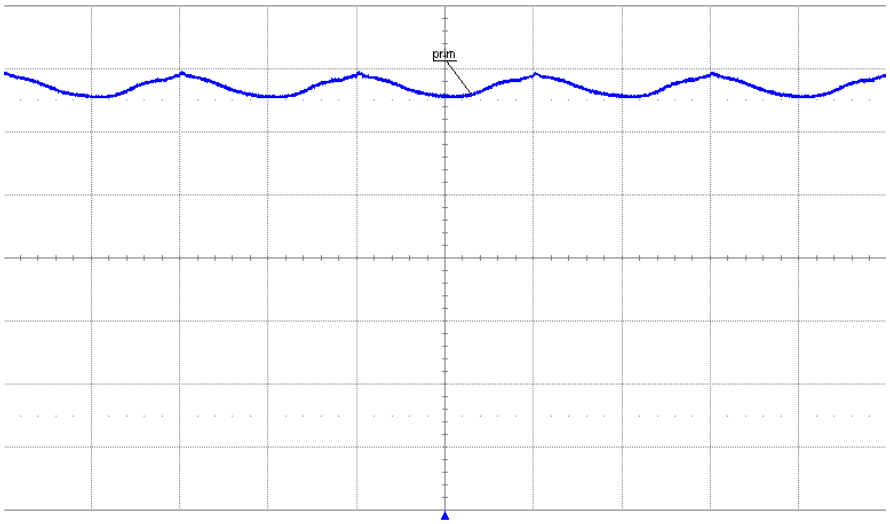
(b)

Fig 6.34: Switching test at 87% Duty Cycle (10.3V; 13.2A) **(a)** PE module temperature **(b)** 2A Ripple Current; 22A mean winding current

87.5% Duty Cycle



(a)



(b)

Fig 6.35: Switching test at 87.5% Duty Cycle (10.3V; 14A) (a) PE module temperature (b) 2.1A Ripple Current; 23.6A mean winding current

The test was stopped at 87.5% duty cycle because the die temperatures were close to the maximum operating temperatures. It is important to point out that although Q2 is switched off, the temperature measured for it is due to heating effects of the nearby conducting devices. Figure 6.36 shows the maximum prototype component temperature distribution with increasing Duty cycle. From 86% Duty Cycle, the bare dies' temperatures increase sharply with slight increase in Duty Cycle. Furthermore, from the graph, the hot winding temperature profile is similar to the SiC MOSFETs' – suggesting good thermal coupling between both components.

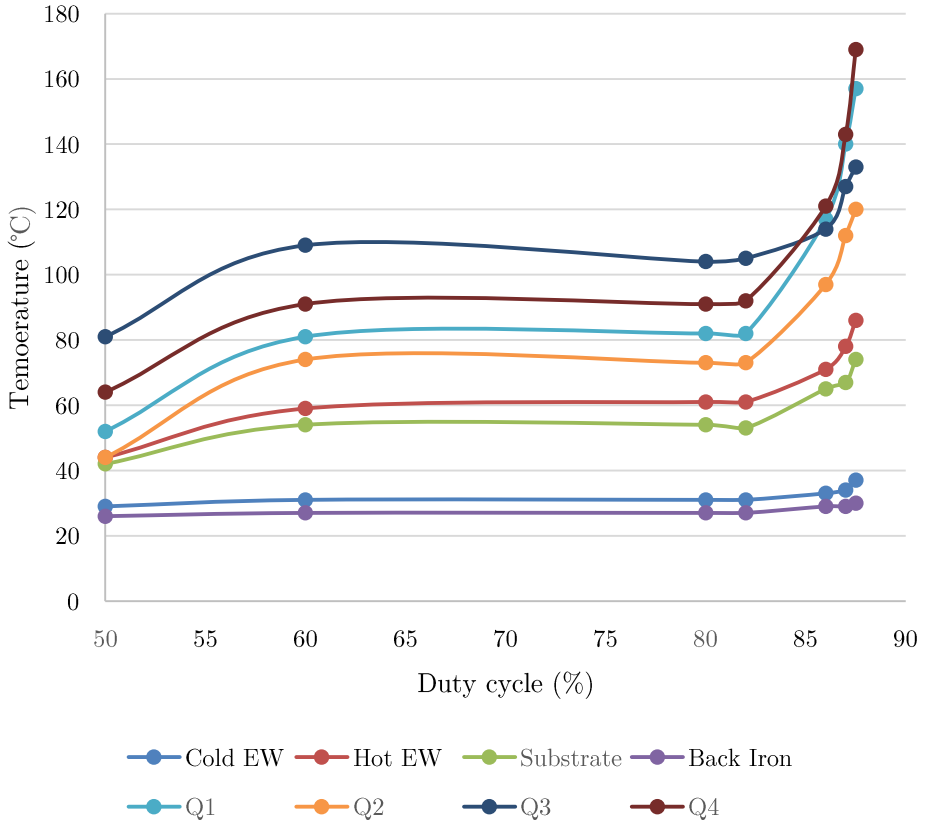


Fig 6.36: Component temperature with varying Duty Cycle

After 86% duty cycle, the temperatures of the bare dies increase rapidly due to increased losses through the devices. With the devices conducting for a longer period the effects of thermal drift due to the pores in the solder structure.

Compared to the substrate temperature reading at 87.5% duty cycle (maximum temperature conditions), for less than 10mm, a temperature difference of 46°C is measured. This highlights the high thermal flux of the bare dies and the prominent thermal path for heat dissipation. Although the AlN substrate acts as a heat spreader, it is evident that the copper winding offers a less resistive thermal path for heat dissipation hence the high temperature readings recorded in the lower half of the substrate. The heat flow is predominantly vertical through the substrate and into copper winding rather than laterally across substrate. Also, the substrate thermocouple position is away from the maximum substrate temperature. Furthermore, the hot end winding is more responsive to thermal changes in the MOSFET compared to the substrate the devices are mounted on. This further shows the heat from the PE module is dissipated through the fan cooled winding.

6.5. Conclusion

Prototype 2 was successfully manufactured and tests to validate the software simulations were performed. The thermal test was aimed at investigating the heat distribution in the PE module and the fan cooled winding. The switching test investigated the PE module switching at high frequencies. It also explored the thermal distribution in the sample when specific switches were energised. Although measures were undertaken to ensure the Prototype assembly process produced a similar sample to the ANSYS modelled geometry, there were slight variations in both geometries. The most visible variation was the solder layer structure - with the simulation model containing no voids. This attachment layer proved to be critical in heat dissipation from the PE module to winding.

For the thermal tests, the MOSFETs' body diodes were used for conduction resulting in higher device losses and temperatures. The fan speed was modulated to regulate the coolant flow rate and investigate the temperature distribution in the sample with respect to varying flow rates. Also, the thermal resistance of the die to inlet coolant was measured for the flow rates analysed. Diodes Q3 and Q4 recorded higher temperatures compared to Q2 and Q3 due to the presence of more voids in the solder structure around their location. This highlighted the importance of the solder layer as a heat transfer medium with temperature differences up to 16°C for the devices showing similar losses. Despite this, the results

were favourable with good agreement between experimental and simulation results – the comparison between both results is analysed in Chapter 7. The major limitation in heat dissipation was the choice of air as the coolant. Its low thermal conductivity limits the amount of heat it can dissipate. Utilising a higher thermal conductivity coolant like water or non-conductive oils will produce a more effective thermal management solution.

The temperature distribution on the PE module shows the maximum temperatures are concentrated around the devices (lower half of the substrate). This means that the top half of the substrate where the DC-link capacitors and steel connectors are located can be redesigned to reduce the total surface area. A cascaded structure could be implemented with a substrate housing the capacitors and connectors mounted on the devices' substrate.

The switching tests showed the PE module's performance at high switching frequencies. The tests highlight how the loss distribution among the devices change the heat transfer from the PE module to the fan cooled winding. Changes in the duty cycle also resulted in the redistribution of losses amongst the devices.

The next chapter analyses the simulation and experimental results and offers explanations for discrepancies in the results, if any. It also highlights how small variations in both geometries affect the results.

Chapter 7

Analysis of Experimental and Simulation Results

7.1. Introduction

In this chapter, the simulation and experimental results are analysed. It also highlights the effects of subtle changes in geometry and initial assumptions made for the simulation boundary conditions on the results. This chapter also aims to investigate the efficacy of CFD modelling as an appropriate tool for thermal validation.

7.2. Comparison between Simulation and Experimental Results

The thermal tests described in Chapter 5 validate the software simulation results. The simulated geometry differs slightly from the manufactured experimental sample. This was due to the complexity and computational cost of modelling certain geometries. Also, the boundary conditions were set to closely replicate the experimental conditions. However, assumptions were made (outlined in Chapter 5) leading to differences in results between the CFD and experimental results. The individual components are analysed based on both simulation and experimental results.

7.2.1. Bare Dies

From Chapter 5, the simulation results show the windings act as a heat sink for heat dissipation from the PE module. The power devices were the hottest components in the system with devices Q1 and Q2 producing the highest temperatures. The massive lateral temperature gradient on the substrate (of both simulated and experimental results) also highlights the large heat flux on the devices and that the prominent path for heat transfer from the PE module to the winding is through the intervening solder attachment layer. From the experimental results, Q3 and Q4

produced the hottest temperatures. Figure 7.1 shows the difference in temperatures between the CFD and experimental results.

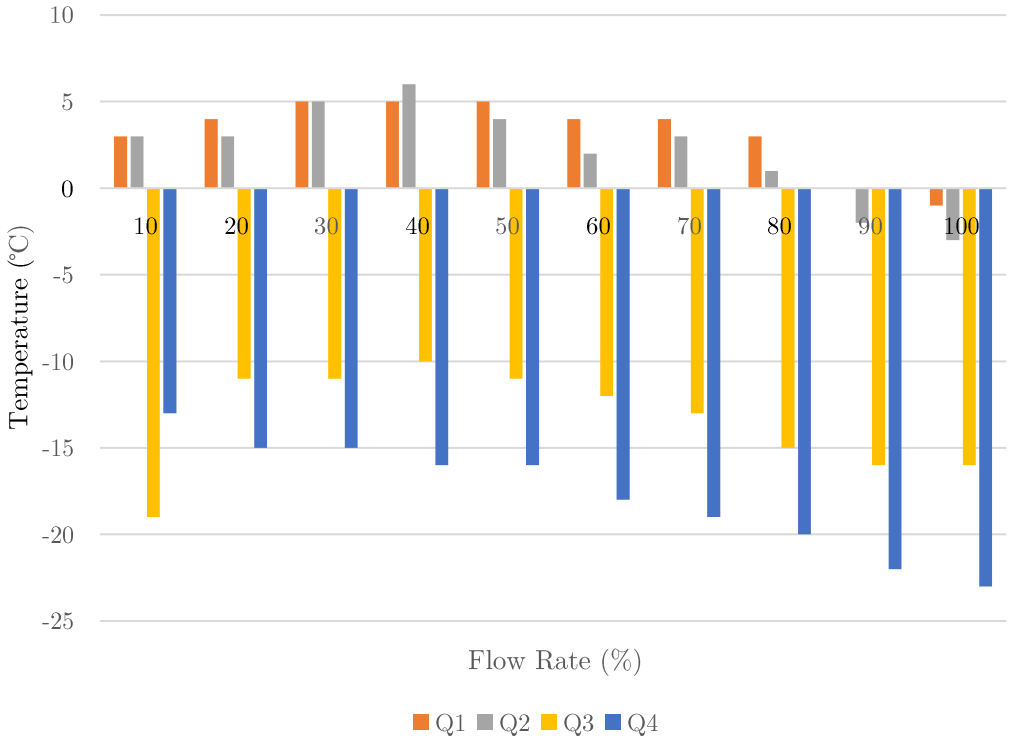


Figure 7.1: Differences in temperature between CFD and Experimental results for the bare dies

For Q1 and Q2, the maximum temperature difference between the CFD and experimental results is 6°C - with the CFD results recording the higher temperature. However, for Q3 and Q4, the experimental result temperatures are higher with the difference between both temperatures (CFD and experimental) reaching up to 23°C - representing an 18% increase in temperature. The maximum percentage of temperature drop from the SiC device junction temperature to the inlet coolant temperature for the experimental and CFD results is 79% and 75% respectively. This suggests a very high accuracy between both experimental and simulation

results with only a 4% difference between both results. The only major difference between the CFD and experimental result temperatures is that Q1 and Q2 have the highest temperatures in the CFD simulation with Q3 and Q4 slightly lower while the highest temperatures from the experimental results are recorded for Q3 and Q4. However, this can be attributed to assumptions made for the solder layer geometry modelled in the CFD simulation.

From Figure 7.1, it can also be observed that the difference in temperatures between the CFD and experimental samples for Q3 and Q4 increases with increasing flow rate. The large discrepancies in temperatures are only recorded for Q3 and Q4 with Q1 and Q2 showing a high accuracy between the simulated and experimental results. The difference in temperatures between the experimental and CFD simulation for Q3 and Q4 may be attributed to the quality of the solder attachment layer between the substrate and end winding. From Figure 6.13 (Chapter 6), Q3 and Q4 are mounted on a poor solder layer location riddled with voids in the structure. This increases the thermal resistance between these devices and the windings, ultimately leading to higher temperatures for these devices compared to Q1 and Q2. Q1 and Q2 have the highest temperatures in the simulation result because the devices are mounted on only two copper turns for heat dissipation compared to the three turns which Q3 and Q4 are mounted on. This means the devices (Q1 and Q2) have a smaller heat sink area compared to Q3 and Q4. The thermal

coupling due to Q1 and Q2 being in close proximity also leads to the increased temperatures recorded for Q1 and Q2. However, from the simulation results, it is evident that the slight difference in heat sink area and thermal coupling between devices only results in minimal temperature differences between the devices. The main factor that affects temperature distribution between the devices for equal input losses remains the quality of the solder layer, with the junction to heatsink (copper winding) thermal resistance increased due to the presence of voids in the solder layer. This ultimately leads to poor heat distribution between the substrate and copper winding.

7.2.2. Substrate

The substrate temperatures recorded for both experimental and CFD analysis prove fairly consistent with a maximum temperature difference of 6°C. This represents a maximum percentage temperature difference between substrate and inlet coolant of 77% and 76% for simulation and experimental results respectively. With a 1% difference in results between simulation and experimental results, this infers a very high accuracy between both results. With the substrate geometry fairly uniform for both experimental and simulation and the assumptions made on the CFD geometry barely affecting the overall temperature distribution in the geometry, the accuracy in results is high – evident in the small difference in temperatures for simulation and experimental results for all flow rates.

Figure 7.2 shows the temperature of the substrate at different flow rates for both simulated and experimental samples.

The probe point on both samples were kept constant (middle of the substrate). The large temperature gradient measured across the substrate shows the heat concentration is at the lower half of the PE module (where the power devices are located). Furthermore, it shows the efficacy of the winding as a heat dissipater. The similarities in results also proves a high accuracy of the CFD model. It also shows the fan speed (flow rate) influences the effective heat transfer performance of the winding, resulting in a change in the heat flux distribution. This leads to heat flowing vertically (through the substrate to the copper winding) instead of spreading across the substrate. This leads to the heat concentration on the lower half of the substrate for both CFD and experimental results.

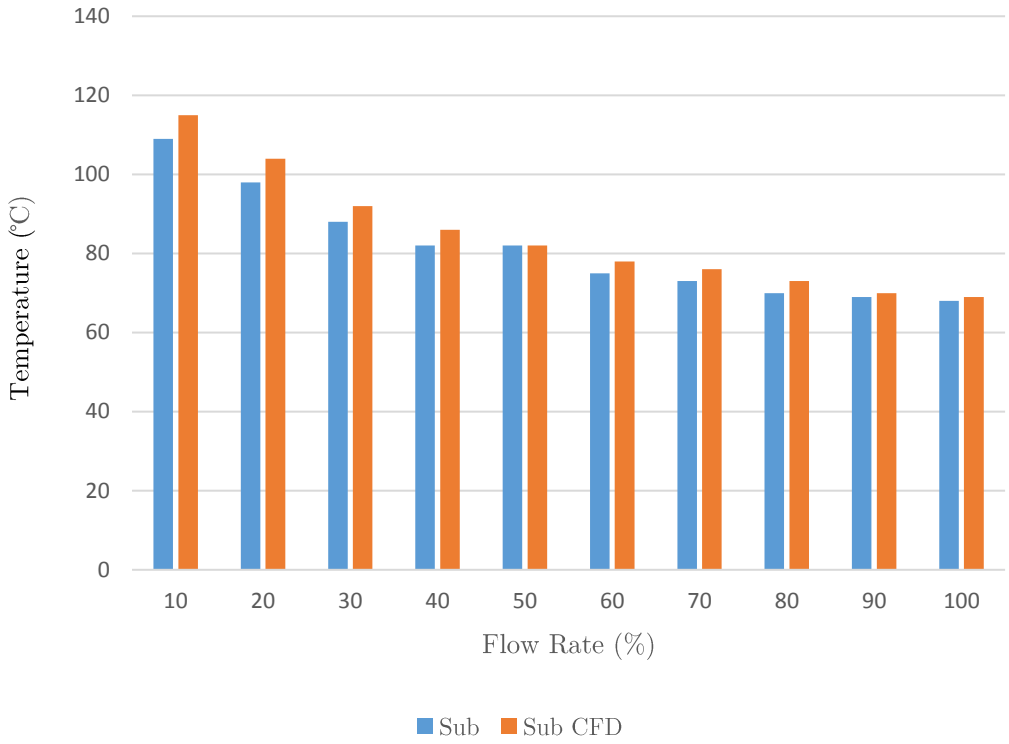


Fig 7.2: Differences in temperature between CFD and Experimental results for the Substrate

7.2.3. Copper Winding

For the coper winding, the probe points during the experimental tests were limited due to assembly of the sample. The CFD results show the hottest point on the winding is the region under the solder layer. However, it was impossible to physically measure this temperature. Figure 5.14 shows the probe points used as point of reference for hot and cold End winding temperatures for both CFD and experimental results.

Comparing simulation and experimental values, the copper winding temperatures show consistent temperatures for the hot and cold end

windings. Figure 7.3 shows the maximum temperatures recorded for both hot and cold End windings from the experimental and CFD samples. The graph shows a high correlation between the CFD and experimental results with only a maximum of 5℃ error for the hot and cold end windings. This represents only a 2% difference between both results for the maximum temperature difference between copper winding and inlet coolant temperatures. With increasing flow rates, the maximum temperature and temperature difference between both CFD and experimental results decrease. The high accuracy of the CFD model is due to heat transfer model for flow across the winding being fairly uncomplicated – with a heating source applied to one end of the winding and the opposite end cooled.

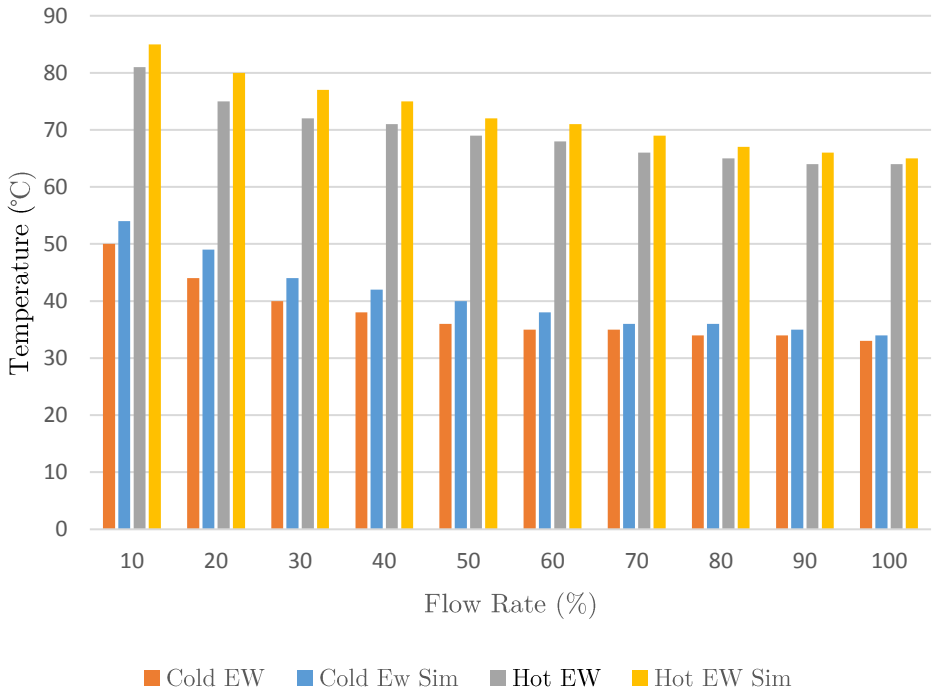


Fig 7.3: Differences in temperature between CFD and Experimental results for the Windings

7.2.4. Back Iron

The 80mm, 0.1mm stacked laminations manufactured for the experimental sample was modelled as a single block in the CFD model geometry. The poor contact between the windings and the tooth restricts its responsiveness to temperature changes from the heat source (bare dies. Figure 7.4 shows the CFD and experimental values for the steady state temperatures at varying flow rates.

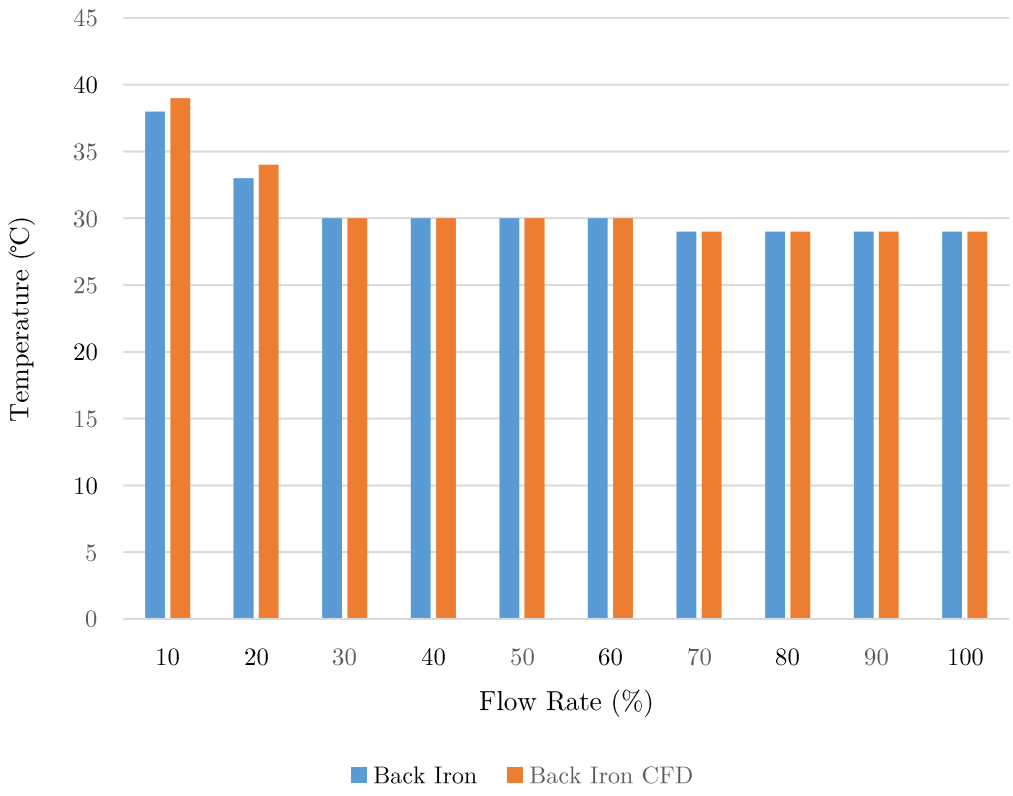


Fig 7.4: Differences in temperature between CFD and Experimental results for the Back Iron

The Back Iron only plays a minor role in heat dissipation from the PE module. Furthermore, the winding to Back Iron is not a critical thermal

path for heat dissipation. The CFD and experimental results show good correlation with a maximum of 1℃ between both values. The results also show the Back Iron temperature only rises slightly above ambient temperature (with a maximum temperature increase of 13℃). Both results also show very little changes in temperature with increasing flow rate – further highlighting the Back Iron's insensitivity to temperature changes.

7.3. Conclusion

The simulation and experimental results show very good correlation for the individual components. The Back Iron, copper winding and substrate show a small difference between experimental and simulation results, suggesting high accuracy in the CFD simulations. It also suggests the assumptions made for boundary conditions and geometry simplification in the CFD model were accurate. However, the maximum temperature recorded for the experimental sample, namely in devices Q3 and Q4, was over 20℃ higher than the CFD results. Compared to other IMD components with a maximum of 6℃ difference between experimental and simulated values, this discrepancy was only observed in devices Q3 and Q4. This was primarily due to the solder layer modelled in the CFD geometry. The presence of voids in the experimental sample led to an increase in the thermal resistance between the winding and substrate ultimately leading to higher temperatures for Q3 and Q4.

The next chapter presents the overall conclusion of the thesis and recommendations for future work on End Winding mount IMD.

Chapter 8

Conclusion and Future Work

8.1. Conclusion

This thesis investigates a novel winding mount integration configuration. It presents already established Integrated Motor Drive concepts and their potential advantages and disadvantages. The concepts analysed are - surface mount integration, end plate mount integration and stator iron mount integration. The benefits of these IMD concept include high power density motor drives, lower losses, modular operation and lower lifetime and maintenance costs.

The most popular of these IMD options is the surface mount integration – were the PE module is mounted on the machine enclosure. This is due to its ease of implementation compared to the other IMD options. Furthermore, the PE module – which is the most delicate component, is sectioned away from the machine. This arrangement usually has a specialised cooling system for the motor drive with the machine cooled after or not at all. The overall volume of this motor drive configuration is usually large compared to other options.

The end plate and Back Iron integration options have the PE module mounted inside the machine enclosure. This is more complicated to implement due to the PE module in close proximity to other heat sources – the Back Iron and copper winding. These configurations offer a more power dense option compared to the surface mount option. However limitations in this configuration include, long connecting cables from the PE module to the machine and complicated cooling system.

With the PE module in the machine enclosure, the devices are subjected to high temperatures and vibration levels. Wide band gap devices are presented as the future of semiconductor devices in industry. This is due to their high power ratings, thermal conductivity and operating temperature compared to industry standard Silicon devices.

An End winding mount IMD concept is presented as a novel integration configuration in motor drives. The PE module is mounted on the machine end windings with the latter serving as a heat sink for the PE module. A simple initial prototype was manufactured to investigate the feasibility of the proposed concept, especially from a thermal perspective. Software simulation methods were used for the initial thermal analysis. Thermal resistance networks offer a quick analysis method by utilising thermal nodes to create heat transfer paths. Its limitation is the input data it heavily relies on for accuracy. Also, the accuracy of the model depends on the number of thermal nodes created further complicating the model. FEA offers a 3D model of the geometry simulated. It improves on the Lumped Parameter model by providing a holistic thermal analysis with investigation of critical thermal paths and potential hot spots in the system. Its limitations include a high computational cost compared to Lumped Parameter models and a heavy reliance on the heat transfer coefficient values inputted.

CFD analysis produces the most accurate result of the three numerical analysis methods by offering both air flow and heat transfer modelling. However, for large scale, multi domain models like an IMD, the computational cost of CFD is relatively high.

The initial thermal analysis was performed to investigate the heat distribution in the system and the critical thermal paths for heat

dissipation. After manufacturing the first Prototype it became evident that the major challenge was in the Prototype assembly. Silver sintering was used for the PE module to End winding attachment. Although silver sintering offers advantages in high temperature operation, its mechanical strength was very weak compared to solder (up to five times less). Also, the silver sintering process is not optimised for large areas resulting in the weakness of the sinter layer. For pressure assisted sintering – which offers higher mechanical strength compared to pressure-less silver sintering, the high pressures the PE module was subjected to resulted in the damage of the substrate and power devices.

Solder offers a compromise between high mechanical strength and thermal conductivity. Although theoretically silver sintering promises higher mechanical strength, operating temperature and thermal conductivity, in reality, solder offers a mature option with tested high mechanical strengths for large area bond. The voids present in the solder structure was found to adversely affect the substrate to end winding thermal resistance leading to high device temperature.

Improvements from the first prototype also included – using laminations for the Back Iron to reduce losses, manufacturing a bespoke copper winding to ensure a flat surface for mounting the PE module and designing and manufacturing a functional PE module. The first prototype solely focused on the heat transfer from the heat source (bare die) to the

winding. By utilising a functional PE module, current can be driven (and controlled) through the winding – akin to a functional motor drive.

The results – both simulation and experimental, demonstrate the feasibility of the winding mount configuration concept as a viable option for drive integration. The experiment was focused on the thermal and mechanical challenges of close coupling integration and it addresses the inaccurate assumption that the power electronics fails near other heat sources. The effectiveness of the attachment layer as a thermal path between the winding and substrate is determined by the quality of the layer as opposed to its material properties. This was highlighted by the minimal changes in component temperature when the attachment layer was changed from solder to silver. Also, the thermal coupling between the devices was minimal despite the devices close to each other, further demonstrating the effectiveness of the winding and cooling system for heat dissipation.

During the switching tests to investigate the functionality of the PE module, current was successfully controlled and driven through the windings. Although this thesis does not focus on optimising control techniques, it demonstrates the functionality of the PE module at high frequencies. It also demonstrates the prototype is able to operate under uneven thermal load conditions. With only specific devices conducting,

the solder layer is subjected to uneven thermal stresses similar to an actual motor drive.

Changing the coolant from air to a higher thermal conductivity fluid like water or mineral oils was understood to produce substantial improvements in heat dissipation in the system. Even at low speeds, the high thermal conductivities of these fluids improved heat dissipation compared to air. However, the cost, complexity and added losses associated with implementing this cooling system especially for the scope of this thesis proved obstructive.

8.2. Future Work

Despite the initial success in validating - through simulation and experimental results, the end winding mount IMD concept, ample further work needs to be done to take the concept prototype to a complete IMD.

- The most challenging aspect of developing the End winding mount IMD concept was the thermo-mechanical management. Physically attaching the PE module on the heat sink to provide both thermal and electrical connection between both components was complicated. In the final prototype manufactured, solder was used to provide both thermal and electrical connection between the winding and PE module. However, the presence of voids in

the structure invariably compromises efficient heat transfer from the PE module to end winding. Silver sintering offers a more uniform structure with less voids. However, its low mechanical strength for large areas remains problematic. Further research into improving silver sintering techniques – especially pressure-less sintering for large areas, will ensure efficient heat transfer from the PE module to winding.

- FEA on the long term thermo-mechanical stress effects and reliability of the solder layer junction should be investigated. With thermal cycling of the PE module, the solder layer is subjected to high thermal stress levels. This could also potentially lead to more void formation in the solder layer leading to more system losses.
- With the quality of the attachment layer between the PE module and winding critical in heat dissipation from the PE module, 3D printed copper windings on the PE module offers a possibility to bypass an extra thermal resistance node further increasing heat distribution in the system. Initial work on 3D printing metals on copper have been promising and could offer a realistic solution especially for the proposed concept. Moreover, by changing the grain structure and orientation of the copper, the intrinsic properties of the material can be altered leading to potential changes in resistivity and thermal conductivity. Full control over the size and shape of the turns can also be guaranteed with 3D

printing. This adapts the windings to the confined space in the machine enclosure and the copper tracks on the bottom side of the substrate.

- A fully functional driver circuit should be developed and integrated in the machine enclosure. The driver circuit and the PE module could be designed and manufactured as a single unit and mounted on the end winding.
- Finally, a full end winding mount IMD should be manufactured.

References

[1] Bartos F. J., “Combination motors and drives move to make their mark” Control Engineering Online, December 2000, http://www.csemag.com/single-article/combination-motors-and-drives-move-to-make-their-mark/d9a8ab08897749f02e39653c06a6cc49.html

[2] Bartos, F.J., "Integrated Motor-Drives Seek Wider Market, User Acceptance," Control Engineering, pp. 19-23, December 2000.

[3] Viorel. I. A., Szabo. L., Ciorba. R. C., “Integrated motor and control unit for industrial variable speed drive” Accessed November 2015 http://citeseerx.ist.psu.edu/viewdoc/download?doi=10.1.1.301.2182&rep=rep1&type=pdf

[4] Hornberger J. M, Cilio E., Schupbach R. M., et al, “A high-temperature multichip power module (MCPM) inverter utilizing silicon carbide (SiC) and silicon on insulator (SoI) electronics”, Power Electronics Specialists Conference PESC, 2006, pp. 1-7

[5] Babb M., Bartos F., "Integrated motor drive combinations," Control Engineering Europe, 57, (21), 2001. pp. 66

[6] Wang J., Li Y., Han Y., “Evaluation and design for an integrated modular motor drive (IMMD) with GaN devices”, Energy Conversion Congress and Exposition (ECCE), 2013. IET, pp. 4318 – 4325

[7] Agarwald S. H., Ryu S. H., Krishnaswami S., et al., “a review of high power, high temperature SiC devices”, High Temperature Electronics Conference HITEC 2006, May 2006.

[8] Williamson S., Jackson D.C., "Integrated drives for industrial applications", Proc. of PCIM'99, Intelligent Motion, pp. 9-13, 1999.

[9] Thoegersen P., Blaabjerg F., "Adjustable speed drives in the next decade. The next step in industry and academia", Proc. of PCIM '00, Intelligent Motion, pp.95-104

[10] Vas P., Dury W., "Electrical machines and drives: present and future", in Proc. of Electrotechnical Conference (MELECON '96), 1, pp. 67-74

[11] Brown N. R., Jahns T. M., Lorenz R. D., “Development of a converter for an integrated modular motor drive”, Centre for Power Electronics Systems (CPES) 2007. CPES, pp. 419-425

[12] Nie Z., Emadi A., “Integrated converters for switched reluctance motor drives”, Power Electronics and Motion Control Conference, 2004. IPEMC 2004, 2, pp. 487 – 490.

[13] Marz M., Schletz A., Eckardt B., Egelkraut S., Rauh H., “Power electronics system integration for electric and hybrid vehicles”, Integrated Power Electronics Systems (CIPS), 2010 6th International Conference IEEE. pp. 1-10

[14] Mohammed O. A., Liu S., Liu Z., “Physical modelling of PM synchronous motors for integrated coupling with machine drives”, IEEE Transactions on Magnetics, 2005. 41, (5), IEEE. pp. 1628 – 1631

[15] Zeng L., Chen X., Nong X., San X., “FE-based physical model of LPMBDCM for integrated motor drive system analysis”, Innovative Computing Information and Control, 2008. ICICIC '08. 3rd International Conference. IEEE. p. 581

[16] Klumpner C., Nielsen P., Boldea I., et al., “A new matrix converter motor (MCM) for industry applications”, IEEE Trans. on Industrial Electronics, 2002. 49, pp. 325-335

[17] Haghbin S., Khan K., Zhao S., et al., “An integrated 20-kW motor drive and isolated battery charger for plug-in vehicles”, IEEE Transactions on Power Electronics, 28, (8), 2013. pp. 4013 – 4029

[18] Haghbin S., Thiringer T., Carlson O., “An integrated split-phase dual-inverter permanent magnet motor drive and battery charger for grid-connected electric or hybrid vehicles”, 20th International Conference on Electrical Machines (ICEM). 2012. IEEE. pp. 1941 – 1947

[19] Pickering S., Thovex F., Wheeler P., et al., “Thermal design of an integrated motor drive”, IECON 2006 - 32nd Annual Conference on Industrial Electronics .IEEE. pp. 4794 – 4799

[20] Tenconi A., Profumo F., Bauer S. E., et al., “Temperatures evaluation in an integrated motor drive for traction applications”, IEEE Transactions on Industrial Electronics, 2008. 55, (10), IEEE. pp. 3619 – 3626

[21] Wolmarans J. J., Gerber M. B., Polinder H., et al., “A 50kW integrated fault tolerant permanent magnet machine and motor drive”. IEEE Power Electronics Specialists Conference 2008. IEEE. pp. 345 – 351

[22] Biswas P. S., Das N., Biswas S. K, “Design consideration of an integrated induction motor drive to replace auxiliary dc motors in locomotives”, International Conference on Power Electronics and Drives Systems 2005. 2. IEEE. pp. 872 – 875

[23] Shakweh Y., Owen G.H., Hall D.J., et al., “Plug and play integrated motor drives,” in Proc. of IEE Power Electronics, Machines and Drives Conference (PEMD’02), 2002. pp. 655-661

[24] Farina, F.; Rossi, D.; Tenconi, A.; Profumo, F.; Bauer, S.E., "Thermal design of integrated motor drives for traction applications," Power Electronics and European Applications, 2005, pp.10.

[25] 'Schneider Lexium 32i' http://download.schneider-electric.com/files?p_Reference=0198441113956-EN&p_EnDocType=User%20guide&p_File_Id=681840597&p_File_Name=LXM32iECT_Manual_V100_EN.pdf, Accessed November 2015.

[26] 'Danfoss VLT DriveMotor FCM 300' http://www.danfoss.com/NR/rdonlyres/40FA1C95-CFB6-4BA1-A69D-D36F61436B59/0/FCM300_FactSheet_PF009A02.pdf, Accessed November 2015.

[27] 'VEMoDRIVE – variable speed drives' http://www.vem-group.com/fileadmin/content/pdf/Download/Brosch%C3%BCren/Flyer_VEM-motors/28_PB_en.pdf, Accessed November 2015.

[28] 'Innovative motor technology for hybrid and electric vehicles' http://w3.siemens.com/topics/global/de/elektromobilitaet/PublishingImages/antriebe-pkw/pdf/sivetec-mrs-mri-siemens_en.pdf, Accessed November 2015.

[29] 'Lenze Inverter Drives 8400 motec' http://www.actechdrives.com/PDF/Lenze/Lenze-8400-Motec-Inverters.pdf, Accessed November 2015.

[30] 'Siemens Multiple Drive for Vertical Mills' http://www.industry.siemens.com/drives/global/en/gear-units/application-specific-gear-units/vertical-mills/flender-multiple-drive/pages/default.aspx, Accessed November 2015.

[31] Wheeler P. W., Clare J. C., Apap M., et al., “An integrated 30kW matrix converter based induction motor drive”, PESC '05. 2005. IEEE 36th Power Electronics Specialists Conference, IEEE. pp. 2390 – 2395

[32] Wheeler P. W., Rodriguez J., Clare J. C., et al., “Matrix converters: a technology review”, IEEE on Industrial Electronics, 2002. 49, (2), pp. 276-288.

[33] ‘UQM and Kinetics present integrated motor and multi-speed transmission for commercial Evs’ https://chargedevs.com/newswire/uqm-and-kinetics-present-integrated-motor-and-multi-speed-transmission-for-commercial-evs/, Accessed November 2015

[34] ‘Bonfiglioli 600D - Electric powertrains for lightweight vehicles’ http://www.bonfiglioli.co.uk/en-gb/mobile/products/electric-solutions/powertrains/product/600d-electric-powertrain/, Accessed November 2015

[35] ‘E-Trac IMD integrated motor drive’ http://www.southernpower.com/pdf/woods/electronic_products_guide.pdf, Aceessed November 2015

[36] Henze, M. “The Integral Motor – a new variable-speed motor drive”, https://library.e.abb.com/public/82be3ed09497afb3c1256ddd00346fb6/04-08m181.pdf, Accessed November 2015

[37] Fraser, A. “IN-WHEEL ELECTRIC MOTORS - The packaging and integration challenges,” http://www.proteanelectric.com/wp-content/uploads/2013/07/In_Wheel_Electric_Motors_AFraser_ProteanV4.pdf Accessed Apr. 12, 2015.

[38] Perovic, D. “Making the impossible, possible – Overcoming the design challenges of in wheel motors,” EVS26 International Battery, Hybrid and Fuel Cell Electric Vehicle Symposium, 2012, 5, pp 514-519.

[39] Mueller S. I., Nellis G. F., T. M. Jahns, “Model and design of an aircooled thermal management system for an integrated motor-controller”, in Proc. of 2005 CPES Power Electronics Seminar, pp. 145-152

[40] ‘Integrated IE4 motor-drive is 'up to 40% smaller' Yaskawa 4kW http://en.ofweek.com/new-products/Integrated-IE4-motor-drive-is-up-to-40-smaller-23406 , accessed November 2015

[41] ‘Baldor SmartMotor’ http://www.baldor.com/Shared/manuals/750-902.pdf, Accessed November 2015

[42] ‘Getting more from the motor’ http://eandt.theiet.org/magazine/2015/02/efficient-motor-drives.cfm, Accessed November 2015

[43] ‘Grundfoss E-pumps’ https://us.grundfos.com/content/dam/GPU/Literature/LCSE-LFE/LCBSSL04-0614-Grundfos-E-Pump-Brochure.pdf, Accessed November 2015

[44] ‘Rockwell Automation – Kinitex 6000’ http://literature.rockwellautomation.com/idc/groups/literature/documents/td/gmc-td001_-en-p.pdf, Accessed November 2015

[45] ‘Variable speed motor or geared motor’ http://www.leroy-somer.com/documentation_pdf/3415_en.pdf, Accessed November 2015

[46] ‘MOVIMOT® gearmotor with integrated frequency inverter’ http://www.seweurodrive.com/produkt/movimot-gearmotor-with-integrated-frequency-inverter.htm, Accessed November 2015

[47] 'Lenze smart motor M300' http://www.lenze.com/fileadmin/lenze/documents/en/catalogue/CAT_MT_MS_13449851_en_GB.pdf, Accessed November 2015

[48] Miller. T. J., "Electrical Energy Storage for Vehicles: Targets and Metrics" http://www.arpa-e.energy.gov/sites/default/files/documents/files/Ford%20Presentation.pdf, Accessed November 2015

[49] 'Alpha step series' http://www.orientalmotor.com/products/stepper-motors/ASX-series-all-in-one-stepper-motor.html, Accessed November 2015

[50] INMOCO http://www.inmoco.co.uk/pegasus_integrated_servo_system, Accessed November 2015

[51] 'AXOR fastback' http://www.motioncontrolproducts.com/pdfs/axor-fast-back-brushless-motor-with-drive.pdf, Accessed November 2015

[52] Johnson R. W., "A review of high temperature electronics packaging," Proceedings of the 1989 ' High Temperature Electronics Conference.

[53] Olesen K., Bredtmann R., Eisele R. , ""ShowerPower" new cooling concept for automotive applications", Automotive Power Electronics. 2006

[54] Hearn J. A., "Future packaging technologies for hybrid electronics in automotive underhood environment," Proceedings of the 1989 High Temperature Electronics Conference, 1989.

[55] Stolpa S., "Turbulent heat transfer". Department of Aerospace and Mechanical Engineering, University of Notre Dame, Notre Dame, USA, April 2004.

[56] McClusky P., Grzybowski R. R., et al., "Packaging of electronics for high temperature applications," International Journal of Microcircuits and Electronic Packaging, 1997. 20, (3)

[57] Mantooth H. A., Mojarradi M. M., Johnson R. W., “Emerging capabilities in electronics technologies for extreme environments. Part I - High temperature electronics”, IEEE Power Electronics Society Newsletter, issue 1, 2006.

[58] Şenyıldız T., Eisele R. , Olesen K., “Thermal management concepts for power electronic modules” Danfoss Silicon Power GmbH, 2003.

[59] Liang Z., Ning P., Wang F., “Advanced packaging of sic power module for automotive applications," Energy Conversion Congress and Exposition (ECCE), Sept. 2013 IEEE, pp.2884,2891, 15-19.

[60] Liang Z, Li L., "HybridPACK2 - advanced cooling concept and package technology for hybrid electric vehicles," Vehicle Power and Propulsion Conference, Sept. 2008. VPPC '08. IEEE, pp.1, 5, 3-5

[61] Haque S., Xing K.; Suchicital C., et al., "Thermal management of high-power electronics modules packaged with interconnected parallel plates," Semiconductor Thermal Measurement and Management Symposium, Mar 1998. SEMI-THERM Proceedings 1998, Fourteenth Annual IEEE, pp.111, 119, 10-12

[62] Yong W., Guang Y., Yong-Kyu Y., et al., "Active cooling substrates for thermal management of microelectronics," Components and Packaging Technologies, IEEE Transactions on , 28, (3), 2005. pp.477-483

[63] Ozpineci B., Tolbert L. M., Islam S. K., et al., “Testing, characterization and modelling of SiC diodes for transportation

applications", IEEE Power Electronics Specialists Conference 2002. IEEE. pp. 1673–1678

[64] Ghandhi S. K., "Semiconductor power devices", Wiley, 1977 republished 1998.

[65] Baliga B. J., "Physics of semiconductor power devices". JWS Publishing, 1996.

[66] Shur M. S., Gaska R., Khan A., Simin G., "Wide band gap electronic devices", Fourth IEEE International Caracas Conference on Devices, Circuits and Systems 2002. IEEE pp. 51-58

[67] O'Connor J., Smiltens J., "Silicon carbide, a high temperature semiconductor", New York: Symposium Publications Division, Pergamon Press, 1960.

[68] Hudgins J. L., Simin G. S., Khan M. A., "A new assessment of the use of wide bandgap semiconductors and the potential for GaN", Power Electronics Specialists Conference, 2002.4, pp. 1747-1752

[69] Hornberger J., Lostetter A. B., Olejniczak K. J., et al., "Silicon-carbide (SiC) semiconductor power electronics for extreme high-temperature environments", Aerospace Conference, 2004. Proceedings, 4, IEEE. pp. 2538 – 2555

[70] Trivedi M., Shenai K., "Performance evaluation of high-power wide band-gap semiconductor rectifiers", Journal of Applied Physics, 1999. 85, (9), pp. 6889-6897

[71] v. Muench M., Hoeck P., Pettenpaul E., IEEE Int. Electron Device Mtg. Tech. Dig. 337 1977.

[72] Ebert W., Vescan A., Borst T. H., Kohn E., IEEE Intl. Electron Device Mtg. Tech. Dig. 419 1994.

[73] Shin M. W., Trew R. J., Bilbro G. L., “High temperature DC and RF performance of p-type diamond MESFET: comparison with n-type GaAs MESFET”, IEEE Electron Device Letters, 15, pp. 1994. 292-294

[74] Weitzel C. E., Palmour J. W., Carter C. H., et al., “Silicon carbide high power devices”, IEEE Transactions, Electron Devices, 1996. 43, (10), pp. 1732-1741

[75] Ozpineci B., Chinthavali M. S., Tolbert L. M., “Enhancing power electronic devices with wide band gap semiconductors”, International Journal of High Speed Electronics and Systems, 2006 APA. pp. 545-556

[76] Ozpineci B., Tolbert L. M., “Comparison of wide-band gap semiconductors for power electronics applications”. United States. Department of Energy, 2003.

[77] Shenai K., Scott R. S., Baliga B. J., “Optimum semiconductors for high power electronics”, IEEE Trans Electron Devices, 36, (1811), 1989.

[78] Bhalla A., Chow T. P., “Examination of semiconductors for bipolar power devices”, Inst Phys Conf Ser, 137, (621), 1994.

[79] Bhalla A., Chow T. P., “Bipolar power device performance: dependence on materials, lifetime and device ratings”, in: Proceedings of the 6th International Symposium on Power Semiconductor Devices and ICs, 1994. pp. 287-292

[80] Baliga B. J., “Power semiconductor device figure of merit for high frequency applications”, IEEE Electron Device Letters, 1989. 10, (10), pp. 455-457

[81] Chow T. P., Tyagi R., “Wide bandgap compound semiconductors for superior high-voltage power devices”, IEEE Trans Electron Devices, 41, (8), 1994. pp. 1481-1483

[82] Chow T.P., Khemka V., Fedison J., et al., “SiC and GaN bipolar power devices”, Solid-State Electronics, 2000. 44, (2), pp. 277-301

[83] Mishra U., “Compound semiconductors; GaN and SiC, separating fact from fiction in both research and business” http://www.apec-conf.org/wp-content/uploads/2014/01/2_APEC2013Plenary_Compound_Semiconductors_GaN___SiC_Mishra_Transphorm.pdf Accessed 10 Apr, 2015

[84] Trivedi M., Shenai K., “High temperature capability of devices on Si and wide bandgap materials”, Industry Applications Conference, 1998. IEEE, 2, pp. 959-962

[85] Microsemi PPG, “Gallium nitride (GaN) versus silicon carbide (SiC) In the High Frequency (RF) and power switching applications” http://www.digikey.co.uk/Web%20Export/Supplier%20Content/Microsemi_278/PDF/Microsemi_GalliumNitride_VS_SiliconCarbide.pdf?redirected=1 Accessed 08 Apr, 2015.

[86] Extance A., “SiC and GaN power devices jostle to grow their role”, Yole Development, Issue 9, 2013 http://www.yole.fr/iso_upload/mag/powerdev_april2013_ir.pdf 09 Apr, 2015

[87] Tolbert L. M., Ozpineci B., King T. J., Cambell J. B., et al., “Power electronics for distributed energy systems and transmission and distribution applications”, 2005.

[88] Pearton S. J., Zolper J. C., Shul R. J., et al., “GaN: processing, defects, and devices,” Journal of Applied Physics, 1999. 86, (1)

[89] Dang G. T., Zhang A. P., et al., “High-voltage GaN schottky rectifiers,” IEEE Transactions on Electron Devices, 2002. 47, (4), pp. 692–696

[90] Hudgins J. L., Simm G. S., Khan M. A., “A new assessment of the use of wide bandgap semiconductors and the potential of GaN,” The 33d Annual IEEE Power Electronics Specialists Conference (PESC02), 2002. pp. 1747–1752

[91] Trivedi M., Shenai K., “Performance evaluation of high-power wide bandgap semiconductor rectifiers” American Physics Institute Journal of Applied Physics, 1999. 85, (9), pp. 6889–6897

[92] Benţia I., Ruba M., Szabó L., “Modular electrical machines – a survey” Proceedings of the International Scientific Conference MicroCAD, 2010.

[93] van der Duijn Schouten, N.P.; Gordon, B.M.; McMahon, R.A.; Boger, M.S., "Integrated drives as single-phase motor replacement," Industry Applications Conference, 1999. Thirty-Fourth IAS Annual Meeting. Conference Record of the 1999 IEEE, 2, pp.922, 928

[94] März M.: Technology Choices for Automotive Applications. Int. Conf. on Automotive Power Electronics (APE), Paris, 2007

[95] Klumpner C., Blaabjerg F., Thogersen P., “Evaluation of the converter topologies suited for integrated motor drives”, 38th IAS Annual Meeting Conference Record of the Industry Applications Conference, 2003, 2, IEEE. pp. 890 – 897

[96] Simon O., Mahlein J., Muenzer M. N., Bruckmarm M., “Modern solutions for industrial matrix-converter applications”, IEEE Transactions on Industrial Electronics, 2002, 49, (2), IEEE. pp. 401 – 406

[97] Pan M. J., Randall C. A., “A brief introduction to ceramic capacitors,” Electrical Insulation Magazine, 2010. 26, (3), pp. 44-50

[98] Randall M., Skamser D., Kinard T., “Thin film MLCC”, in CARTS 2007 Symposium Proceedings, Albuquerque, 2007. NM, pp. 1–12,

[99] Takamizawa H., Utsumi K., Yonezawa M., et al., “Large capacitance multilayer ceramic capacitor”, IEEE Transactions on Components, Hybrids, and Manufacturing Technology, 1981. 4, (4), pp. 345-349

[100] Yano Research Institute, “Capacitor market in japan: key research findings 2009,” Yano Research Institute, Tokyo, Japan, Nov. 2009.

[101] Phillips R., Bultitude J., Gurav A, et al., “High temperature ceramic capacitors for deep well applications”, CARTS International Proceedings, 2013.

[102] Kim W., Shin S. H., Ryu D. S., “Reliability evaluation and failure analysis for high voltage ceramic capacitor”, Advances in Electronic Materials and Packaging, 2001. pp. 286-195

[103] Al Ahmar J., Wiese S., “Fracture mechanics analysis of cracks in multilayer ceramic capacitors”, Electronics System-Integration Technology Conference (ESTC), 2014. pp. 1-15

[104] Teverovsky A., “Insulation resistance and leakage currents in low-voltage ceramic capacitors with cracks”, IEEE Transactions on Components, Packaging and Manufacturing Technology, 2014. 4, (7), pp. 1169-1176

[105] B. Kirisken, H. F. Ugurdag, “Cost-Benefit Approach to Degradation of Electrolytic Capacitors”, Reliability and Maintainability Symposium, pp. 1-6, 2014.

[106] Deshpande R. P., “Capacitors: technology and trends” Tata McGraw-Hill Education, 2012.

[107] Bramoulle M., “Electrolytic or film capacitors”, Industry Applications Conference, Thirty-Third IAS Annual Meeting, 1998. 2, pp. 1138-1142

[108] Parler Jr. S. G., "Deriving life multipliers for electrolytic capacitors," IEEE Power Electronics Society Newsletter, 2004. 16, pp. 11-12

[109] Maddula S.K., Balda J.C., "Lifetime of electrolytic capacitors in regenerative induction motor drives," in Power Electronics Specialists Conference, 2005. pp. 153- 159

[110] Spanik P., Frivaldsky M., Kanovsky A., “Life time of the electrolytic capacitors in power applications”, ELEKTRO, 2014. 233-238

[111] Sarjeant W. J., Zirnheld J., MacDougall F. W., “Capacitors”, IEEE Transactions on Plasma Science, 1998. 26, (5), 1368-1392

[112] Yaohong C., Fuchang L., Hua L., “Study on self-healing and lifetime characteristics of metallized film capacitor under high electric field”, 2011. Pulsed Power Conference (PPC), pp. 711-716

[113] “The new high temperature dielectric film for power capacitors” Accessed November 2015 http://www.birkelbachfilm.de/pdf/datenblaetter/DTF_Teonex_HV_0912.pdf

[114] Caliari L., Bettacchi P., Boni E., et al., “KEMET film capacitors for high temperature, high voltage and high current”, CARTS International Proceedings – ECA, 2013.

[115] Klumpner C., Blaabjerg F., Thogersen P., “Converter topologies with low passive components usage for the next generation of integrated motor drives”, Power Electronics Specialist Conference, PESC '03. 2003 IEEE 34th Annual, 2, IEEE. pp. 568 – 573

[116] Lewandowski A., Jakobczyk P., Galinski M., et al., “Self-discharge of electrochemical double layer capacitors”, Physical Chemistry Chemical Physics, 2013. 22, (15), pp. 8692-8699

[117] Becker H. I., U.S. pat., 2800.616 to General Electric Co., 1957.

[118] Wang G., Zhang L., Zhang J., “A review of electrode materials for electrochemical supercapacitors”, Chemical Society Reviews, 2012. 2, (41), pp. 797-828,

[119] Burke A., “Power sources”, 2000, 91, 37. 2000.

[120] Chen H., Cong T. N., Yang W., Tan C., et al., Prog. Nat. Sci., 19, 291, 2009.

[121] Lambert S.M., Pickert V., Holden J., et al., "Comparison of supercapacitor and lithium-ion capacitor technologies for power electronics applications," 5th IET International Conference on Power Electronics, Machines and Drives (PEMD 2010), April 2010. pp.1,5, 19-21

[122] Neudeck P.G., Matus L.G., “An overview of silicon carbide device technology,” Ninth Symposium on Space Nuclear Power Systems, 1992. pp. 12–16

[123] Casady J. B., Dillard W. C., Johnson R. W., etal., “A hybrid 6H-SiC temperature sensor operational from 25 C to 500 C,” IEEE Transactions on Components, Packaging and Manufacturing Technology, 1996. 19, (3), pp. 416–422

[124] Khazaka R., Mendizabal I., Henry D., et al., "Survey of high-temperature reliability of power electronics packaging components," , IEEE Transactions on Power Electronics, 2015. 30, (5), pp.2456-2464

[125] Funaki T., Balda J.C., Junghans J., et al., "Power conversion with SiC devices at extremely high ambient temperatures," IEEE Transactions on Power Electronics, July 2007. 22, (4), pp.1321, 1329

[126] Bai J. G., Yin J., Zhang Z., et al.,, “High temperature operation of SiC power devices by low-temperature sintered silver die-attachment,” IEEE Trans. Adv. Package., 2007. 30, (3), pp. 506–510

[127] Lei T. G., Calata J. N., Luo S., et al., “Low temperature sintering of nanoscale silver paste for attaching large-area (>100 mm2) chips,” IEEE Trans. Comp. Package. Technol., 2010. 33, (1), pp. 98–104

[128] Savrun E., “Packaging considerations for very high temperature microsystems,” in Proc. 1st IEEE Sens., 2002. 2, pp. 1139– 1143

[129] Das M. K., Sumakeris J. J., Hull B. A., et al., "Drift-free, 50 A, 10 kV 4H-SiC pin diodes with improved device yields", Materials Science Forum, 2005. 483-485, pp. 965-968

[130] ROHM full SiC power Module Data sheet Available http://rohmfs.rohm.com/en/products/databook/datasheet/discrete/sic/power_module/bsm180d12p2c101.pdf Accessed 08 Apr, 2015.

[131] Mitsubishi SiC Power modules. http://www.mitsubishielectric.com/semiconductors/catalog/pdf/SiCPowerModules_E_201409.pdf Accessed Apr 08, 2015.

[132] Schupbach R. M., McPherson B., McNutt T., et al., “High temperature (250 ∘C) SiC power module for military hybrid electrical vehicle applications,” in NDIA Ground Veh. Syst. Eng. Technol. Symp., Aug. 2011, pp. 1–7.

[133] Horio M., Iizuka Y., Ikeda Y., “Packaging technologies for SiC power modules”, Fuji Electric Review, 2012. 58, (2), pp. 75-78

[134] Chen Z., Yao Y., Boroyevich D., et al., "A 1200 V, 60 A SiC MOSFET multi-chip phase-leg module for high-temperature, high-frequency applications," Applied Power Electronics Conference and Exposition (APEC), 2013 Twenty-Eighth Annual IEEE, pp.608-615

[135] Ning P., Lai R., Huff D., Wang F., et al., “SiC wirebond multichip phase-leg module packaging design and testing for harsh environment,” IEEE Trans. Power Electron., 2010. 25, (1), pp. 16–23

[136] Katsis D., Zheng Y., “Development of an extreme temperature range silicon carbide power module for aerospace applications,” in Proc. 39th IEEE Power Electron. Spec. Conf., 2008. pp. 290–294

[137] Yao Y., Chen Z., Lu G.-Q., “Characterization of encapsulants for high-voltage high-temperature power electronic packaging,” IEEE Trans. Components, Packaging and Manufacturing Technology, 2012. 2, (4), pp. 539–547

[138] Yiying Y., Guo-Quan L., Boroyevich D., et al., "Survey of high-temperature polymeric encapsulants for power electronics packaging," . IEEE Transactions on Components, Packaging and Manufacturing Technology, 2015, 5, (2), pp.168-181

[139] Kodani K., Tsukinari T., Matsumoto T., "New power module concept by forced-air cooling system for power converter," Power Electronics Conference (IPEC), June 2010. International, pp.542, 545, 21-24

[140] Johnson R. W., Palmer M., Wang C., et al., "Packaging materials and approaches for high temperature SiC power devices", Advancing Microelectronics, 2004. 31, (1), pp. 8-11

[141] Mustain H. A., Lostetter A. B., Brown W. D., “Evaluation of gold and aluminium wire bond performance for high temperature (500 °C) silicon carbide (SiC) power modules”, Electronic Components and Technology ECTC 2005, 2, pp. 1623-1628

[142] Salmon J. S., Johnson R. W., Palmer M., “Thick film hybrid packaging techniques for 500°C operation,” in Proc. 4th Int. High Temp. Electron. Conf. (HITEC), 1998. pp. 103–108

[143] Jian Y., Zhenxian L., van Wyk J. D., "High temperature embedded SiC chip module (ECM) for power electronics applications," , IEEE Transactions on Power Electronics , 2007. 22, (2), pp.392-398

[144] Bower G., Rogan C. P. E., Kozlowski J., et al., "SiC power electronics packaging prognostics", aerospace conference, 2008. pp. 1-12

[145] Zhenxian L., "Packaging technologies to exploit the attributes of WBG power electronics," IEEE Workshop on Wide Bandgap Power Devices and Applications (WiPDA), 2014, pp. 1-73

[146] Pooch M. H., Dittmer K. J., Gabisch D., "Investigations on the damage mechanism of aluminium wire bonds used for high power applications," in Proc. Eur. Conf. Electr. Packaging Technol., 1996. pp. 128–131

[147] Chen L., Neudeck P. G., "Thick and thin film materials based chip level packaging for high temperature SiC sensors and devices," Tech. Rep., AYT/NASA Glenn Research Center, 2001.

[148] Cressler, J. D., Mantooth H. A.,"Extreme Environment Electronics" (CRC Press, Florida, 2012)

[149] Cheng, C.H.; Hsiao, H.L.; Chu, S.I.; Shieh, Y.Y.; Sun, C.Y.; Peng, C., "Low cost silver alloy wire bonding with excellent reliability performance," in Electronic Components and Technology Conference (ECTC), 2013 IEEE 63rd , vol., no., pp.1569-1573, 28-31 May 2013.

[150] Lu, C., "Review on silver wire bonding," in Microsystems, Packaging, Assembly and Circuits Technology Conference (IMPACT), 2013 8th International , vol., no., pp.226-229, 22-25 Oct. 2013

[151] Xiao, Y.; Natarajan, R.; Chow, T.P.; Rymaszewski, E.J.; Gutmann, R.J., "Flip-chip flex-circuit packaging for 42 V/16 A integrated power electronics module applications," in Applied Power Electronics

Conference and Exposition, 2002. APEC 2002. Seventeenth Annual IEEE , vol.1, no., pp.21-26 vol.1, 2002

[152] Bai, John G.; Guo-Quan Lu; Liu, Xingsheng, "Flip-chip on flex integrated power electronics modules for high-density power integration," in Advanced Packaging, IEEE Transactions on , vol.26, no.1, pp.54-59, Feb. 2003.

[153] Muralidharan G., Tiegs T. N., "Composite die-attach materials for high-temperature packaging applications", High Temperature Electronics Conference HITEC, 2006.

[154] Jacob P., Held M., Sacco P., et al., "Reliability testing and analysis of IGBT power semiconductor modules," The IEEE Colloquim IGBT Propulsion Drives, 1995. pp. 4/1–4/5

[155] Knoerr M., Kraft S., Schletz A., "Reliability assessment of sintered nano-silver die attachment for power semiconductors," in Proc. 12th Electron. Package. Technol. Conf., 2010. pp. 56–61

[156] Buttay C., Masson A., Li J., et al., "Die attach of power devices using silver sintering bonding process optimization and characterization," The IMAPS High Temperature Electron. Netw., 2011.

[157] Manikam V. R., Cheong K. Y., "Die attach materials for high temperature applications: a review," IEEE Trans. Compon., Package. Manuf. Technol., 2011. 1, (4), pp. 457–478

[158] Hopkins D. C., Kellerman D. W., Wunderlich R. A., et al., "High-temperature, high-density packaging of a 60kW converter for >200°C embedded operation", Applied Power Electronics Conference and Exposition, 2006.

[159] Humpston G., Jacobson D. M., "Principles of Soldering", ASM International, 2004.

[160] Welch III W. C., Chae J., Najafi K., “Transfer of metal MEMS packages using a wafer-level solder transfer technique”, IEEE Transactions on Advanced Packaging, 2005. 28, (4), pp 643–649

[161] Bai J. G., Zhang Z. Z., Calata J. N., et al., “Low-temperature sintering of nanoscale silver paste: a lead-free die-attach solution for high-performance and high-temperature electronic packaging”, High Temperature Electronics Conference, 2012.

[162] Pan Wei Chih; Mesa, B.J.A.; Xie Hong; Goh Min Hao, "Application and high temperature storage test on Zn-Al-Ge high temperature solder for die attach," in Electronics Packaging Technology Conference (EPTC), 2014 IEEE 16th , vol., no., pp.463-468, 3-5 Dec. 2014

[163] McCluskey F. P., Wang Z., Dash M., Huff D., “Reliability of high temperature solder alternatives”, High Temperature Electronics Conference HITEC, 2006.

[164] Lu G-Q., Calata J. N., Zhang Z., Bai J. G., “A lead-free, low-temperature sintering die-attach technique for high-performance and high temperature packaging”, IEEE CPMT Conference on High Density Microsystem Design and Packaging and Component Failure Analysis HDP 2004, pp. 42–46

[165] Wu M., Lu G-Q, Yin J., et al., “Thermal modelling and electrical analysis of the nano-silver paste die-attached power device package at high temperature”, CPES Conference and Site Visit, 2006.

[166] Joo S., Baldwin D. F., “Rapid prototyping of micro-systems packaging using a data-driven chip-first process and nano-particles metal colloids”, Advancing Microelectronics, 2006. pp. 11-14

[167] Parylene Properties. Available: http://scscoatings.com/what_is_parylene/parylene_properties.aspx, Accessed Apr. 8, 2015.

[168] Miyoshi, Hiromasa; Endoh, Keiichi; Kurita, Satoru, "Application of Silver Nano Particle to Pressureless Bonding onto a Copper Surface - Consideration of Substitute Material for Lead Solder," in Integrated Power Systems (CIPS), 2014 8th International Conference on , vol., no., pp.1-5, 25-27 Feb. 2014

[169] Cao X., Wang T., Ngo K. D. T., et al., "Parametric study of joint height for a medium-voltage planar package," IEEE Trans. Comp. Package. Technol., Sep. 2010. 33, (3), pp. 553–562

[170] Cao X., Wang T., Ngo K. D. T., et al., "Height optimization for a medium-voltage planar package," in Proc. 24th Annual. IEEE Appl. Power Electron. Conf. Expos., Washington D.C., Feb. 2009, pp. 479– 484.

[171] Zhang Z., Bai J. G., Lu G-Q, et al. "Low-temperature Sintering Nanoscale Silver Paste as an High-Temperature package Solution", CPES Conference and Site Visit, 2005.

[172] Cyclotene* 3000 Series—Processing Procedures for CYCLOTENE 3000 Series Dry Etch Resins. Available: http://msdssearch.dow.com/PublishedLiteratureDOWCOM/dh_08b4/0901b803808b4ed7.pdf?filepath=/888-00006.pdf&fromPage=GetDoc. , Accessed Apr. 8, 2015.

[173] Cyclotene* 4000 Series—Processing Procedures for CYCLOTENE 4000 Series Resins-DS3000 Immersion Develop Process. Available: http://msdssearch.dow.com/PublishedLiteratureDOWCOM/dh_08b4/0901b803808b4eda.pdf?filepath=/888-00008.pdf&fromPage=GetDoc. Accessed Apr. 9, 2015.

[174] P84 Polyimide Solution—Technical Information. Available: http://hppolymer.com/pdfs/P84-%20Polyimide%20Solution1.pdf, Accessed Apr. 9, 2015.

[175] Davis J. H., Rees D. W., Riley I. H., "Silicone encapsulating and potting materials," Proc. IEE-B, Electron. Commun. Eng., 1962. 109, (21), pp. 266–270

[176] Wong C. P., Segelken J. M., Balde J. W., "Understanding the use of silicone gels for non-hermetic plastic packaging," IEEE Trans. Compon., Hybrids, Manuf. Technol., Dec. 1989. 12, (4), pp. 421–425

[177] Durapot Epoxies—High Performance Casting, Embedding and Encapsulating Compounds. Available: http://www.cotronics.com/vo/cotr/pdf/860.pdf, accessed Apr. 8, 2015.

[178] CF-4721—Technical Data Sheet. Available: http://nusil.com/products/ProductProfiles/CF-4721/CF-4721P.pdf, accessed Apr. 9, 2015.

[179] Technical Data Sheet—QSIL 550 2-Part Addition Cure Encapsulant. Available: http://www.acc-silicones.com/content/products/qsil573.ashx, Accessed Apr. 8, 2015.

[180] EPM-2422—Technical Data Sheet. Available: http://www.silicone-polymers.com/pdfMaster/EPM-2422P.pdf, accessed Apr. 9, 2015.

[181] R-2188—Technical Data Sheet. Available: http://nusil.com/products/ProductProfiles/R-2188/R-2188P.pdf, accessed Apr. 8, 2015.

[182] Scofield J. D., Merrett J. N., Richmond J., et al., "Performance and reliability characteristics of 1200 V, 100 A, 200°C half-bridge SiC MOSFET-JBS diode power modules," in Proc. Int. Conf. High Temperature Electron. (HiTEC), Albuquerque, NM, USA, May 2010.

[183] Niwa, K.; Nakamura, J.; Murakawa, K.; Nakamura, M., "New alumina substrate for hybrid integrated circuits," IEEE Transactions on Parts, Hybrids, and Packaging, Dec 1974. 10, (4), pp.262, 266

[184] Ji H., Cheng X., Chen H., et al. "Direct bonding of alumina substrate with copper heat sink in air assisted by ultrasonic vibrations for high power LEDs devices," 14th International Conference on Electronic Packaging Technology (ICEPT), Aug. 2013, pp.1158,1161, 11-14

[185] Chen L. Y., "Temperature dependent dielectric properties of polycrystalline AlN substrates with yttrium oxide additives", High Temperature Electronics Conference HITEC 2006, May 2006.

[186] Savrun E., Wu D., "High-temperature dielectric properties of aluminum nitride", High Temperature Electronics Conference HITEC 2006, May 2006.

[187] Mounce S., McPherson B., Schupbach R., et al., "Ultra-lightweight, high efficiency sic based power electronic converters for extreme environments," Aerospace Conference, 2006 IEEE, pp.19

[188] Beica, R., "Flip chip market and technology trends," Microelectronics Packaging Conference (EMPC), 2013 European, pp.1,4, 9-12 Sept. 2013. Chou, B.; Beilin, S.; Jiang, H.; Kudzuma, D.; Lee, M.; McCormack, M.; Massingill, T.; Peters, M.; Roman, J.; Takahashi, Y.; Wang, V., "Multilayer high density flex technology," Electronic Components and Technology Conference, 1999. 1999 Proceedings. 49th, vol., no., pp.1181, 1189, 1999.

[189] van der Duijn Schouten, N.P., Gordon, B.M., McMahon, R.A., et al.: 'Integrated drives using high voltage power ICs'. Eighth Int. Conf. on Power Electronics and Variable Speed Drives, 2000. (IEE Conf. Publ. No. 475), pp. 554–559

[190] Chou, B.; Beilin, S.; Jiang, H.; et al., "Multilayer high density flex technology," Electronic Components and Technology Conference, 1999. Proceedings. 49th, pp.1181, 1189

[191] Woo, D.R.M., Hwang H. Y., Li J.A.J. et al., "High power SiC inverter module packaging solutions for junction temperature over 220°C," Electronics Packaging Technology Conference (EPTC), Dec. 2014. IEEE 16th , pp.31,35, 3-5

[192] Pascariu, G.; Cronin, P.; Crowley, D., "Next generation electronics packaging utilizing flip chip technology," Electronics Manufacturing Technology Symposium, July 2003. IEMT 2003. IEEE/CPMT/SEMI 28th International, pp.423, 426, 16-18

[193] X. Liu, S. Xu, G.-Q. Lu, and D. A. Dillard, “Effect of substrate flexibility on solder joint reliability,” Microelectron. Rel., vol. 42, pp. 1883–1891, 2002

[194] Bivragh, M.; Kelley, M.; Van Sinte Jans, J.-B.; Indrajit, P.; Slattery, O.; Barton, John; O'Mathuna, S.C.; O'Flynn, B.; Malshe, A.P., "Thermo-mechanical modelling and thermal performance characterisation of a 3D folded flex module," in Electronic Components and Technology Conference, 2006. Proceedings. 56th , vol., no., pp.6 pp.-, May 30 2006-June 2 2006

[195] Stockmeier, T., Beckedahl, P., Gobl, C., Malzer, T., “SKiN: Double side sintering technology for new packages”, ISPSD 2011.

[196] Savrun E., “Packaging considerations for very high temperature Microsystems,” Proc. IEEE, 2002. 2, (6), pp. 1139–1143

[197] Sugawara Y., Takayama D., Asano K., “3 kV 600 a 4H-SiC high temperature diode module,” in Proc. Power Semicond. Devices ICs, 2002. pp. 245–248

[198] Nawa K., "Reliability study for CTE mismatching in build-up structure," Electronic Components and Technology Conference, 2001. Proceedings, 51st, pp.1154, 1158

[199] Chandran B., Schmidt W.F., Gordon M.H., "A novel bonding technique to bond CTE mismatched devices," Electronic Components and Technology Conference, May 1996. Proceedings, 46th , pp.1151,1158, 28-31

[200] Gerber M., Marz M., "System integration in automotive power systems," European Conference on Power Electronics and Applications, Sept. 2005, pp.10 -14

[201] Jain, P.K., "Power electronics for low voltage semiconductor technology: challenges and some possible solutions," Power Electronics and Motion Control Conference, Aug. 2004. IPEMC 2004. The 4th International, 1, pp.20, 28 14-16

[202] Kolar J., Drofenik U., Biela J., et al., "PWM converter power density barriers," Power Conversion Conference - Nagoya, April 2007. PCC '07, pp. 2-5

[203] Centner M, Sabelfeld I. “Coupled fluid-thermal network modeling approach for electrical machines,” International Conference on Electrical Machines (ICEM); 2-5 Sept, 2012. p. 1238-41.

[204] Stanislas Hasco¨et, Cyril Buttay, Dominique Planson, Rodica Chiriac, Amandine Masson. “Pressureless Silver Sintering Die-Attach for SiC Power Devices,” ECSCRM, Sep 2012, St Petersburg, Russia. trans tech publications, 4p, 2012

[205] C. Pes et al., "Two-Dimensional and Three-Dimensional Mechanical Analyses of the Superconducting Outsert of the LNCMI Hybrid Magnet,"

in IEEE Transactions on Applied Superconductivity, vol. 26, no. 4, pp. 1-5, June 2016

[206] Masson A, Sabbah W, Riva R, Buttay C, Azzopardi S, Morel H "Die attach using silver sintering practical implementation and analysis" https://hal.archives-ouvertes.fr/hal-00874465/document

[207] Connor, P. "Computational Fluid Dynamics Modelling of a Synchronous Electric Generator" [PhD Thesis]: University of Nottingham; 2014.